Interfacial Heat Transfer and Solidification of Mg and Al Alloys in a Single Belt Casting Process

Jinsoo Kim

A thesis submitted to the Faculty of Graduate Studies and Research
in partial fulfillment of the requirements for the degree of
Doctor of Philosophy

Department of Metals and Materials Engineering
McGill University
Montréal, Québec, Canada
October, 2005

Library and
Archives Canada

Published Heritage
Branch

395 Wellington Street
Ottawa ON K1A 0N4
Canada

Bibliothèque et
Archives Canada

Direction du
Patrimoine de l'édition

395, rue Wellington
Ottawa ON K1A 0N4
Canada

Your file Votre référence
ISBN: 978-0-494-21663-7
Our file Notre référence
ISBN: 978-0-494-21663-7

NOTICE:
The author has granted a non-exclusive license allowing Library and Archives Canada to reproduce, publish, archive, preserve, conserve, communicate to the public by telecommunication or on the Internet, loan, distribute and sell theses worldwide, for commercial or non-commercial purposes, in microform, paper, electronic and/or any other formats.

The author retains copyright ownership and moral rights in this thesis. Neither the thesis nor substantial extracts from it may be printed or otherwise reproduced without the author's permission.

AVIS:
L'auteur a accordé une licence non exclusive permettant à la Bibliothèque et Archives Canada de reproduire, publier, archiver, sauvegarder, conserver, transmettre au public par télécommunication ou par l'Internet, prêter, distribuer et vendre des thèses partout dans le monde, à des fins commerciales ou autres, sur support microforme, papier, électronique et/ou autres formats.

L'auteur conserve la propriété du droit d'auteur et des droits moraux qui protège cette thèse. Ni la thèse ni des extraits substantiels de celle-ci ne doivent être imprimés ou autrement reproduits sans son autorisation.

In compliance with the Canadian Privacy Act some supporting forms may have been removed from this thesis.

While these forms may be included in the document page count, their removal does not represent any loss of content from the thesis.

Conformément à la loi canadienne sur la protection de la vie privée, quelques formulaires secondaires ont été enlevés de cette thèse.

Bien que ces formulaires aient inclus dans la pagination, il n'y aura aucun contenu manquant.

Canada

ACKNOWLEDGEMENTS

No thesis is ever the work of a single individual, but a reflection of love, support and experiences received from his neighborhood. In completing this thesis, I am grateful to my supervisor, Prof. R.I.L. Guthrie, who has drawn to my attention the fascinating world of process metallurgy. I cannot express my gratitude enough for his consistent advice and support.

I am also thankful to Dr. Mihaiela Isac for her enlightening guidance and fruitful discussions about my work and life. It was a privilege itself working with her.

Particular thanks are due to Dr. Jiyoung Byun, Dr. Hiroshi Nogami, Prof. Reza Aboutalebi for discussing computer programming codes and Mr. Alain Gagnon for the experimental set-up.

My very special thanks are due to Dr. Donghui Li. Some of results were heavily based on the collaborative work with him.

Most of all, I would like to thank my family, especially my mother, Jungja Song. Her patience and support will never be forgotten in my life.

ABSTRACT

Strips of magnesium (AZ91 and AM50) and aluminum (AA6111) alloys were cast on a moving mold system devised for simulating single belt casting operations. Different type of substrates were used for the moving mold; copper, low carbon steel, alumina coated steel, nickel coated steel, and zirconia coated steel. Interfacial heat fluxes between the solidifying strip and the moving mold substrate were calculated by the IHCP (Inverse Heat Conduction Problem) technique. The temperature history of the solidifying strip was calculated using the Enthalpy FVM (Finite Volume Method) associated with Scheil's model of solidification. The influence of: thermophysical and morphological properties of mold substrates, wetting environment, casting speed, melt superheat, and grain refiner, on strip microstructures and their cooling rates, were thoroughly investigated.

Maximum heat fluxes appeared about 0.1~0.2 seconds after the moment of thermal contact. For a copper substrate, these reached up to 7 MW/m^2, whereas those for a steel substrate were ~3 MW/m^2. The rate of heat transfer to coated substrates was significantly delayed and reduced because of the low thermal conductivity of coating layers. Maximum cooling rates of aluminum and magnesium strips reached about 200°C/s on copper and about 150°C/s on steel.

It was found that the major thermal resistance resided in an interfacial layer separating the strip from the substrate. This interfacial layer presumably corresponded to the shrinkage of solidified skin or the entrainment of a thin air film resulting in numerous air pockets at the bottom surface of strips. Oil spraying onto the mold surface changed the interfacial wettability and dramatically improved the cast surface of the strips. The good quality of strip samples obtained suggests the high potential for the direct casting of these alloys on single belt casters.

RÉSUMÉ

Des bandes d'alliages de magnésium (AZ91 et AM50) et d'aluminium (AA6111) ont été coulées sur un système de moule mobile conçu pour simuler des opérations de coulée en bande à courroie simple. Différents types de substrats ont été employés pour le moule mobile; cuivre, acier à faible teneur en carbone, acier avec revêtement d'alumine, acier avec revêtement de nickel et acier recouvert de zirconium. Les flux de chaleur à l'interface de la bande solidifiant et du substrat en mouvement ont été calculés par la technique de l'*Inverse Heat Conduction Problem* (problème inverse de conduction de la chaleur). L'historique de température de la bande solidifiant a été calculé en utilisant l'enthalpie *Finite Volume Method* (méthode de volume fini) liée à la méthode de Scheil. L'influence de nombreuses propriétés (propriétés thermophysiques et morphologiques des substrats, mouillabilité, vitesse de coulée, surfusion du métal liquide, affineur de grain) sur la microstructure des bandes et leurs taux de refroidissement, a été rigoureusement étudiée.

Les flux maximums de chaleur sont apparus 0.1~0.2 secondes après le contact thermique. Pour un substrat de cuivre, ceux-ci ont atteint jusqu'à 7 MW/m^2, alors que pour un substrat en acier les valeurs étaient de ~3 MW/m^2. Les taux de transfert thermique aux substrats avec revêtement ont été significativement diminués et retardés en raison de la basse conductivité thermique des couches superposées. Les taux de refroidissement maximaux de bandes de 1 mm d'aluminium et de magnésium ont atteint jusqu'à 200°C/s sur le cuivre et environ 150°C/s sur l'acier.

Il a été déterminé que la résistance thermique majeure provenait de l'interface séparant la bande métallique du substrat. Cette couche a vraisemblablement provoqué l'apparition d'une mince couche d'air ayant pour résultat de nombreuses aspérités à la surface inférieure des bandes solidifiées. L'application d'huile sur la surface du moule a modifié la mouillabilité et a grandement amélioré la qualité de surface des bandes métalliques solidifiées. La bonne qualité des échantillons obtenus avec les bandes suggère le haut potentiel d'application pour couler ces alliages directement sur la machine de coulée à courroie simple.

TABLE OF CONTENTS

CHAPTER 3. INTERFACIAL HEAT TRANSFER 57

CHAPTER 4. EXPERIMENTAL APPRATUS & METHODOLOGY 78

CHAPTER 5. EXPERIMENTAL RESULTS 97

LIST OF TABLES

CHAPTER 1. INTRODUCTION

CHAPTER 2. LITERATURE REVIEW

CHAPTER 3. INTERFACIAL HEAT TRANSFER

CHAPTER 4. EXPERIMENTAL APPRATUS & METHODOLOGY

CHAPTER 5. EXPERIMENTAL RESULTS

CHAPTER 6. DISCUSSION

APPENDICES

LIST OF FIGURES

CHAPTER 1. INTRODUCTION

CHAPTER 2. LITERATURE REVIEW

CHAPTER 3. INTERFACIAL HEAT TRANSFER

CHAPTER 4. EXPERIMENTAL APPRATUS & METHODOLOGY

CHAPTER 5. EXPERIMENTAL RESULTS

CHAPTER 6. DISCUSSION

APPENDICES

CHAPTER
1

INTRODUCTION

1.1 INTRODUCTION

When a novel metallurgical process is suggested, it experiences many steps prior to commercialization, and much effort is made in order to modify, elaborate, and complete the process techniques during each stage of its development. It is the aim of the process metallurgist to develop these techniques, in order to replace an old process and to improve the product quality. Near net shape casting is such a process that has been dreamt of for the last 200 years but is only now coming to fruition. Some of these near-net-shape casting processes are shown in Fig. 1.1.1 schematically [1]. Compared to ingot or conventional casting, they have the following advantages:

- (i) Elimination of strands for roughing passes, which in turn, also avoids cooling down, reheating, and the accompanying energy loss;
- (ii) Production in smaller tonnages of various steel grades and quality;
- (iii) Reduction of operational costs and capital investment;
- (iv) High potential for producing metal alloys with good mechanical properties due to its high rate of solidification;
- (v) Energy savings.

In conventional slab casting, Fig. 1.1.1 (a), the strand thickness at the lower end of the mold is about 250 mm. After it is extracted from the mold, the slabs are cooled down and transported to the hot rolling mills where they are reheated to a hot rolling temperature. The thin slab casting, Fig. 1.1.1 (b), is similar to conventional casting except casting and hot rolling mills are closely linked to constitute an integrated production line, and no rougher is required. Thus, the initial slab thickness is about 60 mm which means they need less hot rolling steps to reduce their thicknesses. However, a faster casting speed is needed to maintain the productivity of a conventional caster. Both these processes use stationary molds, which reach an upper limit of casting speed of about 10 m/min due to the friction between strand and mold. With moving mold techniques, the limit of casting speed can be overcome and high casting speeds can be achieved to keep pace with the productivity of conventional casting. The twin roll casting process, Fig. 1.1.1 (c), was recently brought to commercial success, because of the satisfactory quality of the final product. However, the roll diameters need to be larger and larger to provide sufficient cooling length if one desires to increase casting speed and match the productivity of conventional casting. For instance, the productivity of high speed casting for 250 mm thick slabs with 2 m/min casting speed would require twin roll caster to have 2.46 m roll diameter for 3 mm thick strips with 21.5 revolutions/min or 5.09 m roll diameter for 8mm thick slabs with 3.9 revolutions/min respectively. In principle, the casting speed of the twin roll process can be raised, for the required strip thickness, by increasing the length of the cooling surface, that is by increasing the diameters of the rolls, but their size becomes pretty impractical [2]. On the other hand, to get the same productivity prescribed, the metallurgical length of a single belt caster (Fig. 1.1.1 (d)) just needs 11.4 m for 10 mm thick strip with the same casting speed of 2 m/min. If the casting speed increases, the metallurgical length can be decreased dramatically. In this regard, the single belt casting process has the following operational advantages compared to other competitive near net shape casting processes:

(i) High productivity strip production;
(ii) Low investment and operational cost;
(iii) Facilitated melt feeding and low sensitivity to breakouts of liquid steel;

In a single belt casting process, as shown in Fig. 1.1.2, a liquid metal film is to be established onto a moving belt, where it is to be cooled and solidified by water sprays. These emerge from nozzles located under the belt. The result possible is a solid strip with the desired uniform thickness. The system determines how liquid metal will be fed onto the cooling belt and is responsible for an even distribution of liquid metal across the width and thickness of the cast strip. From Fig. 1.1.3 which compares the productivities of various near net shape casting processes, a productivity of 100 tph/m width for 4 mm thickness would require a belt speed of about 60 m/min or 1 m/s. With this speed range, it is essential to feed liquid metal onto the moving belt in a stable manner while achieving required thicknesses. Furthermore, the solidification between the liquid metal and the belt should be controlled precisely, so as to get the required microstructures within the strips produced. In particular, interfacial heat transfer from the solidifying strip to the belt is one of the most important factors since the thermal history of strip has a great influence on a quality of the product as well as the caster's productivity.

Since 1987, funded by ECSC in Europe, the single belt casting process has attained much interest worldwide with a variety of research partners. Main cooperation companies, as well as installed institutions, are summarized in Table 1.1.1.

Table 1.1.1. Single belt strip casters and cooperating companies [3]

Installed Institution	Cooperation Companies
Clausthal, Germany	Mannesmann-Demag AG, Salzgitter AG, Thyssen-Krupp Stahl AG, Preussag Stahl AG
MEFOS, Sweden	Mannesmann Demag Hüttentechnik, AB Sandvik Steel, SSAB Tunnplåt AB, Avesta AB, Rautaruukki Oy
MSA, Brazil	Mannesmann Demag Hüttentechnik, Daido Steel (Japan), Vitcovice Steel (Czech Republic)

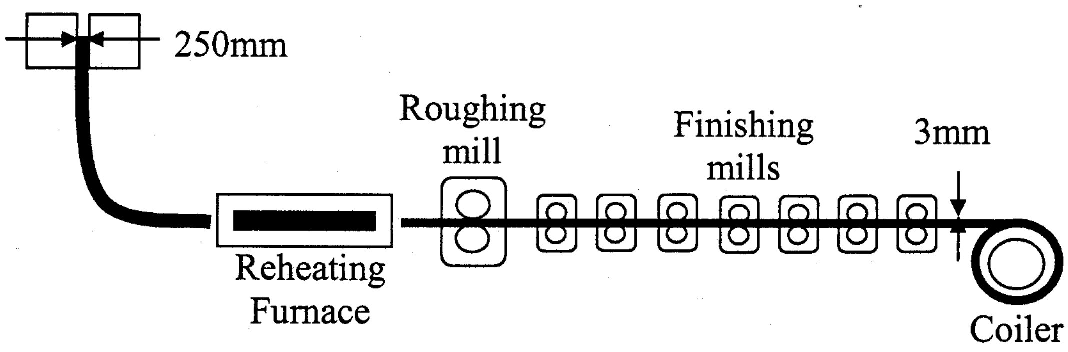

(a) Conventional slab casting

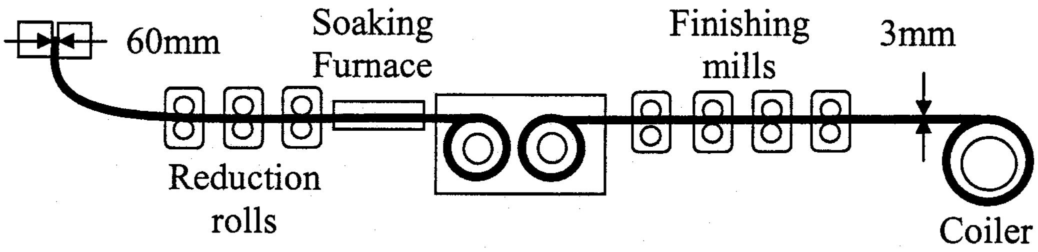

(b) Thin slab casting

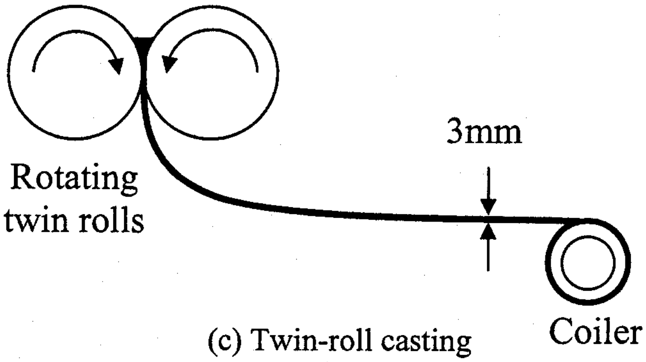

(c) Twin-roll casting

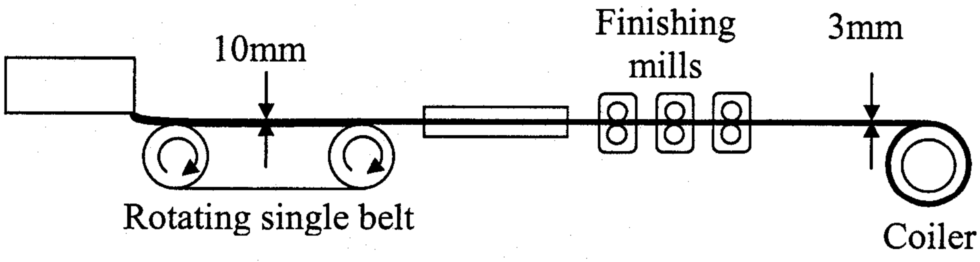

(d) Single belt casting

Fig. 1.1.1. Layout of various processes for thin strip production [1]

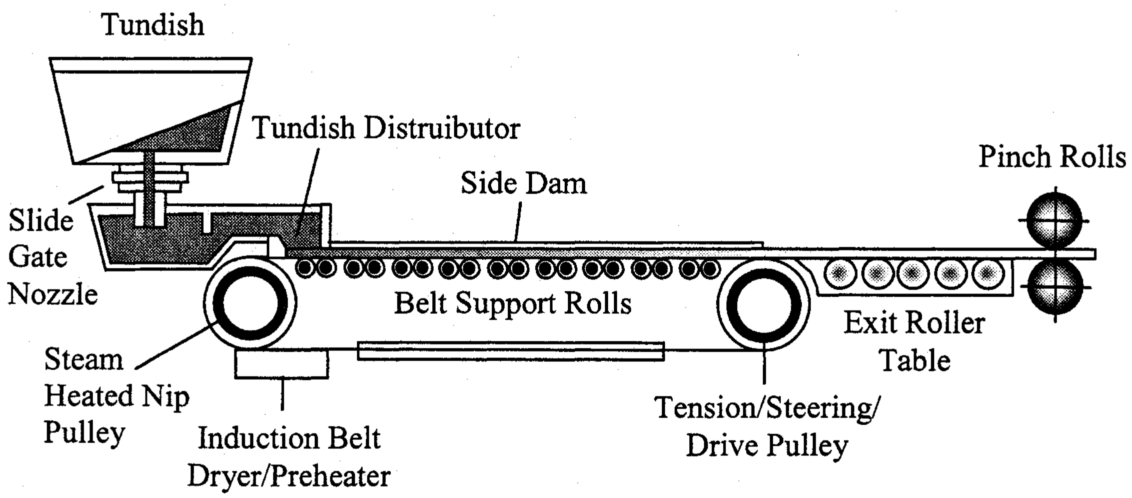

Fig. 1.1.2. Schematic diagram of Hazelett single belt strip caster

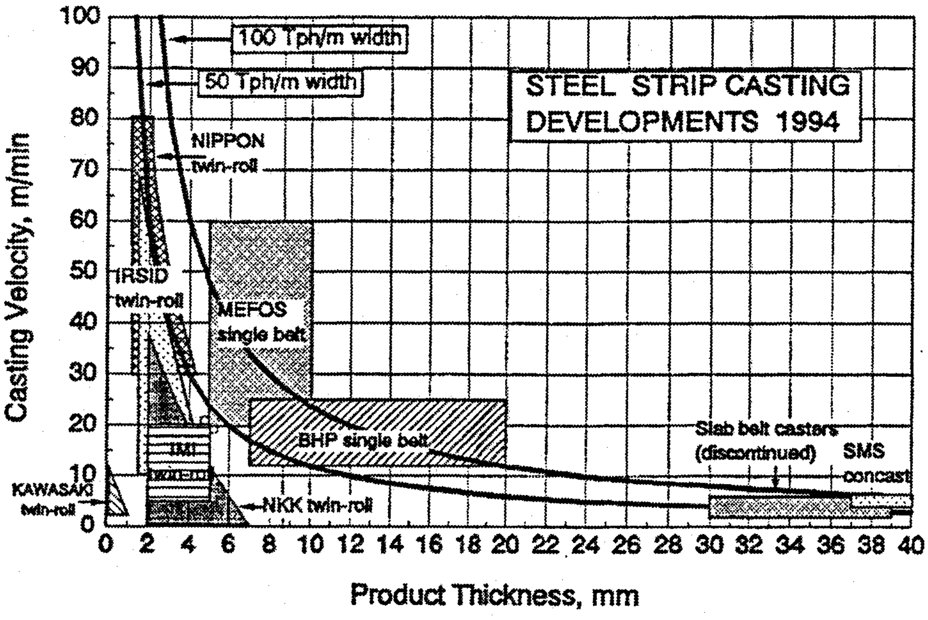

Fig. 1.1.3. Summary of the productivity of near net shape steel casters [4]

1.2 THESIS OUTLINE

During the 1990s, in the MMPC, many consecutive studies have been carried out to verify the eligibility of the single belt casting process and to operate the Hazelett pilot-caster gifted from B.H.P. Australia to Dr. Guthrie. Physical modelling of various delivery systems have been tested. As well, computational modelling has been performed [4-6]. In addition, a small scale strip casting simulator (SCS) was devised to cast real alloys under different conditions of cast alloy chemistries, mold substrate velocity, substrate materials, substrate coatings, substrate roughness, melt superheat, etc.

In the present work, using the SCS prescribed, the major effort was placed into analyzing the rate of interfacial heat transfer into cooling substrates and the effect of heat extraction rates on the microstructures of strip samples produced. The work was aimed at understanding the fundamentals of metal/mold heat transfer occurring in the belt casting process and the effect of operating parameters in affecting product quality. Magnesium alloys of AM50 and AZ91, as well as the aluminum alloy of AA6111, were selected as main casting metals.

The work embodied in this thesis is described in a total of six chapters:

In Chapter 1, introductory remarks are given and a general description of the outline and scope of the work is presented.

In Chapter 2, an extensive literature review for this Ph.D.'s work is carried out. Various experimental results regarding interfacial metal-mold heat transfer were investigated. The interfacial heat transfer analysis between the solidifying strip and the cooling substrate is presented. The Inverse Heat Conduction Problem (IHCP) method and the Enthalpy Finite Volume Method (FVM) are also explained in detail.

In Chapter 3, the interfacial heat transfer between the solidifying metal and the cooling mold is mathematically investigated assuming one-dimensional heat transfer.

In Chapter 4, experimental details of the SCS and the various experimental conditions studied, and experimental procedures are described.

In Chapter 5, casting results of magnesium and aluminum alloys were presented. Results contain the interfacial heat flux, heat transfer coefficient, temperature profiles of the strip produced, the metallography of microstructures, the SDAS (Secondary Dendrite Arm Spacings) and grain size measurement, and the local cooling rate.

In Chapter 6, an in-depth discussion of the experimental results is presented. A model to simulate the interfacial heat flux is suggested and the effects of experimental variables thereby analyzed.

In Chapter 7, some important conclusions drawn from the present study are summarized, together with suggestions for future work and contributions to original knowledge.

REFERENCES

1. Klaus Schwerdtfeger, Benefits, Challenges and Limits in New Routes for Hot Strip Production, *ISIJ International* **38**, 1998, pp. 852 - 861

2. K. H. Spitzer & K. Schwerdtfeger, Production of Steel Strip With a Single-Belt Process, *I&SM*, 1995, pp. 47 – 53

3. G. Carlsson, R. Nyström, H. Sandberg, W. Reichelt & U. Urlau, Single belt casting: A promising technique for the production of steel strip, *Scan. J. Metall.* **26**, 1997, pp.242-248

4. C. Jefferies, Modelling a novel, thin strip, continuous steel caster delivery system, *Ph.D. Thesis*, McGill University, 1995

5. P. G. Q. Netto, Mathematical and Physical Modelling of a Single Belt Casting Process, *Ph.D. Thesis,* McGill University, 1998

6. K. H. Moon, Physical and Mathematical Modelling of a Metal Delivery System for a Single Belt Caster, *Ph.D. Thesis,* McGill University, 2003

CHAPTER
2

LITERATURE REVIEW

2.1 SINGLE BELT CASTING PROCESS

The single belt casting process for steel strip production began in 1987, as a joint development project by Mannesmann Demag Hüttentechnik (MDH) in cooperation with MSA in Belo Horizonte, Brazil. Unreported trials by a Japanese company on an upwardly inclined single belt caster were apparently also carried out prior to that time. The Mannesmann casting project involved a variety of partners using laboratory and pilot-scale units located at the University of Clausthal, MSA, and MEFOS. Independently and simultaneously, the concept was filed for patent applications by Guthrie and Herbertson (1987), and they made arrangements with Prof. Belton, Director of Research, BHP, to initiate hot metal casting at BHP, Newcastle, to trial the concept, using a belt caster purchased from Hazelett Strip Casting Corp. in 1989. In 1999, the Hazelett single belt caster was moved and installed in the MMPC foundry, Canada. Table 2.1.1 provides a brief summary of casting facilities at these institutions and these casters are presented from Fig. 2.1.1 to Fig. 2.1.4.

Table 2.1.1. Single belt strip casting facilities [1]

Institution	Manufacture	Ladle (ton)	Strip size (mm t × mm w)	Casting speed (m/min)	Start up
Clausthal, Germany	MDH	0.12-0.5	10-15 × 170-300	8-18	1989
MSA, Brazil	MDH	5-7	10-15 × 900	20-40	1989
MEFOS, Sweden	MDH	4-6	10-15 × 450-870	20-60	1992
MMPC/BHP, Canada/Australia	Hazelett	1.0	2-10 × 200	24	1989

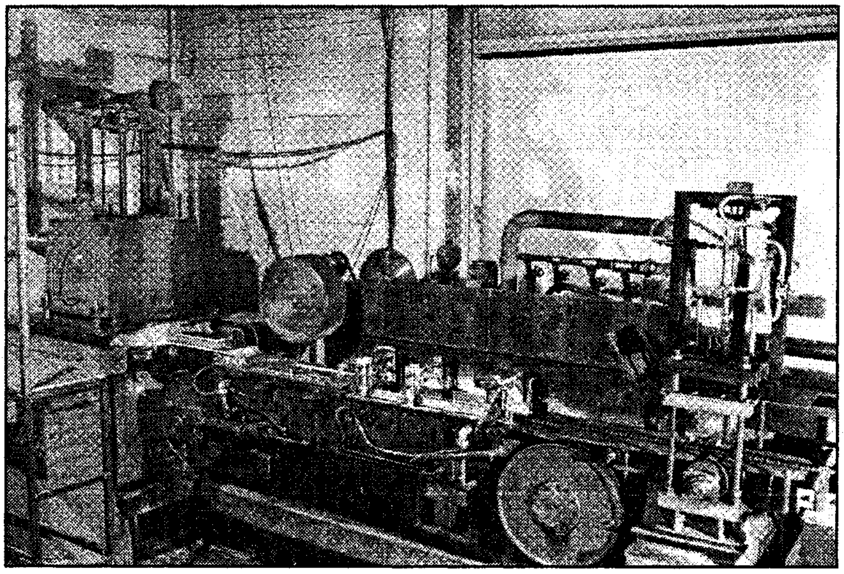

Fig. 2.1.1. Single belt caster at Clausthal, Germany [2]

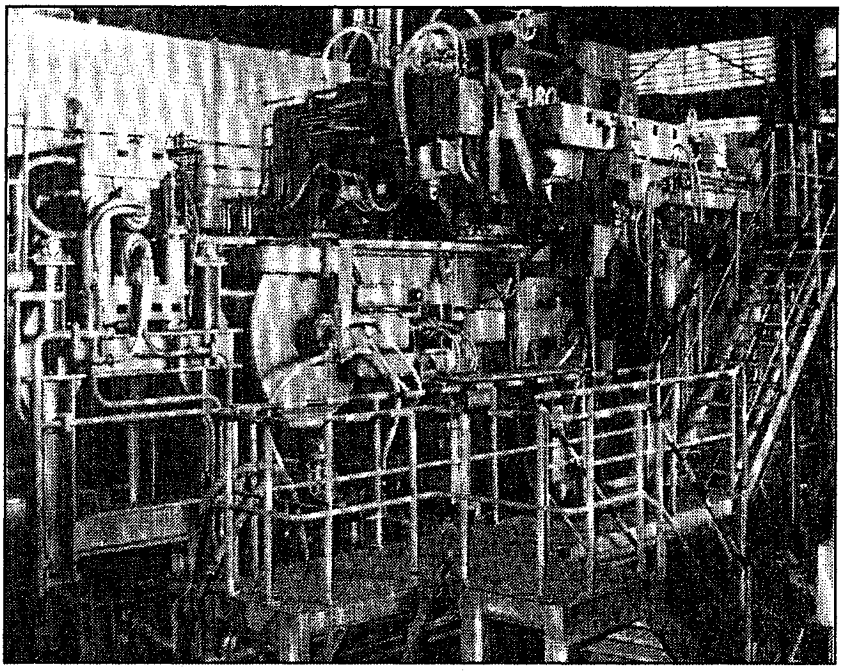

Fig. 2.1.2. Single belt caster at MSA, Brazil [3]

Fig. 2.1.3. Single belt caster at MEFOS, Sweden [4]

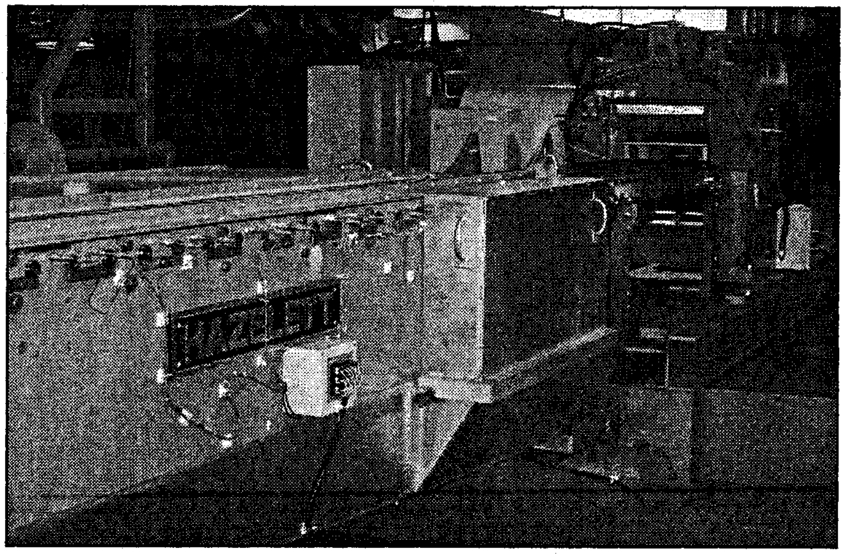

Fig. 2.1.4. Single belt caster at MMPC, Canada [5]

In a single belt caster, liquid metal can, with appropriate fluid flow delivery systems, be fed onto a moving belt resulting in a solid strip of metal of uniform and desired thickness. To provide stable conditions during the feeding of molten metal, metal delivery is of paramount importance. In order to meet these requirements, several methods for the delivery of molten steel have been proposed so far:

(i) Low Pressure System (LPS) developed at Clausthal. [4]
(ii) Tube Feeding System (TFS) deveolped at MEFOS. [4]
(iii) Extended nozzle system developed at McGill. [6]
(iv) Zig-zag nozzle system developed at Clausthal. [2]
(v) Argon rake nozzle developed at Clausthal. [7]
(vi) Three-chamber tundish developed at McGill. [8]

The low pressure system (Fig. 2.1.5) achieved the superior physical conditions for feeding liquid metal but involved handling difficulties. On the other hand, the tube feeding system (Fig. 2.1.6) was easy to handle but resulted in poorer conditions of flow at the point of transport onto the moving belt. A shrouded extended nozzle system (Fig. 2.1.7) was suggested to improve the stability of feeding by the insertion of flow modifiers but potentially encounters problems with nozzle clogging. The zig-zag nozzle system (Fig. 2.1.8) had an inclined plane where liquid metal flows in parallel channels with a free surface but non-uniform feeding was observed due to clogging of nozzles. Furthermore, modified zig-zag nozzle with argon rakes (Fig. 2.1.9) was developed to get the lateral melt distribution onto the belt. However, this multi-hole nozzle leads to the overlapping of hydraulic jumps of each impinging jet, which induces unstable meniscus. Recently, in McGill, a three-chamber type tundish (Fig. 2.1.10) was being developed and installed, which controls the slag level, tundish head, and melt distribution.

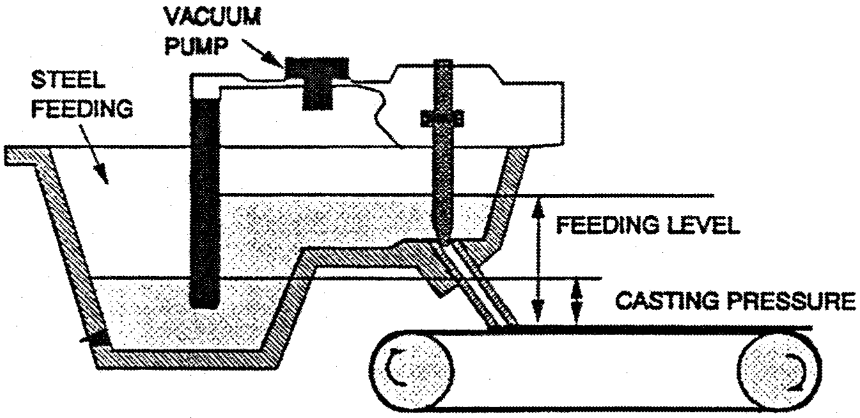

Fig. 2.1.5. Low Pressure System (LPS) with adjustable casting pressure

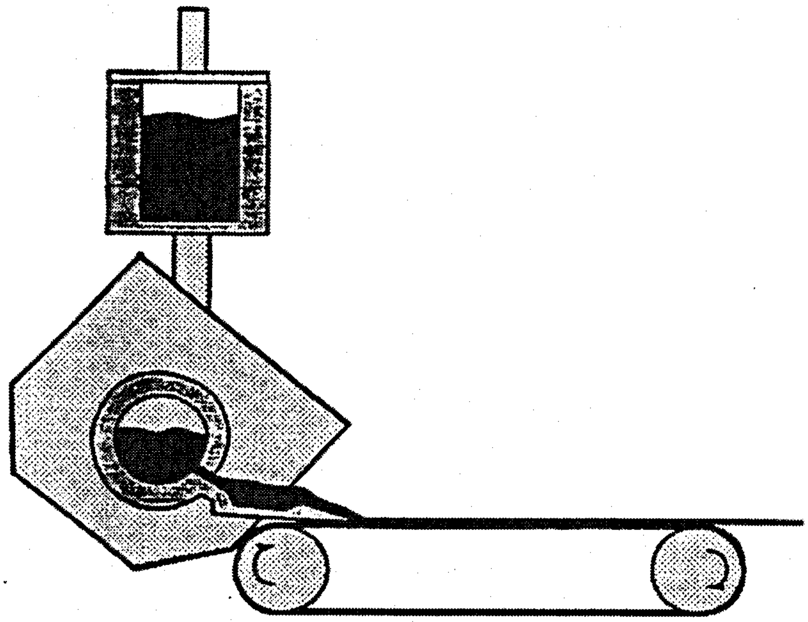

Fig. 2.1.6. Open Tube Feeding System (TFS)

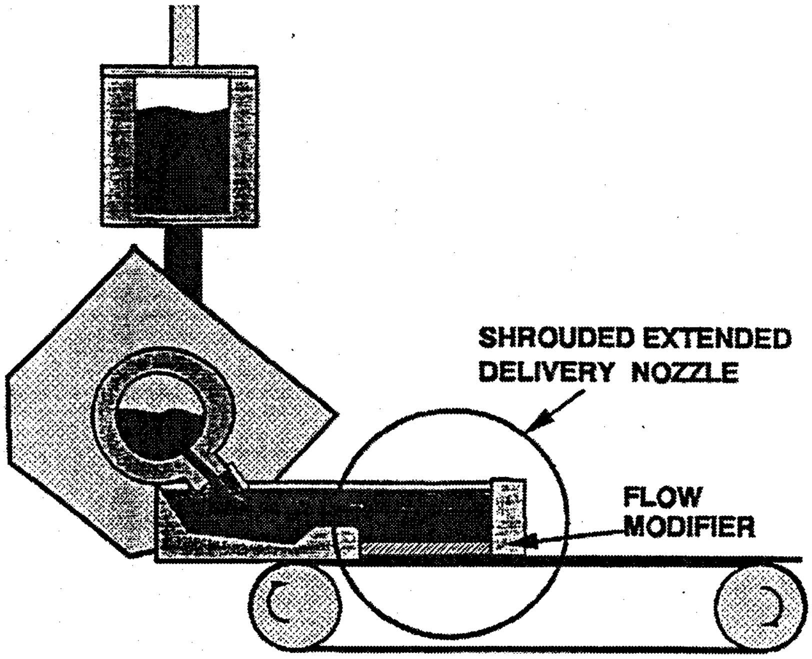

Fig. 2.1.7. Shrouded extended nozzle with flow modifier

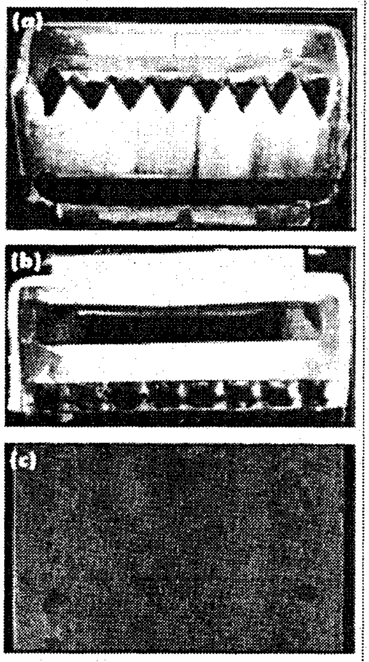

Fig. 2.1.8. Zig-zag nozzle system: (a) front, (b) bottom, and (c) the steel plate product

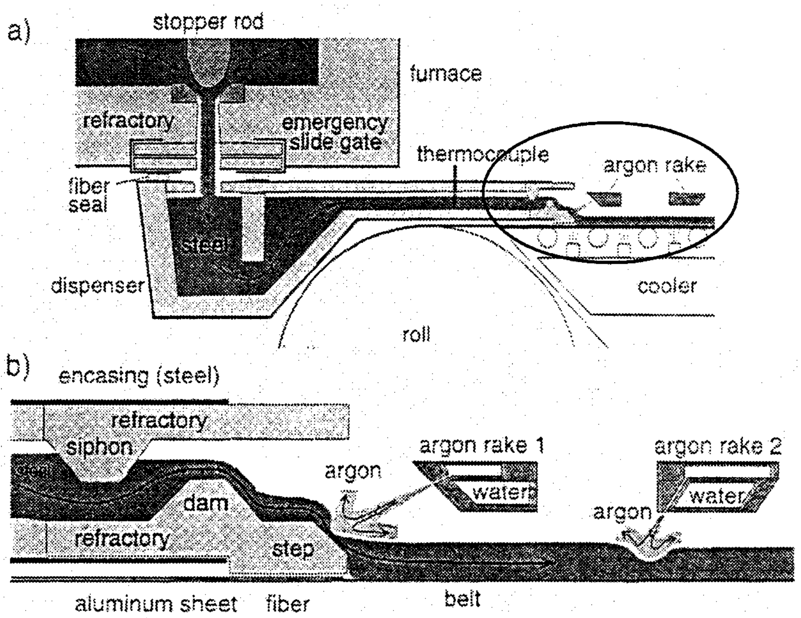

Fig. 2.1.9. Argon rake nozzle system:

a) Cross-section of the tundish and b) enlarged nozzle area with argon rakes

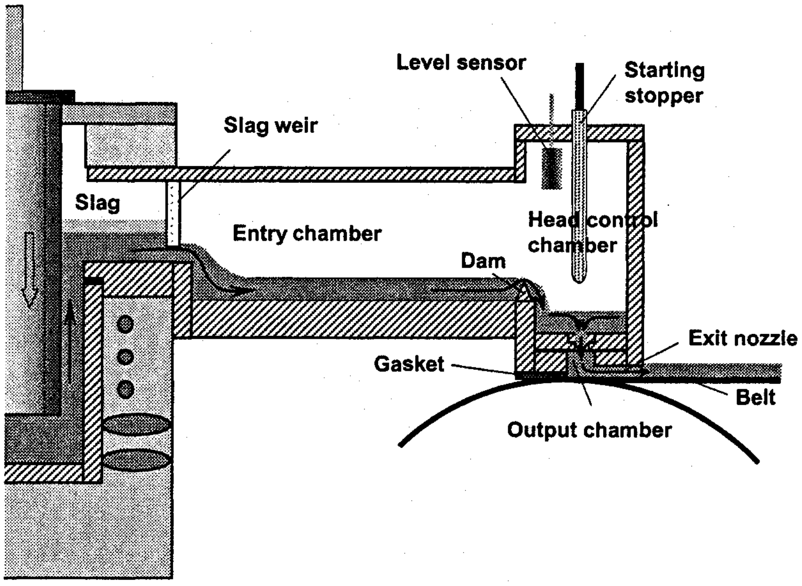

Fig. 2.1.10. Three-chamber tundish system

2.2 METAL-MOLD INTERFACIAL HEAT TRANSFER

2.2.1 Analytical interfacial heat transfer

As well as the delivery of liquid metal, interfacial heat transfer rates from the solidifying strip to a single belt caster are another important factor. It determines the quality of the product because the thermal history of the strip greatly influences the microstructures of the final strip produced. When liquid metal is spread onto the belt's surface, heat is simultaneously transferred from the top and bottom surfaces of the strip. Heat transfer from the top is governed by radiation and convection, while that from the bottom surface is mostly dominated by unsteady state heat conduction towards the belt.

Extensive effort has been made for the last thirty years to determine the precise interfacial heat fluxes and heat transfer coefficients at the metal-mold interface. Among the mathematical methods described in the literature, three main groups may be identified, including purely analytical, semi-analytical or empirical, and numerical techniques based on finite difference or finite element methods. In purely analytical techniques, the assumption of a constant interfacial heat transfer coefficient is made in order to obtain an analytical solution for the Fourier heat conduction equation [9-11]. On the other hand, the use of semi-analytical or empirical techniques do not attempt to rigorously solve the Fourier equation, but involve analyzing experimental data by means of semi-analytical formula [12]. Finally, numerical techniques, referred to as methods for solving the inverse heat conduction problem (IHCP), are used to determine the exact values of the time dependent interfacial heat fluxes, and by extension, instantaneous heat transfer resistances at the interface [13].

Garcia *et al.* [9,10] developed a mathematical heat transfer model by considering the solidification of metal under the superimposed effects of thermal conduction and Newtonian thermal contact. They assumed that the thermal properties of metal and mold are invariant during solidification including the heat transfer coefficient. Lead and aluminum alloys were used as cast metals and the Virtual Adjunct Method (VAM) was developed to predict the temperature profiles within the metal and cooling mold.

Lipton *et al.* [11] extended this concept to describe temperature distributions and the position of the solidus and liquidus isotherms. An Al-4.5%Cu melt was solidified in a water-cooled mold. They showed that the solidus and liquidus isotherm positions could be described by a quadratic polynomial function of temperature distribution in the solid, mushy zone, and liquid, by error functions.

Based on work with Al-Cu alloys and permanent Cu molds, Prates *et al.* [12] evaluated the value of heat transfer coefficients as a function of the surface density of pre-dendritic nuclei and heat extraction capacity. They also proposed a nucleation mechanism to explain the initial formation of a metal-mold interface with solid-solid contact. The postulation is based on the fact that, on a microscopic scale, the chill surface is not completely smooth and consists of small asperities protruding from the surface profile. Their results showed that for a critical value of heat transfer coefficient larger than 2.5 kW/m^2K, the multiplication mechanism was not effective in the formation of the chill zone even in the presence of highly turbulent flow. A multiplication mechanism corresponds to the separation of crystals from the dendrites growing in a thermal or constitutionally supercooled liquid. For a coefficient lower than this, the laminar-turbulent transition of fluid flow greatly improved the effectiveness of the multiplication mechanism.

2.2.2 Numerical analysis of interfacial heat transfer

As solidification progresses, the metal and mold either stay in contact at isolated asperities on the microscopically rough surfaces, or an interfacial gap separating the metal and mold gradually develop. One of the first significant works on this interfacial heat transfer mechanism for metal-mold systems was carried out by Ho and Pehlke [14-16]. They determined the value of h via the two independent methods:

(i) A computer solution of the inverse heat conduction problem (IHCP) using thermocouple measurements at selected locations in the casting and mold.

(ii) Measurements of the variation of interfacial gap size with time and deriving the values of h from heat transfer data across a static gap.

In their first type of experiments, Fig. 2.2.1, a copper chill was placed on top of a cylindrical, bottom-gated, casting, and a clearance of gap was detected by measuring the relative displacement of two transducers and by loss of electrical continuity. The second type of casting, Fig. 2.2.2, had a similar design except the chill was placed at the bottom. Thanks to the effect of gravity in this case, solid to solid contact was maintained at the metal-chill interface, but the high degree of interfacial non-conformity still resulted in a relatively low thermal conductance as indicated by the solution of the IHCP.

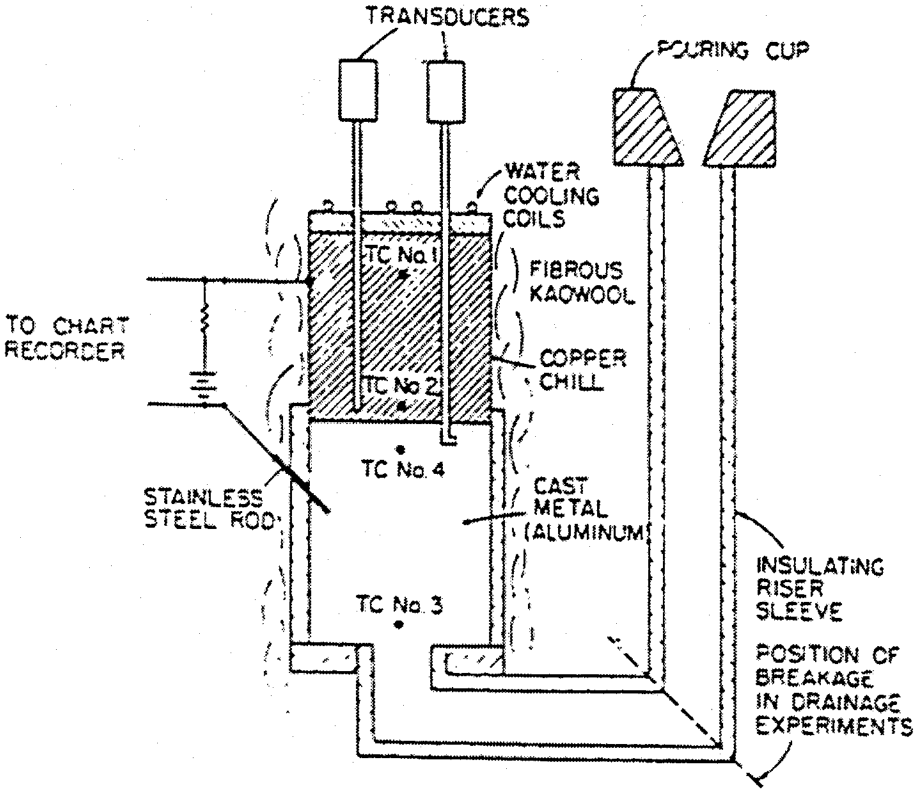

Fig. 2.2.1. First type of experimental casting (Top placed chill) [14]

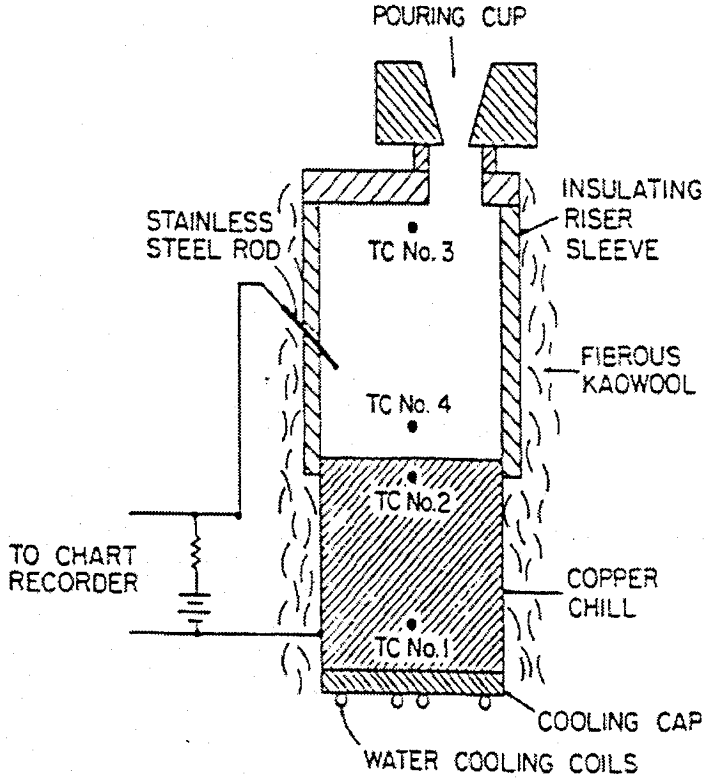

Fig. 2.2.2. Second type of experimental casting (Top placed chill) [16]

For both types, a rapid drop of interfacial heat transfer coefficient occurs during the initial stages of solidification due to changes in interfacial conformity. In the case of an interfacial gap, the heat transfer coefficient is affected by the magnitude of interfacial separation. On the other hand, provided that interfacial contact pressure remains relatively constant, the final thermal conductance for the case of a contacting metal-chill interface is principally a function of the mechanical finish of the mold as well as the material properties with respect to oxide formation and wetting.

Similar experiments were carried out by Nishida *et al.* [17] for cylindrical and flat castings of pure Al and Al-13.2%Cu alloy. The mold shape was found to affect the heat transfer coefficient and the formation of the air gap was detected by monitoring mold and casting movements during the solidification. In the case of cylindrical molds, the mold moves outwards away from the casting, while in rectangular molds, the mold surface moves first inwards towards the casting, then outwards. It was also found that for the weakly constrained rectangular mold, the inward movement is even larger than for a strictly constrained one.

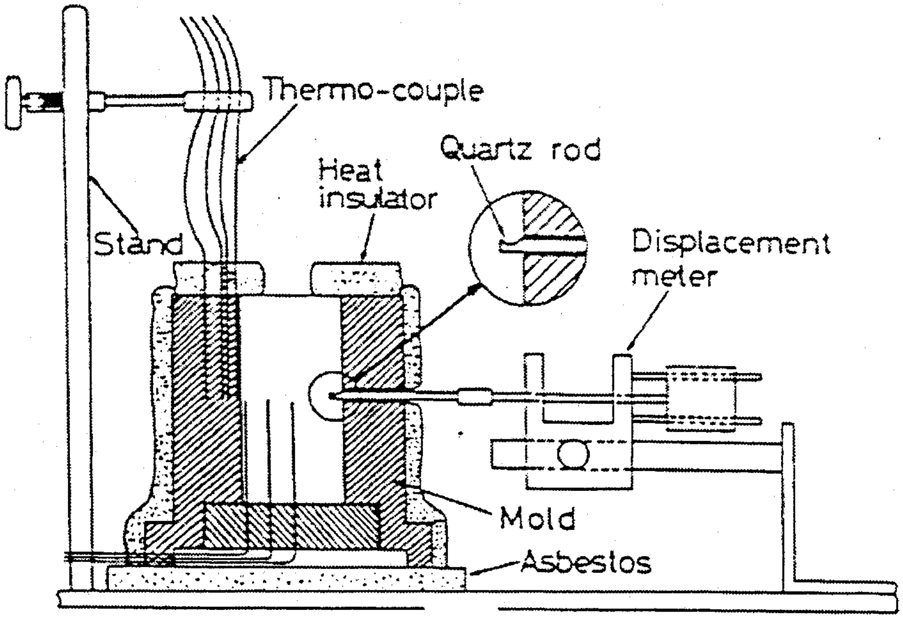

Fig. 2.2.3. Measurement of casting displacement and temperature [17]

An effort to empirically model the interfacial heat transfer was first tried by Kumar *et al* [18]. They attempted to make an accurate model of the heat transfer across the interface depending on the knowledge of interface temperatures, surface characteristics, thermophysical properties of the gap material, and those of the coating material. Al-13.2%Si eutectic and Al-3%Cu-4.5%Si long freezing range alloys were selected as the cast metals. Four different thicknesses of chill made of copper, cast iron, and die steel were used. The heat flow at the casting/chill interface was modelled in three steps: (Fig. 2.2.4.)

(1) Knowing the thickness d and the thermal diffusivity α of the chill material, the maximum heat flux value, q_{max}, was calculated using the expression $q_{max} = A \cdot (d / \alpha)^B$ where A and B are constants. It was assumed that the mold

was filled instantaneously and that the thermophysical properties were independent of temperature.

(2) The expression $\frac{q}{q_{max}} \times \alpha^{0.05} = C \cdot t^D$ was used to calculate the q values as a function of time ten seconds after solidification set in. C and D are constants obtained from experiments.

(3) The heat flux values for the intervening period of 10 seconds were estimated by linearizing the flux values between q_{max} and the q value for the 10th second.

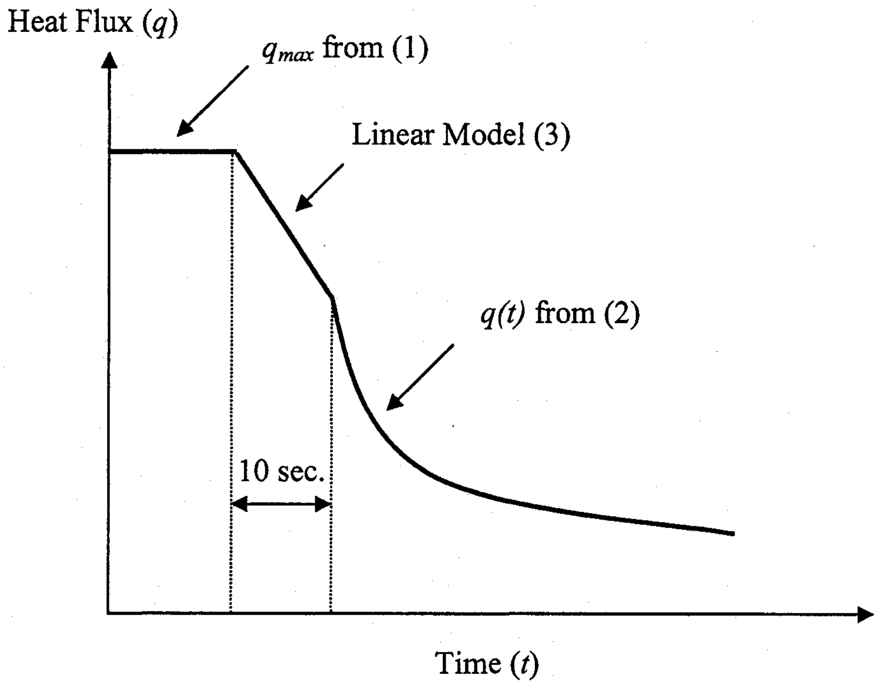

Fig. 2.2.4. Kumar & Prabhu's heat flux model [18]

A more elaborate empirical model was proposed by Krishnan *et al* [19]. Both bottom-chilled and top-chilled experiments were performed using LM6 (Al-11.5%Si), LM24 (Al-9.5%Si-3.6%Cu), and Al-2.7%Li alloy as cast metals with the cast iron chill. Sprue height and casting height were varied to control the metallostatic pressure and the interfacial gap was measured using an inductive gauge. Fig. 2.2.5 shows the variation of heat transfer coefficient with time during solidification.

During stage I, a stable liquid metal cannot be established adjacent to the chill surface because solidified skin formed undergoes continuous deformation and rupturing due to turbulence in the liquid metal. This condition of high turbulence helps to maintain the metal in a molten condition adjacent to the chill surface. In fact, at the moment of contact, the wetting between the liquid and the chill surface is not instantly established because the liquid needs time to respond to the exact texture of the chill surface where it starts to spread out and solidify. Therefore, the value of heat flux begins from a finite value, or from zero, instead of the theoretical value of infinity for perfect thermal contact. In these cases where a distinct stage II appeared, it was related to the freezing time of the ingate. The results of the constant metallostatic head experiments showed that no distinct stage III was observed and both the casting and sprue heights affected the slope of stage III (i.e. dh/dt). Note that in the diagram, (1) and (4) indicates a receding interface; (2) indicates a constant pressure and (3) is an increasing pressure case.

Transient heat transfer during the early stages of solidification on a water-cooled chill has been studied by Muojekwu *et al* [20]. The subsequent evolution of microstructure was quantified in terms of secondary dendrite arm spacings (SDAS). Based on dip tests of the chill, the influence of process variables such as mold surface roughness, mold material, metal superheat, alloy composition, and lubricant on heat transfer and cast structure were determined using Al-Si alloys, as shown in Fig. 2.2.6. In addition, a modified version of an empirical heat flux model was proposed using a curve-fitting technique with the heat flux as the dependent variable and the factors mentioned earlier as the independent variables.

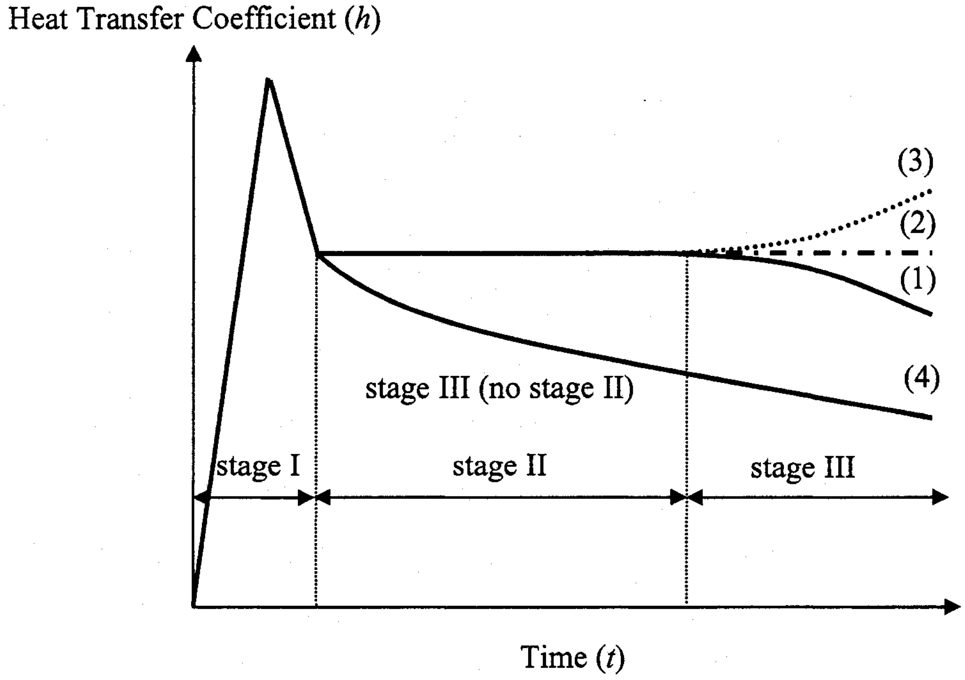

Fig. 2.2.5. Krishnan & Sharma's heat transfer coefficient model [19]

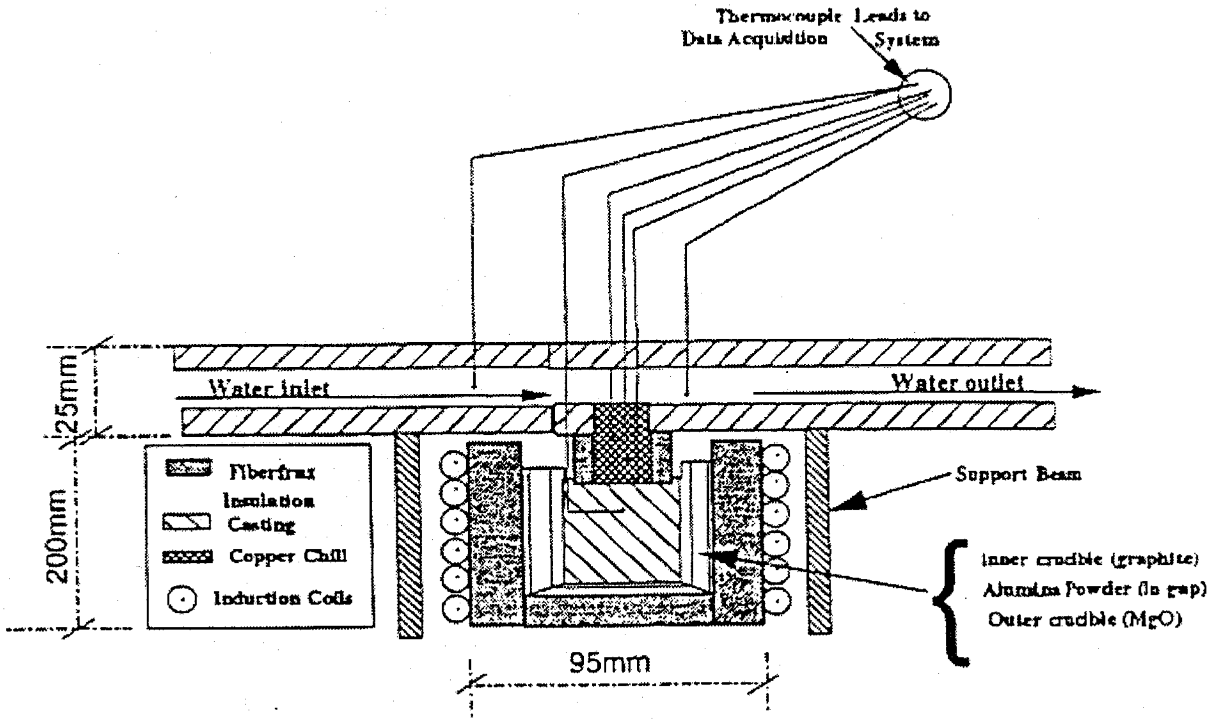

Fig. 2.2.6. Muojekwu's experimental set-up [20]

The empirical model of heat flux developed in their study is similar to that developed by Kumar *et al.* [18], but included more variables that are known to affect the interfacial heat transfer. Three stages involved are shown in Fig. 2.2.7:

(1) Stage I : Initial linear increase from time zero to the time when the maximum heat flux is attained. The maximum heat flux can be expressed as

$$q_{\max} = C_0 \left(\frac{T_c}{T_m} \right)^a \left(\frac{\alpha_m}{X_m} \right)^b R_a^c \ (W/m^2)$$

where T_c is the casting temperature, T_m is the mold temperature, α_m is the thermal diffusivity of the mold, X_m is the mold thickness, and R_a is the surface roughness of the mold. The constant C_0 was found to increase with expanding mushy zone (T_L - T_S).

(2) Stage II : The heat flux for 10 seconds beyond the time of q_{max} was estimated by linearizing the heat flux values between q_{max} and the q values obtained by (3) for 10 seconds.

(3) Stage III : The flux at any time greater than 10 seconds after the q_{max} was estimated as

$$\frac{q}{q_{max}} = C_1 \left(\frac{\mu_m}{\mu_c} \right)^d \alpha_m^e \, t^f \ (\mathrm{W/m^2})$$

where μ is a linear thermal expansion coefficient and t is a casting time.

In their experiments, SDAS increased with increasing distance from the chill surface because a higher heat extraction rate close to the chill surface leads to a finer microstructure. The heat extraction increased with decreasing surface roughness of the chill, resulting in an increased shell thickness and a decrease in SDAS. Also, the shell's surface roughness increased with an increasingly rough chill surface. The heat flux and heat transfer coefficient increased with increasing thermal diffusivity of the chill material. The interfacial heat flux and heat transfer coefficient increased with superheat temperature. This higher rate of heat extraction resulted in a thicker shell and smaller

SDAS. The surface of the solidified shell became smoother as the superheat increased, which showed an improved metal-mold wetting.

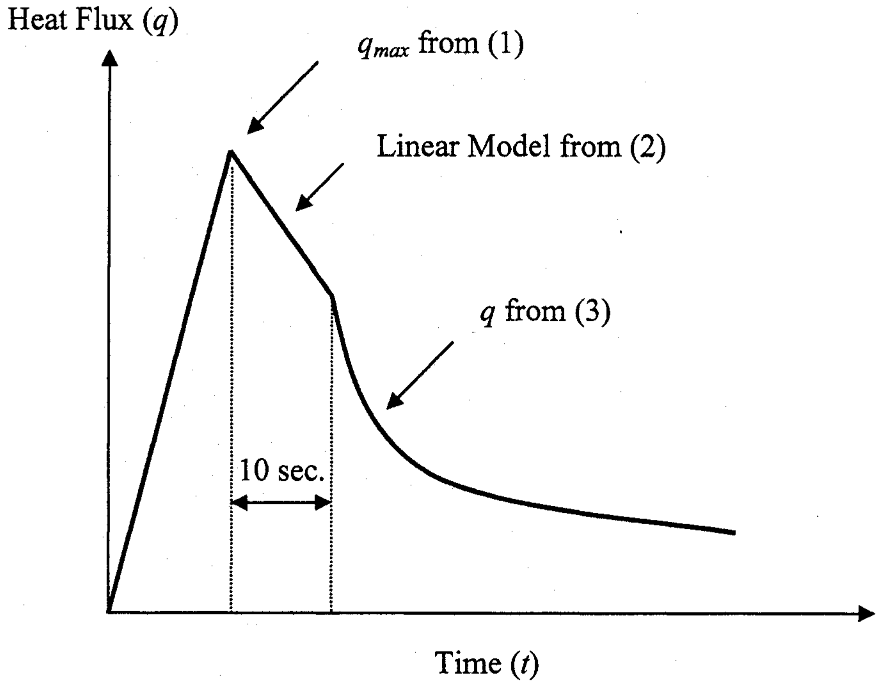

Fig. 2.2.7. Muojekwu, Samarasekera & Brimacombe's heat flux model [20]

2.2.3. Interfacial heat transfer from various casting experiments

As previously mentioned, the interfacial heat transfer between a solidifying molten metal and a mold is a critical parameter for many material processing and manufacturing operations, such as continuous slab casting, thin strip casting, melt-spinning, and spray deposition.

Assar *et al.* [21-25] researched the interfacial metal-mold heat transfer using various lead, aluminum, and zinc alloys. They studied the effect of melt superheat, gap size, chill material, specimen length, and mold surface roughness on the interfacial heat transfer. According to their experiments, the maximum value of heat transfer coefficient *h* was obtained when the interfacial temperature of the liquid metal was close to the liquidus. Higher *h* values and smaller gap sizes were also obtained with higher superheat. Observation of microstructure revealed that increasing melt superheat increases the length of the columnar zone, and that this is shorter for alloys than for commercially pure metals. The columnar to equiaxed transition was found to occur at a critical temperature gradient and growth rate. The grain size of columnar and equiaxed was found to follow a power relationship with respect to the rate of solidification. Moreover, the interfacial heat flux decreased with increasing mold surface roughness.

This behavior of increased heat flux with decreased mold roughness was also observed by Coates *et al.* [26]. Using the L-shaped casting mold, pure aluminum was cast onto the steel chill with different chill roughnesses and melt superheats. The higher values of heat transfer coefficient were obtained on smoother chill surfaces (R_a=1.41) compared to rougher surfaces (R_a=20.72). The increase in melt superheat increased the interfacial heat transfer coefficient and this behavior was more prominent for smoother chill surfaces. The separation of cast product from chill surface by forming an air gap at the interface was detected using a displacement sensor-LVDT (Linear Variable Differential Transformer), as shown in Fig. 2.2.8. The formation of an air gap greatly reduced the interfacial heat transfer.

Prabhu *et al.* [27] estimated the heat transfer coefficient between the plate type of casting of a general purpose Al-Cu-Si gravity die casting alloy (LM-21), and cast iron molds of varying thickness. Microstructural analysis was carried out to measure SDAS at various locations in the casting, and local solidification times were also calculated. To analyze their experimental data, they introduced the casting/mold wall thickness parameter, H_i defined as: $H_i = D_c^{1.5}/D_m^{0.15}$ where D_c and D_m are the casting and mold wall thicknesses. The peak temperature attained by the mold surface increased with increase in H_i. With increase in H_i, the dendrite structure became coarser for molds with coating thicknesses of 100 and 200 μm. However, an opposite trend was observed in the case of molds having a coating thickness of 500 μm. For these molds, the dendrite structure became finer with increase in H_i.

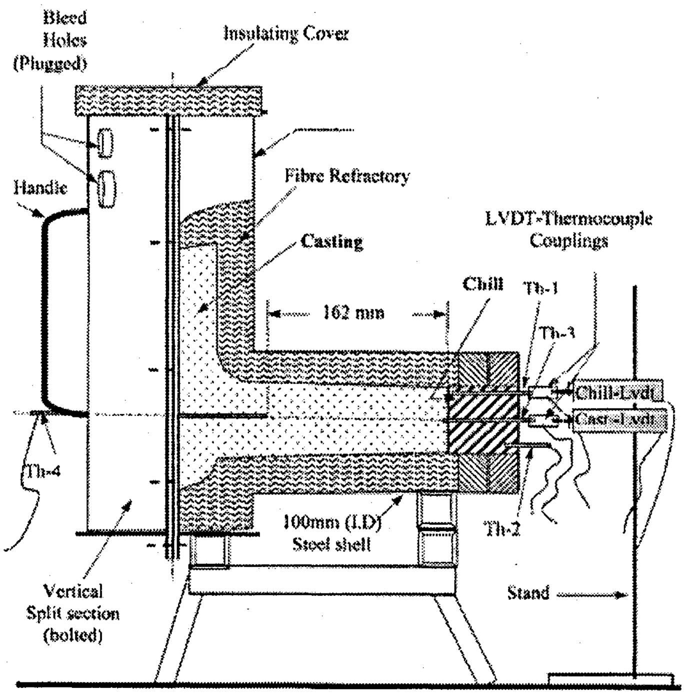

Fig. 2.2.8. Mold apparatus for measuring displacements and temperatures in casting and chill [26]

Hwang *et al.* [28] measured the heat transfer coefficient by employing two methods suggested by Ho *et al.* [14-16]. The casting metal was A356 aluminum alloy. Resin-bonded sand was used as the mold material. The value of *h* started from a finite value, and gradually increased to a peak value. Following this, the metal temperature dropped more rapidly, the metal shrinking to form a larger gap, and as a result, a smaller *h*. They explained the initial increase in the *h* value as being due to the imperfect contact between the molten metal and the mold when it was first poured into the casting mold. Due to the roughness of the mold, they argued it took a certain time to wet the mold and to establish the condition of close contact. In their experiment, no interfacial gap was formed until the eutectic temperature was reached because the liquid-solid mixture at that stage still maintained good contact with the mold wall. When the eutectic formed, the strength of the solid shell increased, and this was sufficient to resist the hydrostatic pressure of the molten metal tending to push the metal shell outward. This explains the sudden change of *h* value at the liquidus temperature obtained by Assar *et al* [21-25]. Heat transfer during filling procedures in the casting process was examined by Schmidt

[29]. In his experiment, the *h* values obtained in this filling procedure were certainly lower than in the static case. Lau *et al.* [30] also investigated heat transfer behavior between a cylindrical cast iron mold and metals such as pure aluminum, gray cast iron, and speroidal graphite iron. Their results reconfirmed that the thermal expansion of the mold and shrinkage of cast metals after solidification played an important role on the interfacial heat transfer coefficient.

Mehrotra *et al.* [31] measured the heat transfer coefficient *h* from a heated stainless steel block to a water cooled copper block, They foundd out the effect of operating parameters, e.g. the substrate surface roughness and that of the solidified metal, cooling conditions prevailing at the outer surface of the substrate. Rough surfaces led to the entrapment of air pockets at the interface which acted as thermal insulators. Consequently, the resistance to heat flow increased, resulting in the reduced *h* values observed. Once this air film was formed, and physical contact between the two metallic surfaces was interrupted, any variations in film thickness proved to have only a marginal effect on *h*, as one might expect. In addition, it was found that the cooling condition in terms of spray water pressure and the number of spray nozzles involved had nearly negligible effect on *h*.

Griffiths *et al.* [32-33] studied the effect of process variables such as roughness of chill surfaces, mesoscale deformation of the casting skin by thermal stress, and macroscale movements of the casting and the chill due to their relative thermal expansion and contraction, on heat transfer. Al-7%Si alloy and Al-4.5%Cu alloy were poured onto a water-cooled chill surface of copper. A finite difference method was employed to estimate the interfacial heat transfer coefficient. Different mold systems were designed with orientations of the casting; vertically upwards, horizontal, and vertically downwards. All casting surfaces produced, revealed a bulging convex shape towards the chill surface, with a maximum departure from a planar surface across individual casting surfaces varying from 6 to 19 μm. This is due to the fact that the heat transfer from the casting to the chill would take place through two distinct regions, a central contact region where the surface of the casting was in contact with the rough chill and a surrounding annulus where a local separation occurred. Unfortunately, no correlation between measured surface roughness and orientation of the casting solidification direction was observed. Neither was a correlation found between surface roughness and their mean values of h in their experiments.

Velasco *et al.* [34] reported on the process of heat transfer during unidirectional solidification of an Al-8%Si-3.7%Cu alloy, and studied how this was affected by solidification kinetics. They interpreted that the values of heat transfer coefficient depended on the kinetics of solidification, since h remained constant while the alloy was liquid and increased as soon as the dendrites started to form. Later, the heat transfer decreased at the eutectic temperature, decreasing further once the alloy was fully solidified.

Trovant *et al.* [35-36] investigated the mechanism of heat transfer between the cooling molds (copper, graphite, and sand) and solidifying metals (pure aluminum, aluminum alloys, and tin). Using cylindrical casting of metal-mold system, as shown in Fig. 2.2.9, they mainly found out the effect of air gap size and the mold roughness on the interfacial heat transfer. A simplified viscoelastic/plastic model was also adopted to simulate the heat transfer mechanism. It was shown that the effect of mold roughness was correlated with the air gap size during the casting. The effect of mold roughness on the interfacial heat transfer was the highest during the initial stage of solidification and decreased rapidly as the gap size grew.

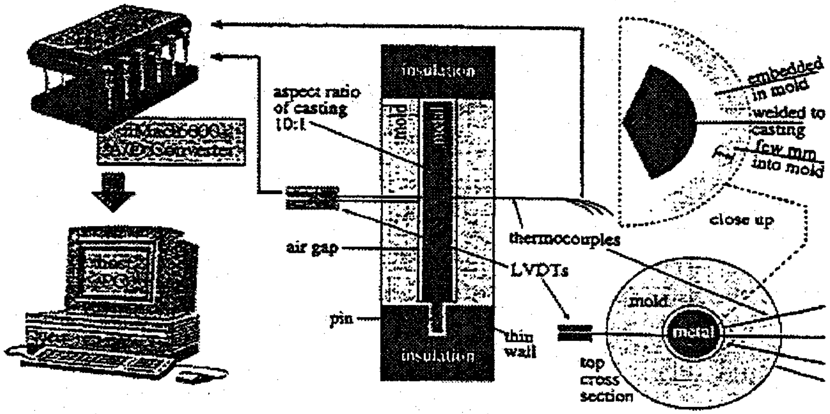

Fig. 2.2.9. Schematic of cylindrical metal-mold system [35]

2.2.4. Interfacial heat transfer in belt casting processes

For a fundamental understanding of heat transfer in single belt casting, Spitzer and Schwerdtfeger [3, 37-38] performed a static mold experiment using the least square minimization method to calculate heat transfer parameters, prior to operating the real belt caster in Clausthal. They simplified the problem by assuming that the heat transfer coefficient follows the power-law with the time. Liquid steel was poured into a vertical cylinders placed on the water-cooled steel belt, 1.5mm thick, with and without graphite coating. The average heat transfer coefficients were about 3 kW/m^{2}K for the first two seconds and 1.2 kW/m^{2}K afterwards. The heat transfer coefficient between belt and cooling water was chosen to be 10 to 50 kW/m^{2}K. The experimental set-up is sketched in Fig. 2.2.10.

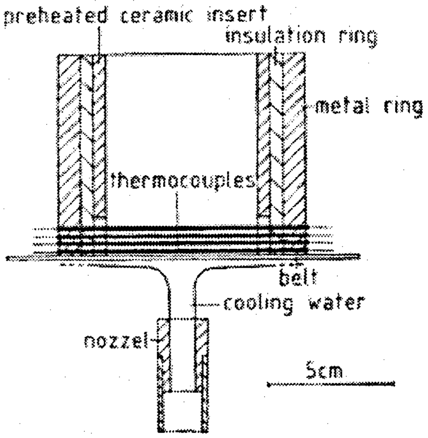

Fig. 2.2.10. Apparatus to solidify the steel cast on water-cooled belt [37]

In 1989, the first casting experiment with the first Clausthal single belt caster of 1500 mm belt length and 300 mm width succeeded in casting steel strips 6 m long, 150 mm wide, and 10 mm thick [3]. While the surface evenness needed to be improved, the quality of the strip produced proved to be satisfactory, with minor microsegregation, and no macrosegregation. This caster was upgraded further in cooperation with Salzgitter AG, SMS Demag AG and Thyssen Krupp Stahl AG for in-line hot rolling. A sketch of this pilot caster is shown in Fig. 2.2.11. Using a reduced pressure system in the cooling chamber (Fig. 2.2.12) and a tension roll for belt stabilization against thermal distortions, satisfactory thickness uniformity could be obtained [38]. Fig. 2.2.13 shows the transverse thickness profiles of low carbon steel strip in the as-cast condition, and after hot rolling.

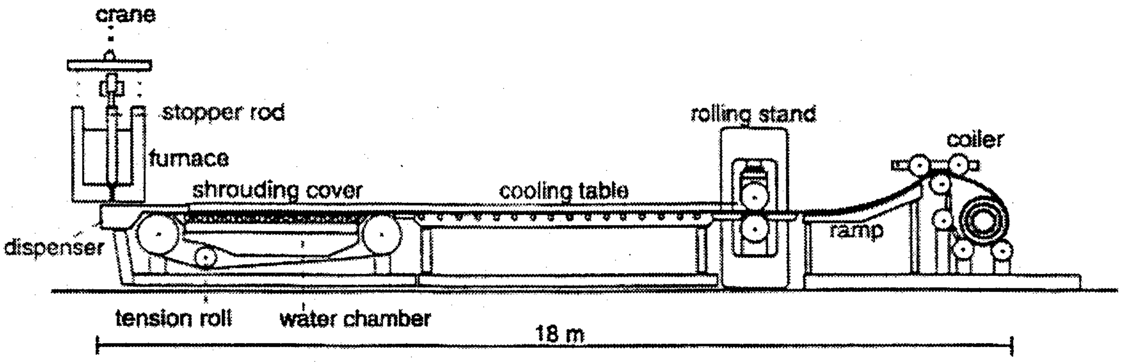

Fig. 2.2.11. Sketch of the pilot installation for the integrated single belt casting/hot rolling process at Clausthal

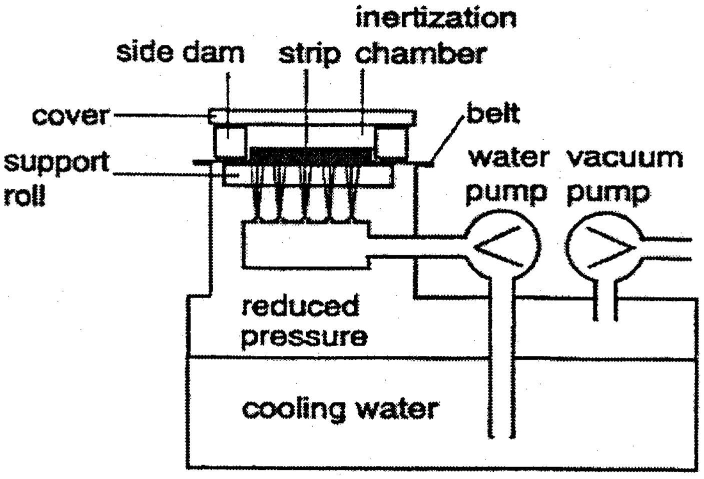

Fig. 2.2.12. Cross-section of caster showing the reduced pressure system in cooling chamber for belt stabilization

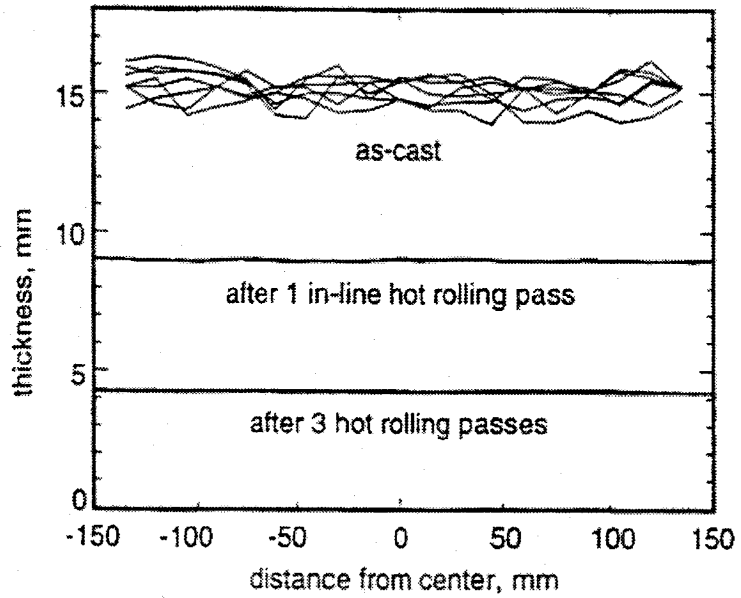

Fig. 2.2.13. Transverse thickness profiles of strip (carbon steel with 0.12%C) in the as-cast state and after hot rolling [38]

In other studies, Chen *et al.* [39] investigated interfacial heat transfer from free-jets (wood's alloy and water) impinging onto a moving substrate (steel, aluminum, and plexiglass). The jet's velocity of impingement and substrate velocity were fixed, and the melt superheat varied. Their results showed that the effect of increasing the melt superheat was to delay the onset of solidification, even though the interfacial heat flux increased. The strip thickness decreased with increasing melt superheat while its width tended to increase. These results could be caused by two factors: (1) increasing superheat reduces flow viscosity (i.e. improves fluidity) and thus reduces film thickness and (2) higher superheats delay the solidification times and thus allow the melt to spread out further to the sides. Increasing the thermal conductivity of the substrate greatly improved the rate of solidification and produced cast strips with very fine and uniform microstructures. In their experiment, an aluminum substrate produced the best strip quality.

Transient heat transfer between a solidifying aluminum strip and a moving steel substrate was also investigated by Netto *et al* [40]. In these experiments, the substrate was flame sprayed with various coatings, while its speed and the thicknesses of strip produced matched industrial values. Peak values of heat flux between 0.66 and 2.0 MW/m^2 were found for the diverse experimental conditions investigated , while values of h ranged from 1200 – 3600 W/m^2·K. The heat transfer coefficient was found to increase with initial superheat, thickness of strip and smoother coatings.

The effort to understand the behavior of interfacial heat transfer at the melt/substrate interface was continued by Strezov *et al.* [41] using 304 austenitic stainless steel as the melt, with various experimental variables such as substrate (copper) roughness, gas atmosphere, immersion paddle velocity, and melt superheat. Their experimental set-up is drawn in Fig. 2.2.14.

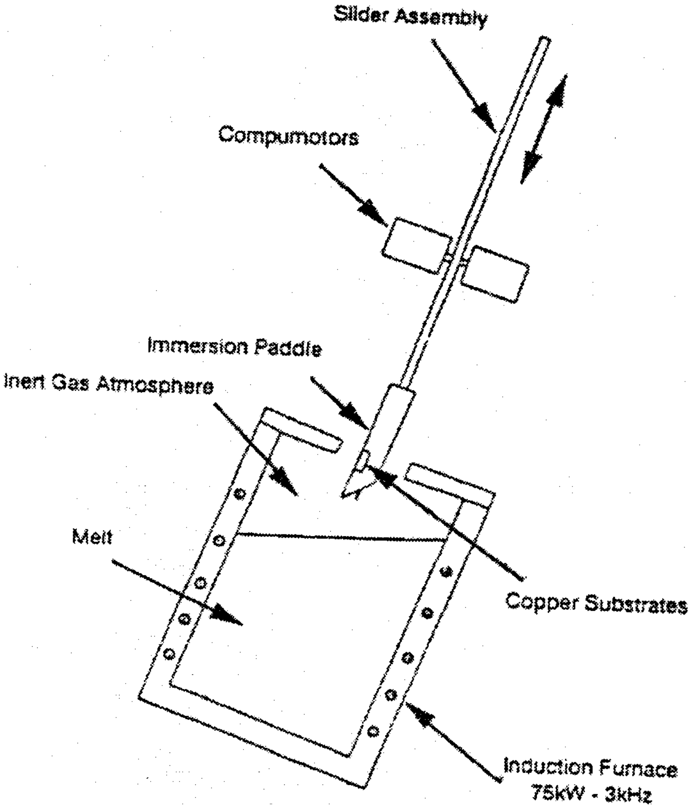

Fig. 2.2.14. Schematic representation of the experimental apparatus [41]

The peak heat flux for a smooth copper substrate was found to be significantly lower than that for the textured copper substrates. Gas atmospheres showed little effect on heat transfer kinetics. The peak heat flux for both substrates, smooth and textured, increased with immersion velocity, but the effect was more evident with the textured substrates. This increase implies an improvement in melt/substrate wetting resulting in finer microstructures and greater nucleation densities during the initial stages of solidification of metal onto both substrates. On the other hand, unexpectedly, increased superheats corresponded to decreased peak heat fluxes. It is worthwhile mentioning that the surface solidification structures were coarse dendritic, and that their coarseness increased with increasing superheat; i.e. nucleation density decreased with increasing superheat. In their experiments, the reduced driving force for nucleation presumably offset any anticipated enhancement in melt/substrate wetting with increased superheat. Moreover, transverse microstructures of the samples solidified at 10°C superheat showed a considerable increase in shell thickness, compared to those at 100°C superheat, reflecting the decreased requirement for sensible heat removal. The microstructure of the sample solidified at 100°C superheat was fully columnar, while a 10°C superheat produced a partially columnar structure with a transition to equiaxed crystals at about one third of the final thickness. This was consistent with the increased tendency for equiaxed growth with reducing superheat.

2.2.5. Early solidification phenomena using splat quenching experiments

The early stages of solidification is important to understand in terms of the mechanism of initial solidification onto a cooling substrate surface, and the resulting microstructures of the solidifying metal. The initial metal/mold contact profoundly affects the subsequent nucleation and growth stages in conjunction with the development of morphology in microstructures within the bulk of the casting. This initial thermal contact is influenced by many factors such as casting geometries, cast materials, mold materials, mold surface textures, melt superheats, casting atmosphere, etc. In this regard, a free fall splat quenching test is easy to carry out and provides many aspects applicable to solidification processes practice.

Table 2.2.1. Estimated *h* for melt spinning and splat cooling [44]

	Metal	Wheel	u_W (m/s)	h_1	h_2 (W/m^{2}K)	h_3
PFMS①	Ni-P	Copper	17	7×10^5	1.5×10^5	
			23	1.05×10^6	1.5×10^5	
			33	1.3×10^6	1.5×10^5	
			43	1.1×10^6	1.5×10^5	
		Steel	22	6×10^5	2.0×10^5	
			27	6.5×10^5	2.0×10^5	
			31	7.5×10^5	2.0×10^5	
		Stainless Steel	31	4×10^5	1.6×10^5	
			36	1.0×10^6	2.5×10^5	
			43	1.1×10^6	2.5×10^5	
PFMS②	Fe-C	Stainless Steel	5	9×10^5	10^3 - 10^5	
			8	8×10^5	10^3 - 10^5	
			30	8×10^5	10^3 - 10^5	
		Cu-Cr	-	2.5×10^5	10^3 - 10^5	
PFMS②	Fe-Si	Steel	-	1.5×10^6		
PFMS③	Steel	Steel	15	10^8	10^5	
PFMS④	Fe-Si	Steel	10	5×10^6	$(0.6 - 2)\times10^5$	
PFMS⑤	FeBSi	Cu-Cr	15	5×10^5		
			20	10^6		
			27	2×10^6		
PFMS⑥	Al-Cu	Cu-Cr	14	4×10^5		
"Gun" Splat⑦	Al	Ni	-	$(1 - 3)\times10^5$		
	Ag	Ni	-	$(0.6 - 2)\times10^6$		
Drop⑧ Smasher	Al	SS	-	1.8×10^5	1.2×10^5	1.7×10^4
	Pb	SS	-	2.1×10^5	1.6×10^5	4.6×10^4
	Solder	SS	-	1.9×10^5	1.6×10^5	5.0×10^4

① Takeshita and Shingu (1986); ② Vogt (1987); ③ Muhlbach et al. (1987); ④ Frommeyer and Ludwig (1992); ⑤ Huang and Fiedler (1981a); ⑥ Gong *et al.* (1991); ⑦ Predecki *et al.* (1965); ⑧ Harbur *et al.* (1969)

Wang *et al.* [42-45] tabulated Table 2.2.1 of the estimated heat transfer coefficients obtained from melt spinning and splat cooling experiments. Except for one high value of 10^8 W/m^{2}K (③), the value of h ranged from 10^5 to 5×10^6 W/m^{2}K. Note that h_1 is an average value under the puddle and h_2 is after the puddle for PFMS (Planar Flow Melt Spinning) and gun splat experiment (①-⑦). In the case of the drop smashing experiment (⑧), h_1 was during liquid cooling, h_2 was during solidification and h_3 was measured during solid cooling stage. Compared to the melt spinning in which the high speed melt impinges on the rotating roll to produce a thin solidified layer of a few microns thick, usual strip casting or free fall splat cooling (FFSC) experience relatively poor thermal contact. Another table of the estimated *h* from strip casting and free fall splat cooling experiments is given in Table 2.2.2.

Table 2.2.2. Estimated *h* for strip casting and free fall splat cooling [44]

	Metal	Wheel	b (mm)	h_1	h_2 (W/m^{2}K)	h_3
Single Roll①	SS	-	0.8	0.8×10^4		
		-	1.2	1.9×10^4		
		Cu	0.6	2.0×10^4		
Twin Roll①	SS	-	-	1.2×10^4		
		-	0.5-3	$(0.4\text{-}2.1)\times10^4$		
		-	5	0.6×10^4		
		-	10	0.3×10^4		
		Cu	6-7.5	0.8×10^4		
Twin Belt②	Steel	(Coated)	-	0.2×10^4		
FFSC③	SS	Cu	-	$(3\text{-}4)\times10^4$	$(0.5\text{-}1.5)\times10^4$	
FFSC④	Tin	Ni	4	3×10^4	$(0.7\text{-}1)\times10^4$	
FFSC⑤	Ni	Quartz	0.4	0.9×10^4		
		Al	0.3	0.45×10^4	0.2×10^4	
		SS	0.3	1.3×10^4	0.2×10^4	
		Cu	0.2	1.4×10^4	0.2×10^4	
FFSC⑥	Pb	Cu	-	1.5×10^4		
		Pyrex	-	10×10^4		

① Essadiqi *et al.* (1989) (Note that some of these data were quoted from the references); ② Farouk *et al.* (1992); ③ Mizukami *et al.* (1992, 1993); ④ Loulou *et al.* (1994); ⑤ Liu *et al.* (1992); ⑥ Bennett and Poulikakos (1994)

The effect of casting speed and strip thickness on the interfacial heat transfer is plotted in Fig. 2.2.15 and 2.2.16 respectively. In terms of the superheat, a strong effect of melt superheat on *h* existed when the molten nickel was cast on a copper substrate while this effect did not appear when cast on an aluminum substrate [45]. On the other hand, when the tin droplet was cast on an aluminum substrate, the increase superheat increased the value of *h* [43]. In general, it was observed that the melt superheat moderately improved the thermal contact during the initial stage of contact and especially for substrates with smoother surfaces.

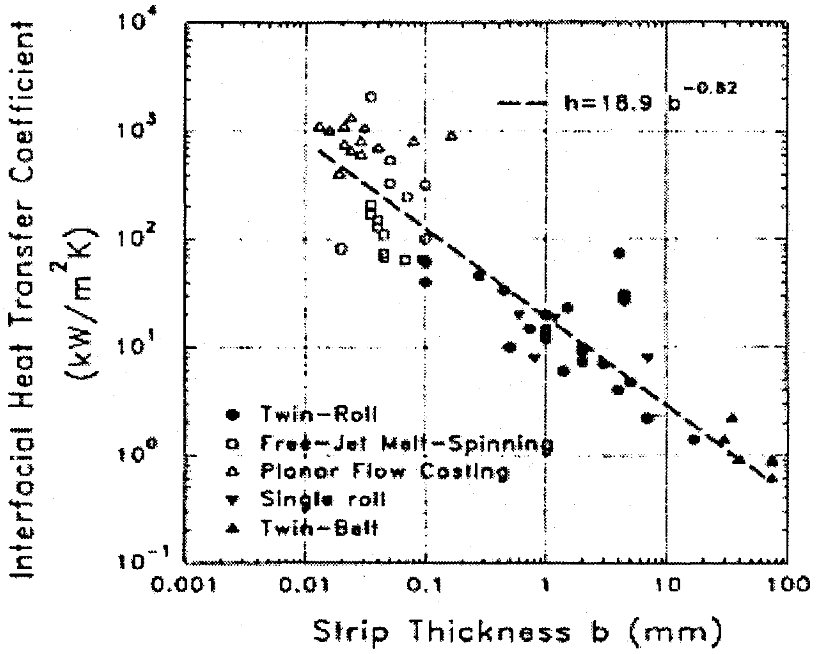

Fig. 2.2.15. Correlation between the interfacial heat transfer coefficient *h* and strip thickness [45]

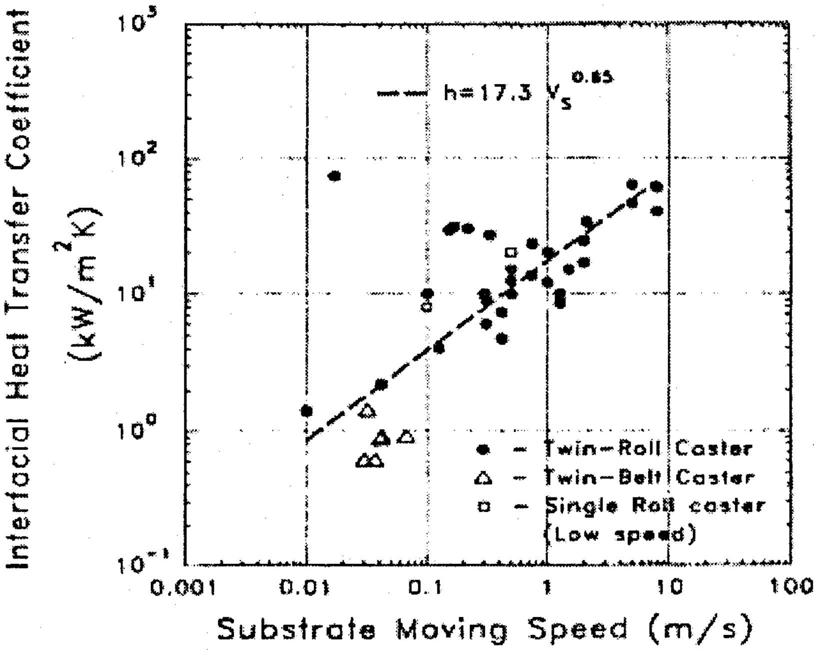

Fig. 2.2.16. Effect of the moving speed of substrate on the interfacial heat transfer coefficient *h* [45]

Todoroki *et al.* [46] investigated the heat transfer behavior of pure iron, nickel, stainless 304 and IF steel, droplets using the droplet ejection technique. The heat flux and the heat transfer coefficients were determined during the first 0.5 seconds of solidification. Their experimental apparatus is sketched briefly in Fig. 2.2.17.

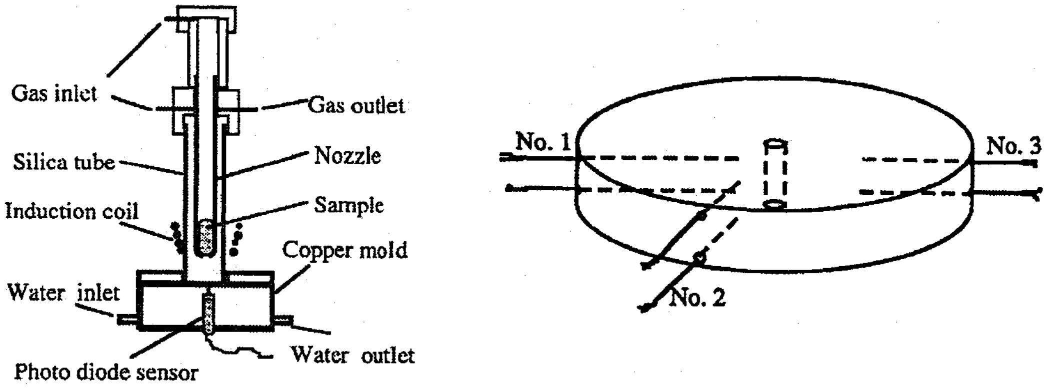

Fig. 2.2.17. Experimental set-up of Todoroki *et al.* [46]

In their experiments, the cast surface produced became flatter with increasing superheat except for the 304 stainless steels, which goes through a peritectic phase transformation during cooling. Pt, the maximum profile depth, values decreased with an increase in superheat; i.e. better fluidity of molten metal with higher superheat enhanced spreading of melt across the chill surface. Contrary to the results of Strezov *et al.* [41], especially for the 304 steel of low sulfur content, the grain size became smaller with increasing the superheat. Microstructural observations revealed that SDAS increased from 2 to 10 μm with distance from the bottom surface of the casting, and decreased with an increase in superheat. The cooling rate ranged from 10^3 to 10^5 °C/s and decreased with distance from the specimen surface. Columnar dendrite grew perpendicularly to the surface in the direction of the heat transfer and equiaxed dendrites were also observed on the top surfaces of the specimens.

Extensive experiments by Misra *et al.* [47] revealed that a liquid oxide film improved the metal/mold contact and increased the rate of heat transfer when various grades of steel droplets impinged onto a copper substrate. In particular, the presence of liquid MnO-SiO_2 films, in Mn-Si killed steels, and of FeO films in pure iron, significantly increased the initial heat transfer rate during the first 20 mille-seconds by as much as a factor of more than two. To enhance the rate of heat transfer by oxide films in practice, they suggested that the film should be liquid over a significant temperature range below the melting point of the cast metal, and be sufficiently wettable between the liquid metal and mold surface.

Loulou *et al.* [48-50] carried out another set of experiments using tin, lead, and zinc droplets on nickel substrates. They observed that the increase in superheat and decrease in substrate roughness improved wettability, and that the presence of lubricant (oil > grease > air) at the interface enhanced the rate of heat transfer by minimizing the effect of numerous micro-cavities filled by air. The higher latent heat of liquid metal resulted in the faster cooling rate. In particular, the following steps during the process of solidification were suggested and shown pictorially Fig. 2.2.18.

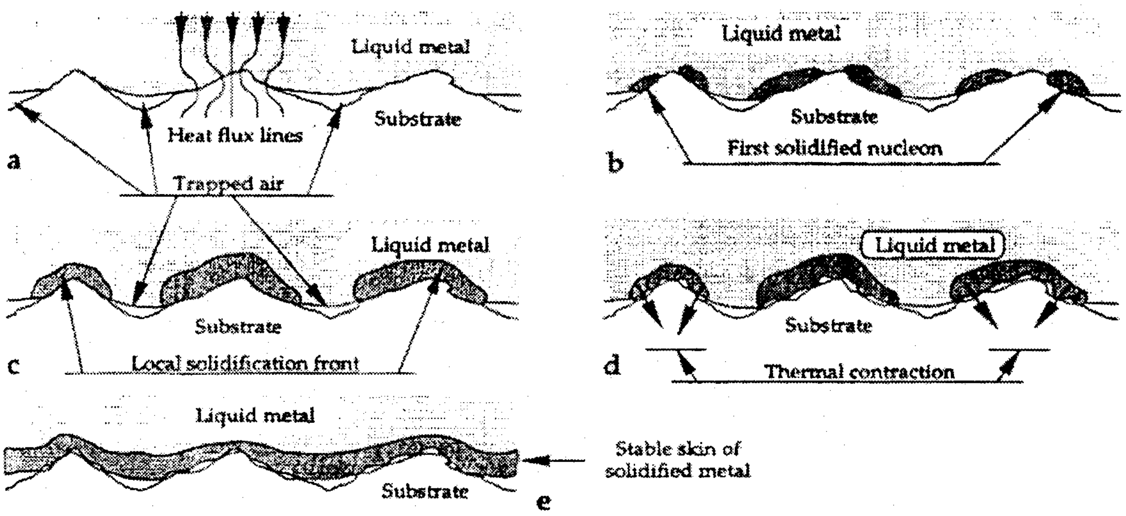

Fig. 2.2.18. Schematic of the evolution of solidification at the interface [50]

During stage **a**, interfacial thermal contact is a strong function of substrate roughness, surface tension and metallostratic pressure of the liquid metal, wettability, and the nature of the trapped gas. At the end of stage **a**, the heat flux to the substrate is a maximum and the interfacial thermal resistance is a minimum. As nucleation begins at the triple points of liquid metal, substrate, and trapped air, stage **b** of nucleation develops. Around each local surface peak of the substrate, the nucleation continues to progress to form a solidified ring around the surfaces' peaks. These rings grow to form solid caps of metal over the roughness peaks in stage **c**. Stage **d** can be characterized in terms of an increase in interfacial thermal resistance. The thickness of solidified metal crust increases progressively, while shrinkage of liquid metal occurs over the interface regions above air gaps. The end of this stage is distinguished by a stabilization of thermal contact resistance which corresponds to the initiation of the stage **e**. At stage **e**, the stable skin of solidified metal grows and the transient state of heat transfer is mainly affected by the growing thickness of the solidifying shell.

It should be also noted that the surface roughness of the solidified metal (R_a = 1.10 μm and R_a = 1.42 μm) was higher than that of the mold substrates (R_a = 0.30 μm and R_a = 0.66 μm). However, this result was opposite (R_a = 12.27 μm) when a higher value of the substrate roughness (R_a = 15.58μm) was used. They concluded that, between these values, there was a critical roughness where this change in behavior occurs. Similar results were observed by Prates *et al.* [12], Muojekwu *et al.* [20], and Kim *et al.* [51]

More recently, Leboeuf *et al.* [52-53] experimented with the impingement of an aluminum droplet onto a copper substrate, using a high speed camera (10^4 frames/sec) in conjunction with 1000 Hz frequency temperature measurements. Fig. 2.2.19 is a schematic of the experimental apparatus. Their investigations revealed that the maximum heat flux (~ 30 MW/m^2) was achieved as soon as the droplet spread over the substrate (about 5ms after the moment of contact). Also, a change in casting atmosphere affected the rate of heat transfer and subsequent microstructures of the solidified metal. A helium atmosphere produced finer microstructures of aluminum droplets compared to the sample cast on air atmosphere, while argon atmosphere produced the coarser structure. In particular, they observed the successive bouncing of a droplet when it hit the substrate surface in highly purified argon atmospheres with less than 0.02% O_2. This resulted in negative heat fluxes to the substrate during the times the droplet had bounced off the substrate. Clearly, wetting of the substrate was minimal under these conditions.

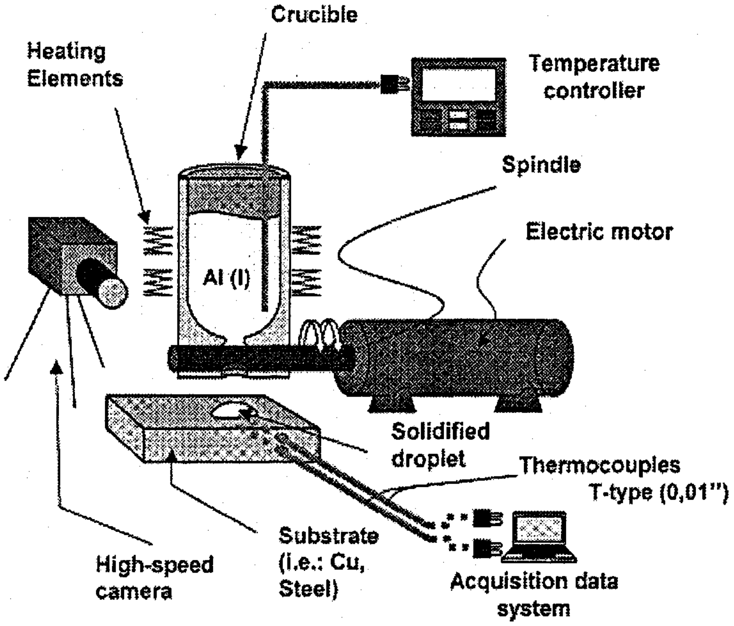

Fig. 2.2.19. Experimental set-up for the simultaneous characterization of dynamic wetting and heat transfer at the initiation of Al solidification [52]

2.3 INTERFACIAL HEAT TRANSFER ANALYSIS

2.3.1. Inverse heat transfer problem techniques

The "direct problem" in heat conduction involves predicting the interior temperature distribution within a body being heated or cooled. Such internal temperature distributions can be solved based on boundary conditions of the surface temperature or the surface heat flux. This is classified as a well-posed problem, which exhibits the following characteristics:

(i) Existence of solution
(ii) Uniqueness
(iii) Stability of solution

On the other hand, the purpose of the **I**nverse **H**eat **C**onduction **P**roblem (IHCP) is to determine the surface temperature or the surface heat flux for a given temperature distribution at interior points near the surface. However, the IHCP is an ill-posed problem, which does not satisfy the stability criterion and is so sensitive to the accuracy of the measured temperature input that small errors in the temperature data can result in large oscillations of the values of heat flux. In practice, the estimation of the transient heat flux (q) and the heat transfer coefficient (h) at the metal/mold interface needs to be calculated through the IHCP method, based on the temperature information obtained from experimental measurements. A well-known algorithm for solving the IHCP is Beck's sequential function specification method [13]. This method involves the concept of future for the estimation of q (or h) at each time step. A brief outline of the method is given below.

The fundamental principle of the Beck's technique is to assume that the entire process is divided into M time intervals and q_m is a constant within a given time interval ($t_m < t < t_{m+1}$). Then, q_m can be estimated for each interval using the measured temperature at the interior locations. Assuming that all the values of q before t_m (i.e. q_1, q_2,

..., q_{m-1}) already have been estimated, q_m can be estimated by minimizing the sum of residuals function, S_m^r:

$$S_m^r(q_m) = \sum_{i=1}^{r} [Y_{m+i-1} - T_{m+i-1}(q_m)]^2 \qquad (2.3.1)$$

where r is the number of future time steps, Y_{m+i-1} is the measured temperature, and $T_{m+i-1}(q_m)$ is the calculated temperature from the direct problem using the estimated q_m at location i and the time instant m respectively.

To minimize equation (2.3.1), the condition $\partial S_m^r / \partial q_m = 0$ can be applied:

$$\sum_{i=1}^{r} [Y_{m+i-1} - T_{m+i-1}(q_m)] \frac{\partial T_{m+i-1}(q_m)}{\partial q_m} = 0 \qquad (2.3.2)$$

The first derivative of the calculated temperature (dependent variable) with respect to the heat flux (the unknown) is called the sensitivity coefficient ϕ and is defined as follows:

$$\phi_{m+i-1}^r(q_m) = \frac{\partial T_{m+i-1}(q_m)}{\partial q_m} \qquad (i=1,\ 2,\ \ldots,\ r) \qquad (2.3.3)$$

Using the Taylor series expansion of $T_{m+i-1}(q_m)$ with respect to the n-th iteration value q_m^n and substituting into equation (2.3.2), the following iterative expression at each time interval can be obtained:

$$q_m^{n+1} = q_m^n + \frac{\sum_{i=1}^{r} \left[Y_{m+i-1} - T_{m+i-1}^n \right] \cdot \phi_{m+i-1}^n}{\sum_{i=1}^{r} \left(\phi_{m+i-1}^n \right)^2} \qquad (2.3.4)$$

where $\phi_{m+i-1}^n = \phi_{m+i-1}(q_m^n)$ and $T_{m+i-1}^n = T_{m+i-1}(q_m^n)$

Finally, the iteration continues until $q_m^{n+1} \approx q_m^n$ and the time index m increases until the last component q_M is achieved.

2.3.2 Heat transfer problem with phase change

The solidification of pure metal occurs at the melting point while that of alloy takes place over a certain range of temperatures. This results in the existence of two phases in a moving mushy zone. This moving boundary problem is not easy to handle because the latent heat is being released following the unknown phase interface. There are many reports in the literature that have dealt with the phase change problems since the 1970s [54-55]. Some analytical methods, including exact solutions and integral methods, were discussed [56] but they were not applicable to use in practical casting problem.

To handle the latent heat being released over the freezing range, several numerical techniques were tried, including:

(i) Front tracking method
(ii) Modified specific heat method
(iii) Enthalpy method

The front tracking method is useful when the alloy has a quite narrow freezing range [57-58]. This method solves the energy equation in the solid and liquid phase respectively, and then matches them at the solid-liquid interface. However, this method is less useful for common alloy systems which have various freezing ranges. Rolph *et al.* [59] and Pham [60-61] tackled the phase change problem with a modified specific heat method. This method solves only one energy equation for both solid and liquid phases using temperature-based specific heat formulation to account for the latent heat effect. This method, however, also needs to be careful when modifying the specific heat in the peak region not so as to ignore the peak of latent heat consequently. Currently, the enthalpy method is widely used [58-59,62] because of its simplicity and stability. In the enthalpy method, the latent heat and sensible heat are combined in the enthalpy term. Even though this method results in an oscillatory solution for the case of pure metals, (which can be tackled by the front tracking method, many alloy solidification problem can be solved easily by the enthalpy method.

The mathematical formulation of this enthalpy method is given by:

$$\rho\frac{\partial H}{\partial t}=\nabla\cdot q \quad \& \quad H=\int_0^T C_p(T)dT+L\cdot f_L \tag{2.3.5}$$

where $C_p(T)$ is a heat capacity, L is the latent heat, and f_L is the liquid fraction. The enthalpy, H, is composed of the first term of the sensible heat and the second of the latent heat fraction. Thus, the effect of latent heat release on solidification is addressed by way of manipulating the liquid fraction f_L over a freezing range. Some of those manipulations include linear or quadratic release of latent heat, the lever rule, and the use of Scheil's equation [63-64].

Exactly speaking, the actual rate of latent heat release depends on many factors such as the alloy composition, the evolution of microstructure, and recalescence phenomena. Kanetkar *et al.* [65] and Rappaz *et al.* [66] suggested a method which combined the microscopic equiaxed nucleation and growth model, with the macroscopic heat transfer model. In their methods, the liquid fraction (or solid fraction) was dependent on the casting time and several variables obtained from experiments. However, the use of these methods is quite limited because of their lack of generality and empirical data.

2.4 SUMMARY

In summary, much effort has been made to study interfacial heat transfer between the molten metal and the mold. Most of the experiments performed have related to stationary ingot casting, while the experimental data for strip casters are insufficient because of its experimental difficulty compared to ingot casting. Based on the present literature survey, some conclusions could be drawn:

(i) The influence of metal/mold heat transfer on microstructure depends on many parameters such as melt superheat, substrate roughness, casting atmosphere, casting velocity, air gap evolution, and thermophysical properties of the cast metal and mold substrate.

(ii) In general, the wettability of liquid metal and the mold substrate seems to be enhanced by increasing melt superheat and mold temperature or by decreasing mold surface roughness and casting velocity as well as by the evolution of lubricant at the interface such as oil or grease.

(iii) A casting atmosphere of helium improves metal/mold heat transfer compared to air or argon atmosphere.

(iv) The interfacial heat flux or heat transfer coefficient reported were strongly dependent on various casting systems of interest and the techniques or assumptions used in the calculations.

(v) The IHCP technique is widely employed to calculate the interfacial heat flux or heat transfer coefficient, while the enthalpy method is an useful tool for phase change problems.

(vi) The complexity of the experimental parameters and solidification mechanism involved in each experiment makes it difficult to simplify and generalize the characteristics of the problem.

2.5 OBJECTIVES OF PRESENT STUDY

Based on the summary drawn from the literature review, the following studies were pursued in this thesis, all aimed at producing high quality sheets of magnesium and aluminum alloys on the pilot scale horizontal belt caster at McGill.

(i) As a preliminary casting simulation of magnesium alloys on a single belt caster, AM50 and AZ91 were selected to investigate their interfacial heat transfer characteristics and solidification mechanisms, using the pneumatically driven strip casting simulator.

(ii) Five different mold substrates (copper, low carbon steel, alumina coated steel, nickel coated steel, and zirconia coated steel) with different roughnesses and coating thicknesses were investigated for casting magnesium alloys.

(iii) The IHCP (Inverse Heat Conduction Problem) technique and the enthalpy method associated with the two dimensional FVM (Finite Volume Method) were used to calculate the interfacial heat flux and the interfacial heat transfer coefficient as well as the temperature fields of strips.

(iv) The microstructures of strips were characterized and the local cooling rates of strips were compared with data reported in the literature.

(v) An improved single belt casting simulator using a spring piston to drive the moving substrate was developed and the thermocouple response was improved. Using this casting simulator, the aluminum alloy of AA6111 was cast on the copper and low carbon steel substrates.

(vi) The improvement of AA6111 strip quality and the refinement of its microstructures was investigated. Experiments included oil spraying on the mold substrates and additions of grain refiners to the melt.

(vii) An ab-initio predictive heat transfer model was developed to help explain observed transient heat fluxes measured during the formation of strip samples on the single belt casting simulator.

REFERENCES

1. K. H. Moon, Physical and Mathematical Modelling of a Metal Delivery System for a Single Belt Caster, *Ph.D. Thesis,* McGill University, 2003

2. K. H. Spitzer & K. Schwerdtfeger, Production of Steel Strip With a Single-Belt Process, *Iron Steelmaker*, 1995, pp. 47 – 53

3. K. Schwerdtfeger, K. H. Spitzer, W. Reichelt & P. Voss Spilker, Strip Casting with the Belt/Roll Process, *SRNC-9*0, October 14-19, 1990, Pohang, Korea, pp.514-525

4. J. Kroos, T. Evertz, M. Dubke, U. Urlaub, W. Reichelt, W. Trakowske, K. H. Spitzer, K. Schwerdtfeger & R. Nyström, The "Direct Strip Casting" Process, *Int. Conf. on New Developments in Metallurgical Process Technology,* June 13-15, 1999, pp.156 - 163

5. J. S. Truelove, T. A. Gray, P. C. Campbell & J. Herbertson, Fluid Dynamics in High-Speed Strip Casting Metal Delivery Systems, *SRNC-9*0, October 14-19, 1990, Pohang, Korea, pp.773-783

6. R. I. L. Guthrie, M. Hasan, C. Jefferies, R. P. Tavares & H. Murakami, Turbulent flow, heat transfer and solidification in thin strip casting machines, *Sec. Canada-Japan Symp. on Modern Steelmaking and Casting Techniques*, August 20-25, 1994, pp. 201-219

7. K. Schwerdtfeger, K. H. Spitzer, J. Kroos, P. Funke & K. H. Hower, Further Results from Strip Casting with the Single-Belt Process, *ISIJ International*, Vol. 40, 2000, pp.756-764

8. K. H. Moon, W. R. Choi, M. Isac, R. I. L. Guthrie & H. Nogami, Physical and Mathematical Modeling in Develoment of Metal Delivery System for Single Belt Casting Process, *ISIJ International*, Vol. 43, 2003, pp.1538-1547

9. A. Gracia & M. Prates, Mathematical Model for the Unidirectional Solidification of Metals: I. Cooled Molds, *Met. Trans.* **9B.**, 1978, pp. 449 – 457

10. A. Gracia, T. W. Clyne & M. Prates, Mathematical Model for the Unidirectional Solidification of Metals: II. Massive Molds, *Met. Trans.* **10B.**, 1979, pp. 85 – 92

11. J. Lipton, A. Garcia & W. Heinemann, An analytical solution of direct solidification with mushy zone, *Arch. Eisenhüttenwes.* **53**, 1982, pp. 469 – 473

12. M. Prates & H. Biloni, Variables Affecting the Nature of the Chill Zone, *Met. Trans.* **3B**, 1972, pp. 1501 - 1510

13. J. V. Beck, B. Blackwell & C. R. St. Clair Jr., *Inverse Heat Conduction: Ill-posed Problems*, Wiley Interscience, New York, 1985

14. K. Ho & R. D. Pehlke, Transient Methods for Determination of Metal-Mold Interfacial Heat Transfer, *AFS Trans.*, 1983, pp. 689 – 698

15. K. Ho & R. D. Pehlke, Mechanisms of Heat Transfer at a Metal-Mold Interface, *AFS Trans.*, 1984, pp. 587 – 597

16. K. Ho & R. D. Pehlke, Metal-Mold Interfacial Heat Transfer, *Met. Trans.* **16B**, 1985, pp. 585 – 594

17. Y. Nishida, W. Droste & S. Engler, The Air-Gap Formation Process at the Casting-Mold Interface and the Heat Transfer Mechanism through the Gap, *Met. Trans.* **17B**, 1986, pp. 883 - 844

18. T. S. P. Kumar & K. N. Prabhu, Heat Flux Transients at the Casting/Chill Interface during Solidification of Aluminum Base Alloys, *Met. Trans.* **22B**, 1991, pp. 717 - 727

19. M. Krishnan & D. G. R. Sharma, Determination of Heat Transfer Coefficient Between Casting and Chill in Unidirectional Heat Flow, *AFS Trans.* **102**, 1994, pp. 769 – 774

20. C. A. Muojekwu, I. V. Samarasekera & J. K. Brimacombe, Heat Transfer and Microstructure during the Early Stages of Metal Solidification, *Met. Trans.* **26B**, 1995, pp. 361 – 382

21. N. A. El-Mahallawy & A. M. Assar, Metal-Mould heat transfer coefficient using end-chill experiments, *J. Mat. Sci. Lett.* **7**, 1988, pp. 205 – 208

22. N. A. El-Mahallawy & A. M. Assar, Effect of melt superheat on heat transfer coefficient for aluminum solidifying against copper chill, *J. Mat.. Sci.* **26**, 1991, pp. 1729 – 1733

23. A. M. Assar, On the interfacial heat transfer coefficient for cylindrical ingot casting in a metal mould, *J. Mat. Sci. Lett.* **11**, 1992, pp. 601 – 606

24. N. A. El-Mahallawy, M. A. Taha, A. M. Assar & R. M. Hamouda, Aluminum and Al-4.5Cu alloy end chill: structural observation and heat flow analysis, *Mat. Sci. Tech.* **9**, 1993, pp. 691 – 697

25. A. M. Assar, Mould surface roughness and interfacial heat transfer using heat flow model, *Mat. Sci. Tech.* **13**, 1997, pp. 701 – 703

26. B. L. Coates, S. A. Argyropoulos & B. Melissari, The Effects of Surface Roughness on the Heat transfer at the Metal-Mold Interface, *Light Metals* 2002, CIM, pp. 487-501

27. K. N. Prabhu, S. A. Kumar & N. Venkataraman, Effect of Coating/Mold Wall/Casting Thickness on Heat Transfer and Solidification of Al-Cu-Si Alloy (LM-21) in Cast Iron Molds, *AFS Trans.*, 1994, pp. 827 – 832

28. J. C. Hwang, H. T. Chuang, S. H. Jong & W. S. Hwang, Measurement of Heat Transfer Coefficient at Metal/Mold Interface During Casting, *AFS Trans.*, 1994, pp. 877 – 883

29. P. Schmidt, Heat transfer during filling in die casting processes, *Mat. Sci. Eng.* **A173**, 1993, pp. 271- 274

30. F. Lau, W. B. Lee, S. M. Xiong & B. C. Liu, A study of the interfacial heat transfer between an iron casting and a metallic mould, *J. Mat. Proc. Tech.* **79**, 1998, pp. 25 – 29

31. S. P. Mehrotra, A. Chakravarty & P. Singh, Determination of the interfacial heat transfer coefficient in a metal-metal system solving the inverse heat conduction problem, *Steel Research* **68**, 1997, pp. 201 – 208

32. W. D. Griffiths, The Heat-Transfer Coefficient during the Unidirectional Solidification of an Al-Si Alloy Casting, *Met. Trans.* **30B**, 1999, pp. 473 – 482

33. R. Kayikci & W. D. Griffiths, The Influence of Surface Roughness on Interfacial Heat Transfer During Casting Solidfication, *Foundryman*, September, 1999, pp.267-273

34. E. Velasco, J. Talamantes, S. Cano, S. Valtierra, J. F. Mojica & R. Colas, Casting-Chill Interface Heat Transfer during Solidification of an Aluminum Alloy, *Met. Trans.* **30B**, 1999, pp. 773 – 778

35. M. Trovant & S. A. Argyropoulos, Finding Boundary Conditions: A Coupling Strategy for the Modeling of Metal Casting Processes: Part I. Experimental Study and Correlation Development, *Met. Trans.* **31B**, 2000, pp. 75-86

36. M. Trovant & S. A. Argyropoulos, Finding Boundary Conditions: A Coupling Strategy for the Modeling of Metal Casting Processes: Part II. Numerical Study and Analysis, *Met. Trans.* **31B**, 2000, pp. 87-96

37. K. H. Spitzer, Investigation of heat transfer between metal and a water-cooled belt using a least square method, *Int. J. Heat Mass Transfer* **34**, 1991, pp. 1969 – 1974

38. K. Schwerdtfeger, Belt casting for steel – a critical review, *The Brimacombe Memorial Symposium*, October 1-4, Vancouver, 2000, pp.613-629

39. S. J. Chen, R. C. Ren & A. A. Tseng, Interface Heat Transfer in Metal Casting on a Moving Substrate, *J. Mat. Proc. & Manu. Sci.* **3**, 1995, pp. 373 – 386

40. P. G. Q. Netto, R. P. Tavares & R. I. L. Guthrie, A technique for the evaluation of instantaneous heat fluxes for the horizontal casting of aluminum alloys, *Light Metals*, 1997, pp. 393 – 407

41. L. Strezov & L. Herbertson, Experimental Studies of Interfacial Heat Transfer and Initial Solidification Pertinent to Strip Casting, *ISIJ International* **38**, 1998, pp. 959 – 966

42. G. X. Wang & E. F. Matthys, Modelling of Heat Transfer and Solidification during Splat Cooling: Effect of Splat Thickness and Splat/Substrate Thermal Contact, *Int. J. Raid. Solidification* **6**, 1991, pp.141-174

43. G. X. Wang & E. F. Matthys, Interfacial Thermal Contact During Rapid Solidification On a Moving Substrate, *Proc. 10th Int. Heat Transfer Conf.*, Brington, UK, 1994, pp.169-174

44. G. W. Wang, Experimental and Numerical Study of Heat Transfer and Solidification for Molten Metal in Contact with a Cold Substrate, *Ph.D. Thesis*, University of California Santa Barbara, 1995

45. G. X. Wang & E. F. Matthys, On the Heat Transfer at the Interface Between a Solidifying Metal and a Solid Substrate, *Melt Spinning, Strip Casting and Slab Casting*, TMS, 1996, pp.205-236

46. H. Todoroki, R. Lertarom, T. Suzuki & A. W. Cramb, Initial Solidification of Iron, Nickel and Steel Droplets, *I&SM*, April, 1999, pp. 57 – 71

47. P. Misra, N. Phininchka & A. W. Cramb, The Effect of the Presence of Liquid Films on a Copper Mold Substrate on the Rate of Heat Transfer during the Solidification of Steel Droplets, *ISSTech 2003*, TMS, Indianapolis, 2003, pp.263-282

48. T. Loulou, E. A. Artyukhin & J. P. Bardon, Solidification of Molten Tin Drop on a Nickel Substrate, *Proc. 10th Int. Heat Transfer Conf.*, Brington, UK, 1994, pp.73-78

49. T. Loulou, E. A. Artyukhin & J. P. Bardon, Estimation of thermal contact resistance during the first stages of metal solidification process: I – experimental principle and modelisation, *Int. J. Heat Mass Transfer* **42**, 1999, pp.2119 – 2127

50. T. Loulou, E. A. Artyukhin & J. P. Bardon, Estimation of thermal contact resistance during the first stages of metal solidification process: II – experimental setup and results, *Int. J. Heat Mass Transfer* **42**, 1999, pp.2129 – 2142

51. J. S. Kim, M. Isac, R. I. L. Guthrie & J. Byun, Studies on Interfacial Heat Transfer Resistances and Characterization of Strip Microstructures for Al-Mg Alloys Cast on a Single Belt Casting Simulator, *Can. Met. Quart.* **41**, 2002, pp.87-96

52. S. Leboeuf, D. Bouchard, J. P. Nadeau, M. Isac & R. I. L. Guthrie, Aluminum droplets impinging on a copper substrate: a dynamic wetting and heat transfer study, *Light Metals 2003 Metaux Légers*, COM, August 24-27, Vancouver, 2003

53. S. Leboeuf, D. Bouchard, R. I. L. Guthrie, M. Isac & J. P. Nadeau, Étude sur la mouillabilité dynamique et le transfert de chaleur de gouttelettes d'aluminium solidifiant sur des substrats de cuivre, *Synergie-Al*, October 22-23, Chicoutimi, 2003

54. D. G. Wilson, A. D. Solomon & P. T. Boggs, *Moving Boundary Problems*, Academic Press, New York, 1978

55. J. Crank, Free *and Moving Boundary Problems*, Clarendon Press, Oxford, 1984

56. A. Mori & K. Araki, Methods for Analysis of the Moving Boundary Surface Problem, *Int. Chem. Engr.* **16**, 1976, pp.734

57. H. L. Tsai & B. Rubinsky, A Numerical Study Using Front Tracking Finite Element on the Morphological Stability of as Planar Interface During Transient Solidification Processes, *J. Crystal Growth* **69**, 1984, pp.29-46

58. H. L. Tsai, K. C. Chiang & T. S. Chen, Movement of Moisture Front and Alloy Solidification in Green Sand Casting, *AFS Transactions* **96**, 1988, pp.191-196

59. W. D. Rolph & K. J. Bathe, An Efficient Algorithms for Analysis of Nonlinear Heat Transfer with Phase Change, *Int. J. Num. Meth. Eng.* **18**, 1982, pp.119-134

60. Q. T. Pham, A Fast, Unconditionally Stable Finite-Difference Scheme for Heat Conduction with Phase Change, *Int. J. Heat Mass Transfer* **28**, 1985, pp.2079-2084

61. Q. T. Pham, The Use of Lumped Capacitance in the Finite-Element Solution of Heat Conduction Problems with Phase Change, *Int. J. Heat Mass Transfer* **29**, 1986, pp.285-291

62. V. Voller & M. Cross, Accurate Solutions of Moving Boundary Problems Using the Enthalpy Method, *Int. J. Heat Mass Transfer* **24**, 1981, pp.545-556

63. M. C. Flemings, *Solidification Processing*, McGraw-Hill, 1974

64. S. C. Flood, L. Katgerman, A. H. Langille & C. M. Read, A Model of Solidification, Fluid Flow and Stress Distribution in DC Casting, *Modeling of Casting and Welding Processes IV*, TMS, 1988, pp.553-561

65. C. S. Kanetkar & D. M. Stefanescu, Equiaxed Dendritic Solidification of Single Phase Alloys: A Solidification Kinetics and Heat Transfer Model, *Modelling of Casting and Welding Processes IV*, TMS, 1988, pp.697-708

66. N. Rappaz & D. M. Stefanescu, Modeling of Equiaxed Primary and Eutectic Solidification, Solidification Processing of Eutectic Alloys, TMS, 1988, pp.133-151

CHAPTER
3

INTERFACIAL HEAT TRANSFER

3.1 INTRODUCTION

The mathematical simulation of casting processes involving unidirectional solidification requires a realistic characterization of the heat transfer phenomena at the metal/mold interface. The contact between the liquid metal and the mold is, thus, one of the crucial features in the casting process. When the metal and the mold surfaces are brought into contact, the interfacial thermal resistance is developed due to several factors, such as cast metal shrinkage, air gap formation, roughness on the substrate surface, and the formation of metal oxides at the interface. This contact resistance is reflected by a steep temperature gradient at the interface region. The magnitude of the thermal resistance is influenced by the wettability of the cast metal on the mold, and the presence of interfacial media of gas or trapped air. The wettability also depends on thermophysical properties, surface roughnesses, geometries, the initial temperature of the mold, melt superheat, contacting pressure, chemical reactions, etc. This interfacial thermal resistance $R(t)$ can be quantified through measured heat flux, $q(t)$, or the heat transfer coefficients, $h(t)$.

$$R(t)=\frac{T(t)_{Metal}-T(t)_{Mold}}{q(t)}=\frac{1}{h(t)} \tag{3.1.1}$$

3.2 METAL-MOLD HEAT TRANSFER

3.2.1. Metal-mold heat transfer without interfacial resistance

It is worthwhile reviewing several analytical solutions of the one-dimensional heat conduction problem. They are only available for time-independent heat transfer coefficient condition. When a pure liquid metal with no superheat is poured against a highly conductive mold surface assuming no interfacial thermal resistance at the interface, a simple analytical solution can be obtained. As the main thermal resistance in heat transfer takes place within the mold in the case of sand casting, a further assumption of no temperature gradient in the solidified shell of the casting can be considered. The equation of the transient temperature profiles developed within the mold is presented in equation (3.2.1), and plotted schematically in Fig. 3.2.1.

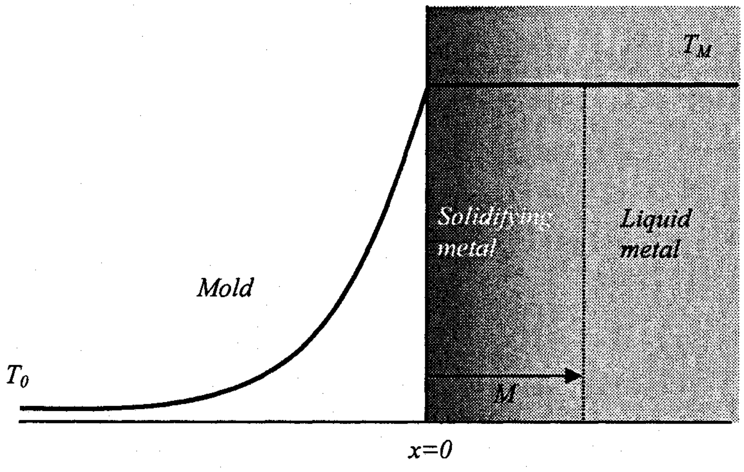

Fig. 3.2.1. Temperature profiles in a solidifying metal and a cooling mold without temperature gradient within the solidified shell

The mold temperature profile takes the form of an error function [1]:

$$T = T_0 + (T_M - T_0) \cdot erfc(-\frac{x}{2\sqrt{\alpha_m t}}) \qquad (3.2.1)$$

and the interfacial heat flux is given by

$$q = \frac{k_m (T_M - T_0)}{\sqrt{\pi \alpha_m t}} = \frac{(T_M - T_0)\sqrt{k_m C_{p,m} \rho_m}}{\sqrt{\pi}} \cdot \frac{1}{\sqrt{t}} \tag{3.2.2}$$

If the solidification of a liquid metal alloy at zero superheat proceeds with no thermal resistance within its mushy zone, the extracted heat flux is related to the density of solidified metal ρ_s, latent heat ΔH_s, and the solidified shell thickness M according to:

$$q = \rho_s \cdot \Delta H_s \cdot \frac{dM}{dt} \tag{3.2.3}$$

Equations (3.2.2) and (3.2.3) are set equal and the integration follows with $M = 0$ at $t = 0$, to give:

$$M = \frac{2}{\sqrt{\pi}} \frac{T_M - T_0}{\rho_s \Delta H_s} \sqrt{k_m C_{p,m} \rho_m} \cdot \sqrt{t} \tag{3.2.4}$$

Here, the product $\sqrt{k \cdot C_p \cdot \rho}$ is defined as the "heat diffusivity ($\varepsilon = \sqrt{k C_p \rho}$)" and should be distinguished from the thermal diffusivity $\alpha (= k / \rho \cdot C_p)$. Heat diffusivity is a measure of the capability of the mold to absorb heat from the solidifying metal and its unit is J/m^{2}Ks$^{1/2}$. On the other hand, thermal diffusivity determines the speed of heat propagation by conduction during changes of temperature with time and its unit is m^2/s, which is nothing to do with the thermal energy itself.

By way of example, a 3mm thick strip of pure magnesium cast on a copper mold using this assumption, reveals that it would take only 5.3 mille-seconds to complete the solidification, as shown in Fig. 3.2.2. Table 3.2.1 shows the thermophysical properties used in this calculation.

Table 3.2.1. Thermophysical properties of pure magnesium and copper mold

Properties	Mg	Cu
Initial temperature (°C)	650	25
Specific heat (J/KgK)	1017	380
Density (Kg/m^3)	1740	8920
Thermal conductivity (W/mK)	150	398
Latent heat (KJ/Kg)	362	203

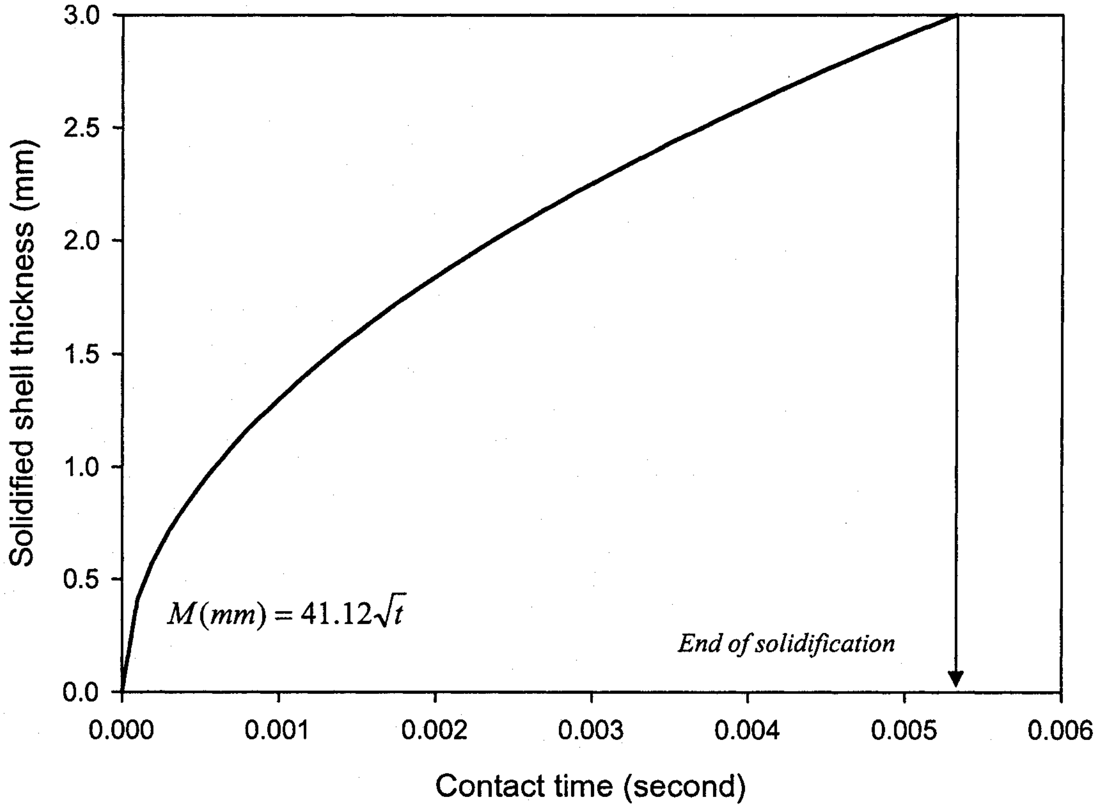

Fig. 3.2.2. Solidified shell thickness vs. solidification time following the thermal contact condition of Fig. 3.2.1.

If the assumption of no temperature gradient in the solidifying metal is discarded but still assuming no thermal resistance at the interface, temperature profiles on both metal and mold follow an error function formulation as shown in Fig. 3.2.3. Equations of both temperature profiles are presented from equation (3.2.5) to (3.2.9). In this case, the interface temperature, T_s*, remains constant to be tackled analytically and is determined by the thermophysical properties of the metal and the mold [2].

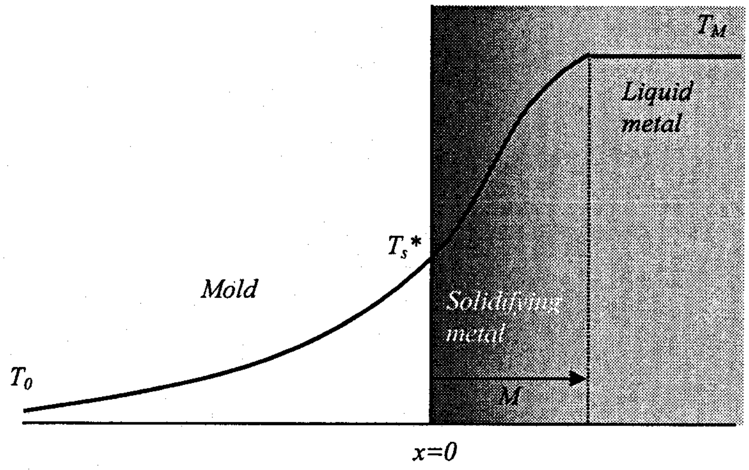

Fig. 3.2.3. Temperature profiles in a solidifying metal and a cooling mold with temperature gradient within the solidified shell

Mold temperature profile: $T = T_0 + (T_s^* - T_0)\cdot erfc(-\frac{x}{2\sqrt{\alpha_m t}})$ (3.2.5)

Solidifying metal temperature profile: $T = T_s^* + A \cdot erf(\frac{x}{2\sqrt{\alpha_s t}})$ (3.2.6)

where A is the constant obtained from the given boundary conditions:

$$T = \begin{cases} T_s^* \;\; at \;\; x = 0 \; and \; t \geq 0 \\ T_M \;\; at \;\; x = M \; and \; t > 0 \end{cases}$$

Substitution gives the value of constant A as

$$A = \frac{T_M - T_s^*}{erf(\frac{M}{2\sqrt{\alpha_s t}})} \tag{3.2.7}$$

As this value is constant,

$$\frac{M}{2\sqrt{\alpha_s t}} = \phi = constant \tag{3.2.8}$$

Here, the solidified shell thickness M can be given by

$$M = 2\phi\sqrt{\alpha_s t} \tag{3.2.9}$$

Heat balance at the metal-mold interface gives

$$q\Big|_{x=0} = -k_m \frac{\partial T}{\partial x}\Big|_{x=0^- (mold)} = -k_s \frac{\partial T}{\partial x}\Big|_{x=0^+ (metal)} \tag{3.2.10}$$

Differentiation of equations (3.2.5) and (3.2.6) followed by the substitution to equation (3.2.10) leads to the interface temperature T_s*.

$$T_s^* = T_0 + \phi e^{\phi^2} \frac{\sqrt{\pi} \cdot \Delta H_s}{C_{p,s}} \sqrt{\frac{k_s C_{p,s} \rho_s}{k_m C_{p,m} \rho_m}} = T_0 + \phi e^{\phi^2} \frac{\sqrt{\pi} \cdot \Delta H_s}{C_{p,s}} \frac{\varepsilon_s}{\varepsilon_m} \tag{3.2.11}$$

where heat diffusivity $\varepsilon = \sqrt{k C_p \rho}$.

At the solidification front, $x=M$, the energy balance gives

$$q\Big|_{x=M} = -k_s \frac{\partial T}{\partial x}\Big|_{x=M} = -\rho_s \Delta H_s \frac{dM}{dt} \tag{3.2.12}$$

From equations (3.2.10) and (3.2.12), the parameter ϕ can be found

$$\frac{T_M - T_0}{\sqrt{\pi}}\frac{C_{p,s}}{\Delta H_s} = \phi e^{\phi^2}\left(\frac{\varepsilon_s}{\varepsilon_m} + erf(\phi)\right) \tag{3.2.13}$$

It should be noted that the parameter ϕ is related to initial temperatures (T_M, T_0), the thermophysical property of the solidifying metal ($C_{p,s}$, ΔH_s), the ratio of the heat diffusivity of the cast metal to that of the mold ($K_\varepsilon = \varepsilon_s/\varepsilon_m$). A low value of K_ε is applicable to a highly conductive casting such as a copper mold system and the value of K_ε increases for lower conductivity molds such as sand casting. Fig.3.2.4 shows the relationship between the parameter ϕ and K_ε. For a given initial condition and solidifying metal, the left hand side of equation (3.2.13) is fixed. The lower value of K_ε results in the higher value of parameter ϕ and the increase in the rate of solidified shell growth.

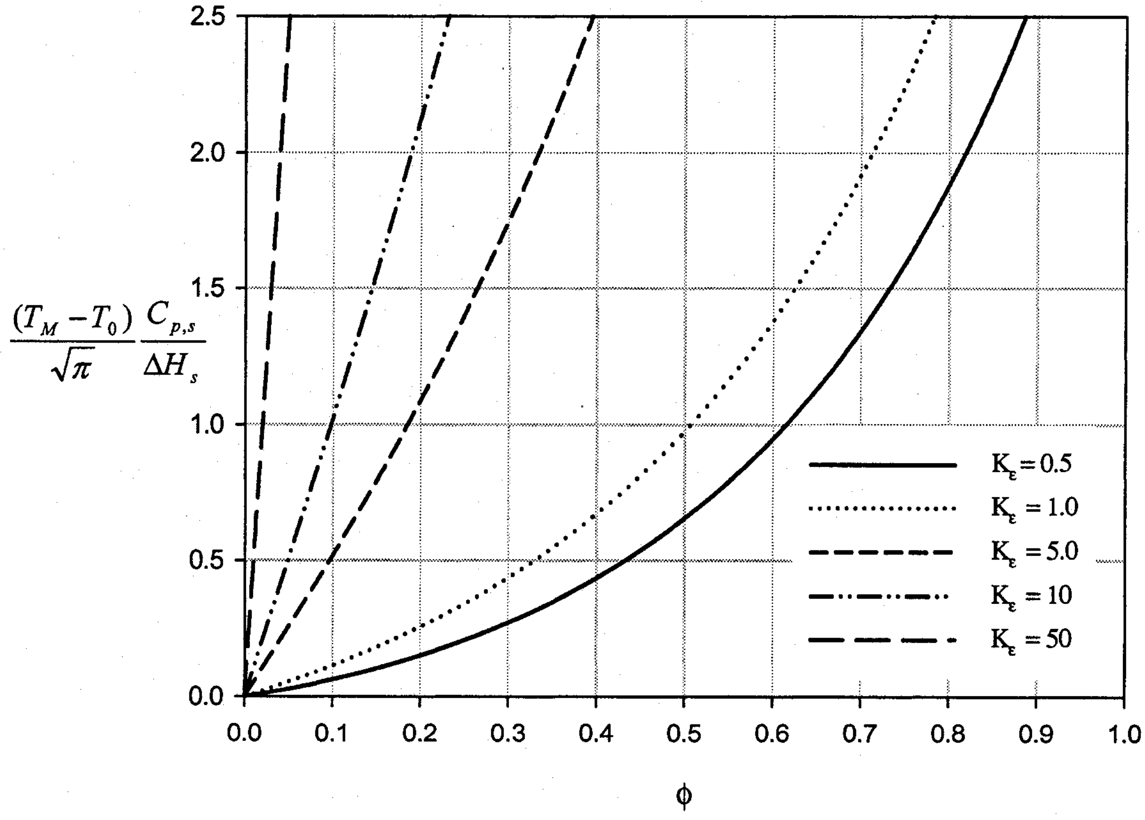

Fig. 3.2.4. Variation of K_ε with ϕ

Fig. 3.2.5 presents the temperature profile considering the temperature gradient in the solidifying pure magnesium on a copper mold. Fig. 3.2.6 also reveals that it takes about 65 mille-seconds which is about 12 times higher compared to the previous case.

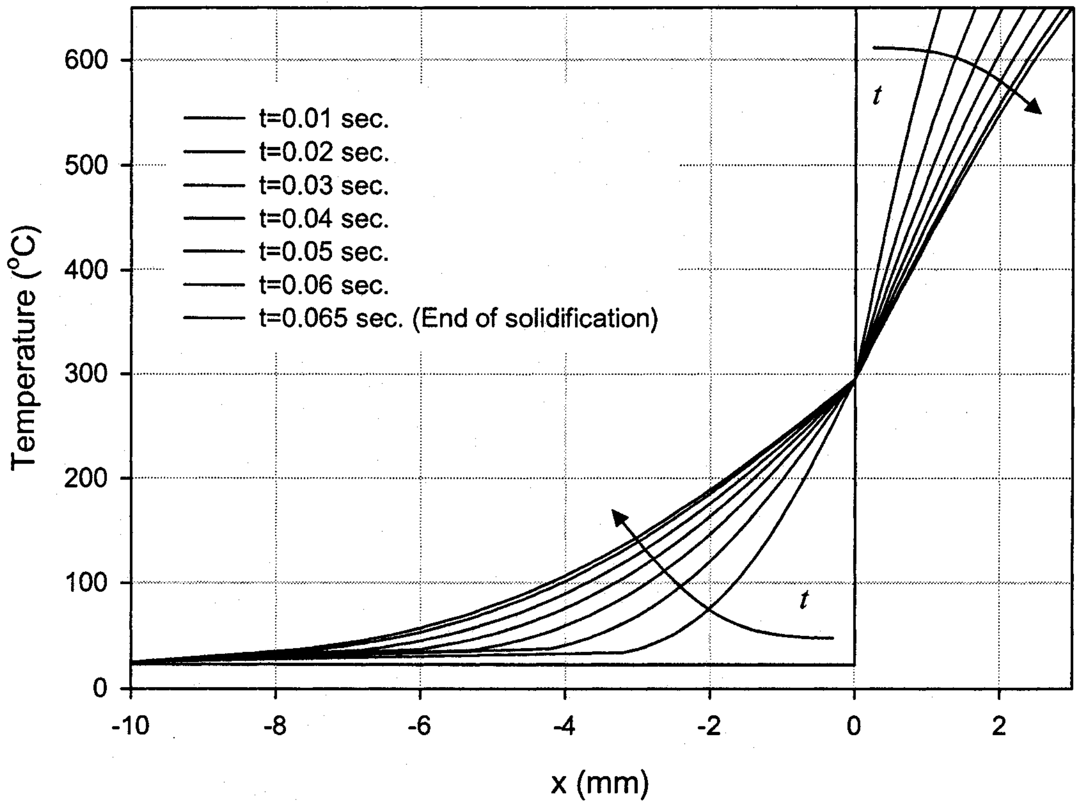

Fig. 3.2.5. Temperature profiles of 3mm solidifying pure magnesium strip on a 10 mm thick copper mold, for perfect interfacial contact (Fig. 3.2.3)

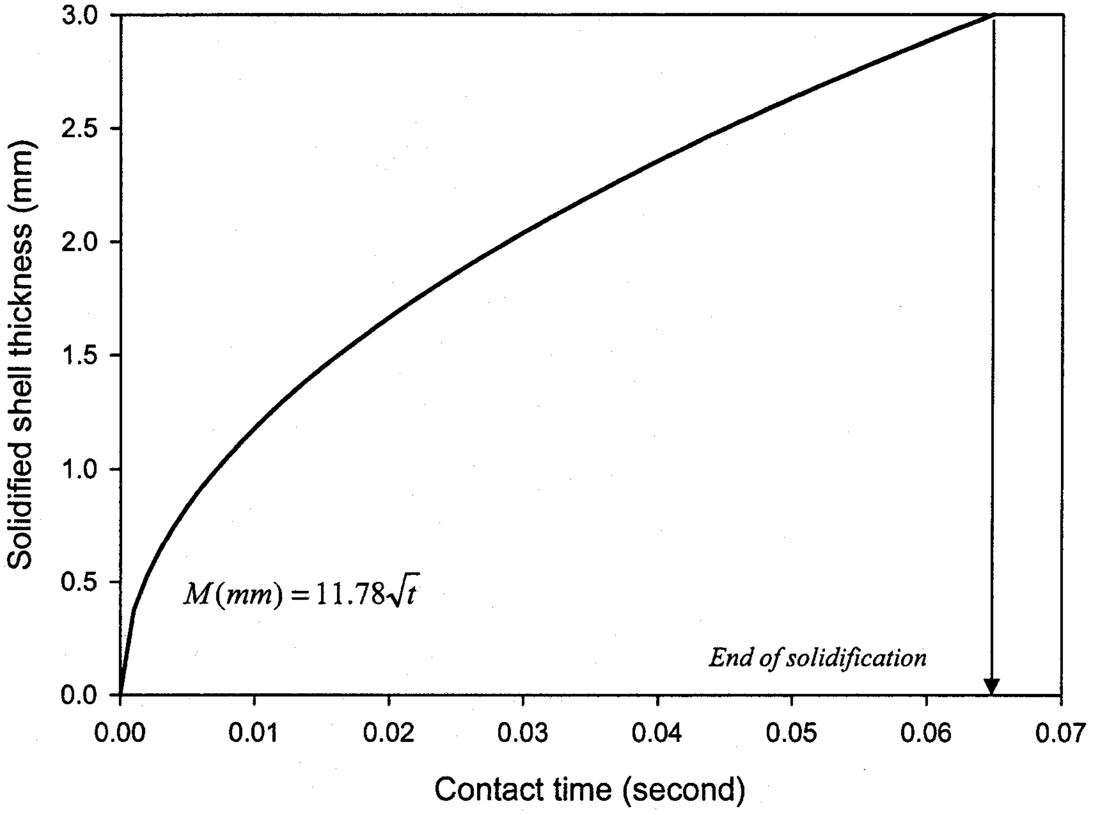

Fig. 3.2.6. Solidified shell thickness vs. solidification time following the thermal contact condition in Fig. 3.2.3.

From equation (3.2.11), the interface temperature $T_s{*}$ is governed by the ratio of the heat diffusivity of the cast metal to that of the mold (K_ε) and the value of the parameter ϕ. The relative metal-mold interface temperature, θ^*, can be defined as:

$$\theta^* = \frac{T_s^* - T_0}{T_M - T_0} = \frac{\varepsilon_s / \varepsilon_m}{\left(erf(\phi) + \varepsilon_s / \varepsilon_m \right)} = \frac{K_\varepsilon}{erf(\phi) + K_\varepsilon} \tag{3.2.14}$$

Fig. 3.2.7 can be used to calculate the relative metal-mold interface temperatures with the given values of thermophysical properties of the cast metal and the mold.

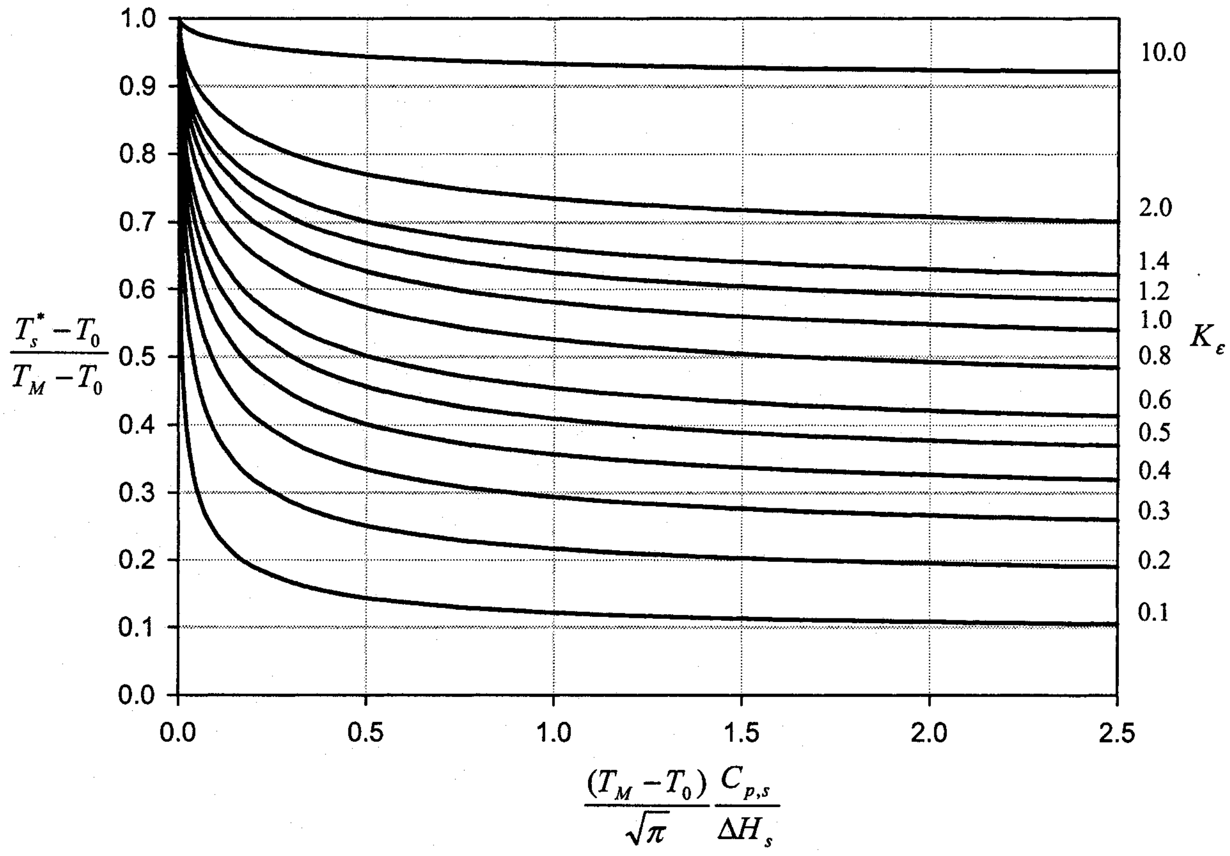

Fig. 3.2.7. Relative metal-mold interface temperatures for unidirectional casting without interfacial resistance

In many metallurgical casting processes, the value of $\frac{(T_M - T_0)}{\sqrt{\pi}} \frac{C_{p,s}}{\Delta H_s}$ is higher than 1 and the value of *erf(ϕ)* is close to unity. Therefore, the relative metal-mold interface temperature can be approximated as:

$$\theta^* = \frac{T_s^* - T_0}{T_M - T_0} \cong \frac{K_\varepsilon}{1 + K_\varepsilon} \qquad (3.2.15)$$

Note that as t→∞, a steady state condition from equation (3.2.6) is achieved and both temperature profiles will be the same and equal to

$$T = T_s^* = T_0 + \frac{K_\varepsilon}{1 + K_\varepsilon}(T_M - T_0) \qquad (3.2.16)$$

If the heat diffusivities of the two semi-infinite plates are equal (K_ε=1), the relative interfacial temperature at a steady state will be θ^* =1/2. If the heat diffusivity of the mold is much higher than that of the liquid metal ($\varepsilon_m >> \varepsilon_s$) such as copper mold and Wood's alloy melt, then $K_\varepsilon \rightarrow 0$. In this case θ^* will have the lowest value possible, equal to zero and $T_s^* \approx T_0$. If the heat diffusivity of the mold is low (K_ε>>1) such as a plaster mold and steel melt, θ^* will be equal to unity and $T_s^* \approx T_M$. Therefore, the value θ^* may be referred to as the mold cooling capability. If θ^* is zero, then the cooling capability will be the highest; and vice versa, when θ^* =1, the cooling effect of the mold will be zero.

In this case, the interfacial heat flux can be calculated as

$$q\big|_{x=0} = \frac{1}{\sqrt{\pi t}}(T_M - T_0)\frac{1}{1/\varepsilon_s + 1/\varepsilon_m} = \frac{1}{2\sqrt{\pi t}}(T_M - T_0)\cdot(HM)_{\varepsilon_s,\varepsilon_m} \qquad (3.2.17)$$

where $(HM)_{\varepsilon_s,\varepsilon_m}$ is a harmonic mean of the heat diffusivities of the solidifying shell and mold, ε_s and ε_m, $(=\frac{2}{1/\varepsilon_s + 1/\varepsilon_m})$.

It clearly shows that the interfacial heat flux is equally affected by heat diffusivities of the cast metal and cooling mold and proportional to their harmonic mean. Also, the infinite value of heat flux at time zero implies a simultaneous interfacial heat transfer coefficient of infinity. Mathematically, it is evident that this value of infinity can be obtained at the initial stage of solidification between the liquid metal and the mold.

3.2.2 Metal-mold heat transfer with interfacial resistance

Even though the interfacial thermal resistance was not considered in the previous analysis, it exists in practice and plays an important role in thin strip casting. Also, the interfacial surface temperature T_s* is not constant, but time-variant. There is no exact analytical solution for the case of imperfect thermal contact, where there is an interfacial resistance between the casting metal and the cooling mold. To keep the problem tractable analytically, Adams [3] proposed to separate the problems into two regions: cooling of the cast metal and heating of the mold. He suggested the following assumptions:

i) The constant interfacial temperature in perfect contact condition still has its physical meaning and regarded as the "imaginary interface temperature" in imperfect contact condition.

ii) The total thermal resistance ($1/h$) can be divided into the casting side ($1/h_s$) and the mold ($1/h_m$). These resistances are determined by the ratio of thermal diffusivity.

By inserting an imaginary reference plane at the interface between the mold and the solidifying metal which is at T_s*, where T_s* is assumed constant and determined by equation (3.2.11), the interface resistance is apportioned on both sides as:

$$\frac{1}{h_s} = \frac{1}{h} \cdot \frac{\varepsilon_m}{\varepsilon_s + \varepsilon_m} \tag{3.2.18}$$

$$\frac{1}{h_m}=\frac{1}{h}\cdot\frac{\varepsilon_s}{\varepsilon_s+\varepsilon_m} \tag{3.2.19}$$

Therefore, the total thermal resistance is

$$\frac{1}{h}=\frac{1}{h_s}+\frac{1}{h_m} \tag{3.2.20}$$

where h is the interfacial heat transfer coefficient, h_s is the coefficient on the metal side and h_m is the coefficient on the mold side.

Fig. 3.2.8 shows an imaginary reference plane inserted at the interface. It should be noted that there are two time-variant surface temperatures, T_{sM}*(metal side) and T_{s0}* (mold side). Also, heat flux balance on both sides gives

$$\frac{\Delta T_{sM}}{\Delta T_{s0}}=\frac{h_s}{h_m}=\frac{\varepsilon_s}{\varepsilon_m}=K_\varepsilon \tag{3.2.21}$$

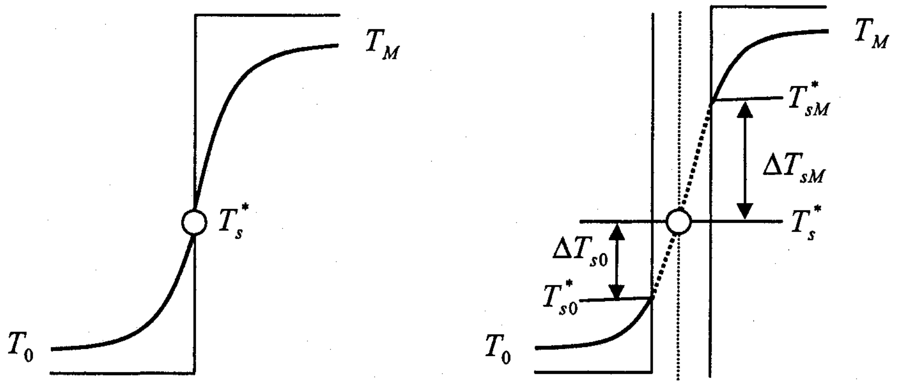

Fig. 3.2.8. Imaginary reference plane inserted at the metal-mold interface

If the temperature profile within the solidifying metal can be assumed as a linear function as shown in Fig. 3.2.9, the problem is more tractable without losing its physical reliability.

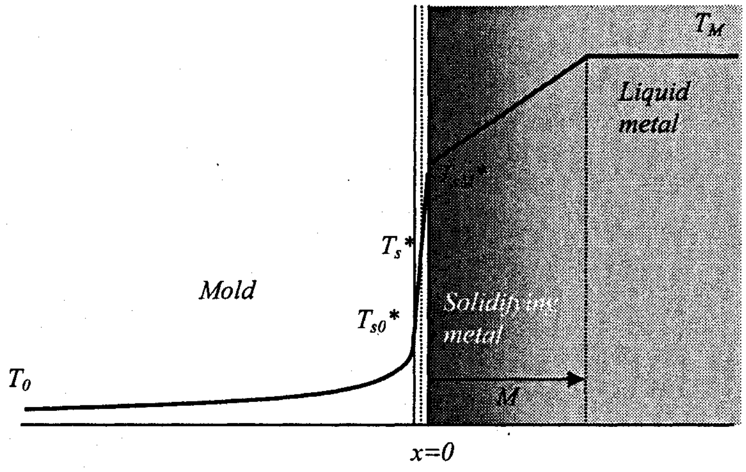

Fig. 3.2.9. Temperature profiles in a solidifying metal and a cooling mold with the interfacial thermal resistance

Balance of the two heat fluxes at the interface gives

$$q\big|_{x=0} = q\big|_{x=M} = \frac{T_M - T_s^*}{1/h_s + M/k_s} \tag{3.2.22}$$

At $x=M$ of the solidifying shell front, latent heat is evolved according to:

$$q\big|_{x=M} = \rho_s \Delta H_s \frac{dM}{dt} \tag{3.2.23}$$

From equations (3.2.22) and (3.2.23), the solidified shell thickness M can be obtained by solving a quadratic equation of

$$M = \frac{h_s (T_M - T_s^*)}{\rho_s \Delta H_s} t - \frac{h_s}{2k_s} M^2 \tag{3.2.24}$$

and

$$M = -\frac{k_s}{h_s} + \sqrt{\left(\frac{k_s}{h_s}\right)^2 + 2\frac{k_s (T_M - T_s^*)}{\rho_s \Delta H_s} \cdot t} \tag{3.2.25}$$

The interface temperature of the solidified metal side T_{sM}* is

$$T_{sM}^{*} = \frac{Bi_s}{1+Bi_s} T_s^{*} + \frac{1}{1+Bi_s} T_M \tag{3.2.26}$$

where the Biot Number of the shell side, $Bi_s = \frac{h_s M}{k_s}$. Note that $T_{sM}* = T_M$ at $M = 0$ and $T_{sM}* = T_s*$ when $h \to \infty$ ($Bi_s \to \infty$).

On the other hand, the temperature profile of mold side can be obtained by

$$\frac{T-T_0}{T_s^{*}-T_0} = erfc\left(\frac{1}{2\sqrt{Fo_m}}\right) - e^{\gamma} \cdot erfc\left(\frac{1}{2\sqrt{Fo_m}} + Bi_m \sqrt{Fo_m}\right) \tag{3.2.27}$$

where the Fourier Number of the mold interface, $Fo_m = \frac{\alpha_m t}{x^2}$, $Bi_m = \frac{h_m x}{k_m}$, and $\gamma = Bi_m + Bi_m^2 \cdot Fo_m$. Also, note that $T = T_{s0}*$ at $x = 0$ and $T_{s0}* = T_s*$ when $h \to \infty$ ($Bi_m \to \infty$). [4].

The same example of a 3mm magnesium strip casting on a copper mold with different interfacial heat transfer coefficients h is solved and the solidified shell thicknesses are presented in Fig. 3.2.10. It reveals that the existence of the interfacial thermal resistance greatly retards the end of solidification time. It takes 3.74 seconds for the completion of 3mm thick magnesium strip with an interfacial heat transfer coefficient of 1000 W/m^{2}K, while 0.42 seconds is expected when the interfacial heat transfer coefficient is 10000 W/m^{2}K. Note that the solidified shell thickness M is proportional to the square root of time from equation (3.2.25). When the heat transfer coefficient h_s goes to infinity, which implies no interfacial thermal resistance, it comes to equation (3.2.28). Compared to equation (3.2.9), this resulted in a faster completion of solidification because the temperature profile in the solidified shell was assumed to be linear here. Fig. 3.2.11 shows that the linear temperature profile inside the solidified shell expected 53 ms from equation (3.2.28) and the error function formulation of the temperature profile predicts 65 ms from equation (3.2.9) and Fig. 3.2.6.

$$M = \sqrt{2\alpha_s \cdot \frac{C_{p,s}(T_M - T_s^*)}{\Delta H_s}} \cdot \sqrt{t} \tag{3.2.28}$$

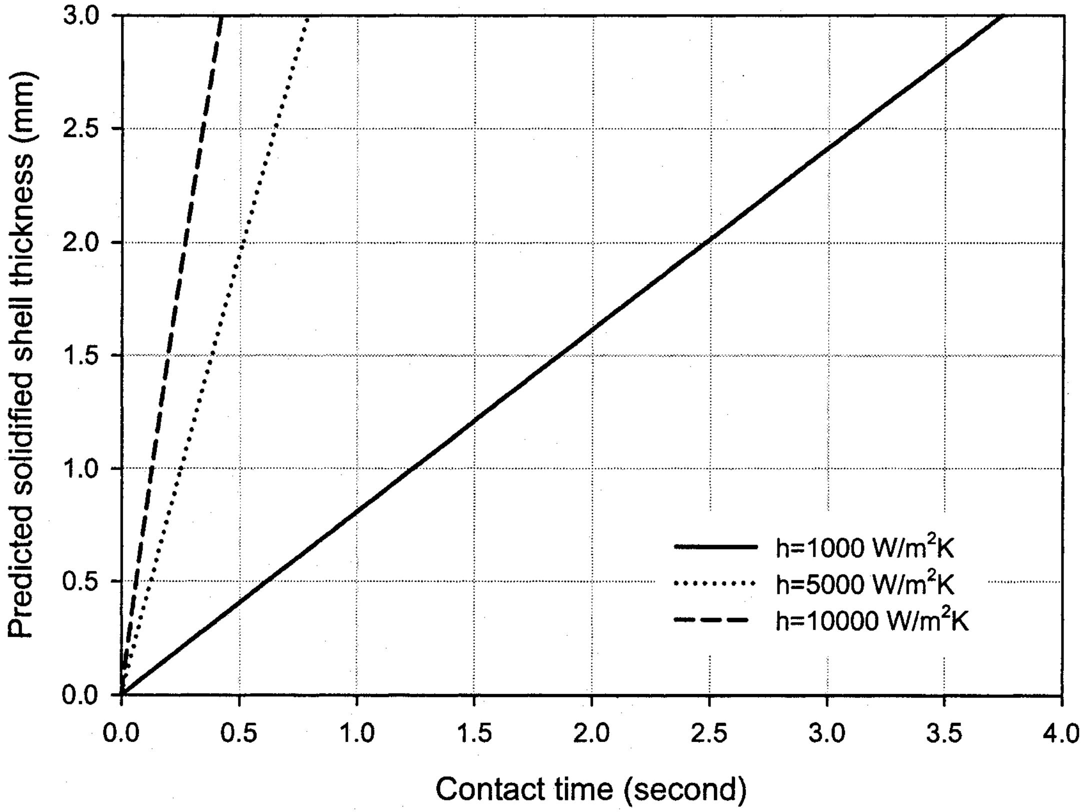

Fig. 3.2.10. Predicted solidified shell thickness vs. solidification time of 3mm thick magnesium strip cast on a copper substrate for various interfacial transfer coefficients

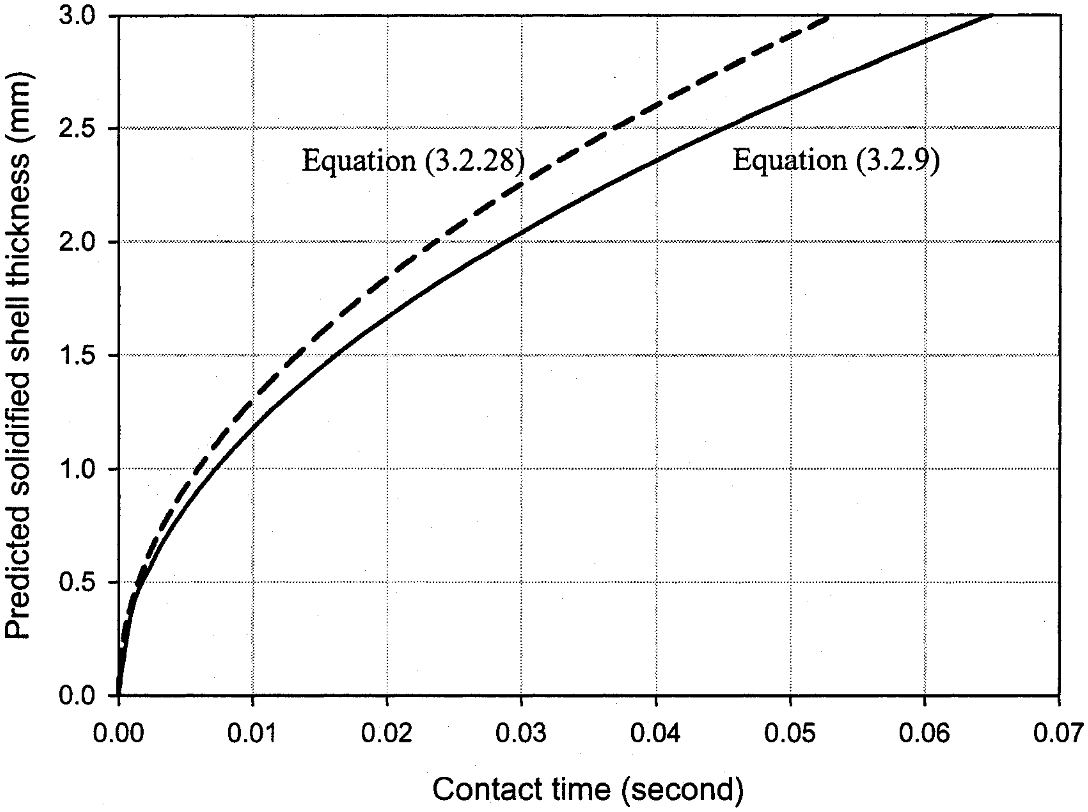

Fig. 3.2.11. Predicted solidified shell thickness vs. solidification time based on equations (3.2.9) and (3.2.28)

Temperature profiles within the copper mold and solidifying magnesium strip are shown in Figs. 3.2.12 to 3.2.14 for the various values of interfacial heat transfer coefficients. It should be noted that the time scale is different for each plot. As solidification proceeds, the surface temperature on the mold side increases, while that of the solidifying metal decreases. The interfacial thermal resistance greatly hinders the rate of heat transfer and delays final solidification. In real casting, the behaviour of the interfacial thermal resistances is much more complex and not even constant. It originates for many reasons, such as shrinkage of the solidified skin, surface oxidation, air-film evolution, chemical reaction, etc. This makes it difficult to predict the rate of interfacial heat transfer theoretically, and empirical measurements are needed.

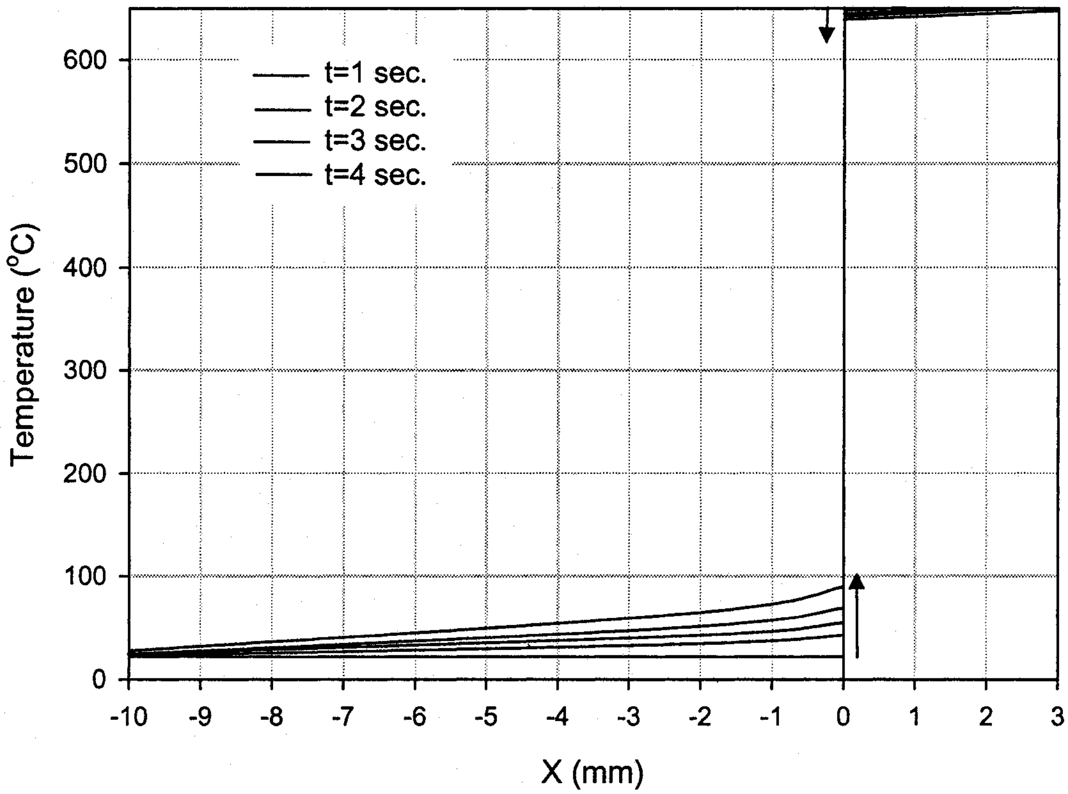

Fig. 3.2.12. Temperature profiles within a 3mm thick strip of pure magnesium strip solidifying on a 10 mm thick copper mold, for an interfacial heat transfer coefficient of 1000 W/m²K

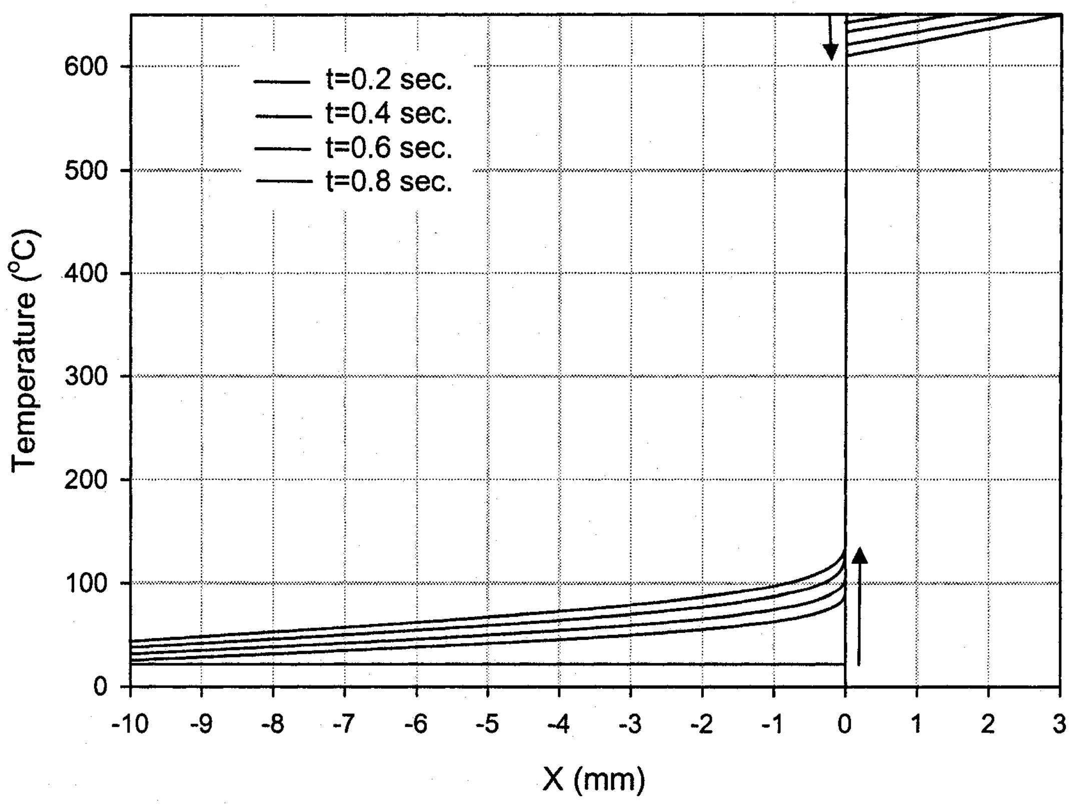

Fig. 3.2.13. Temperature profiles within a 3mm thick strip of pure magnesium strip solidifying on a 10 mm thick copper mold, for an interfacial heat transfer coefficient of 5000 W/m^{2}K

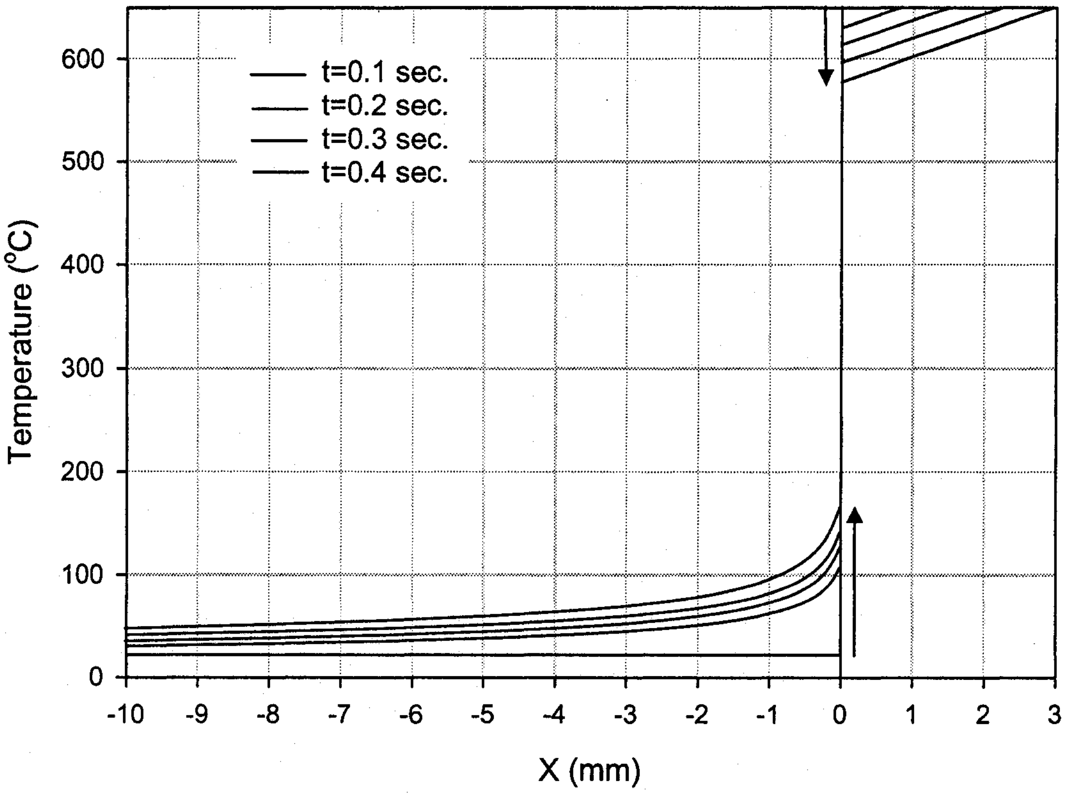

Fig. 3.2.14. Temperature profiles within a 3mm thick strip of pure magnesium strip solidifying on a 10 mm thick copper mold, for an interfacial heat transfer coefficient of 10000 W/m^{2}K

REFERENCES

1. H. S. Carlsaw & J. C. Jaeger, *Conduction of Heat in Solids*, 2nd edition, Oxford, 1959

2. D. R. Gaskell, *An Introduction to Transport Phenomena in Materials Engineering*, 1992, pp.408-420

3. C. M. Adams, *Liquid Metals and Solidification*, ASM, Cleveland, 1958, pp.203-206

4. D. R. Poirier & G. H. Geiger, *Transport Phenomena in Materials Processing*, TMS, 1994

CHAPTER

4

EXPERIMENTAL APPARATUS & METHODOLOGY

4.1 EXPERIMENTL APPARATUS & PROCEDURES

The objective of the experiments performed was to investigate interfacial heat transfer between solidifying magnesium alloy strips and a moving substrate, paying close attention to key factors affecting resistance to heat transfer and the local cooling rate. To achieve this goal, an experimental apparatus simulating a single belt caster, was built.

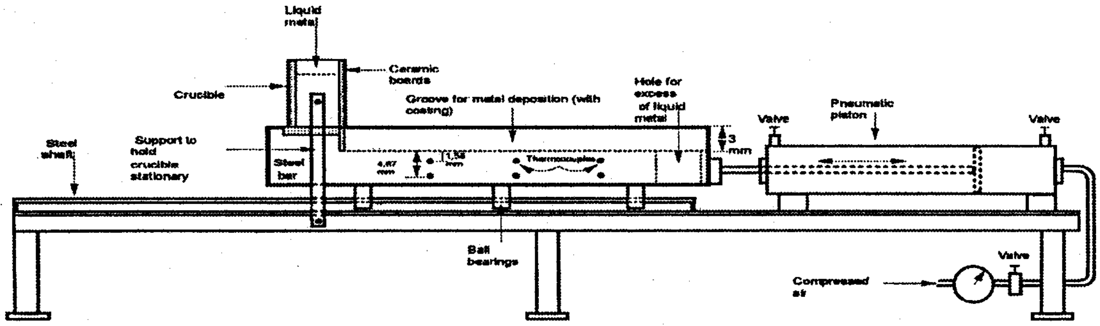

Fig. 4.1.1. Single belt casting simulator

In the single belt casting process, heat is mainly extracted from the liquid metal by a water-cooled belt. During solidification, the thermal history of solidifying strips and the interfacial heat transfer greatly influence the quality of the strips produced and their underlying microstructures. Using the strip casting simulator shown in Fig. 4.1.1, which replaces the water chill by a sold chill block substrate, magnesium alloys were cast on different chill substrates: sand blasted low carbon steel, sand blasted copper, alumina coated steel, zirconia coated steel, and nickel metallic coated steels. This simulator mainly consists of a moving substrate, a pneumatic pump piston, and a stationary refractory mold. The substrate was capable of moving at speeds within the range intended for industrial single belt casters (0.3 – 1.2 m/s), and the thicknesses of the strips could be determined accordingly. The substrate was made from either a low carbon steel or copper bar 1 m long, 75 mm wide and 10 mm thick. Two K-type thermocouples were positioned in the substrate for temperature measurement at a depth of about 1.58 mm and 4.87 mm from the bottom of the groove half way down the length of the bar. A 40 mm wide and 3 mm deep groove for metal deposition was engraved along the longitudinal axis of the substrate as shown in Fig. 4.1.2. The choice of location for the thermocouples was determined by two factors. First, due to inertia of the substrate during its initial period of acceleration, it took some time (a fraction of a second) for the substrate to attain its final speed. The lateral location of the thermocouples ensured the steady state regime of the moving substrate. Secondly, due to the rapid change in the interfacial heat resistance, the thermocouple's stability and sensitivity depend on its location. The vertical positions of 1.58 mm and 4.87 mm were the results of trial and error experiments to optimize conditions. To improve the sensitivity of the thermocouples, they were bonded by OMEGATHERM ®, a high thermal conductivity paste.

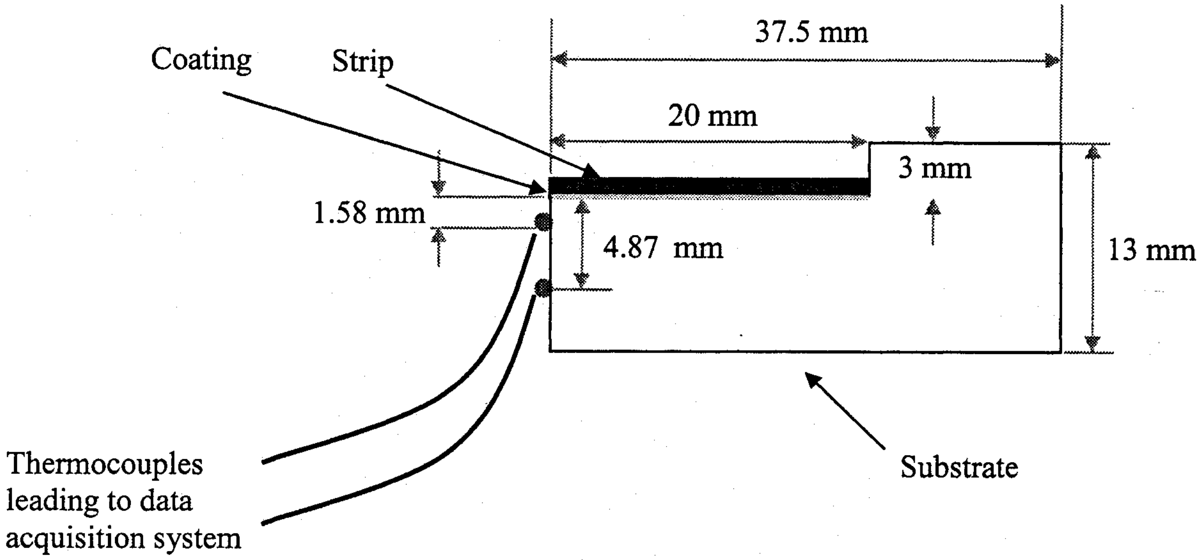

Fig. 4.1.2. Cross-section of the substrate

The steel substrates were coated by flame spraying at the Hazelett Strip Casting Corporation and three different types of coatings (alumina, zirconia, nickel) were applied on respective materials. Coating thicknesses were maintained constant at 75μm. The values of R_a (surface arithmetic average roughness) were derived from the average of five readings. The thermophysical properties of substrates used appear in Table 4.1.1.

Table 4.1.1. Thermophysical properties of substrates used

Substrate material	C_p (J/Kg·K)	k (W/m·K)	ρ (kg/m^3)	R_a (μm)
Carbon steel	430	79.6	7860	3~4
Copper	380	398	8920	3~4
Alumina coating	1070	3.5	3970	7.7
Zirconia coating	475	0.7	5680	6.7
Nickel coating	444	17	8900	7.4

4.1.1. Experiment Materials

Magnesium is the lightest structural metal used worldwide. Its low density and mechanical strength results in a high stiffness-to-weight ratio. The density of magnesium is about two-thirds that of aluminum and a quarter that of steel. Because of this benefit, the need to produce lightweight components for the automobile industry has focused attention on magnesium as a casting alloy. Magnesium has a good EMI (Electromagnetic Interference) shielding ability which gives it high potential for use in the mobile phone industry. Magnesium also absorbs vibration energy effectively, and exhibits good dimensional stability. i.e. the dimensions of magnesium parts are very stable with time and temperature changes. Magnesium alloys are cast using a variety of methods. These include high pressure die casting, low pressure permanent mold casting, sand casting, plaster/investment casting, and thixomolding. Different methods are applied for the various purposes, for a given casting, but the most common for magnesium, are die cast and sand cast parts.

Magnesium sheet production has recently received a lot of interest worldwide. Owing to the HCP (Hexagonal Close Packed) structure of the magnesium, it cannot be hot rolled at temperatures lower than 343 °C [1]. The number of slip planes in a crystal structure determines the capacity for plastic deformations during extrusion, forging, or rolling processes. In the case of magnesium, a hexagonal structure has fewer slip planes than other highly symmetrical structures such as face centered cubic and body centered cubic structures. Thus, plastic deformation of magnesium is not so favorable and is difficult. This negative feature, in turn, makes magnesium a good candidate material for near-net-shape casting. These processes aim to reduce the many rolling steps typically required after casting. Since 1990, according to the AFS Marketing Dept., the U.S. magnesium casting production has increased by 55%, with an average annual growth rate of 15.4%. It is expected to exceed 250 million tons by 2009. In 1999, U.S. sales of magnesium castings were $400 million and these will increase to more than $1.8 billion by 2009 [2].

The main objective for the present experiments was to evaluate the castability of magnesium alloys, AM50 and AZ91, on a single belt casting process and to study the effect of substrate materials on heat transfer and microstructure of the strip. To characterize the microstructure, the SDAS was measured and the cooling rate of the strip was investigated. The reason why AM50 and AZ91 were chosen is that they are used widely and are known to have high strength with good ductility in die casting processes. By comparing the microstructures of these two magnesium alloys having different freezing ranges, it is also possible to guess about the microstructure of AM60 alloy. The aluminum content in these alloys increases mechanical strength, corrosion resistance, and castability. On the other hand, it is also known that the increase of alloying aluminum by up to 13% will increase micro-porosity inside of the microstructure [3]. The nominal compositions of AM50 and AZ91 are given in Table 4.1.2. A binary phase diagram of Mg-Al is shown in Fig. 4.1.3.

Table 4.1.2. Composition of adding element in AM50 and AZ91 magnesium alloys

Mg Alloys	Al	Mn	Si	Zn	Cu	Fe	Ni
AM50	5.01%	0.32%	0.05%	0.05%	50 ppm	10 ppm	6 ppm
AZ91	8.85%	42 ppm	0.18%	0.72%	36 ppm	15 ppm	6 ppm

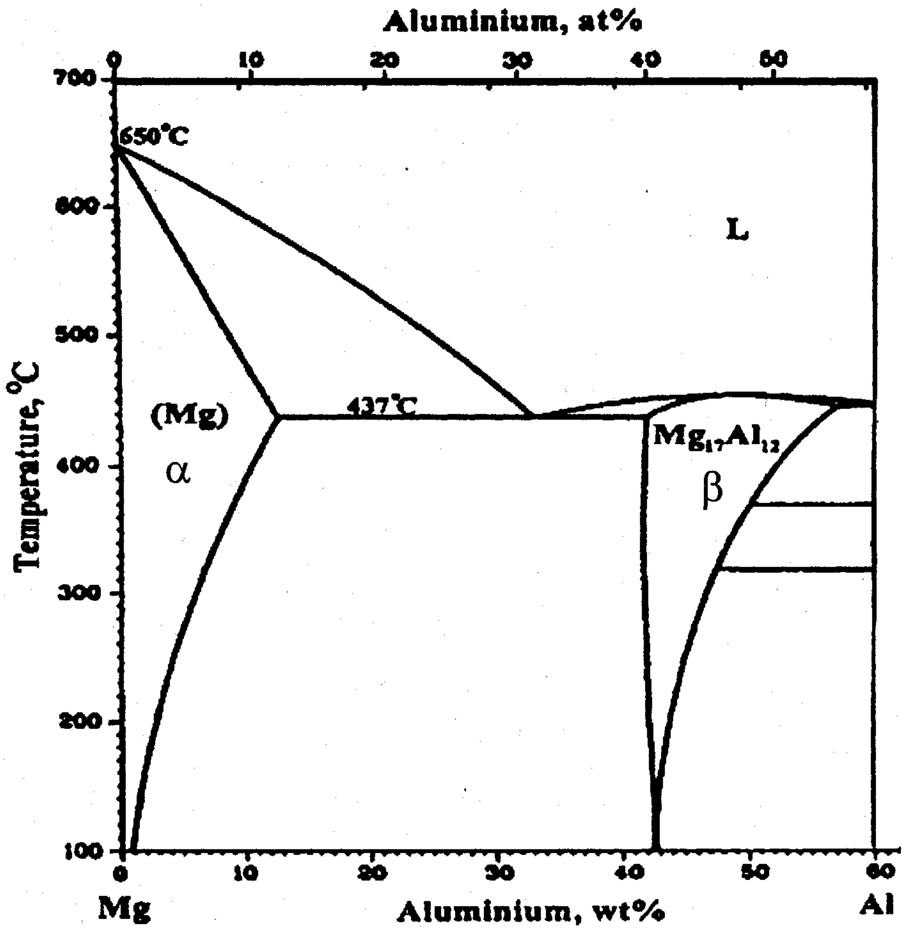

Fig. 4.1.3. Binary Mg-Al phase diagram

4.1.2 Melt treatment

The melting and casting of magnesium alloys requires careful attention to prevent their burning in air. When exposed to air on melting, magnesium burns violently, producing much heat and an intense white light/smoke. Magnesium reacts with both oxygen and nitrogen to produce fumes of MgO and Mg_3N_2 [4]. To prevent burning, a protective gas was blown over the surface during the melting process. A mixture of dry air and 0.35% SF_6 gas was used at a flow rate of 1 liter/min. Unless this flow rate was carefully maintained and the melt was exposed for no more than an hour or so to this cover gas, the melt within the steel crucible would become badly contaminated from thick layers of oxide forming at the meniscus. Then, once this magnesium oxide layer became thicker and thicker, particles of magnesium oxide became easily entrained into the melt by natural convection, owing to the minimal density differences between magnesium and its oxide. To circumvent these problems, rapid casting was needed once the melt had been prepared. Clean strips of magnesium alloys, and a clean melt within the crucible, were possible in this way.

4.2 INVERSE HEAT TRANSFER ANALYSIS

Two pairs of embedded thermocouples in the substrate were used to record temperature transients. Assuming unidirectional heat transfer from the liquid metal to the substrate, the inverse heat conduction problem (IHCP) method algorithm was developed to calculate the interfacial heat flux and the surface temperature. Based on these assumptions, the transient heat conduction equation (Fourier's 2nd Law) reduces to the following one-dimensional form:

$$\rho C_p \frac{\partial T}{\partial t} = k \frac{\partial^2 T}{\partial x^2} \tag{4.2.1}$$

In addition, the initial and boundary conditions for the governing differential equations can be expressed by:

$$T = T_i \qquad @\, t = 0 \tag{4.2.2}$$

$$-k \left.\frac{\partial T}{\partial x}\right|_{x=0} = q(t) \qquad @\, t \geq 0 \tag{4.2.3}$$

$$T(x_1, t) = Y_1(t) \qquad @\, t > 0 \tag{4.2.4}$$

$$T(x_2, t) = Y_2(t) \qquad @\, t > 0 \tag{4.2.5}$$

Note that the temperatures measured further from the interface, Y_2 (x_2 = 4.87mm), were used as boundary conditions while those closer to the interface, Y_1 (x_1 = 1.58mm), were used as the fitting parameter for evaluating the instantaneous interfacial heat flux, $q(t)$.

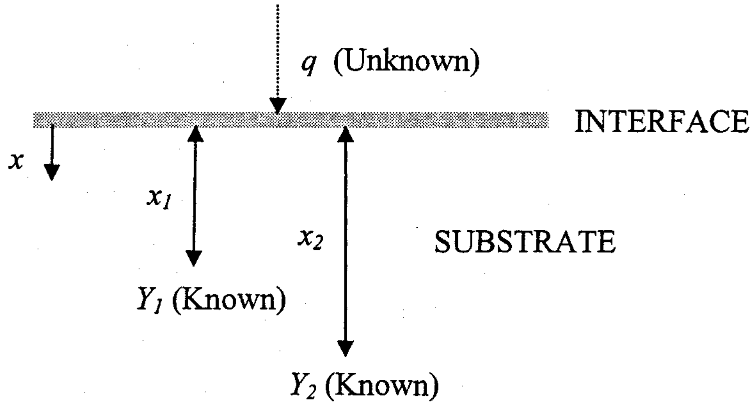

Fig. 4.2.1. Boundary conditions at the interface

The objective of the IHCP algorithm is to determine the instantaneous interfacial heat flux and the surface temperature of the mold substrate. These two unknowns are used further as boundary conditions to calculate the temperature field of the strip cast in the subsequent enthalpy method associated with the finite volume method (FVM).

As briefly described in Chap. 2.3.1., based on the minimization of the sum of residuals function (equation (4.2.6)), S, between the measured temperatures, Y, and calculated temperatures, T, and Duhamel's theorem (equation (4.2.7)), transient values of the substrate surface temperature (equation (4.2.8)), as well the interfacial heat fluxes (equation (4.2.9)), could be calculated. Detailed derivations of these equations are available in the book by Beck *et al* [5].

$$S = \sum_{i=1}^{r} (Y_{M+i-1} - T_{M+i-1})^2 \qquad (4.2.6)$$

$$T(\mathbf{x},t) = T_0 + \int_0^t q(\lambda) \frac{\partial \phi(\mathbf{x}, t-\lambda)}{\partial t} d\lambda \qquad (4.2.7)$$

$$\hat{q}_M = \sum_{i=1}^{r} K_i \left(Y_{M+i-1} - \sum_{j=1}^{M-1} \hat{q}_j \Delta\phi_{M-j+i-1} - T_O \right) \;\&\; K_i = \frac{\phi_i}{\sum_{j=i}^{r} \phi_j^2} \qquad (4.2.8)$$

$$\hat{T}_{O,M} = \sum_{i=1}^{M} \hat{q}_i \Delta\phi_{O,M-i} + T_O \qquad (4.2.9)$$

To validate the code programmed [6], a sample of the test result was compared with that produced by the commercial program IHCP-1D®, courtesy of Beck Engineering Consultants Company (BECC). This test was obtained from an aluminum droplet impingement experiment onto the copper substrate. Given the same input data, excellent agreement, of great accuracy (~98%), was registered between the two codes, as shown in Fig. 4.2.2 and Fig. 4.2.3.

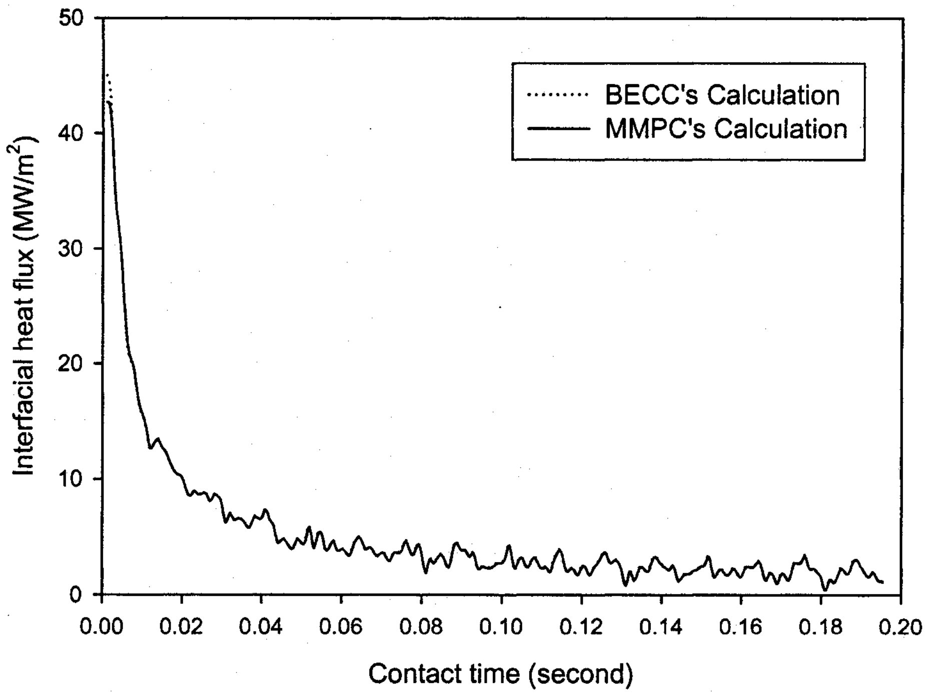

Fig. 4.2.2. Code validation for calculating the interfacial heat flux

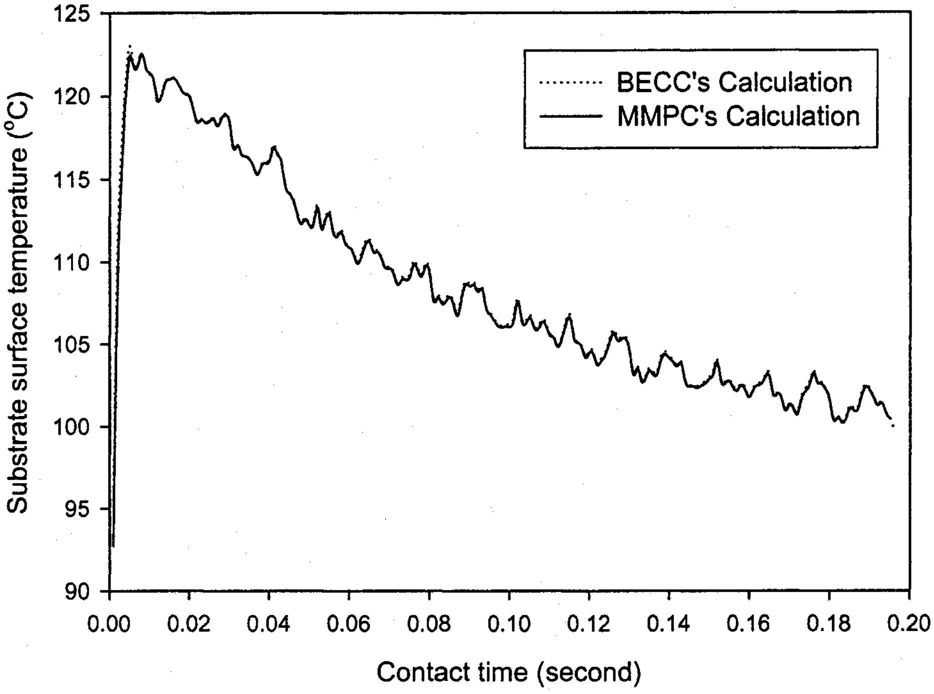

Fig. 4.2.3. Code validation for calculating the substrate surface temperature

4.3 ENTHALPY METHOD

The values of the interfacial heat flux and the temperature at the substrate surface could be obtained during the solution of the IHCP as prescribed. To calculate the temperature of the liquid metal in contact with the substrate surface, the possibility of direct temperature measurements within the solidifying strip samples was considered. Unfortunately, however, it was very difficult to insert a thermocouple into the melt at a fixed location within the 3mm thick solidifying strip, owing to the high velocity of the mold substrate and the inevitable distortion of the temperature field during the response of thermocouple. Therefore, it was necessary to model the heat transfer process in the liquid metal and to include solidification behavior.

To calculate the temperature field within the solidifying strips, the transient interfacial heat flux obtained from the IHCP on the basis of the temperature data measured by the two thermocouples inside the mold substrate were used as the time-varying boundary condition. The finite volume method in conjunction with the enthalpy method was used and a 30×400 grid was generated and relaxation factor of 0.9 used. In order to account for freezing in the edge regions of the strips, a two-dimensional heat conduction approach was adopted.

$$\rho\frac{\partial H}{\partial t}=\frac{\partial}{\partial x}\left(k\frac{\partial T}{\partial x}\right)+\frac{\partial}{\partial y}\left(k\frac{\partial T}{\partial y}\right) \qquad \text{where } H=\int_0^T C_p dT + L\cdot f_L \qquad (4.3.1)$$

The enthalpy, *H*, at any location *x*, *y*, at time *t*, is composed of the sensible heat and the latent heat released during phase change within the mushy zone. Programming codes of the IHCP and enthalpy method appear in Appendix II. Thermophysical properties of magnesium alloys and aluminum alloy AA6111 used in the calculation are tabulated in Table 4.3.1 and 4.3.2.

Table 4.3.1. Thermophysical properties of AZ91 and AM50 magnesium alloys

Mg Alloys	AZ91	AM50
Liquidus (K)	868	893
Solidus (K)	743	833
Density (Kg/m^3)	1826	1800
Liquid C_p (J/Kg·K)	1412	
Solid C_p (J/Kg·K) [7]	$952 + 0.5T - 6.17\times10^{-5}/T^2$	
Liquid k (W/mK)	30	
Solid k (W/mK) [8]	45 + 0.05T	60 + 0.05T
Latent heat (J/Kg)	353914	349722

Table 4.3.2. Thermophysical properties of AA6111 aluminum alloy [9]

Al Alloy	AA6111
Liquidus (K)	923
Solidus (K)	775
Density (Kg/m^3)	2710
Liquid C_p (J/Kg·K)	1080
Solid C_p (J/Kg·K)	917
Liquid k (W/mK)	89
Solid k (W/mK)	198
Latent heat (J/Kg)	321000

To handle the fraction of liquid, f_L, remaining within the mushy zone, several models were tried, such as the linear model, the lever rule, and Scheil's model [10]. The linear model assumes that the latent heat is dissipated linearly over the liquidus-solidus freezing range and this model is widely used because of its simplicity.

$$\text{Linear model:} \qquad f_L = \frac{T - T_S}{T_L - T_S} \quad \text{when } T_S \le T \le T_L \tag{4.3.2}$$

If the solidification occurs very slowly, e.g. complete equilibrium between the sold and the liquid phases, the lever rule would apply:

$$\text{Lever rule:} \qquad f_L = 1 - \frac{1}{1-k}\left(\frac{T - T_L}{T - T_M}\right) \text{ when } T_S \le T \le T_L \tag{4.3.3}$$

where T_M is the melting point of the pure magnesium, 923K, and k is a distribution coefficient defined as

$$k = \frac{T_M - T_L}{T_M - T_S} \tag{4.3.4}$$

This approach implies inter-diffusion of solute between the solid and inter-dendritic liquid.

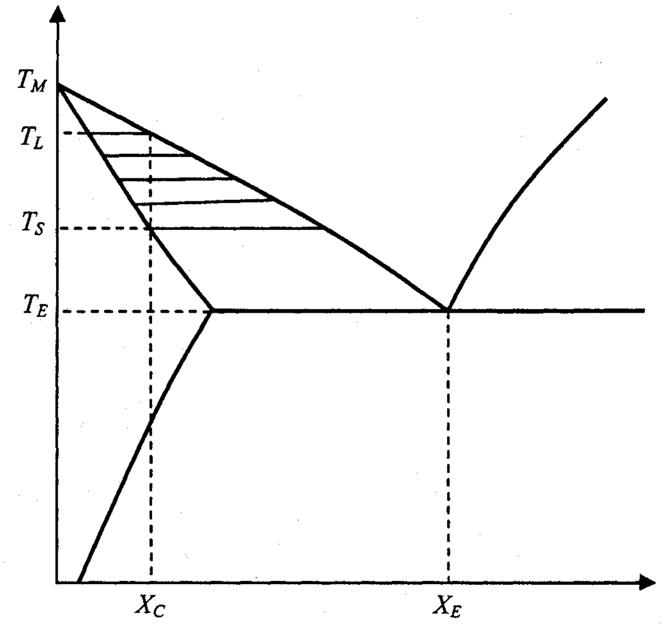

Fig. 4.3.1. Phase diagram of eutectic system

On the other hand, Scheil's model engenders reality in that it neglects the implied diffusion within the solid phases (which is kinetically very slow compared with solidification) and supposes that solidification proceeds until the eutectic temperature of 710K is reached. Note that the total amount of latent heat is the same for these models and their difference lies in the rate of heat release.

$$\text{Scheil's model: } f_L = \left(\frac{T_M - T}{T_M - T_L}\right)^{\frac{1}{k-1}} \text{ when } T_E \leq T \leq T_L \text{ \& } f_L = 0 \text{ when } T = T_E \quad (4.3.5)$$

Fig. 4.3.2 and Fig. 4.3.3 show the change of solid fraction ($f_S = 1 - f_L$) versus strip temperature for AZ91 and AM50 alloy respectively. It reveals the difference in the rate of latent heat release when different models are used. The lever rule and Scheil's model release more heat at the beginning of solidification compared to the linear model. Also, for the same value of solid fraction, the lever rule would give the highest strip temperature owing to having released more latent heat from the onset of freezing. Note that, in the case of the linear model or lever rule, the solidification is completed at the solidus temperature, while in the Scheil's model completion of solidification lingers down to its eutectic temperature (710K).

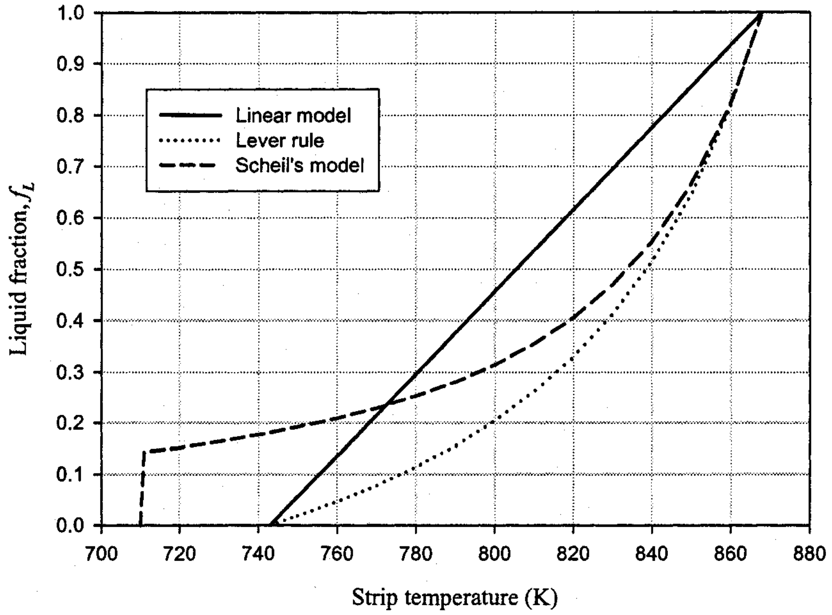

Fig. 4.3.2. Liquid fraction vs. strip temperature with different latent heat release models in AZ91 magnesium alloy (T_L = 868K, T_S = 743K, T_E = 710K)

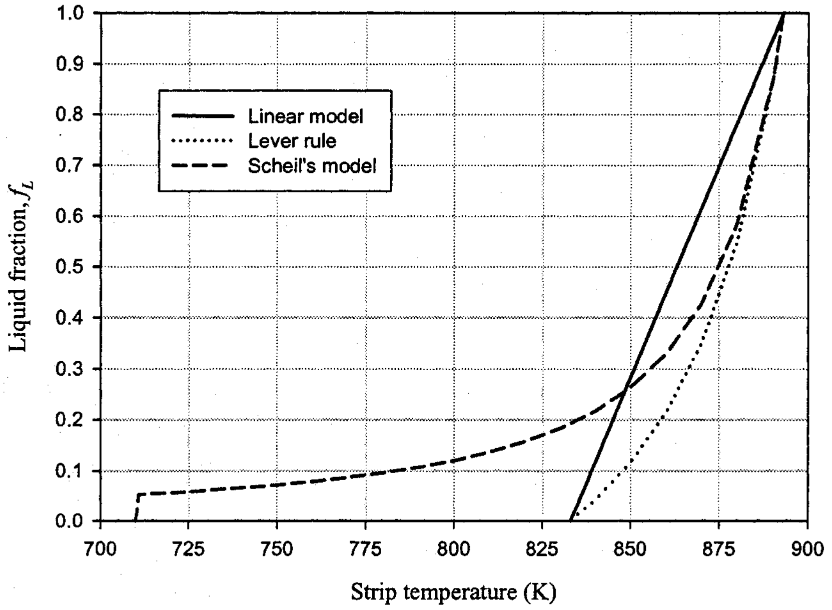

Fig. 4.3.3. Liquid fraction vs. strip temperature with different latent heat release models in AM50 magnesium alloy (T_L = 893K, T_S = 833K, T_E = 710K)

4.4 FINITE VOLUME METHOD

For a phase change problem undergoing solidification, the discretization equation for solidifying strip is obtained by integrating the differential equation (4.3.1) over a given control volume. As the integration is carried out within the control volume of interest, neighboring grid points are included to calculate the dependent variable at a fixed grid point. Fig. 4.4.1 shows the two-dimensional control volume with the associated notations. Generally, the discretization equation in three-dimensional Cartesian coordinates is expressed as:

$$a_P T_P = a_E T_E + a_W T_W + a_N T_N + a_S T_S + a_T T_T + a_B T_B + b \tag{4.4.1}$$

where

$$\begin{aligned} &a_E = \frac{k_e \Delta y \Delta z}{(\delta x)_e},\ a_W = \frac{k_w \Delta y \Delta z}{(\delta x)_w},\ a_N = \frac{k_n \Delta z \Delta x}{(\delta y)_n},\ a_S = \frac{k_s \Delta z \Delta x}{(\delta y)_s}, \\ &a_T = \frac{k_t \Delta x \Delta y}{(\delta z)_t},\ a_B = \frac{k_b \Delta x \Delta y}{(\delta z)_b},\ b = -\rho\left(\frac{H_P - H_P^o}{\delta t}\right)\Delta x \Delta y \Delta z,\ a_P = \sum a_{nb} \end{aligned} \tag{4.4.2}$$

The notation Σa_{nb} means the summation of all neighbor coefficients in equation (4.4.1). Each coefficient implies the conductance between the point **P** and the corresponding neighbor point [11]. To deal with nodes on the boundary, the types of boundary conditions should be specified. There is no difficulty if the boundary condition is known as the specified temperature. However, when the boundary condition is given as the Neumann type, discretization over the control volume at the boundary node shown in Fig. 4.4.2 gives:

$$-q_P \Delta y + q_w \Delta y - q_n \frac{\Delta x}{2} + q_s \frac{\Delta x}{2} = \rho\left(\frac{H_P - H_P^O}{\delta t}\right)\frac{\Delta x}{2}\Delta y \tag{4.4.3}$$

where $q_w = k_w \dfrac{T_W - T_P}{(\delta x)_w}, q_n = k_n \dfrac{T_P - T_N}{(\delta y)_n}, q_s = k_s \dfrac{T_S - T_P}{(\delta y)_s}$ (4.4.4)

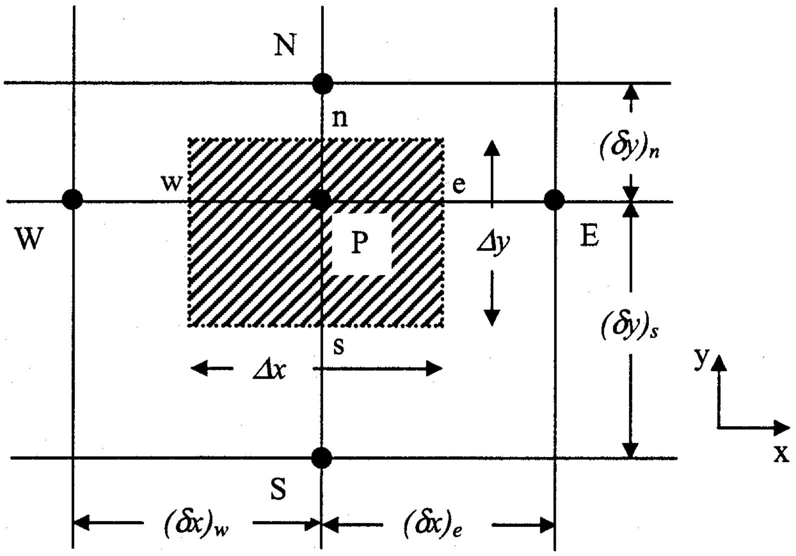

Fig. 4.4.1. Two-dimensional control volume and neighboring notations

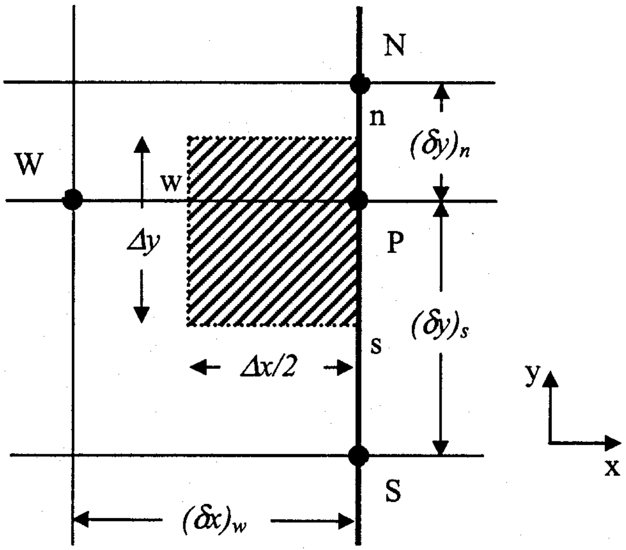

Fig. 4.4.2. Control volume and neighboring notations near the boundary

From equations (4.4.1) and (4.4.3), the boundary heat flux q_P and the rest of coefficients can be classified further following the types of the boundary conditions:

(i) Specified heat flux: $q_P = q_b$

$$b = -\rho\left(\frac{H_P - H_P^o}{\delta t}\right)\frac{\Delta x}{2}\Delta y + q_b \Delta y \qquad \& \qquad a_P = \sum a_{nb} \tag{4.4.5}$$

(ii) Convective boundary condition: $q_P = h_c(T_P - T_\infty)$

$$b = -\rho\left(\frac{H_P - H_P^o}{\delta t}\right)\frac{\Delta x}{2}\Delta y + h_c T_\infty \Delta y \qquad \& \qquad a_P = \sum a_{nb} + h_c \Delta y \tag{4.4.6}$$

(iii) Radiative boundary condition; $q_P = h_r(T_P - T_\infty)$

$$b = -\rho\left(\frac{H_P - H_P^o}{\delta t}\right)\frac{\Delta x}{2}\Delta y + h_r T_\infty \Delta y \qquad \& \qquad a_P = \sum a_{nb} + h_r \Delta y \tag{4.4.7}$$

where $h_r = \varepsilon\sigma(T_P^2 + T_\infty^2)(T_P + T_\infty)$ is a function of temperature T_P.

In the experiment, the strip not only loses heat by interfacial metal/mold thermal conduction but also at the top surface by forced convection and thermal radiation. When the strip moved at 1m/s, the convective heat transfer coefficient was about 5.27 W/m^{2}K [12] and the emissivity of magnesium alloy was taken as 0.5 [8]. To avoid divergence in the solution, the under-relaxation iteration scheme was employed by introducing an under-relaxation factor α.

$$T_P = T_P^* + \alpha\left(\frac{\sum a_{nb} T_{nb} + b}{a_P} - T_P^*\right) \tag{4.4.8}$$

The value of the under-relaxation factor was chosen as 0.9 in the calculation. Furthermore, the discretized equation derived from the control volume method constitutes a system of linear algebraic equations and could be solved iteratively by the 'line-by-line' Tri-Diagonal Matrix Algorithm (TDMA). This method is fast and saves memory storage as well as the computation time.

In summary, a schematic diagram of the experimental methodology is given in Table 4.4.1.

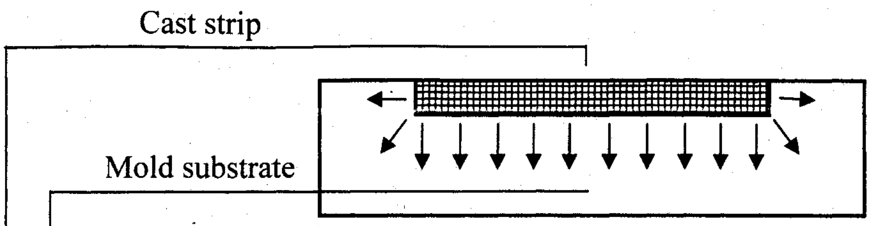

Table 4.4.1. Experimental methodology

Calculation Method	Variables	Investigated Results
IHCP	- Cast alloys - Mold substrates - Melt superheat	- Interfacial heat flux - Mold surface temperature
Enthalpy FVM	- Scheil's model	- Temperature field - Local cooling rate - Interfacial heat transfer coefficient - Microstructure

4.5 MICROSTRUCTURE OBSERVATION

For the characterization of strip microstructures, the samples were cut, polished, and etched. Etching solution was composed of 60% ethylene-glycol, 20% water, 19% acetic acid, and 1% nitric acid [13].

In general, it is common to measure secondary dendrite arm spacings (SDAS) as a means to characterize dendrite structures of solidified alloys, and as a measure of the fineness of a cast structure. The importance of SDAS and its suitability as a reliable structural parameter for process-structure and structure-property relations are manifested in the established dependence of cast metal features such as mechanical properties, fracture characteristics, casting defects, heat treatment, and corrosion behavior on the SDAS. The SDAS were measured under the microscope using a LECO Image Analyzer System.

REFERENCES

1. R. E. Brown, Developments in Magnesium Wrought Products: Rolling and Sheet Casting, *Light Metal Age*, February, 2002, pp.80-83
2. http://www.castingsource.com/tech_art_Magnesium.asp
3. E. J. Whittenberger & F. N. Rhines, Origin of Porosity in Castings of Magnesium-Aluminum and Other Alloys, *J. Metals*, 1952, pp.409-420
4. M. J. Walzak, R. D. Davidson, N. S. McIntyre, D. Argo & B. R. Davis, Interfacial Reactions Between SF6 and Molten Magnesium, *Light Metals 2001*, CIM, Toronto, Canada, 2001, pp.37-41
5. J. V. Beck, B. Blackwell & C. R. St. Clair Jr., *Inverse Heat Conduction: Ill-posed Problems*, Wiley Interscience, New York, 1985
6. R. P. Tavares, Vertical Twin-Roll Caster: Metal-Mould Heat Transfer, Solidification, and Product Characterization, *Ph.D. Thesis,* McGill University, 1997
7. O. Kubaschewski, C. B. Alcock & P. J. Spencer, *Materials Thermochemistry*, 6th ed., Pergamon, Oxford, 1993, pp.289
8. E. F. Emley, *Principles of Magnesium Technology*, Pergamon, Oxford, 1966, pp.736-748

9. W. D. Griffiths, The Heat-Transfer Coefficient during the Unidirectional Solidification of an Al-Si Alloy Casting, *Met. Trans.* **30B**, 1999, pp.473-482

10. S. C. Flood, L. Katgerman, A. H. Langille & C. M. Read, A Model of Solidification, Fluid Flow and Stress Distribution in DC Casting, *Modeling of Casting and Welding Processes IV*, TMS, 1988, pp.553-561

11. S. V. Patankar, *Numerical Heat Transfer and Fluid Flow*, McGraw-Hill, 1980

12. D. R. Gaskell, *An Introduction to Transport Phenomena in Materials Engineering*, Macmillan, 1992

13. K. J. Clark, Metallography and Microstructures, *ASM Handbook*, Vol. 9, 1985, pp.425-434

CHAPTER

5

EXPERIMENTAL RESULTS

5.1 INTRODUCTION

Magnesium sheet casting is a newcomer to the Light Metal's industry, although it should be noted that magnesium sheet production was practised by the Germans in World War II for airframe structures. It was not easily tackled so far because of the difficulty in metallurgical operation and the former high price ratio of magnesium to aluminum, prior to supplies from China. Quite recently, CSIRO in Australia reported technical success of magnesium sheet production using a twin roll caster pilot plant. Commercial quality sheet samples from 2.3-5 mm thick were cast for standard magnesium alloys of AZ31, AZ61, AM60 and AZ91. These were further hot rolled down to 0.5-0.6 mm gauges, followed by finish rolling [1].

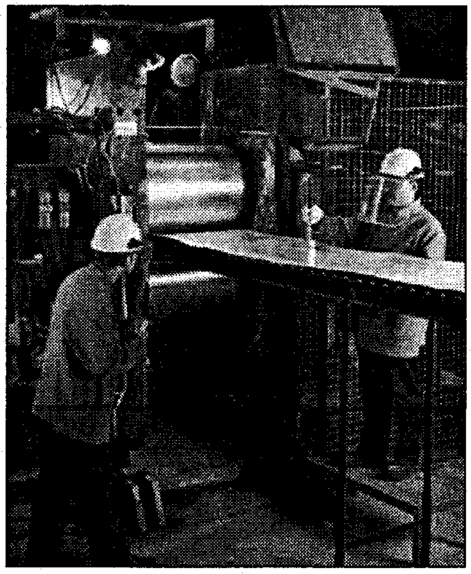

Fig. 5.1.1. Magnesium sheet casting in CSIRO, Australia

In contrast with the success of magnesium sheet production via the twin roll casting process, research with other near-net-shape casting processes has not yet come to fruition. With the benefit of high productivity surpassing any other casting process, therefore, it is highly worthwhile to investigate the producibility of magnesium strips for single belt casting processes. In this chapter, magnesium alloys, AZ91 and AM50, cast on various mold substrates are studied thoroughly in terms of strip quality, heat transfer mechanisms, and microstructural characteristics.

5.2 MELT DELIVERY

As mentioned in Chap.2.1, the melt delivery system plays a crucial role in single belt casting operations. In order to feed liquid metal onto the moving substrate uniformly, simple delivery systems were designed for the small scale single belt casting simulator. Two types of delivery system were devised and used to feed the magnesium melt from the crucible onto the cooling substrate. One was a hole type and the other was a slit type. The dimensions of these delivery systems are shown in Fig. 5.2.1. These were made from marinite plate 5mm thick with boron nitride coating and inserted at the bottom of the mold to control the flow rate of liquid metal.

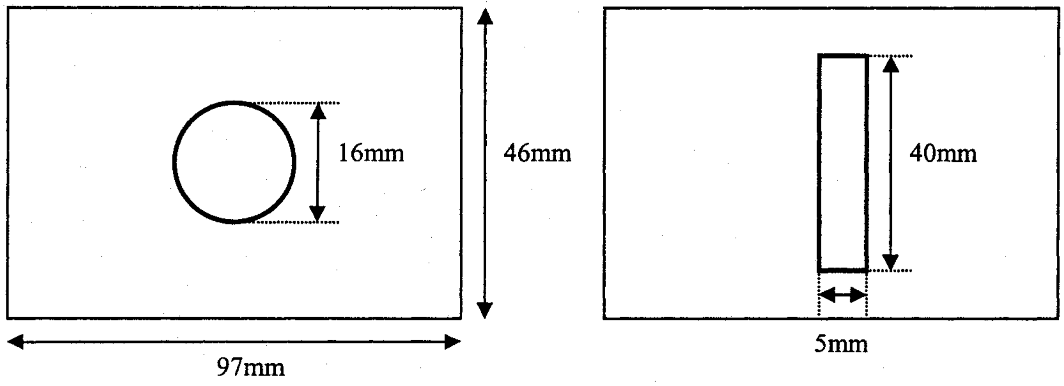

(a) hole type (b) slit type

Fig. 5.2.1. Dimensions of bottom plates inserted on the mold

They had the same cross sectional area but the slit type with 40mm wide produced more uniform thickness of strip compared to the hole type. The melt contracted on the substrate as soon as it was contacted and uniform spreading was hardly achieved. Especially, when the melt superheat was low and substrate speed was high, the hole type delivery system couldn't fill the width of substrate as shown in Fig. 5.2.2. To obtain uniform strip thickness, the slit type was much more effective than the hole type metal feeding system.

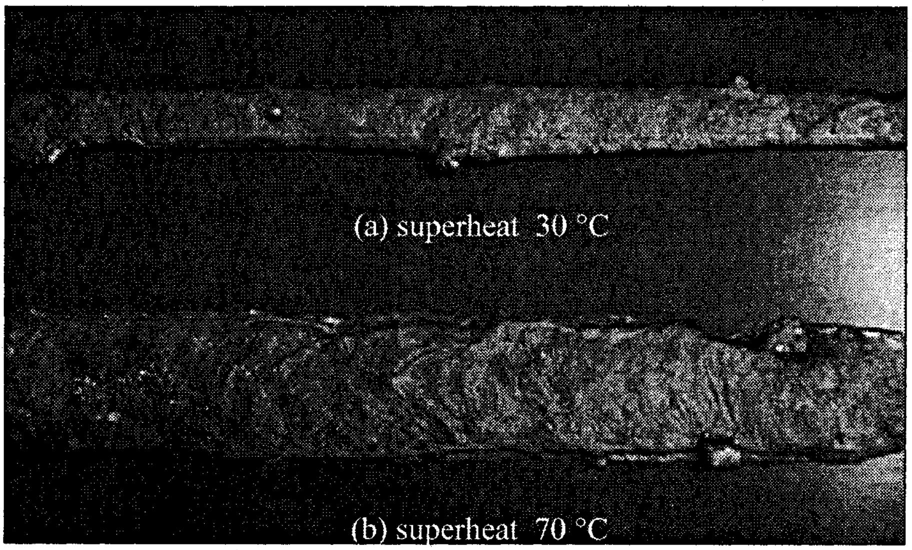

Fig. 5.2.2. Non-uniform feeding by hole type delivery system

Recently, Ditze *et al.* [2] performed sheet production of AZ91 magnesium alloy on the single belt caster at Claustahl. The intended strip thickness was 10mm with strip widths of 152, 165, and 175mm. Melt superheats were varied from 55 °C to 95 °C. They reported that the main difficulty in the casting was to distribute the liquid melt onto the belt uniformly. Previously, in their experiments of casting steel, they obtained major improvements in melt spreading using argon rakes [3] but this approach did not work out well in magnesium casting. Several types of nozzles were tried for magnesium casting as shown in Fig. 5.2.3, while Fig. 5.2.4 shows strip samples resulting from bad feeding. Good feeding of magnesium melt was achieved from types 1, 3, and 6 delivery system. The type 4 inclined plane and the type 5 cascade systems performed well at the beginning, but the stream soon shrank so that they could not fill the entire width of the belt. The array of multiple holes, type 2, produced a strip with 9 separate streams, which did not merge together (Fig. 5.2.4(a)). Also, the contact between the magnesium melt and the stationary side dams resulted in sticking problems and caused bad edges of the strip (Fig. 5.2.4(b)). The surfaces of some strips turned black during casting, the reason for this was not identified clearly (Fig. 5.2.4(c)), but was probably due to oxidation. On the other hand, metal fed without contacting the side dams, successfully produced strip of uniform dimensions (Fig. 5.2.4(d)).

In summary, the casting of magnesium sheet needs a new design of tundish in the future to feed the melt onto the moving belt in a uniform manner. Experiments to cast 3mm thick 40mm wide, strips using a small scale of casting simulator, suggested the efficiency of the slit type nozzle as a delivery system against the hole type. Enlarged scale of experiments performed at Clausthal with various nozzle types also proved that a multiple-hole nozzle had to be excluded, as well as an inclined plane or cascade types. Unlike the steel melt, the magnesium melt neither easily spread enough to fill the entire width of the belt, nor merged together after each stream was discharged from nozzle exit.

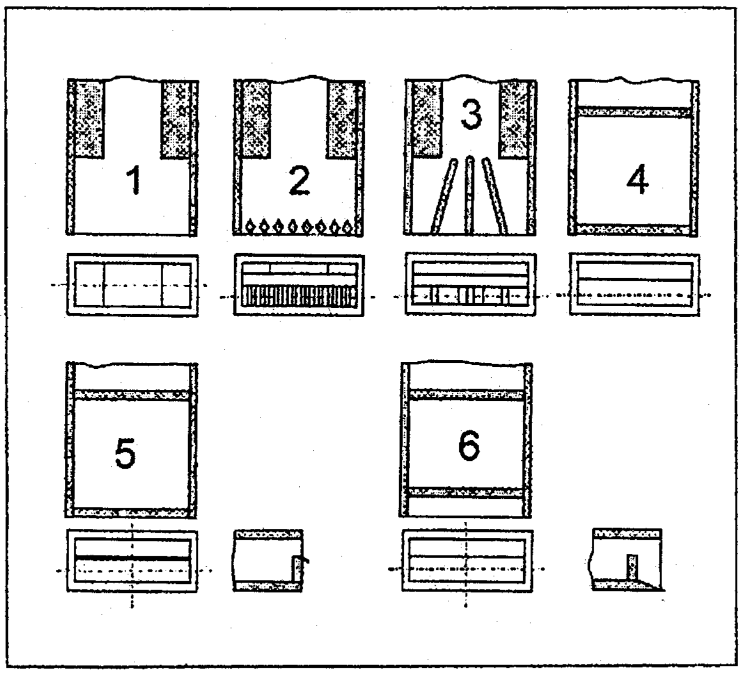

Fig. 5.2.3. Nozzles used to feed the magnesium melt onto the belt [2]

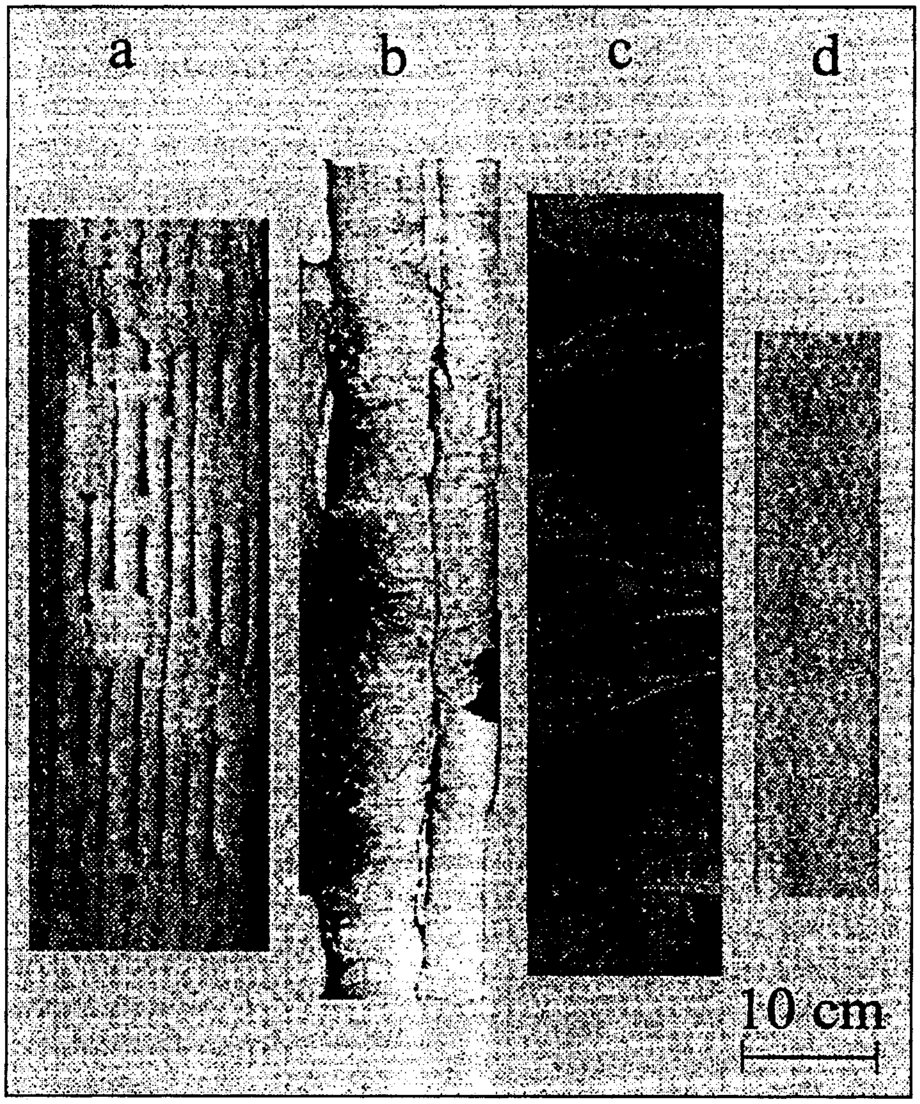

Fig. 5.2.4. Magnesium AZ91 alloy strips: (a) strip obtained from the multiple-hole nozzle type 2 in Fig. 5.2.3, (b) strip with bad side defects caused by sticking to the side dam, (c) strip with black surface, and (d) strip without contacting the side dams [2]

5.3 MACROSCOPIC STRIP QUALITY

Using a slit nozzle of the type prescribed, the casting 40 mm-wide strips of magnesium alloy was successful in the present experiments. In general, the macroscopic quality of the strip revealed the excellent castability of magnesium alloys in a belt casting process. The top surfaces of the strips were clean and bright, even though darkened strip surfaces were reported in the experiments at Clausthal (Fig. 5.2.4(c)). The bottom surfaces of the strips were virtually free of any dents or shrinkage, as shown in Fig. 5.3.1.

Copper and carbon steel substrates produced smooth surfaces of strips. This reveals the good wetting between the melt and the mold substrate. Both substrates were sand blasted before casting and they had surface roughnesses between 4 and 5 µm. In particular, the bottom surface cast on a copper substrate clearly exhibited meniscus traces of the liquid stream of magnesium. The melt flowed faster at the center, compared to the edge regions, sticking of metal with the side dams causing a drag on liquid flow at the edges.

Three coated substrates produced rougher surfaces of strips compared to sand blasted copper or carbon steel substrates. The roughest strip surface was obtained from a zirconia coated substrate, even though their roughnesses of coated substrates were nearly the same of about 7µm. This result implies that the zirconia coating was efficient in increasing the wettability between the melt and mold. It was found later that the rate of heat transfer was the lowest when the zirconia substrate was used and produced the coarsest microstructure. The lower rate of interfacial heat transfer resulted in the decrease in cooling rate of solidifying strip and the prolongation in the time for the magnesium to complete solidification.

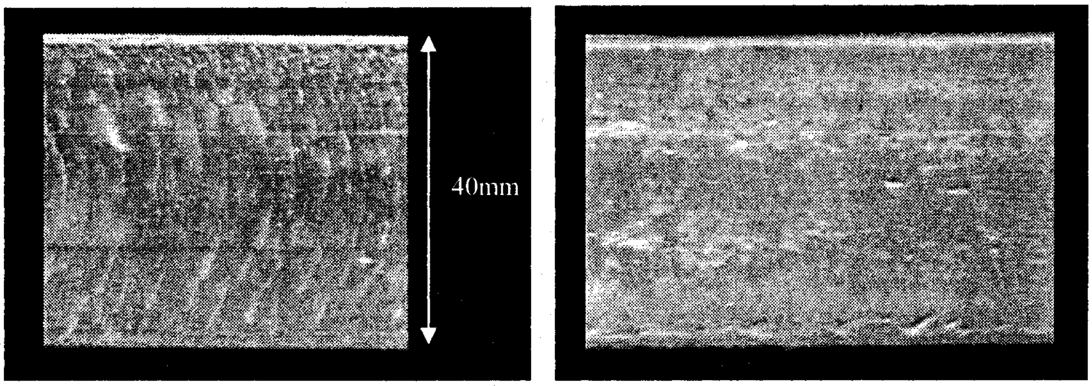

(a) Copper (b) Carbon steel

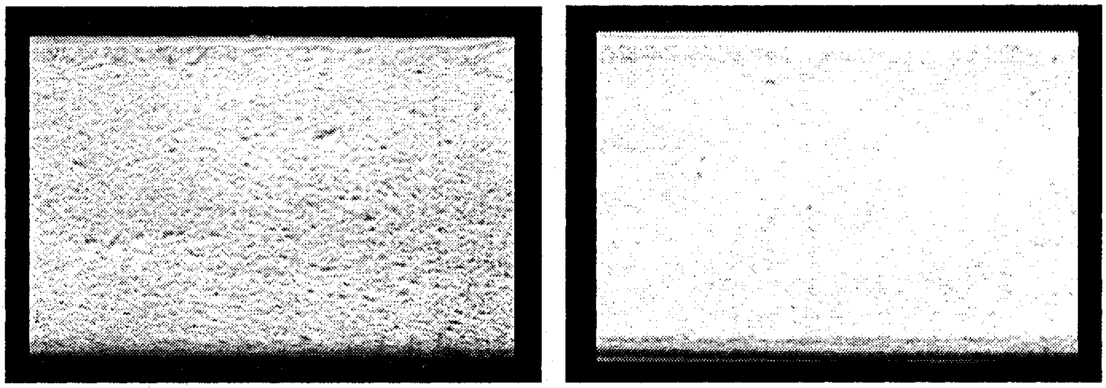

(c) Nickel (d) Zirconia

Fig. 5.3.1. Bottom surfaces of AZ91 strip using different mold substrates

The larger scale castings of AZ91 strips on the Clausthal single belt facility was tried, as shown in Fig. 5.3.2 and various thickness profiles were measured in Fig. 5.3.3. The total fluctuation was within 1mm with about 10mm strip thickness.

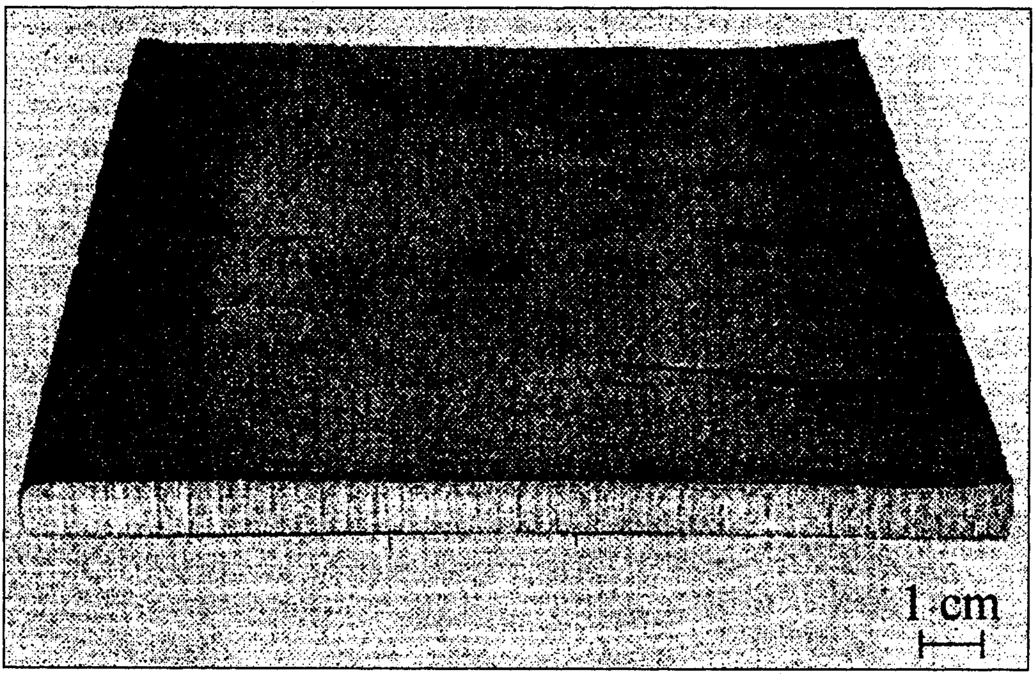

Fig. 5.3.2. Section through an AZ91 strip indicating the uniform strip thickness cast at the Clausthal [2]

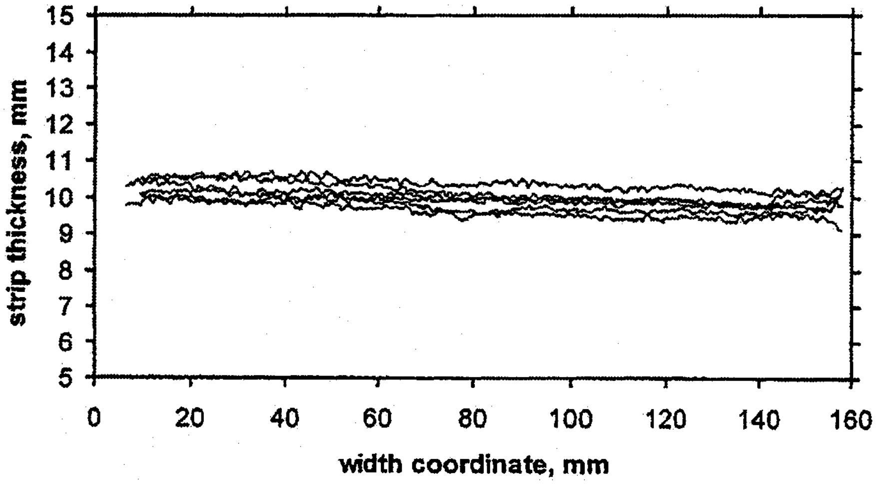

Fig. 5.3.3. Thickness profiles of an AZ91 strip cast at the Clausthal [2]

5.4 AZ91 & AM50 MAGNESIUM ALLOYS

5.4.1 Correction of thermocouple response

In order to estimate the accuracy of the heat flux measurements, the response times of the embedded thermocouples were considered. As will be appreciated, the abrupt change in temperature occurring at the initial moment of thermal contact cannot be fully reflected, and measured owing to the finite response time of thermocouples. This response time can corrupt the actual temperature history which, in turn, affects subsequent values of instantaneous heat fluxes. To correct measured temperature for thermocouple response rate, a small apparatus to determine the response time of the thermocouple was designed, as shown in Fig. 5.4.1.

In this apparatus, a small hole was made at the center of the block of copper and thermopaste was filled inside. Two K-type ungrounded thermocouples were used in this test because they were the ones used in the casting experiments. One submerged thermocouple recorded the pool temperature of the thermopaste, while the other thermocouple was plunged into the pool. When the plunging thermocouple made contact with the thermopaste, the embedded thermocouple records a sudden drop in temperature because of the slight distortion in temperature field within the pool. This moment determines the instant when the dropping thermocouple made contact with the pool. Fig. 5.4.2. shows an example of the temperature readings for response time measurements using a K-type ungrounded thermocouple of 0.032" diameter. It should be noted that it took about 10 seconds to reach the actual pool temperature of 112 °C. Most of strips cast in this work solidified much before this 10 second time period. Thus, corrections in the temperatures of the embedded thermocouples corrected for their response times were important in deducing the instantaneous heat fluxes determined on the basis of actual temperature readings.

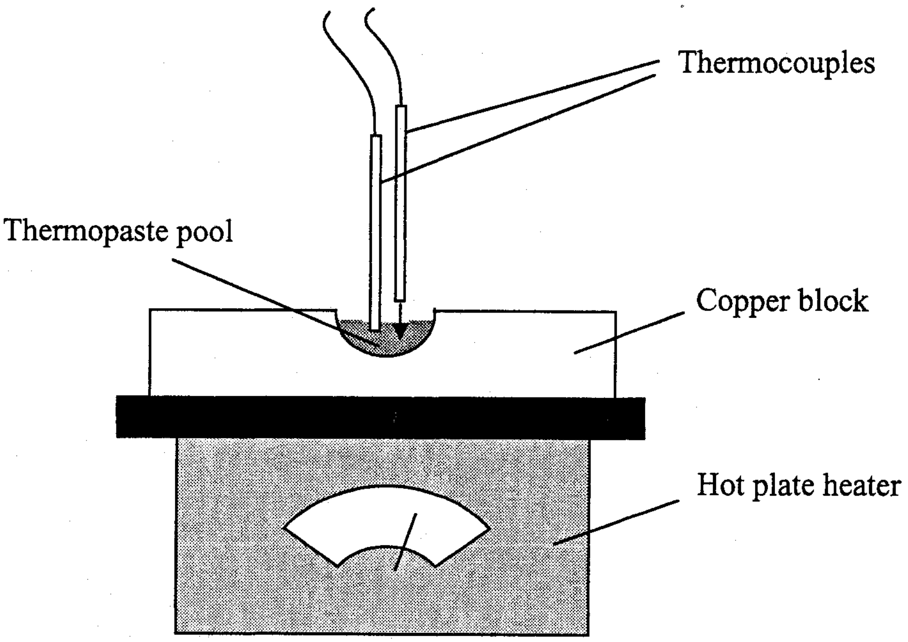

Fig. 5.4.1. Apparatus to measure the response time of the thermocouples

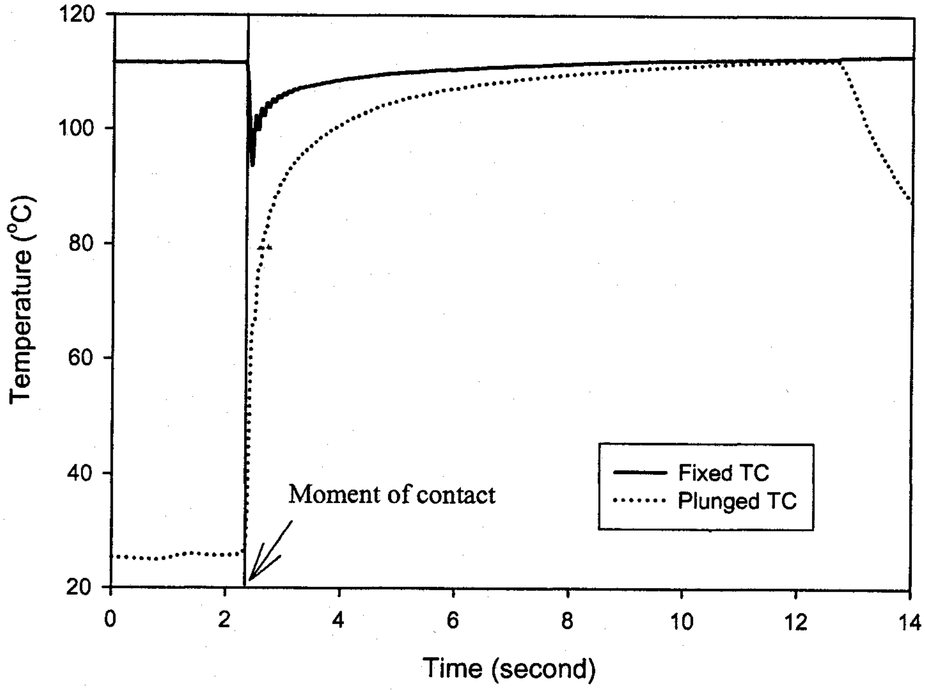

Fig. 5.4.2. The response time of the K-type ungrounded thermocouple (0.032"dia.)

More than 30 tests were carried out to find out the response time of the thermocouples and modal time constants to correct the temperature data. The averaged values of modal time constants τ_1 and τ_2 were 2.11 and 0.025 respectively. Detailed procedures for the correction of thermocouple readings are described in Appendix III. [4]

In Fig. 5.4.3, an example of corrected temperatures are plotted using uncorrected thermocouple readings. These thermocouples were embedded in the copper substrate during the casting of an AM50 magnesium strip 3.1mm thick.

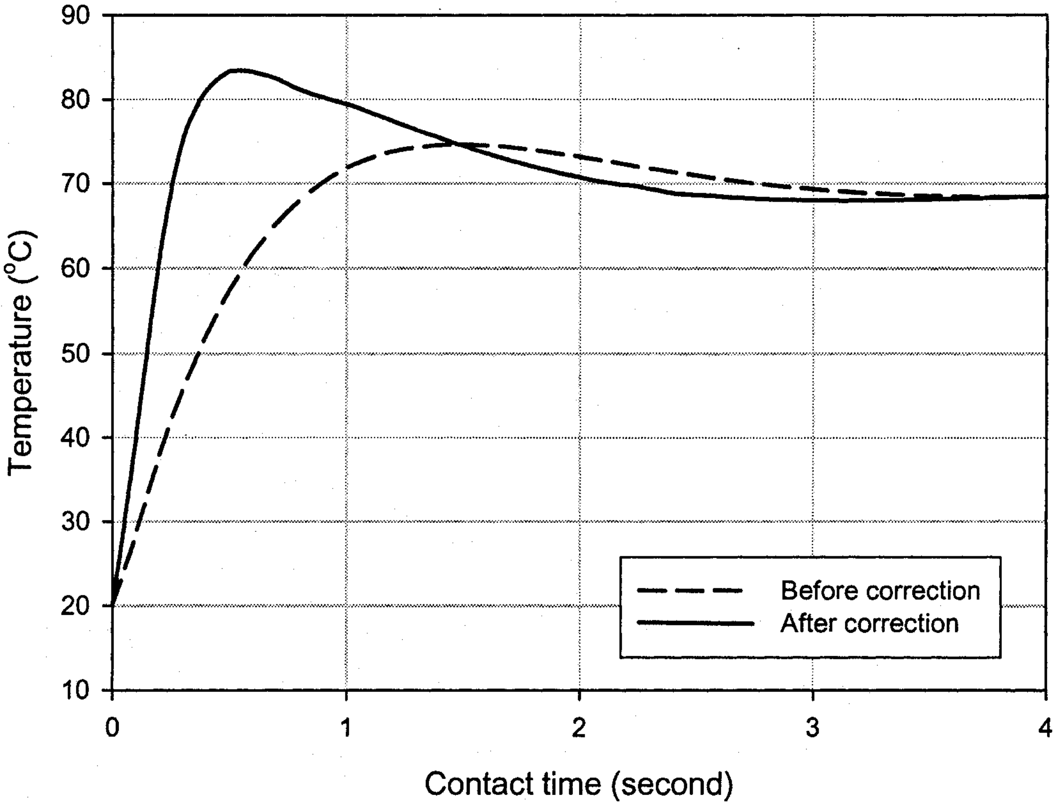

Fig. 5.4.3. An example of the corrected thermocouple data

5.4.2 Interfacial heat fluxes

The general transient heat flux curve (or heat transfer coefficient curve) obtained from experiments is shown in Fig. 5.4.4. where q_i denotes the initial value of the heat flux and t_P denotes the time taken to reach the maximum peak heat flux, q_M. Most of the experimental data plots showed the same shape. From the curve below, one can divide the transient data mainly into two regions:

(i) An initial increase of heat flux from q_i to q_M with contact time

(ii) A decrease from q_M with time of contact

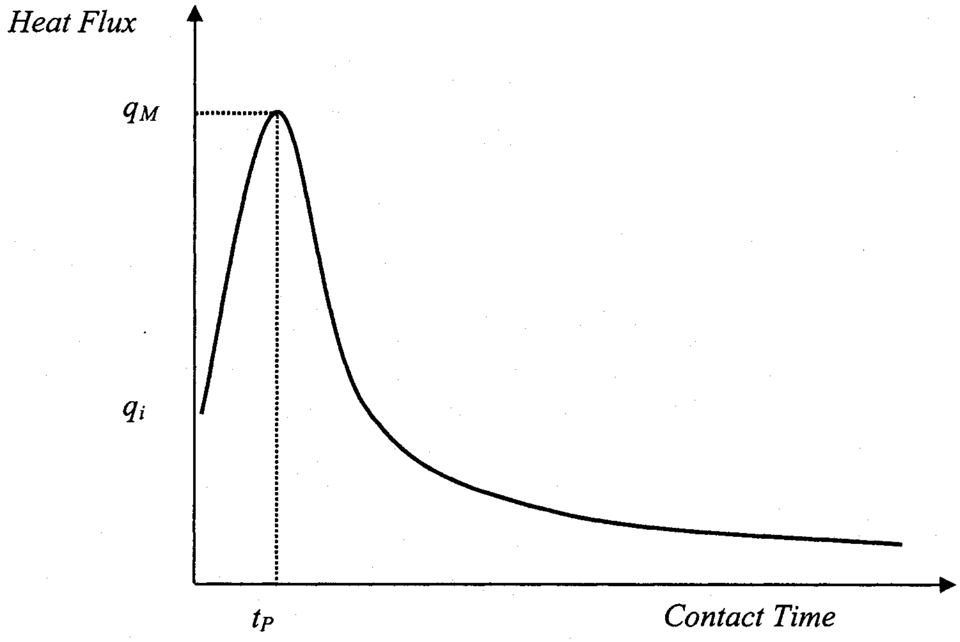

Fig. 5.4.4. Shape of an interfacial heat flux curve

At the moment the liquid metal comes into contact with the substrate, the liquid metal begins to feed onto the substrate and the initial liquid/solid contact enhances the heat transfer to the interface. A considerable amount of heat is transferred in this stage. The initial the value of heat flux, q_i, is determined at the moment of contact and is affected by the temperature difference before the melt and the mold, the mold material, and any pre-existing interfacial resistance, such as a gas layer or mold coating. As solidification begins, the release of superheat and latent heat increases the value of the interfacial heat flux to a maximum, q_M. Also, nucleation initiates and the solidified skin begin to form at the interface. The maximum heat flux, q_M, is highly dependent on interfacial contact, and is influenced by the nature of liquid metal and mold, interface texture, and time-variant interface resistance such as a growing oxide layer, mold expansion, or shrinkage of solidified metal. The growth of the solidified shell changes the interfacial heat transfer from the liquid-solid to solid-solid and the value of heat flux or heat transfer coefficient begins to decrease, resulting in the shrinkage of solidified shell and the formation of the air gap at the interface.

5.4.2.1 Effect of melt superheat

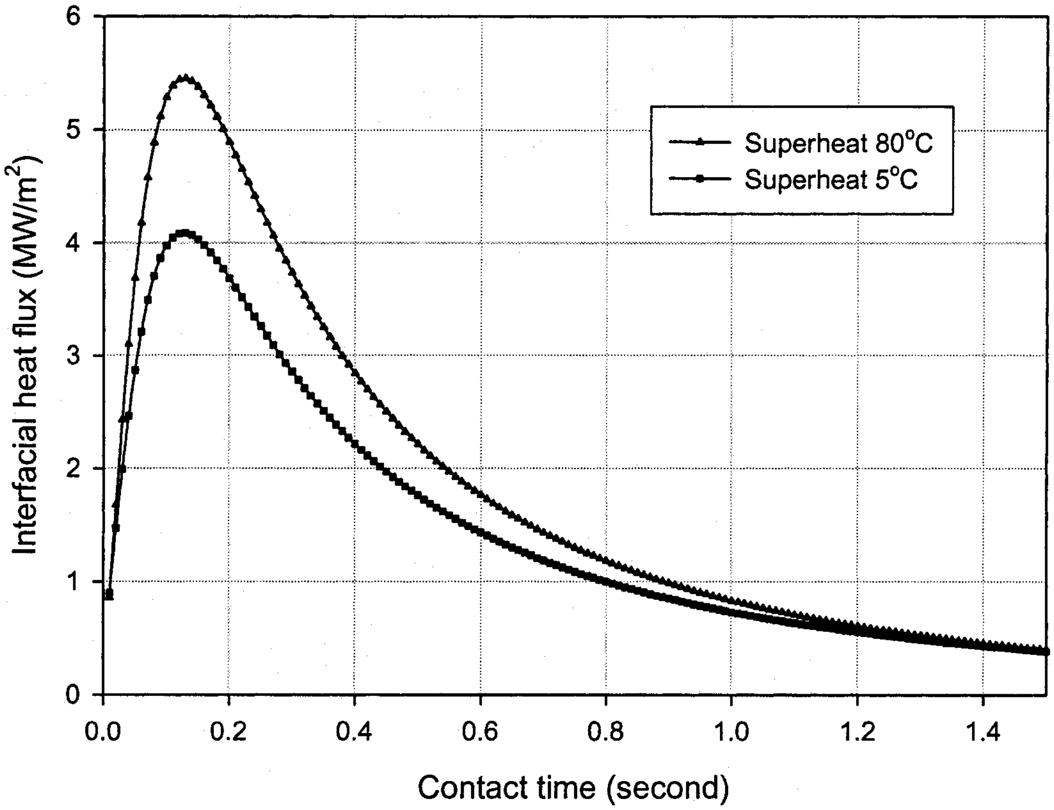

Fig. 5.4.5. AZ91 3mm strips cast on a copper substrate with different superheats (casting speed: 0.8m/s)

Fig. 5.4.5 shows the interfacial heat flux profiles obtained from 3mm strips of AZ91 cast on a copper substrate. The heat flux increased rapidly from a finite value at the moment of contact, reaching a maximum around 130 mille-seconds, then decreasing towards zero. With a 5°C superheat, the maximum heat flux was about 4.09 MW/m^2. Increasing its superheat up to 80°C resulted in an increase in the maximum heat flux to 5.45 MW/m^2. The higher the melt superheat, the higher was the maximum heat flux observed.

5.4.2.2 Effect of substrate material

Heat flux data for various kinds of substrates with the same 3mm strip thickness are given in Fig. 5.4.6. These heat fluxes were calculated from the corrected temperatures considering the response time of thermocouples. The position of the maximum heat fluxes depended on the melt superheat, strip thickness, and substrate chemistry. Contact of AZ91 melts with bare copper substrates led to the highest maximum heat fluxes of about 4.09 MW/m^2, 130 ms after melt contact. By contrast, contact with zirconia coated substrates on steel bars gave the lowest value of interfacial heat fluxes of 1.16 MW/m^2, about 550 ms after contact. The decrease in heat fluxes with coated substrates shows that the coating layer acted as a thermal resistance, absorbed heat during solidification, and delayed the heat pulse due to its low thermal conductivity. Each curve was obtained by averaging 5 experiments respectively, and the temperatures in parenthesis denote superheats.

In the same manner, heat fluxes associated with AM50 alloy strip cast at superheats in the range 5~30°C were plotted in Fig. 5.4.7. Copper substrates exhibited a maximum heat flux of 5.3 MW/m^2. On the other hand, the increased strip thicknesses, cast on alumina and nickel coated steel substrates, resulted in the increase of heat fluxes.

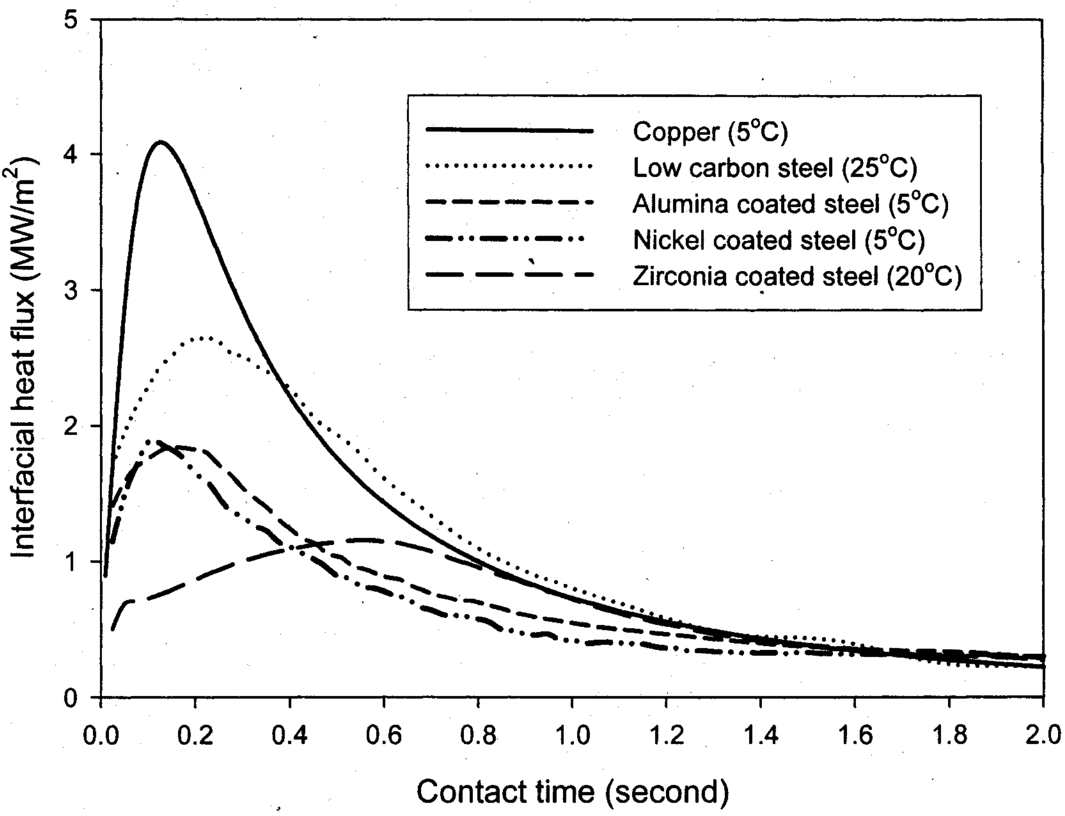

Fig. 5.4.6. Heat flux profiles for various substrates in AZ91 casting (strip thickness: 3mm)

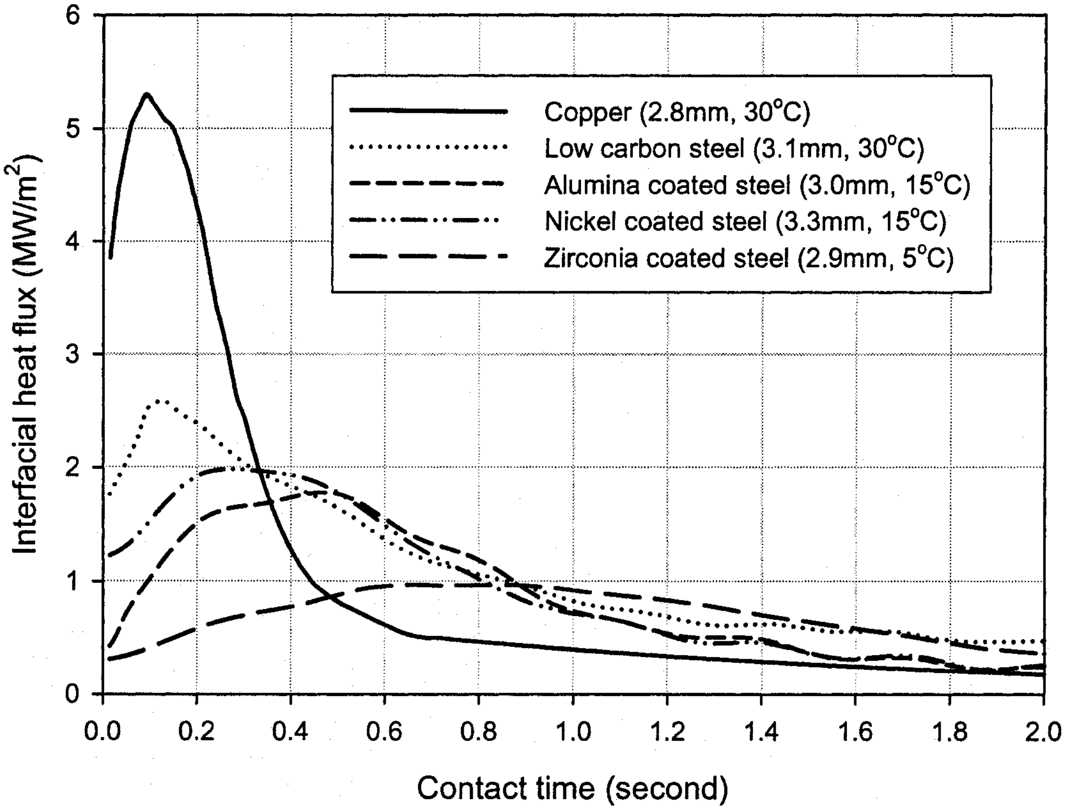

Fig. 5.4.7. Heat flux profiles for various substrates in AM50 casting (melt superheat: 5~30°C)

5.4.3 Strip temperature field

Using the enthalpy method and the boundary condition of interfacial heat flux obtained from the IHCP, the temperature fields inside the strips were calculated. Scheil's model was used to consider the rate of latent heat release. The computed temperature history within the strip cast of AZ91 on a copper substrate with 5 °C superheat is seen in Fig. 5.4.8. The strip lost its superheat within 0.02 seconds, and the temperature of the top surface of the strip dropped to the liquidus (595°C) and the whole thickness of the strip began to solidify. As the bottom surface contacts the cold substrate directly, it experiences the fastest cooling and its temperature decreases most rapidly. This results in the highest local cooling rate and the smallest SDAS values at the bottom surface. Also, it should be noted that the solidification of strip is completed within 0.9 second. This gives an average cooling rate of 175°C/s for this 3mm strip. The local cooling rate, which was obtained from the time-derivative of the curve in Fig. 5.4.8, is plotted in Fig. 5.4.9. In the case of the bottom surface, it gave a maximum cooling rate of 684°C/s after 0.05 seconds of melt-copper substrate contact, while the local cooling rate for the top surface was 28°C/s at that time.

Fig. 5.4.10 shows the temperature variation calculated at the center (half thickness) in the AZ91 and AM50 alloy strips. In the case of the AZ91 alloy, the copper substrate produced a 3mm strip after 0.9 seconds of the initial contact and the low carbon steel substrate produced after 1.6 seconds. On the other hand, the final solidification time of AM50 was delayed compared to the AZ91. It took 1.7 seconds with the copper substrate while 2.6 seconds with the low carbon steel substrate.

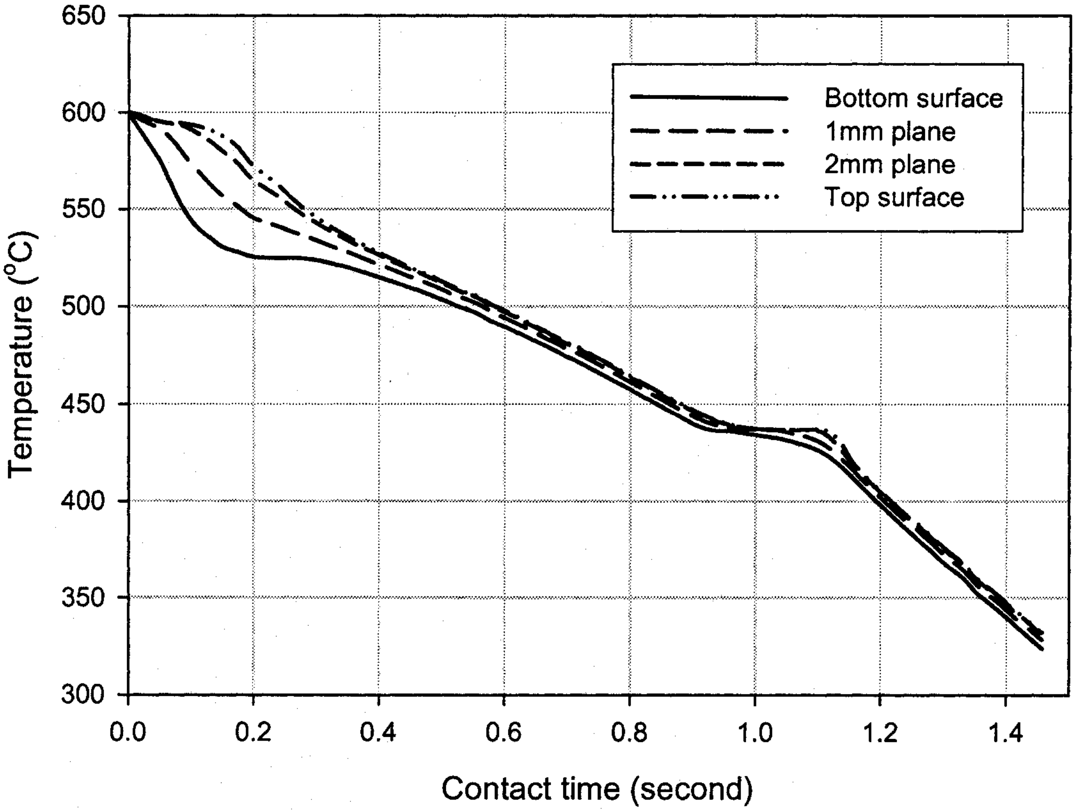

Fig. 5.4.8. The temperature-time profiles of 3mm AZ91 strip, cast on a copper substrate (melt superheat: 5°C)

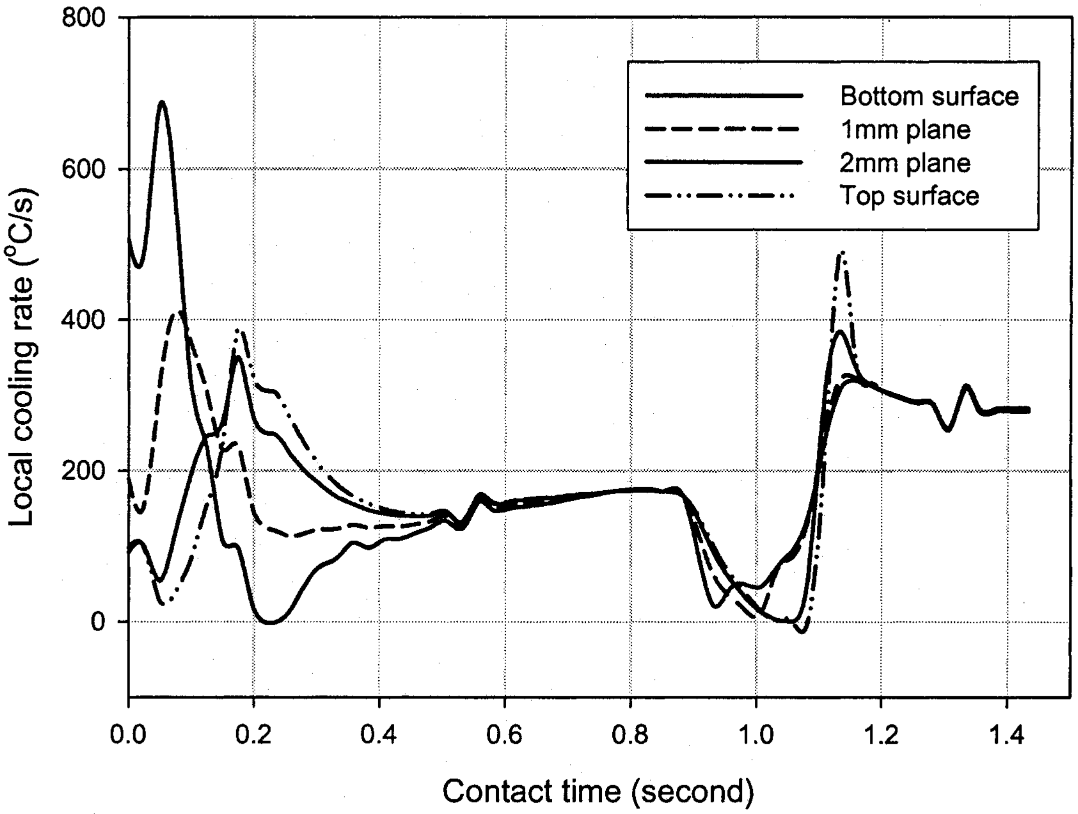

Fig. 5.4.9. The local cooling rates of 3mm AZ91 strip, cast on a copper substrate (melt superheat: 5°C)

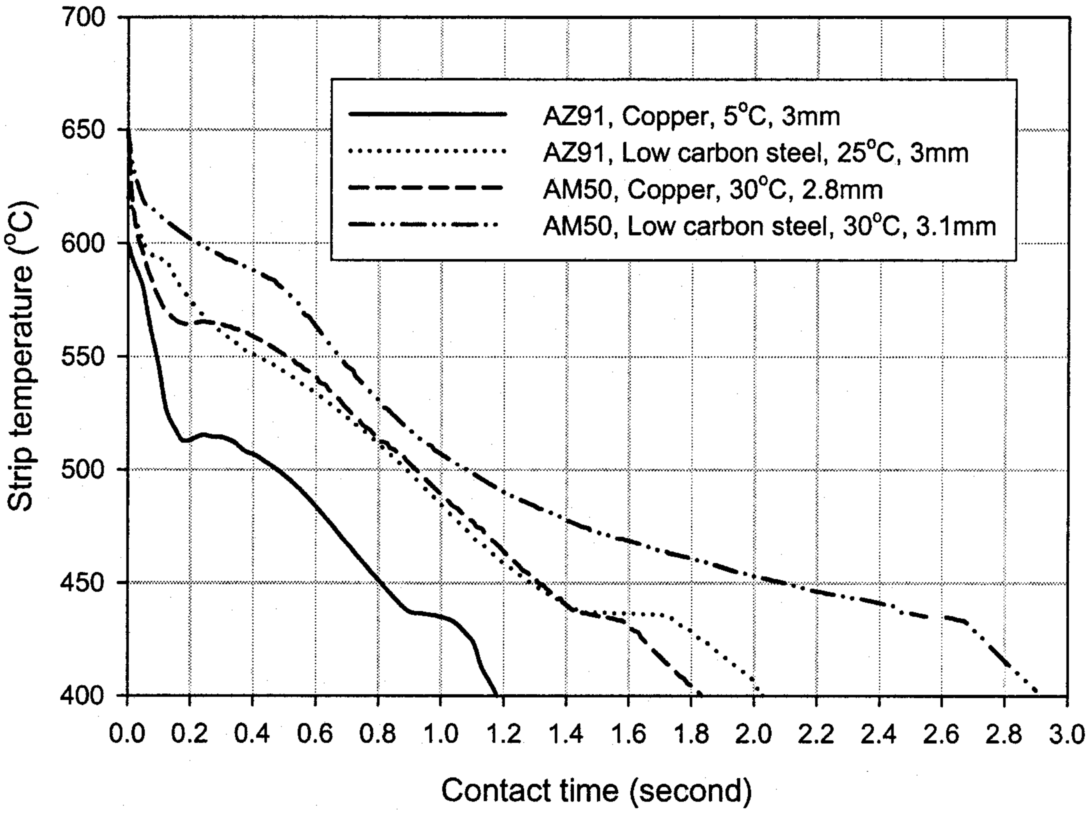

Fig. 5.4.10. Temperature profiles calculated at the center (half thickness) of AZ91 and AM50 strips

Fig. 5.4.11 and Fig. 5.4.12 show the difference of calculated temperatures when different latent heat release models were applied. The data was from the AM50 alloy of 3mm strips, cast on a low carbon steel substrate. The first set of cooling curves was calculated using the linear model and the latter was calculated from the Scheil's model. In the case of the linear model, in which the latent heat is released between the solidus and liquidus values (560 to 620°C) as obtained from the phase diagram. In Scheil's model, limited diffusion in the solid phase delays the end of solidification down to the eutectic temperature (437°C). The model assumes that the latent heat is being released from the liquidus to the eutectic temperature.

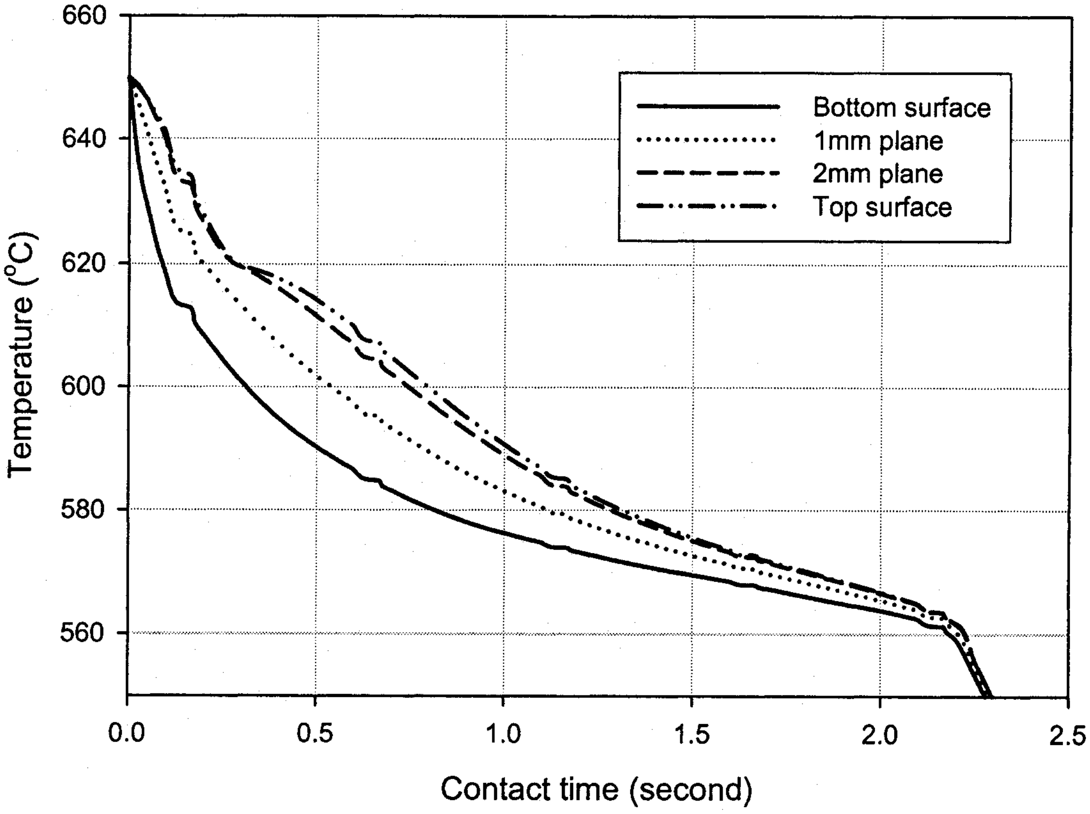

Fig. 5.4.11. Predicted temperature profiles within AM50 strips cast on a low carbon steel substrate, using a linear model

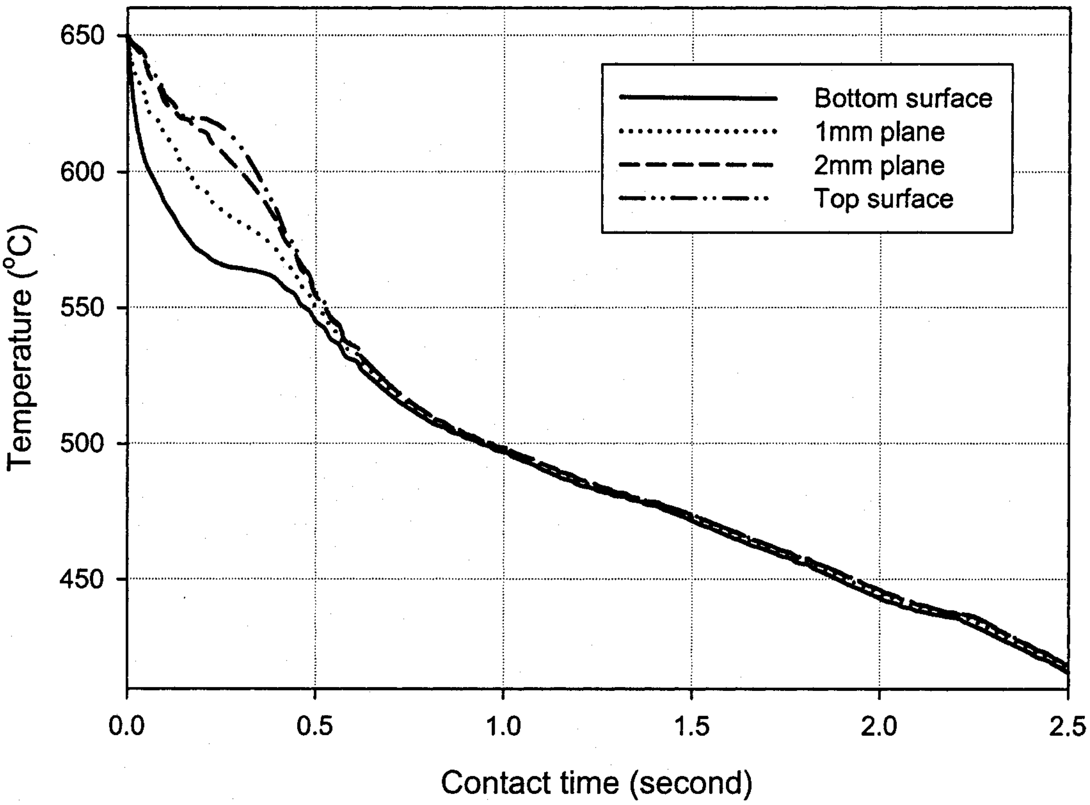

Fig. 5.4.12. Predicted temperature profiles within AM50 strips cast on a low carbon steel substrate, using the Scheil's model of solidification

5.4.4 Interfacial heat transfer coefficient

The interfacial heat transfer coefficient *h* could be calculated from the result of the IHCP and the Enthalpy method. The bottom surface temperature of the strip could be obtained by solving the FVM-Enthalpy method and the mold surface temperature was obtained from the IHCP technique. The general shapes of the curves plotting heat transfer coefficients versus time of contact were similar to those for interfacial heat fluxes versus contact time. Fig. 5.4.13 and Fig. 5.4.14 present averaged transient interfacial heat transfer coefficients for the AZ91 and AM 50 magnesium alloy strips cast.

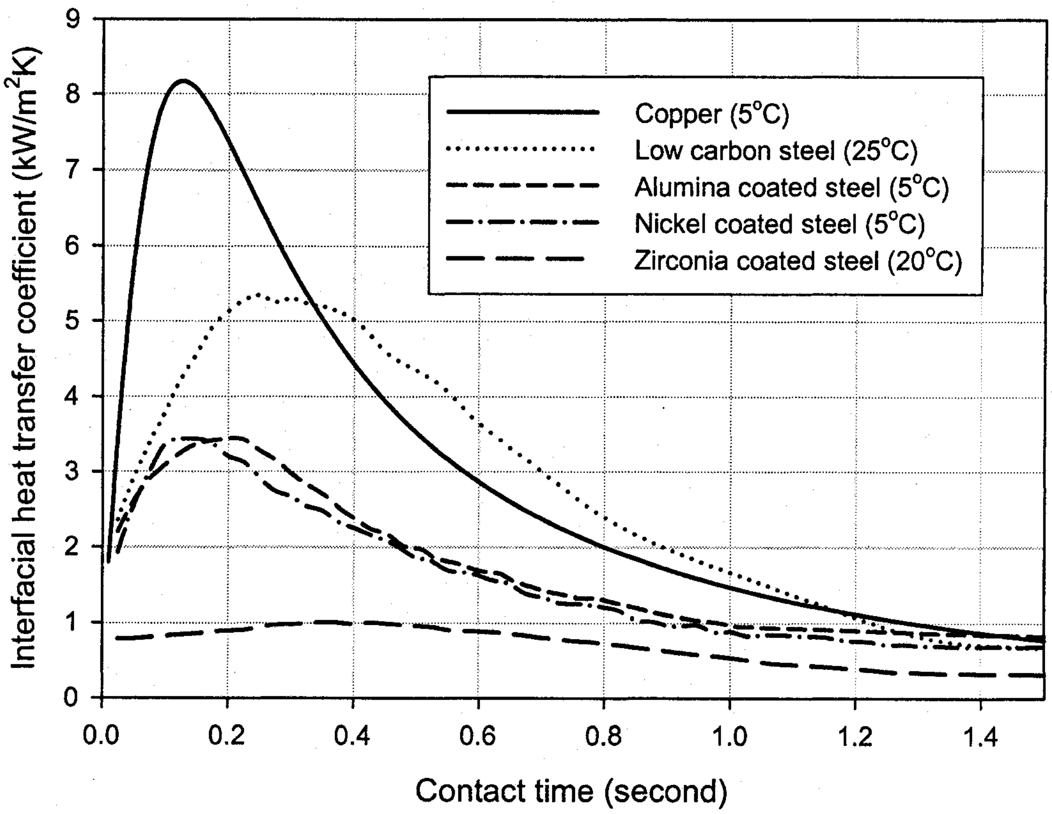

Fig. 5.4.13. Transient heat transfer coefficient profiles for AZ91 cast strips (strip thickness: 3mm)

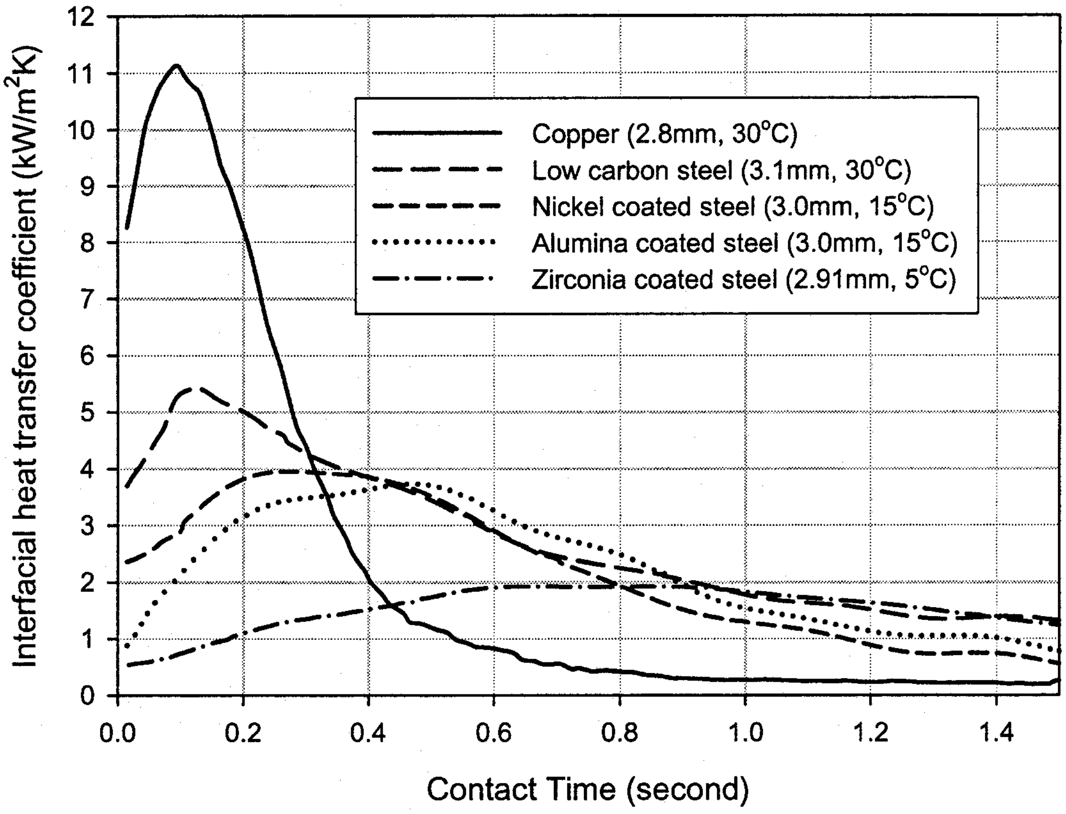

Fig. 5.4.14. Transient heat transfer coefficient profiles for AM50 cast strips (melt superheat: 5~30°C)

5.4.5 Characterization of Microstructure

On analyzing the microstructures of the as cast AZ91 strips, a region of interdendritic porosity was apparent close to the upper surface of the strip. This porosity was mainly the result of shrinkage of liquid metal during solidification. However, in the case of AM50, a much smaller zone of porosity was observed. Fig. 5.4.15 presents a porous section of the casting's microstructure for a strip of AZ91 cast on low carbon steel substrate. Fig. 5.4.16 and Fig. 5.4.17 show examples of the microstructures of AZ91 cast on copper and low carbon steel substrates. The intermetallic compound, $Mg_{17}Al_{12}$, appeared within the interdendritic regions for both AZ91 and AM50 alloys. This second phase increases the yield strength and decreases the ductility of magnesium alloys [5-6].

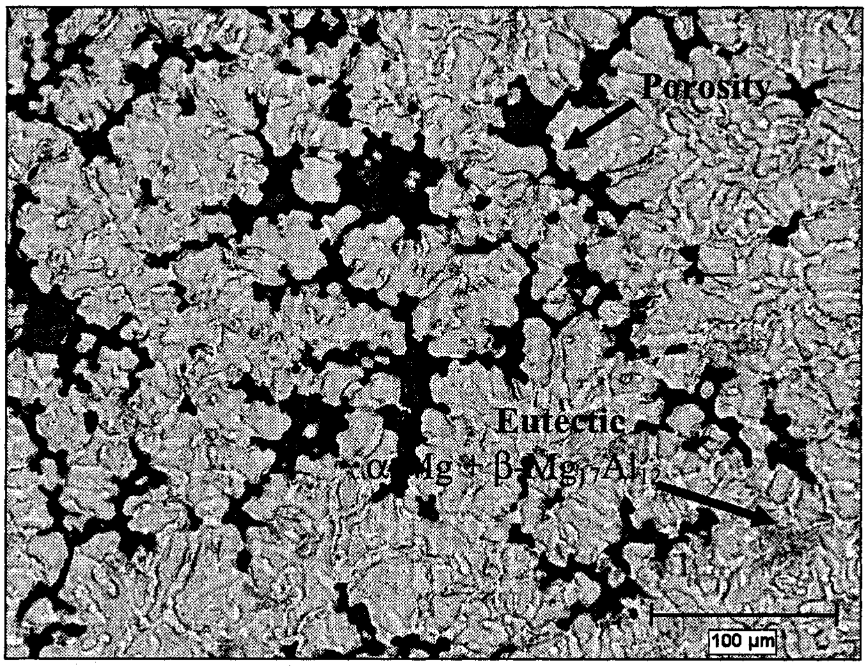

Fig. 5.4.15. Microstructure of AZ91 cast strip showing regions of porosity

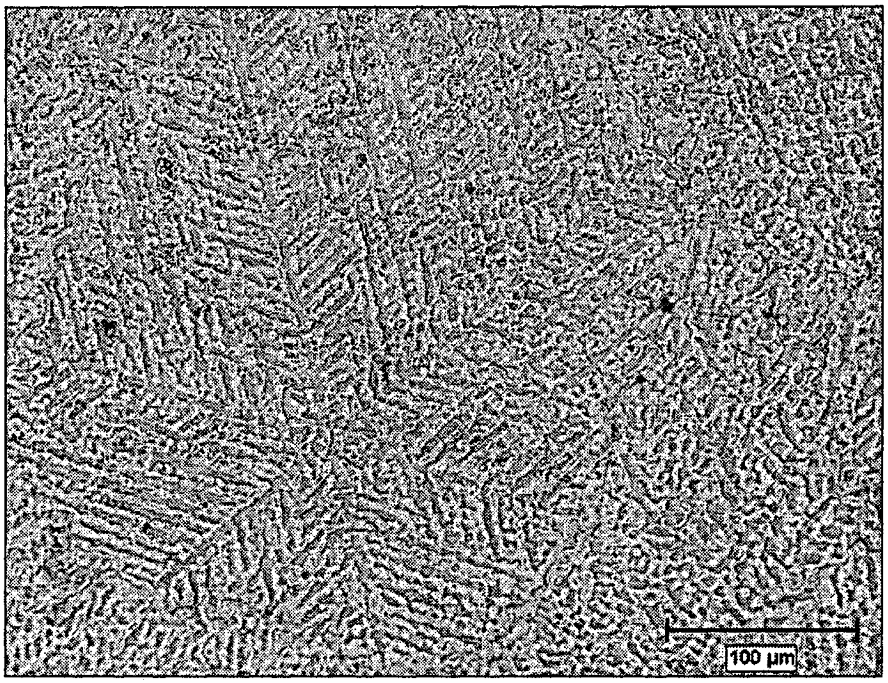

Fig. 5.4.16. Microstructure of 3mm AZ91 strip cast on a copper substrate

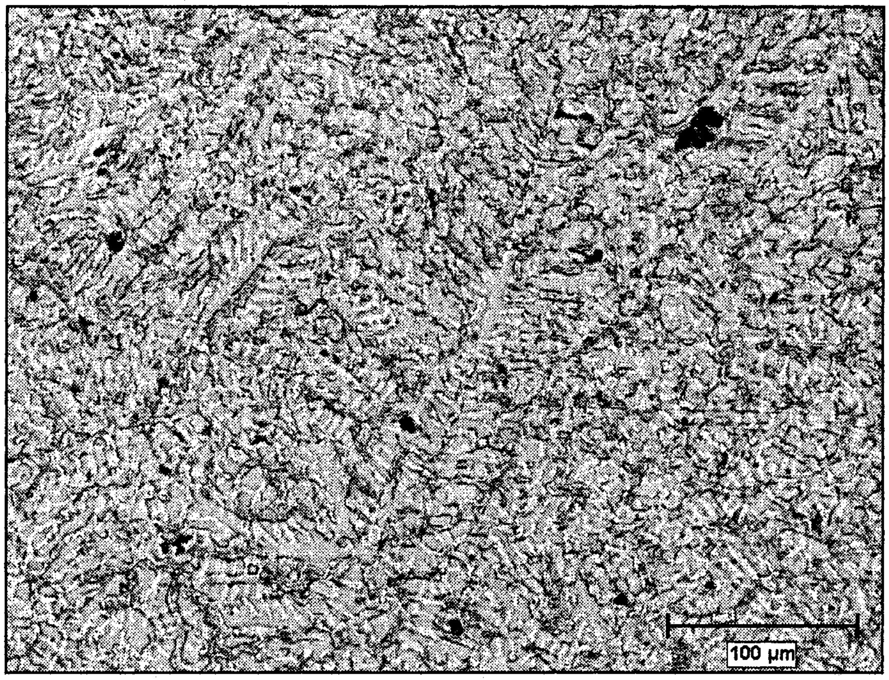

Fig. 5.4.17. Microstructure of 3mm AZ91 strip cast on a steel substrate

The effect of substrate materials on heat extraction and strip microstructure was investigated by measuring the SDAS of the cast samples. Fig. 5.4.18 provides a plot of SDAS levels versus superheat for AZ91 alloy. The smallest SDAS was obtained with 5 ^{o}C superheat on a copper substrate. Increasing melt superheat increased SDAS values for all substrates. Also, when compared to the values of heat fluxes mentioned earlier, the higher the heat flux, the smaller the SDAS.

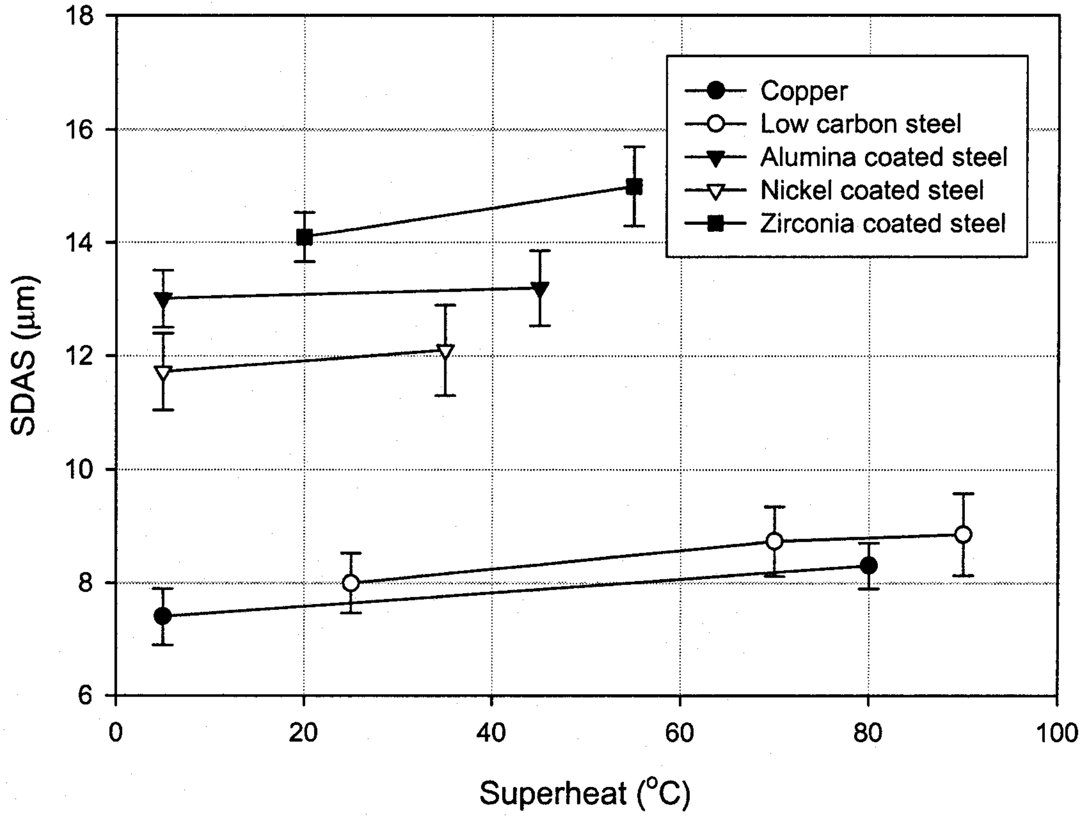

Fig. 5.4.18. The effect of superheat on the SDAS in AZ91 casting

Fig. 5.4.19 shows the result of the SDAS versus the estimated cooling rates in the current work of AZ91 strip casting. As seen, when copper was used as a substrate material, cooling rates exceeded 160°C/s, while the cooling rate was about 20°C/s for zirconia coated steel substrates. In addition, Fig. 5.4.20 shows the SDAS versus the cooling rate for AM50 alloy. Note that, in AM50 strips, the lower cooling rate and increased values of the SDAS were observed compared to AZ91 casting.

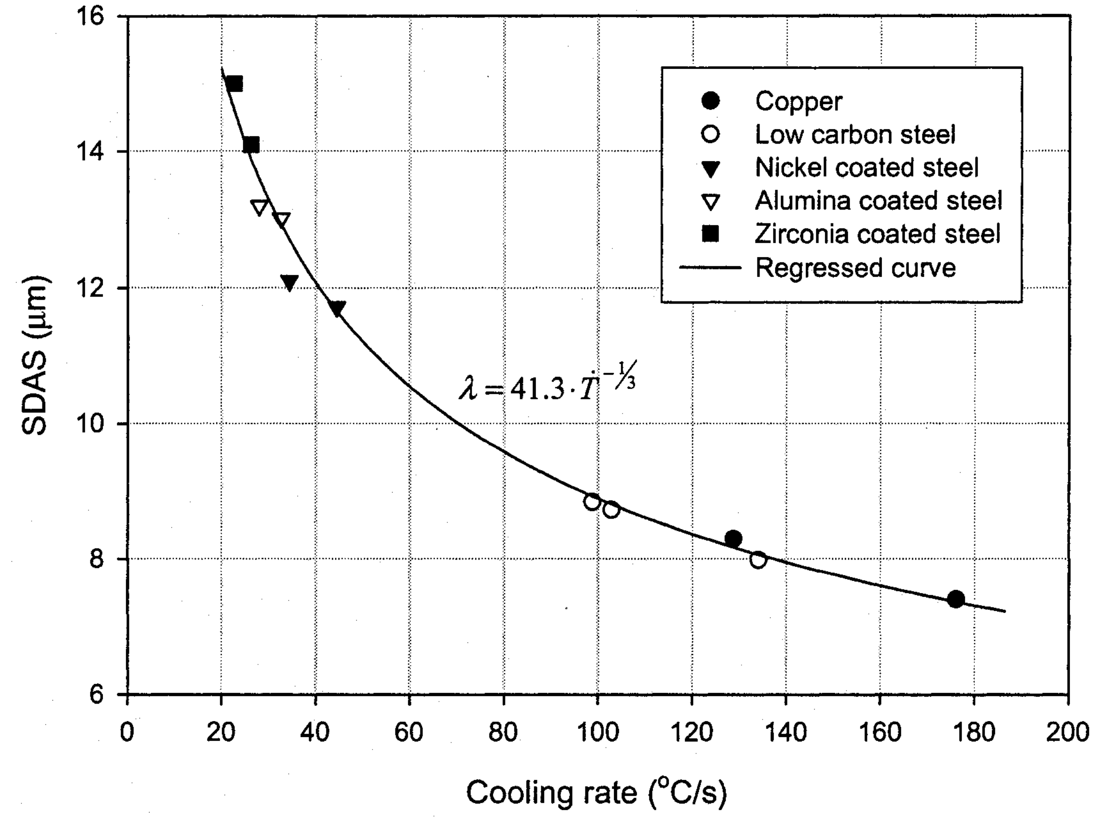

Fig. 5.4.19. The relationship between the SDAS and cooling rates for AZ91 strips

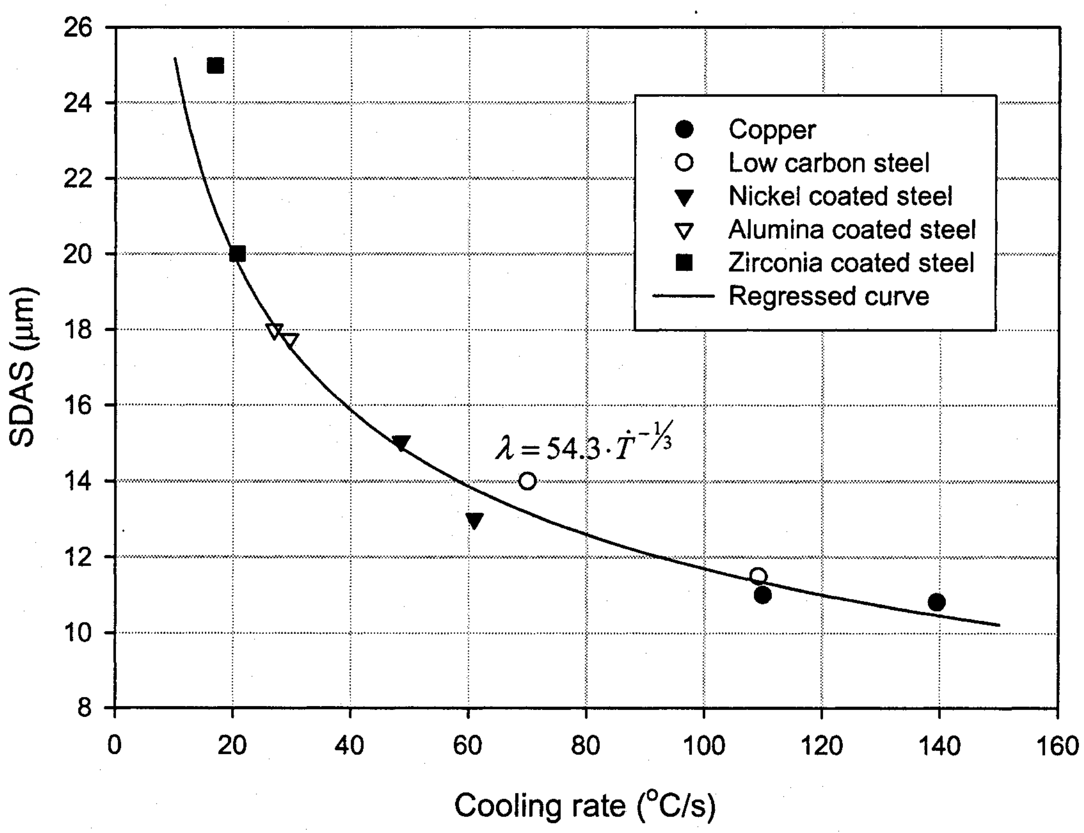

Fig. 5.4.20. The relationship between the SDAS and cooling rates for AM50 strips

5.4.6 Conclusions

From magnesium alloys of AZ91 and AM50 casting, the following conclusions could be drawn.

i) To calibrate the time lag and catch up with the abrupt change of temperature in instantaneous metal-mold contact, correction of the ungrounded thermocouple's response times was needed.

ii) The interfacial heat fluxes and heat transfer coefficients increased from a certain value at the beginning, up to reach their maxima, followed by a decrease with further time of contact.

iii) An increase in melt superheats resulted in an increase in interfacial heat fluxes.

iv) The maximum values of interfacial heat fluxes and heat transfer coefficients of copper substrate were about 1.5~2 times higher than those recorded for low carbon steel substrates. However, the copper substrate recorded faster decays in these values than the low carbon steel substrate.

v) The use of variously coated low carbon steel substrates greatly reduced the rate of interfacial heat transfer and resulted in significantly coarser microstructures compared to uncoated copper and low carbon steel substrates.

vi) AZ91 alloy was solidified about 1.5 times faster than AM50 alloy and produced finer microstructure in terms of the decreased SDAS.

vii) AM50 alloy produced about 50% reduced porosity in microstructure of strips compared to AZ91.

viii) The higher the interfacial heat fluxes measured, the higher were the cooling rates of produced strips and the smaller their SDAS microstructures.

ix) The SDAS of AZ91 alloy ranged from 7 to 15 microns, while that of AM50 was from 11 to 25 microns.

5.5 AA6111 ALUMINUM ALLOY

5.5.1 AA6111 Aluminum alloy

Aluminum alloys, AA6XXX, are considered to be promising wrought alloys versus steel sheet alloys for automotive applications. The reduced vehicle weight and thereby increased fuel efficiency versus steel sheet materials make them interesting candidates for auto bodies. Compared to AA2XXX or AA7XXX alloys, these alloys provide improved corrosion resistance and lower material costs. In particular, AA6111 alloys provide good formability, mechanical strength and weldability. The alloy system contains Mg, Si, and Cu as the major alloying elements, together with Fe and Mn as the minor elements. Table 5.5.1 gives the chemical composition of AA6111 alloy. Because of its wide freezing range and multiplicity of the alloying elements, AA6111 alloy contains a number of intermetallic compounds formed through a series of eutectic and peritectic reactions during solidification. These are listed in Table 5.5.2 [7].

Table 5.5.1. Chemical composition of AA6111 alloy

Al Alloys	Mg	Si	Cu	Fe (max)	Mn
AA6111	0.5 ~ 1.0%	0.7 ~ 1.1%	0.5 ~ 0.9%	~0.4%	0.15~0.45%

Using differential thermal analysis, Chen et al. [7] investigated the series of chemical reactions when AA6111 alloy solidifies. They found that these reactions could be missed at higher cooling rates. Under equilibrium conditions, or very slow cooling rate of 2~3°C/s, α-Al dendrites formed initially, followed by binary Al-Fe intermetallic compounds (Al_6Fe or Al_3Fe). Two ternary phases of α-Al(FeMn)Si and β-Al(FeMn)Si were formed via peritectic reactions between 609 °C and 632°C. Then, other intermetallic compounds of Mg_2Si, AlCuMgSi, Al_2Cu, and Si phase were formed in subsequent reactions. Solidification finally ended around 475°C. On the other hand, in the case of non-equilibrium conditions, it was found that the solidification began at 650°C and ended at a temperature of 502°C using the Gibbs energy minimization method by Thermo-Calc [8].

Table 5.5.2. Solidification characteristics of AA6111 alloy [7]

	Reactions during solidification	Temperature range (°C)
1	L → α-Al (dendrite)	650 – 651
2	L → α-Al + Al_6Fe (or Al_3Fe)	643 – 645
3 (a)	L + Al_6Fe → α-Al + α-Al(FeMn)Si	632 – 609
(b)	L + α-Al(FeMn)Si → α-Al + β-Al(FeMn)Si	
4	L → α-Al + Mg_2Si	588 – 590
5	L → α-Al + Mg_2Si + Si	553 – 555
6 (a)	L + Mg_2Si + Si → α-Al + AlCuMgSi	532 – 535
(b)	L + Mg_2Si → α-Al + AlCuMgSi + Al_2Cu	
7	L → α-Al + Al_2Cu + Mg_2Si	506
8	L → α-Al + Al_2Cu + AlCuMgSi + Si	483 – 485
	End of solidification	475

5.5.2 Spring-driven casting simulator

To maintain the uniform casting speed and to improve the temperature acquisition system, a new casting simulator was designed by Li et al. [9] at McGill. The speed of substrate was more uniform compared to the previous pneumatically driven casting simulator. Also, the installation of exposed thermocouples increased its sensitivity for the initial measurement of heat transfer. Thermocouples were positioned closer to the interface (0.82mm and 3.7mm) compared to the previous experiments (1.58mm and 4.87mm) to improve the sensitivity of temperature change near the interface. Furthermore, these thermocouples were tightly fixed by screwing bolts to maintain their contacts inside the substrate during the movement. This installation of exposed thermocouples greatly improved the reliability of temperature data and corrections of the type presented earlier were not needed. A photograph of the new simulator and a schematic diagram of the thermocouples installation are presented in Figs. 5.5.1 and 5.5.2 respectively.

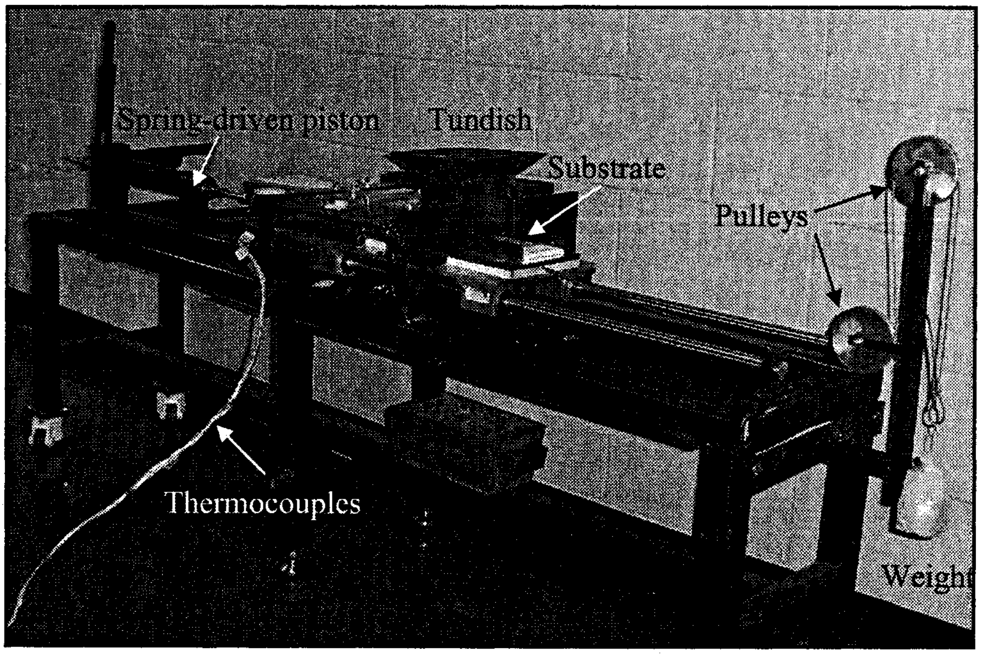

Fig. 5.5.1. New spring-driven casting simulator

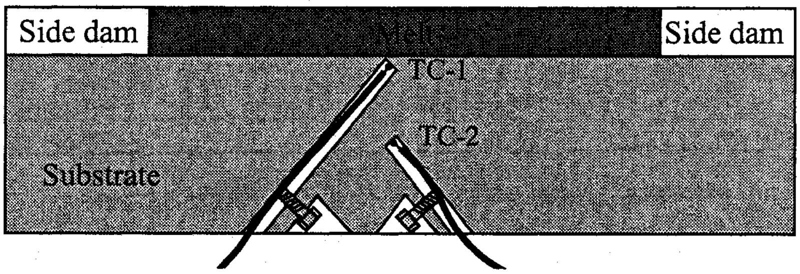

Fig. 5.5.2. Screw squeezed thermocouple installation

5.5.3 Macroscopic strip quality

Copper and low carbon steel substrates were used to cast the AA6111 alloy. An increase in casting speed from 0.2 to 1.5 m/s resulted in a decrease in strip product thickness from 7 to 0.4mm. The top and bottom surface of the AA6111 strip exhibited regular patterns of shrinkage over the entire surface. An example of strip's surfaces is shown in Fig. 5.5.3 when the alloy was cast on a steel substrate.

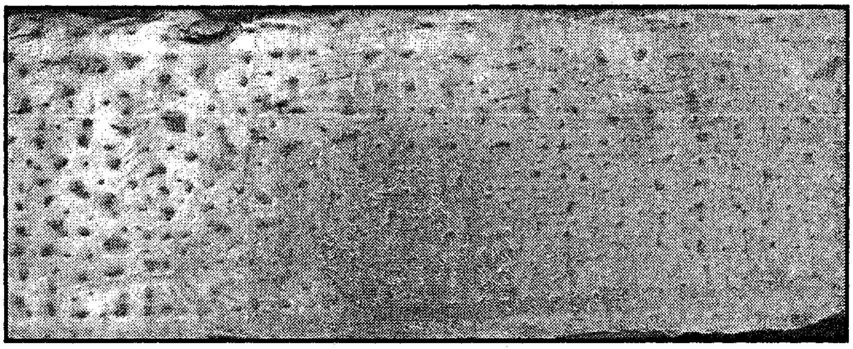

(a) Top surface

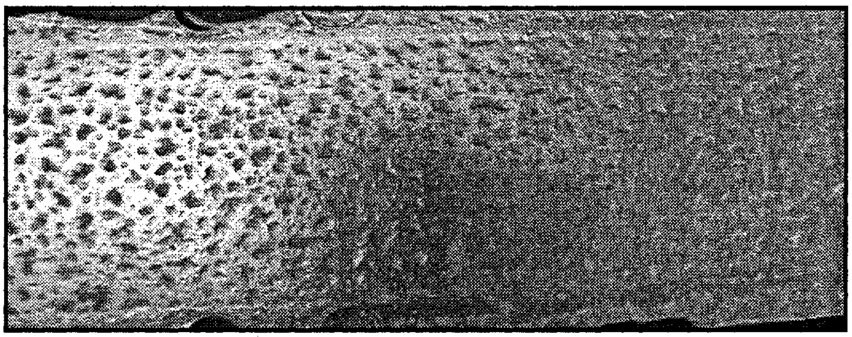

(b) Bottom surface

Fig. 5.5.3. Strip surfaces of AA6111 alloy cast on a steel substrate (thickness: 1.5mm, superheat: 20°C)

The microstructure of the shrinkage area was investigated using an optical microscope. Fig. 5.5.4 shows two area of shrinkage of the AA6111 sample cast on a copper substrate. Corresponding to Fig. 5.5.4, the SEM images of two bottom areas are shown in Fig. 5.5.5.

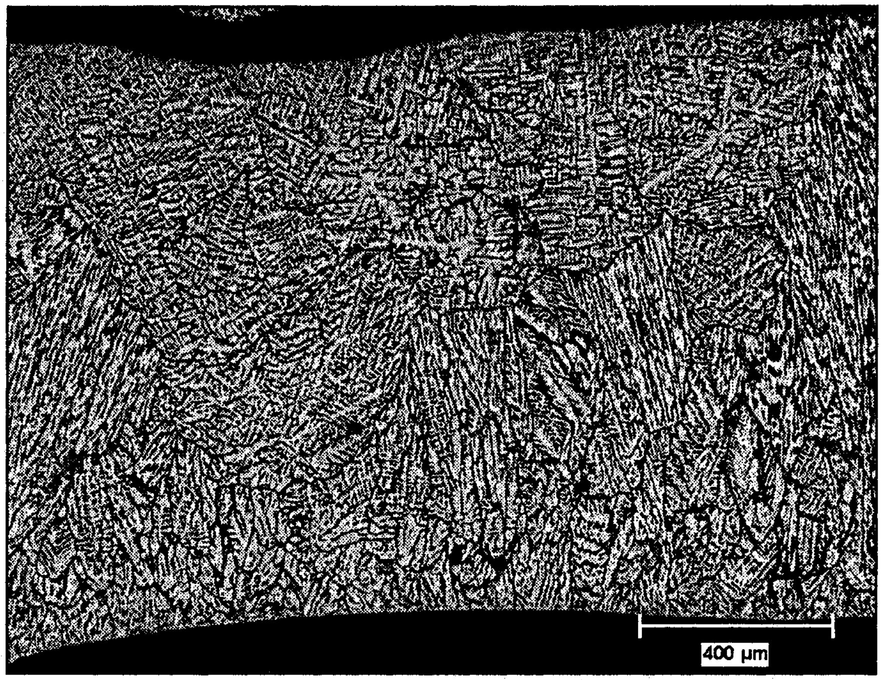

(a) shrunken area of AA6111 alloy

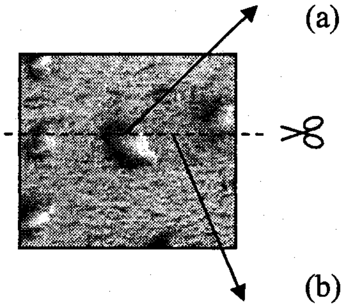

Fig. 5.5.4. Transverse microstructures of AA6111 alloy cast on a copper substrate (thickness: 1.5mm, superheat: 30°C)

(b) flat area of AA6111 alloy

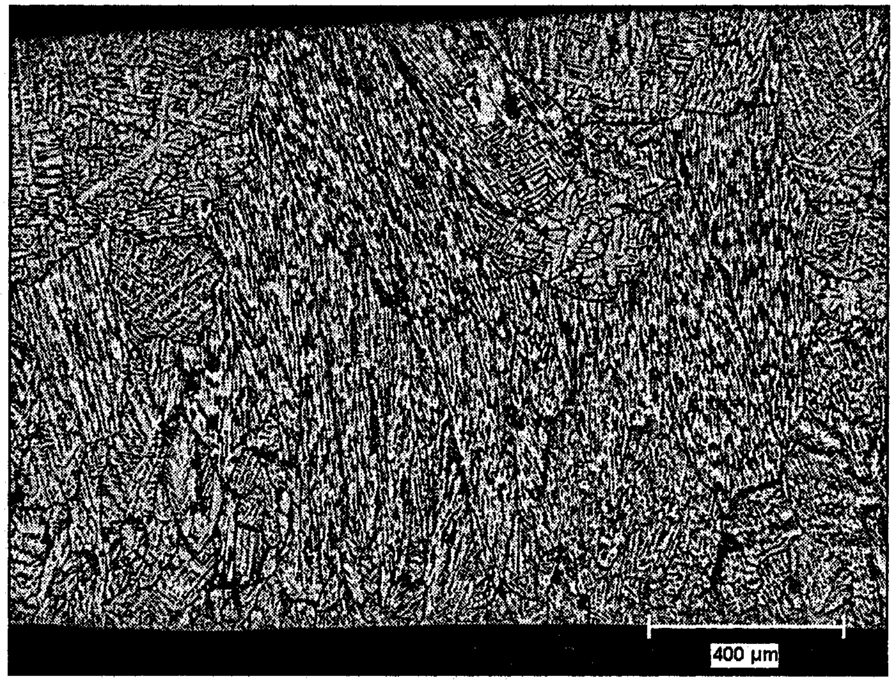

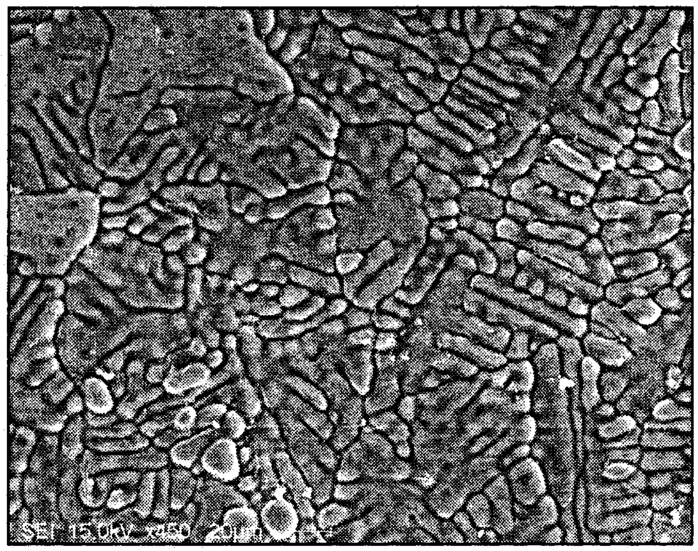

(a) shrunken surface of AA6111 alloy (X450)

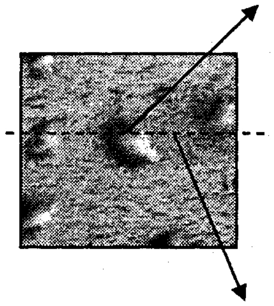

Fig. 5.5.5. Microstructures of the bottom surface of AA6111 alloy cast on a copper substrate (thickness: 1.5mm, superheat: 30°C)

(b) flat surface of AA6111 alloy (X450)

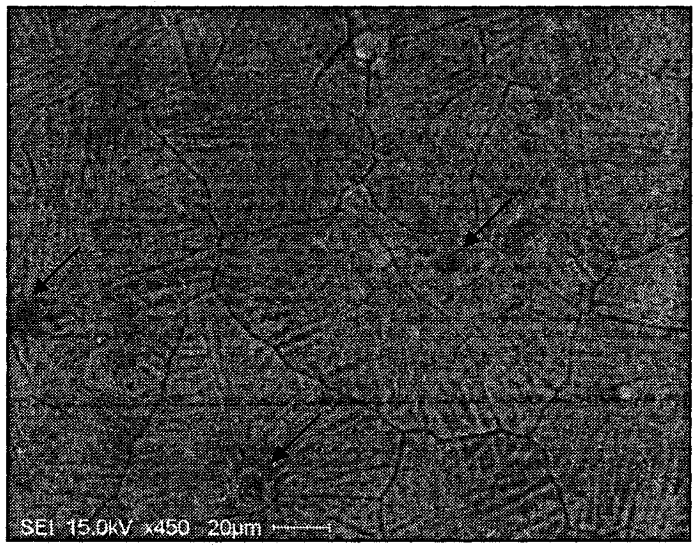

From Fig. 5.5.5 (b), some impingement points could be seen and grain size ranged about 95~110μm. In the shrunken area (a), small scale of 4~5μm SDAS were observed.

5.5.4 Effect of casting speed

Based on the instant temperature measurement system and IHCP technique described previously, interfacial heat fluxes and heat transfer coefficients were estimated for this series of experiments. Fig. 5.5.6 shows the instantaneous heat flux profiles of the AA6111 alloys versus contact time with cooling substrates for various conditions. The decrease in strip thickness was controlled by increasing the casting speed. A casting speed of 0.6~0.8m/s resulted in 3mm thick strip, while 1.0~1.2m/s speed produced a 1mm thick strip. It should be noted that with the increased casting speed i.e. thin strip products, even with a lower superheat, the maximum heat fluxes measured were slightly higher than the thicker strip products. With a copper substrate, the values of the maximum heat flux were 6.6 MW/m^2 for 1.1mm thick strip and 6 MW/m^2 for 3mm thick. With a low carbon steel substrate, they were 3.2 MW/m^2 for 1.2mm thick and 2.7 MW/m^2 for 3mm strips.

In addition, in the case of ~1mm strips, about 1 second from the moment of initial contact of the molten alloy with the chill surfaces, both steel and copper substrate cast strips recorded nearly the same values of heat fluxes. On the other hand, in the case of ~3mm strips, it took 1.5 seconds for them to converge together.

Fig. 5.5.7 shows the corresponding interfacial heat transfer coefficients. Up to 0.3 seconds from the beginning, the value of interfacial heat transfer coefficient was higher for the thinner strips as compared to the thicker strips.

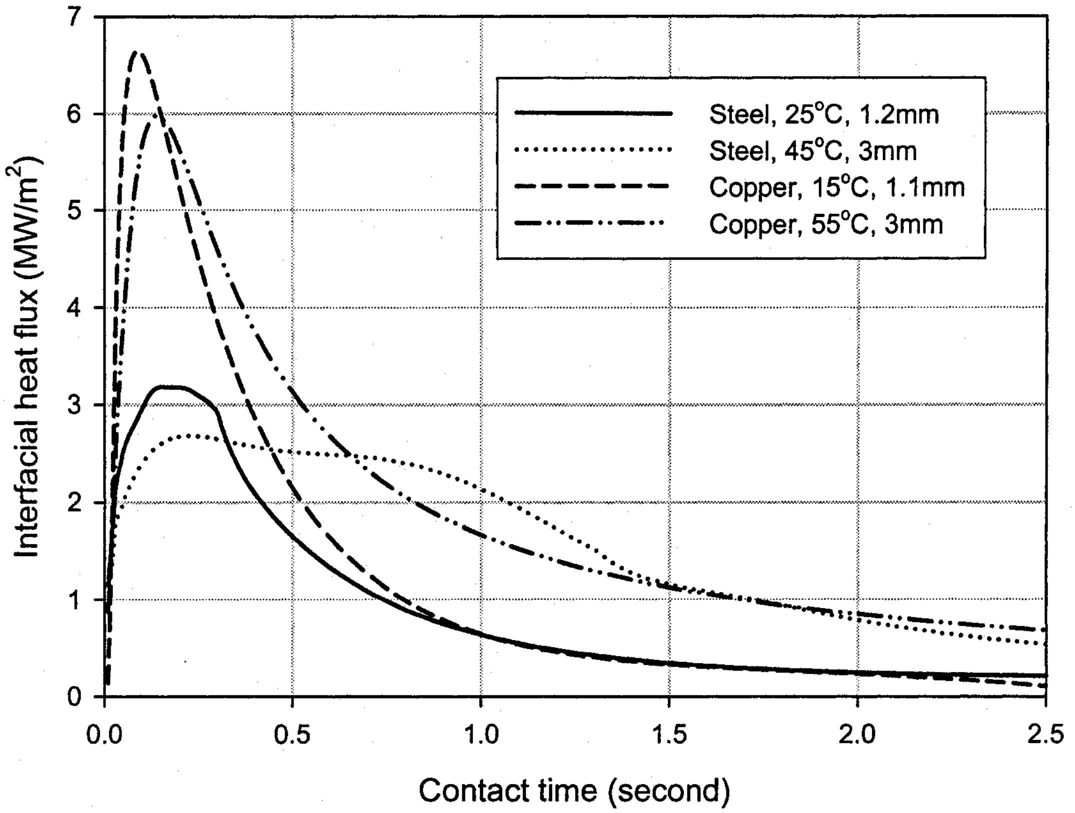

Fig. 5.5.6. Heat flux profiles with steel and copper substrates in AA6111 casting

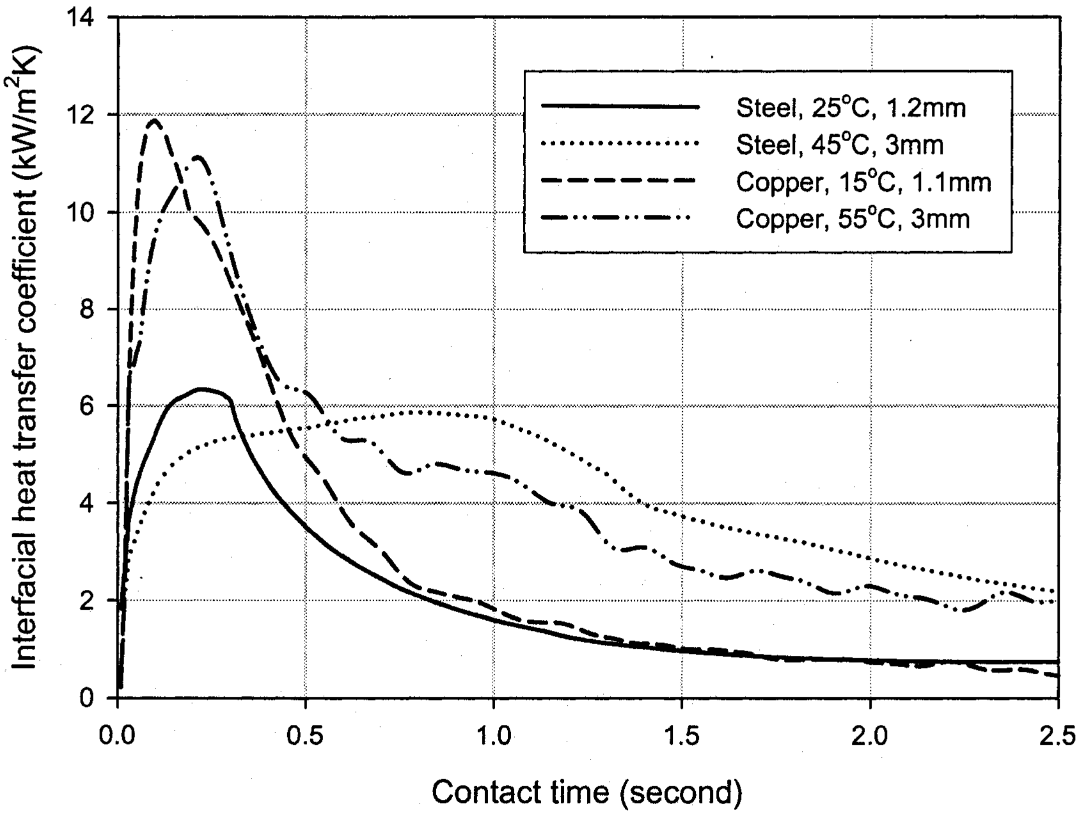

Fig. 5.5.7. Transient heat transfer coefficient profiles for strips of AA6111 cast on steel and copper substrates

Using the previous enthalpy method associated with Scheil's method, the temperature profiles of the solidifying strips were calculated. As shown in Fig. 5.5.8 and 5.5.9, solidification finished earlier for the thinner strips for both substrates. In the case of copper substrate, a 1.1 mm strip finished its solidification within 0.36 seconds of contact, while 3mm strip finished at 1.23 seconds. In the case of steel substrates, 1.2 seconds was required for 1.2mm strip and 1.65 seconds for 3mm strip.

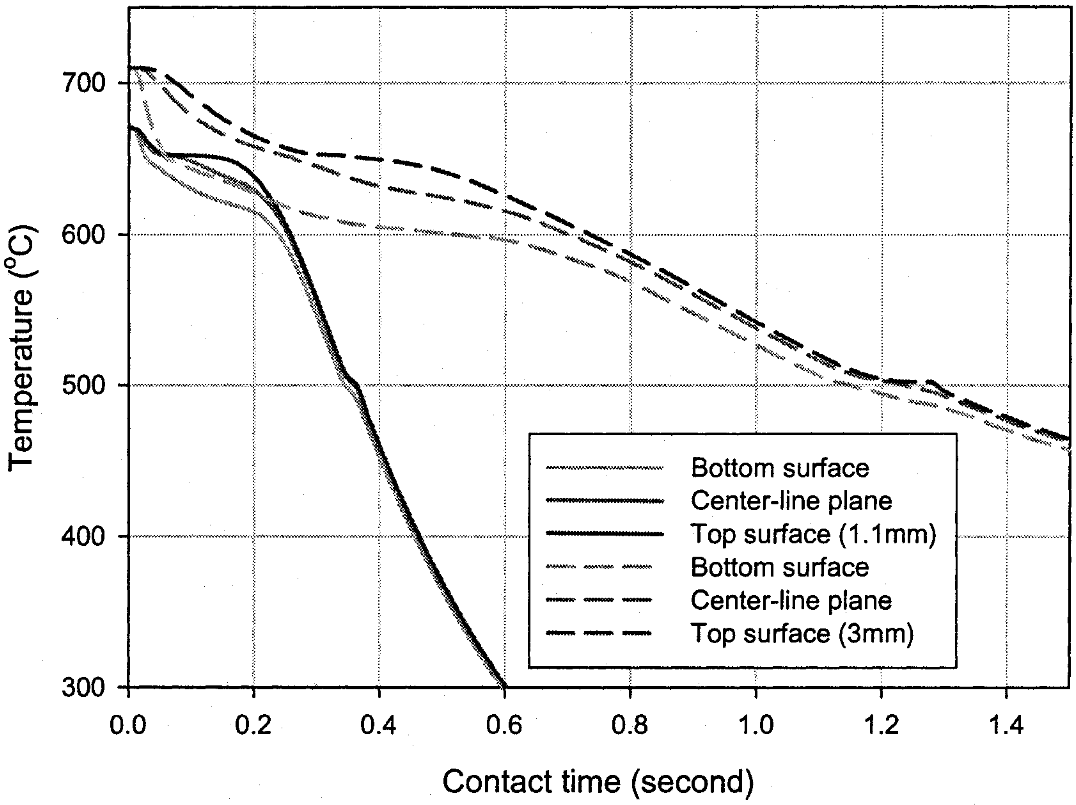

Fig. 5.5.8. Predicted temperature profiles of AA6111 strips cast on a copper substrate

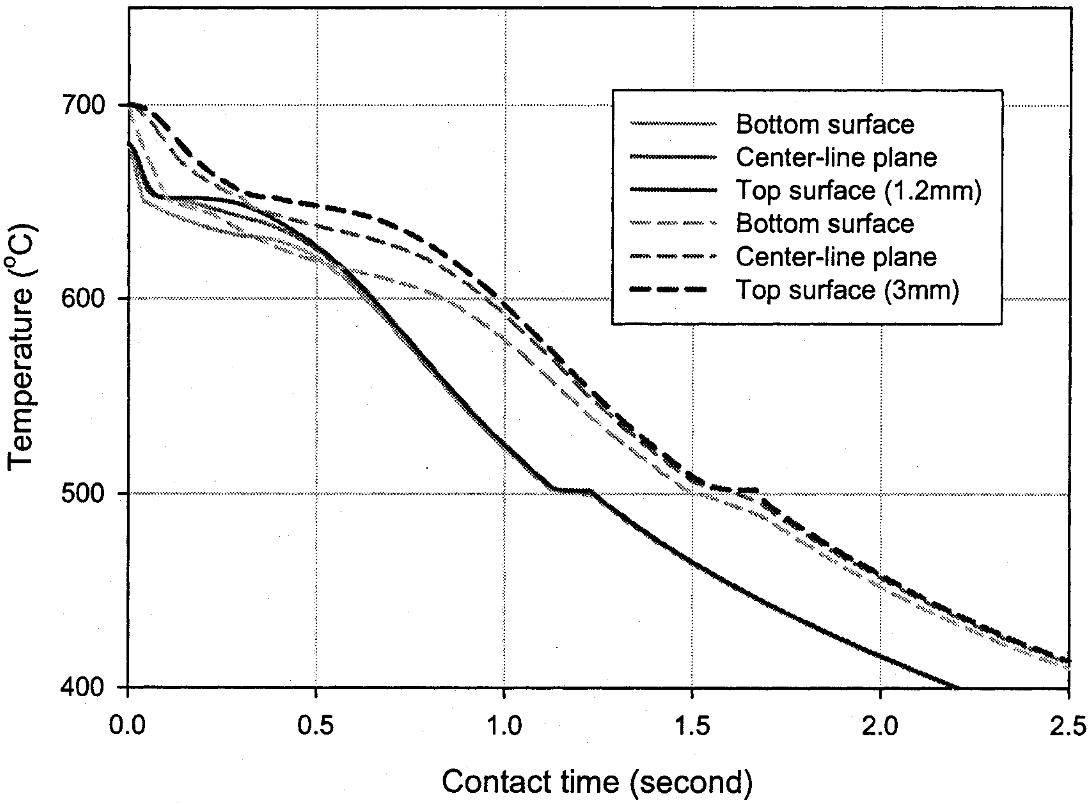

Fig. 5.5.9. Predicted temperature profiles of AA6111 strips cast on a steel substrate

The effect of casting speed on the bottom surface quality of strip was examined, as illustrated in Fig. 5.5.10. Strip thickness can be controlled by changing casting speed, melt head, and the nozzle size. For the same strip thickness at different casting speeds, the macroscopic quality of strip's bottom surface was different. The increase in casting speed from 0.2 m/s to 0.7 m/s degraded the strip's surface quality as a result of more pitted, or dimpled, regions.

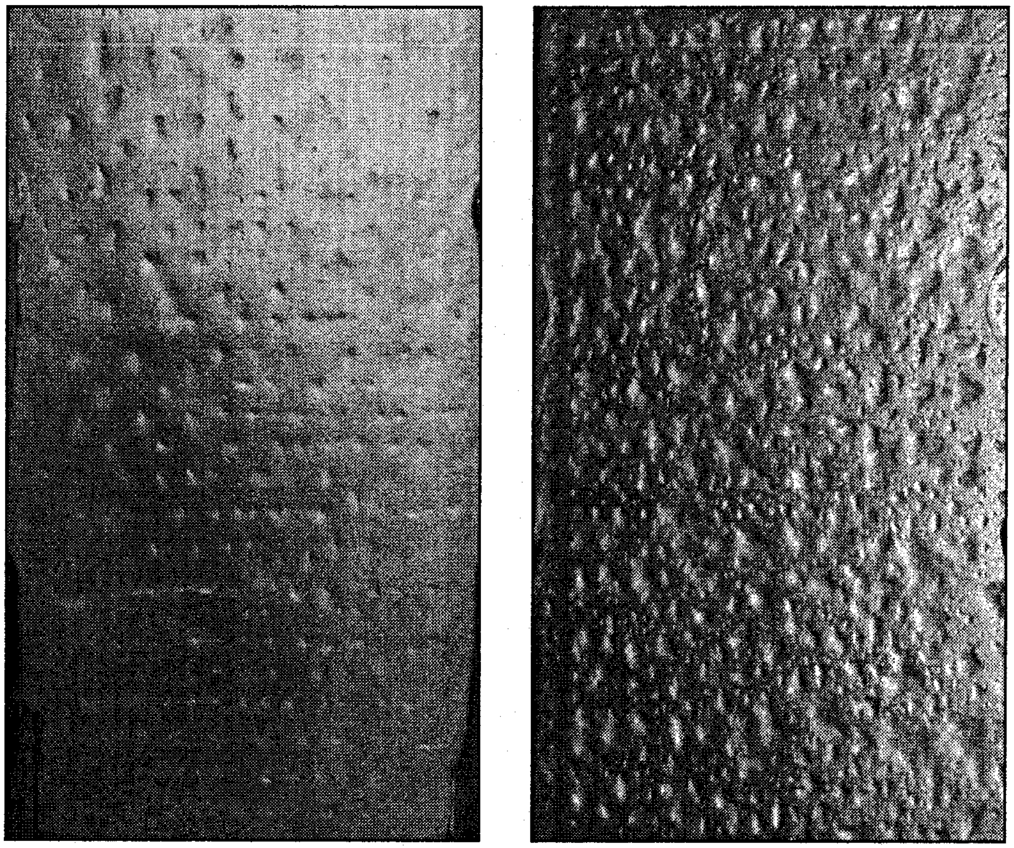

(a) 0.2 m/s (thickness = 3.5mm) (b) 0.7 m/s (thickness = 1.5mm)

Fig. 5.5.10. Bottom surface of AA6111 alloy cast at different speeds on a copper substrate

5.5.5 Characterization of microstructure

Microstructures of the solidified AA6111 alloy strips were shown from Fig. 5.5.11 to Fig. 5.5.16. Both microstructures were similar to each other but comparatively less columnar zone was observed when the strip was cast on a copper substrate. Also, grain size grew from the bottom surface to the top surface. Both strips nearly had the same thickness and superheat. Heat fluxes and strip temperature profiles for these regions are discussed in the previous section 5.5.4.

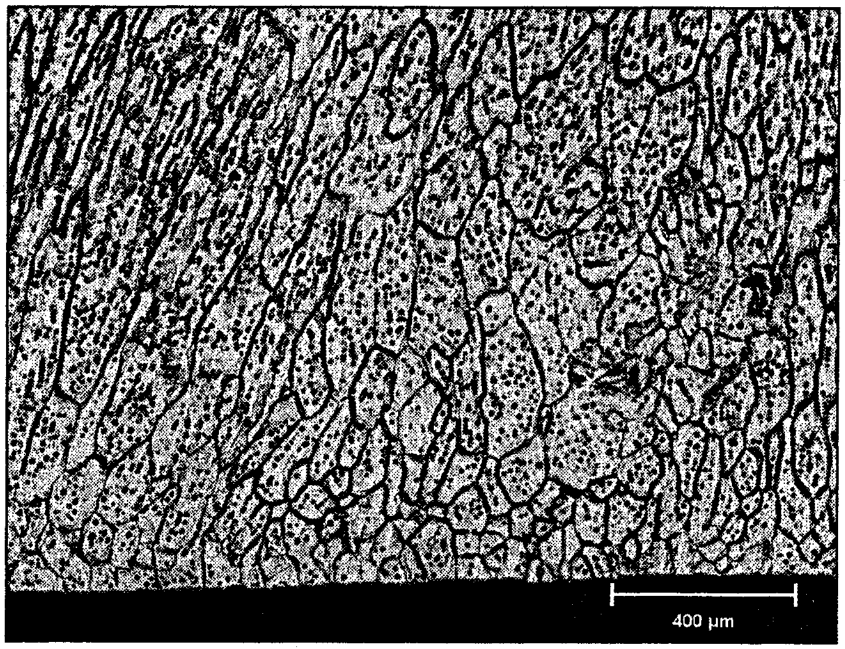

Fig. 5.5.11. Bottom region of strip cast on a copper substrate (3.5mm, superheat: 40°C)

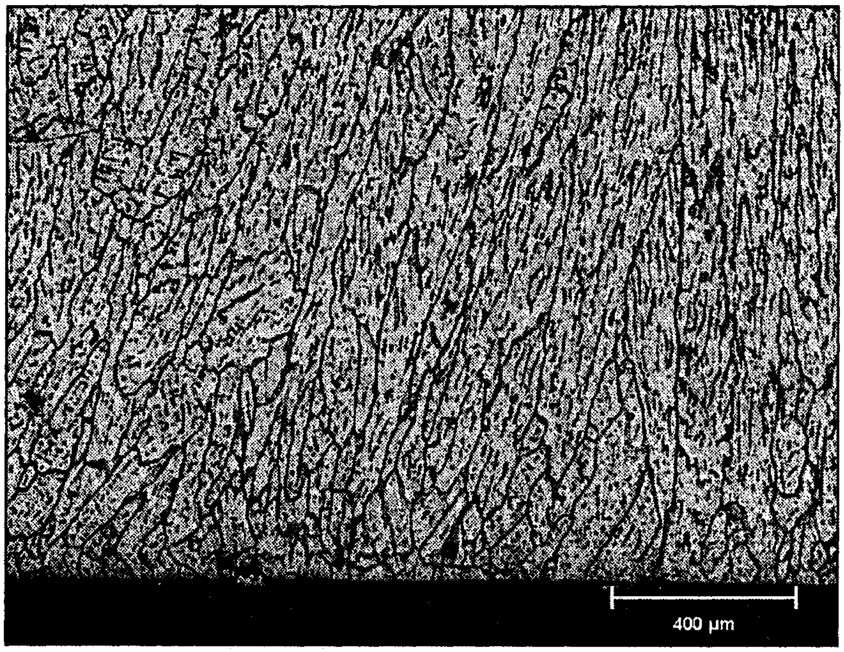

Fig. 5.5.12. Bottom region of strip cast on a steel substrate (3.5mm, superheat: 30°C)

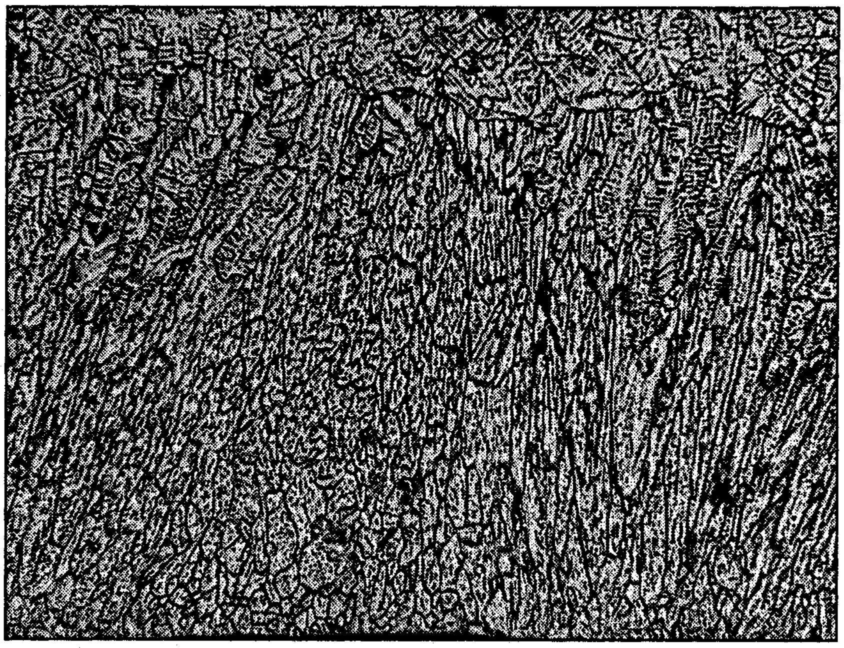

Fig. 5.5.13. Center region of strip cast on a copper substrate (3.5mm, superheat: 40°C)

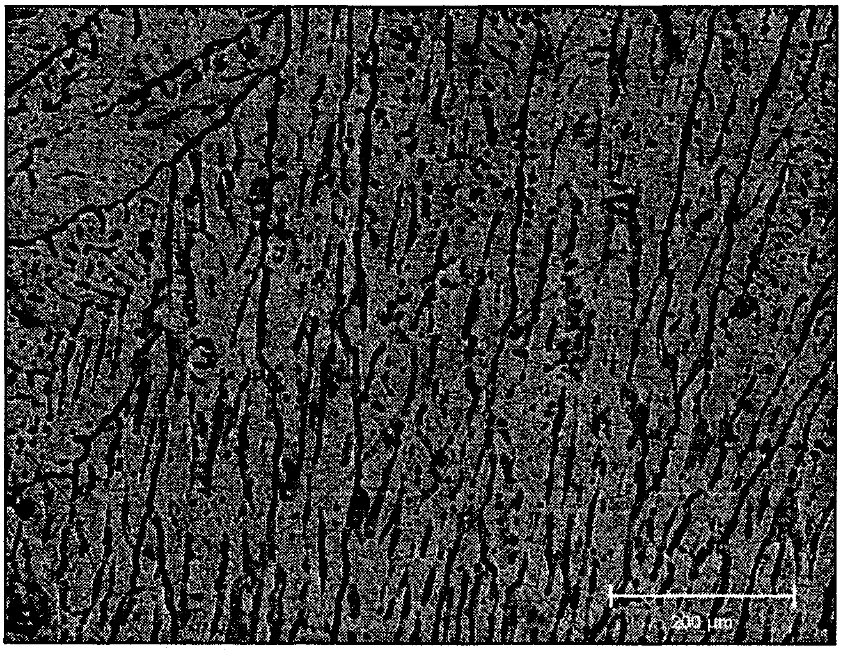

Fig. 5.5.14. Center region of strip cast on a steel substrate (3.5mm, superheat: 30°C)

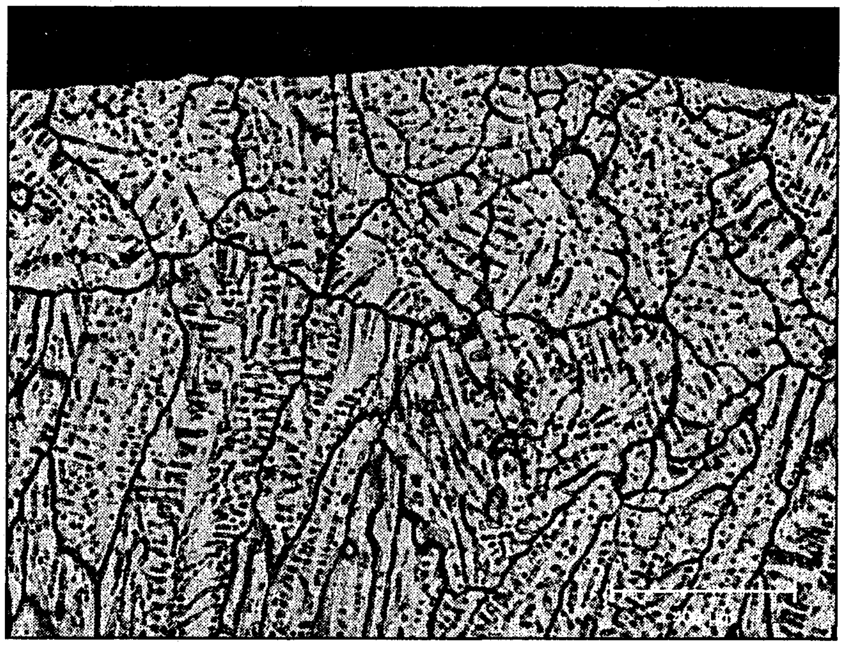

Fig. 5.5.15. Top region of strip cast on a copper substrate (3.5mm, superheat: 40°C)

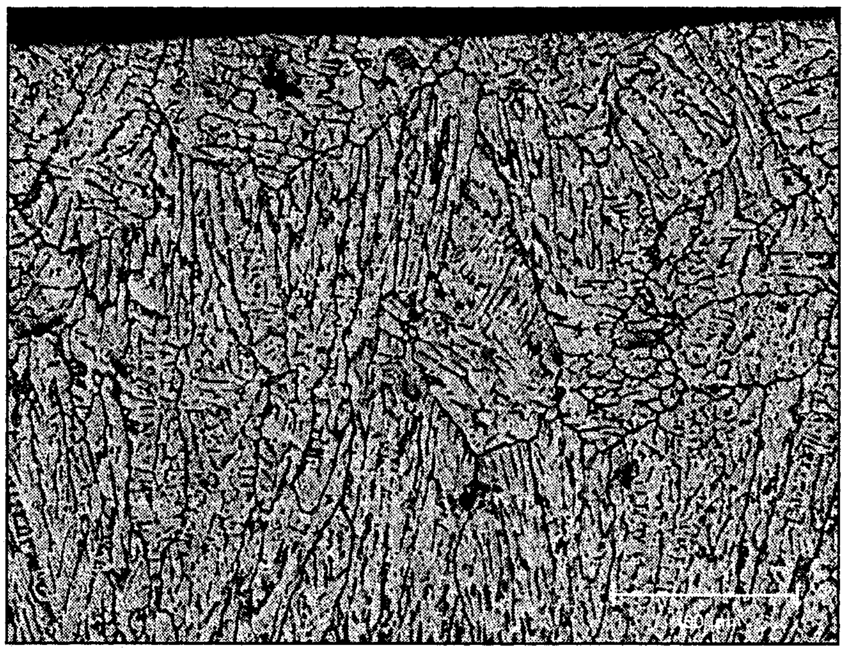

Fig. 5.5.16. Top region of strip cast on a steel substrate (3.5mm, superheat: 30°C)

To control and unify the variable grain size distributions observed, Al-5%Ti-1%B grain refiner was added. The addition ratio of grain refiner was 0.1 wt% of the melt and the holding time was 10 minutes. By adding grain refiner to the melt, numerous heterogeneous nuclei are dispersed and activated to nucleate grains during the solidification. Equiaxed grains achieved by grain refiner addition provide many benefits to a cast product. A fine grained, equiaxed microstructure ensures improved mechanical strength and reduced hot cracking in DC cast ingots. In addition, grain refiners improve feeding rates to regions of the casting approaching 100% solid, eliminating shrinkage porosities, and reducing a variety of surface defects.

Figs. 5.5.17 to 5.5.19 present microstructures of grain refined AA6111 alloy strip (3mm thick and 40°C superheat) cast on a copper substrate. Compared to the previous unrefined samples, it is clearly seen that microstructure attained a uniformity of grain distribution from the bottom to the top surface region. Grain size was about 140±20μm.

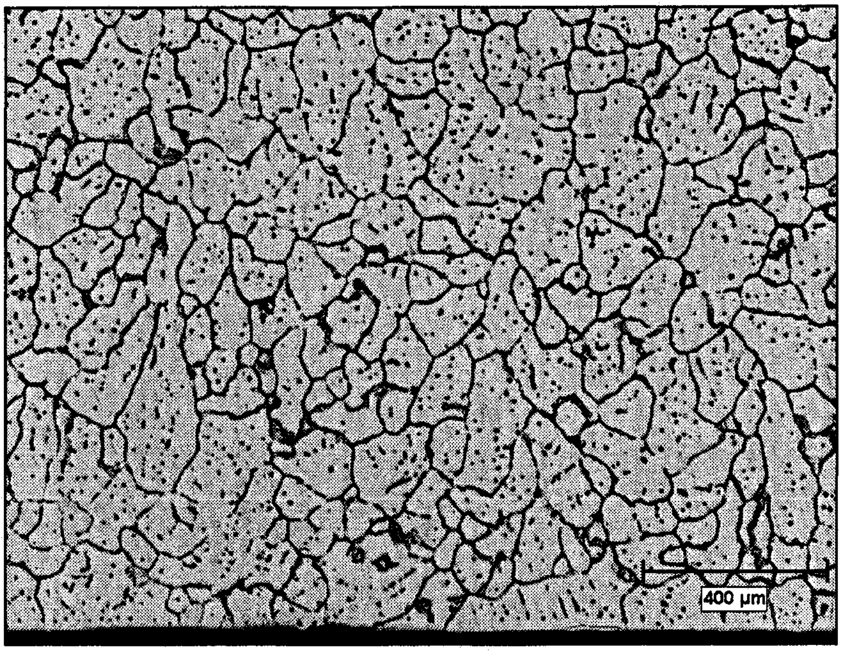

Fig. 5.5.17. Bottom region of grain refined AA6111 alloy strip cast on a copper substrate

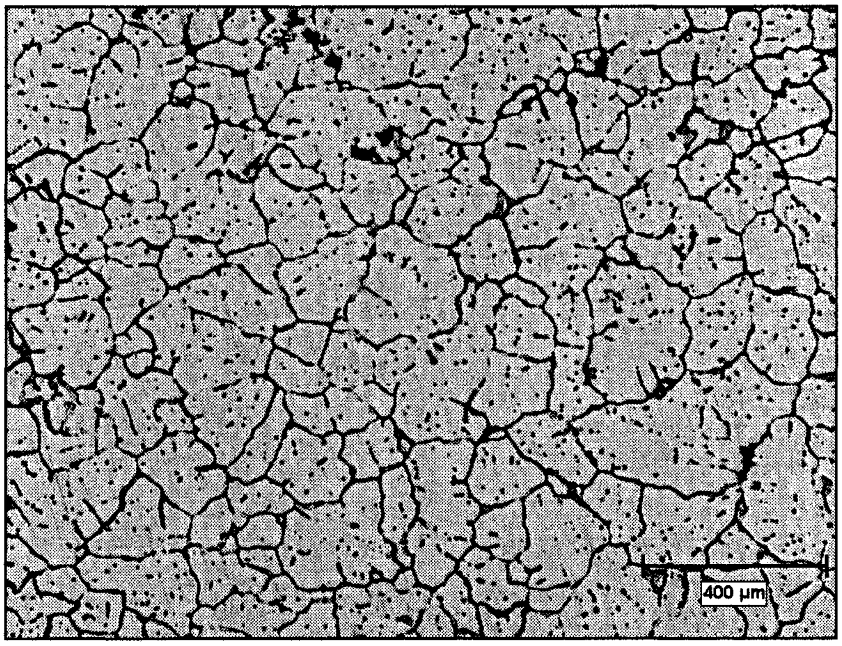

Fig. 5.5.18. Center region of grain refined AA6111 alloy strip cast on a copper substrate

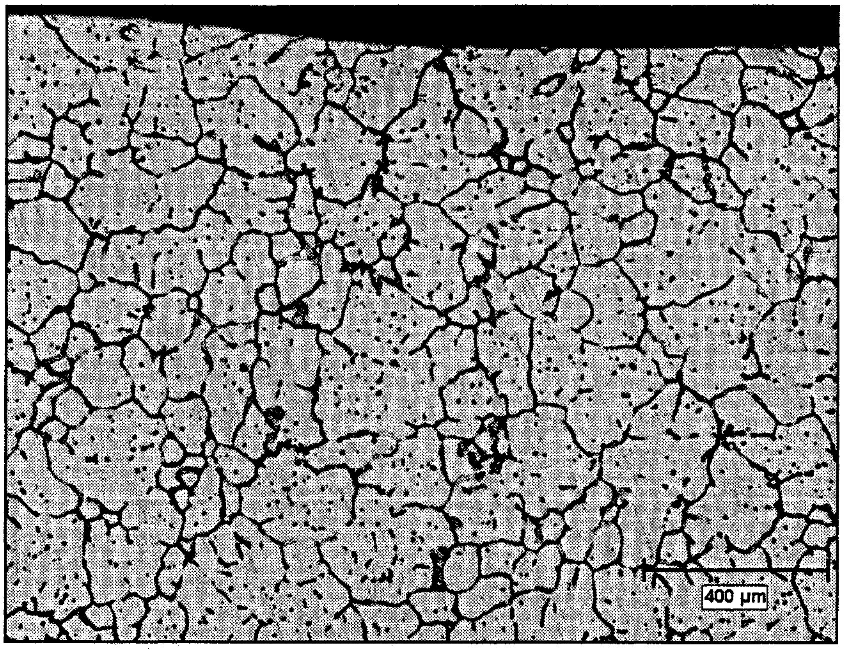

Fig. 5.5.19. Top region of grain refined AA6111 alloy strip cast on a copper substrate

5.5.6 Oil sprayed interface

To improve the bottom surface of the AA6111 strip, cooling PAM oil (mainly composed of oleic acid and linoleic acid) was sprayed on the second part of the copper substrate. Surprisingly, the bottom surface of the AA6111 strip cast on an oil sprayed mold substrate was improved remarkably, without any of the pitted regions forming. This is shown in Fig. 5.5.20.

Fig. 5.5.21 shows the effect of grain refiner and the effect of the PAM™ oil film on the interfacial heat flux when AA6111 alloys were cast on a copper substrate. Both experiments produced strips with a similar range of strip thickness, about 3mm, and a superheat of 30~55°C. The addition of grain refiner decreased the interfacial heat flux while the presence of an oil film on the mold surface increased the rate of heat transfer.

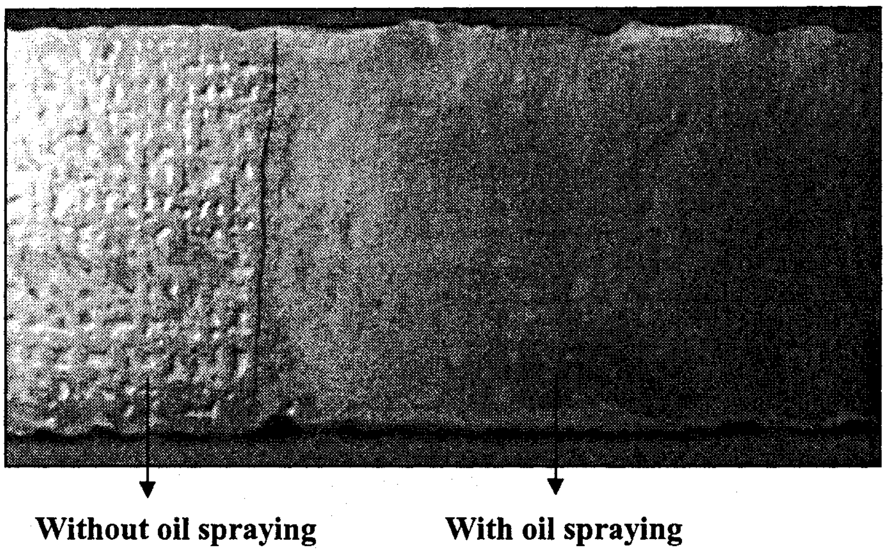

Fig. 5.5.20. Improved surface quality by oil spraying on the copper substrate

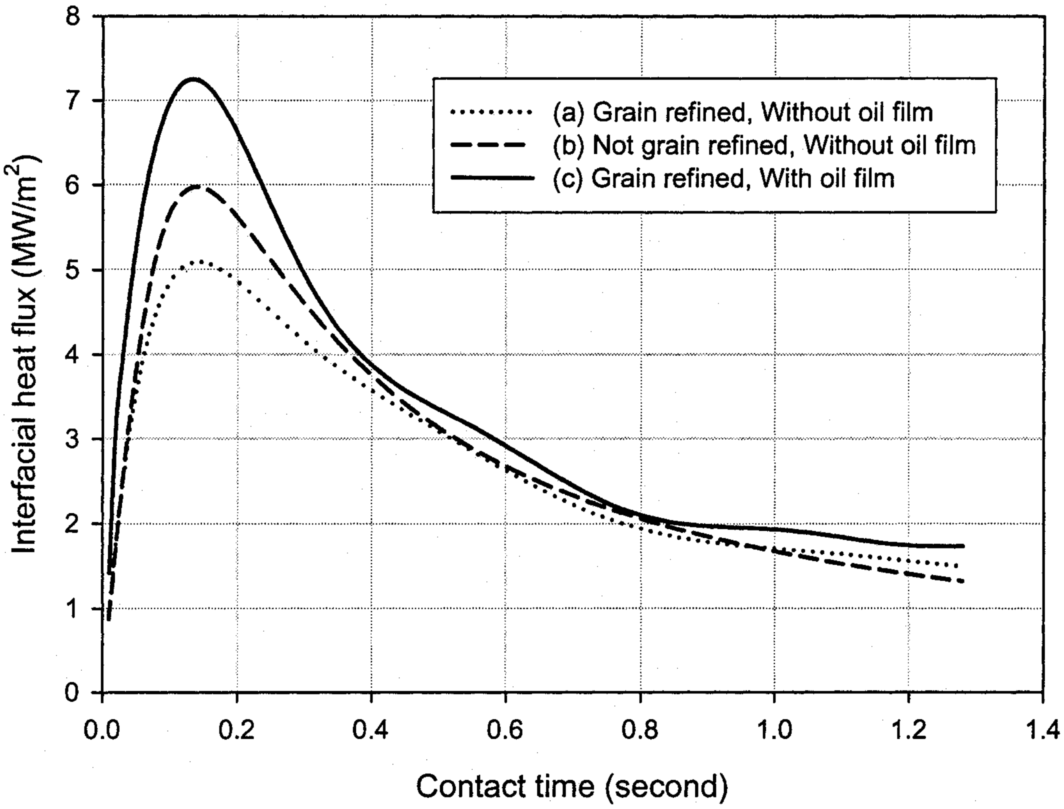

Fig. 5.5.21. Effect of grain refiner and oil film on the interfacial heat flux

It was known that the magnesium in aluminum acts as a surface active element and decreases the surface tension when added [10]. By the addition of grain refiner, the relative amount of magnesium dissolved in aluminum melt could decrease and resulted in the decrease in the interfacial heat flux as well as the increase in surface tension of the melt [11].

5.5.7 Conclusions

From the casting of AA6111 aluminum alloy on a single belt casting simulator, the following conclusions could be drawn

i) To increase the accuracy of the IHCP method, closer installation of thermocouple to the metal-mold interface was carried out. Moreover, the use of an exposed and wedged thermocouple improved the thermocouple response so that the correction of thermocouple data was not necessary.

ii) Strips of AA6111 alloy cast on copper and low carbon steel substrates revealed many shrinkage cavities on the strip surfaces, the cavities surface depressions on the bottom surface were reflected in equivalent depressions in the top surface of the casting.

iii) An increase in casting speed resulted in a decrease of strip thicknesses produced.

iv) The thinner strips recorded slightly higher values of the maximum heat fluxes and heat transfer coefficients but these values decayed faster compared to the thicker strips.

v) An increase in casting speeds worsened the quality of strips produced in terms of increased shrinkage areas.

vi) The spraying of PAM oil on the mold surface before casting remarkably improved the surface quality of strips and eliminated surface cavities, or depressions.

vii) The PAM oil sprayed mold substrates recorded increased values of interfacial heat fluxes of about 21%.

viii) The addition of grain refiner slightly decreased the value of interfacial heat flux (about 6%) but proved quite effective in producing a homogenized fine microstructure.

REFERENCES

1. http://www.cmit.csiro.au/news/viewpress.cfm/132

2. A. Ditze & K. Schwerdtfeger, Strip Casting of Magnesium with the Single-belt Process, *Scan. J. Metall.* **32**, 2003, pp.311-316

3. K. Schwerdtfeger, K. H. Spitzer, J. Kroos, P. Funke & K. H. Hower, Further Results from Strip Casting with the Single-Belt Process, *ISIJ International*, Vol. 40, 2000, pp.756-764

4. R. P. Tavares, M. Isac, F.G. Hamel & R.I.L. Guthrie, Instantaneous Interfacial Heat Fluxes during the 4 to 8 m/min Casting of Carbon Steels in a Twin-Roll Caster, *Metall. Mater. Trans.*, Vol. 32B, 2001, pp.55-67

5. M. S. Yoo, J. J. Kim, K. S. Shin and N. J. Kim, Effect of Second Phases on the High Temperature Mechanical Properties of Squeeze Cast Mg-Al Alloys, *Magnesium Technology 2002*, TMS, Seattle, USA, 2002, pp. 95-100

6. E. A. Payzant, S. R. Agnew, Q. Han and S. Viswanathan, $Mg_{17}Al_{12}$ Phase Precipitation Kinetics in Die Casting of AZ91 magnesium Alloy, *Magnesium Technology 2001*, TMS, New Orleans, USA, 2001, pp.183-187

7. X. G. Chen & J. Langlais, Solidification Behavior of AA6111 Automotive Alloy, *Mat. Sci. Forum*, Vol.331-337, 2000, pp.215-222

8. Thermo-Calc, Division of Physical Metallurgy, Royal Institute of Technology, Stockholm, Sweden, Copyright 1991

9. D. Li, J. S. Kim, M. Isac, R.I.L. Guthrie, Studies of Casting AA6111 Strip on Horizontal Continuous Casting Simulator, *MMPC 2004 Annual Meeting*, McGill, Montreal

10. G. Lang, Effect of added elements on the surface tension of high purity aluminum, Aluminum, vol. 50-1, 1974, pp.731-734

11. S. Leboeuf, Dynamic Wetting and Heat Transfer Behaviour of Aluminum Droplets Impinging and Solidifying on Copper Substrates, *M.Eng. Thesis*, McGill University, 2004

CHAPTER
6

DISCUSSION

6.1 INTERFACIAL HEAT FLUXES

Theoretically, when two bodies at different temperatures contact each other perfectly, the interfacial heat flux is infinite for the first moment of contact. Perfect contact corresponds to zero thermal resistance at the interface. If ideal perfect thermal contact between the hot metal and the cold mold were to be achieved, the interfacial heat flux would begin to drop off exponentially from a value of infinity at the moment of contact. However, in practice, many thermal resistances exist at the interface. These include thin films of trapped air, oxide layers, gaps generated by shrinkage of the solidifying shell from the interface, thermal expansion of the mold, unexpected chemical reactions, etc. These factors greatly decrease the value of heat flux and completely change actual interfacial flows of heat from those applying when perfect thermal contact is achieved. Localized heat flows through "reduced" areas of thermal contact between the melt and substrate result in a significant deviation from the condition of perfect contact. Numerous air pockets at the interface, together with the development of an air gap as the solidifying metal shrinks, greatly hinder the metal-mold heat transfer. This is shown schematically in Fig. 6.1.1. Moreover, in the case of the belt casting process, additional variables such as belt velocity, gas film entraiment, and liquid turbulence, make the problem even more complex.

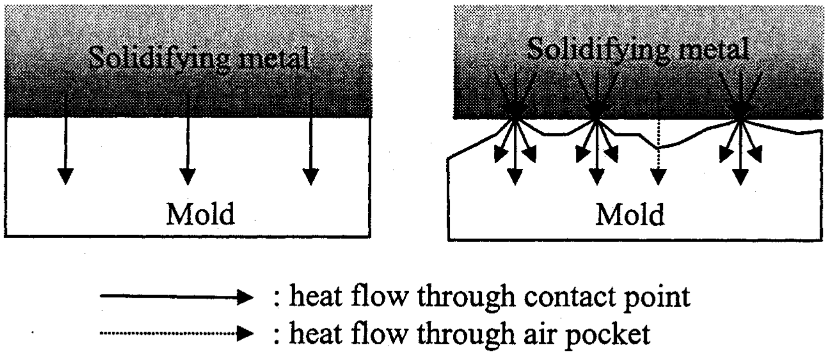

Fig. 6.1.1. Perfect (left) versus imperfect (right) metal-mold contact

6.1.1. Interfacial heat flux in imperfect metal-mold contact surface

From section 3.2.2. of chapter 3, when there is a thermal resistance such as an air gap, of thickness δ, between two semi-infinite bodies of metal and mold, two interface temperatures, T_{sM}* and T_{s0}*, can be defined and the interfacial heat flux can be obtained from equation (6.1.1).

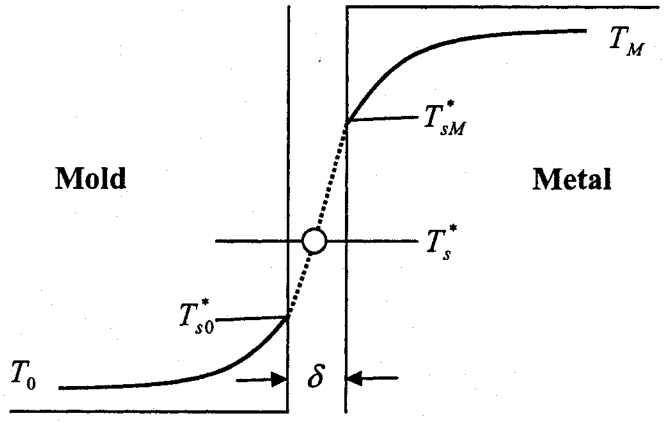

Fig. 6.1.2. Discontinuous temperature profile by the existence of thermal resistance of air gap thickness, δ, at the interface

$$q = h(T_{sM}^{*} - T_{s0}^{*}) \tag{6.1.1}$$

The interface temperature on the solidified metal side T_{sM}* and that on the mold side T_{s0}* can be obtained from equation (3.2.27) and are shown in equations (6.1.2) and (6.1.3).

$$\frac{T_{sM}^{*} - T_M}{T_s^{*} - T_M} = 1 - \exp\left[\frac{h_s^2}{k_s^2}\alpha_s t\right] \cdot erfc\left[\frac{h_s}{k_s}\sqrt{\alpha_s t}\right] \tag{6.1.2}$$

$$\frac{T_{s0}^{*} - T_0}{T_s^{*} - T_0} = 1 - \exp\left[\frac{h_m^2}{k_m^2}\alpha_m t\right] \cdot erfc\left[\frac{h_m}{k_m}\sqrt{\alpha_m t}\right] \tag{6.1.3}$$

From equations (3.2.18) and (3.2.19), it can be shown that the right hand side of equations (6.1.2) and (6.1.3) are identical because

$$\frac{h_s}{k_s}\sqrt{\alpha_s t} = \frac{h_s}{\varepsilon_s}\sqrt{t} = h\left(\frac{\varepsilon_s + \varepsilon_m}{\varepsilon_s \varepsilon_m}\right)\sqrt{t} = \frac{h_m}{\varepsilon_m}\sqrt{t} = \frac{h_m}{k_m}\sqrt{\alpha_m t} \tag{6.1.4}$$

Substitutions leads to the equation for the interfacial heat flux as:

$$\begin{aligned} q &= h(T_M - T_0) \cdot \left[\exp(u^2) \cdot erfc(u)\right] \\ &= \frac{T_M - T_0}{\sqrt{t}}\left(\frac{1}{1/\varepsilon_s + 1/\varepsilon_m}\right) \cdot \left[u \cdot \exp(u^2) \cdot erfc(u)\right] \end{aligned} \tag{6.1.5}$$

where $u = h\left(\frac{1}{\varepsilon_s} + \frac{1}{\varepsilon_m}\right)\sqrt{t}$. Note that, from the equation (6.1.5), the interfacial heat flux q is a function of initial temperatures and heat diffusivities of cast metal and mold, as well as the interfacial heat transfer coefficient h.

It can be shown that a large value of u gives [1]

$$\exp(u^2) \cdot erfc(u) \approx \frac{1}{\sqrt{\pi}}\left(\frac{1}{u} - \frac{1}{2u^3} + \frac{3}{4u^5} - \cdots\right) \tag{6.1.6}$$

As the thermal resistance (*1/h*) reduces to zero (i.e. $h \rightarrow \infty$), the value of $u \cdot \exp(u^2) \cdot erfc(u)$ in equation (6.1.5) converges to $\frac{1}{\sqrt{\pi}}$ and it comes to equation (6.1.7). The plot of $u \cdot \exp(u^2) \cdot erfc(u)$ vs u is plotted in Fig. 6.1.3.

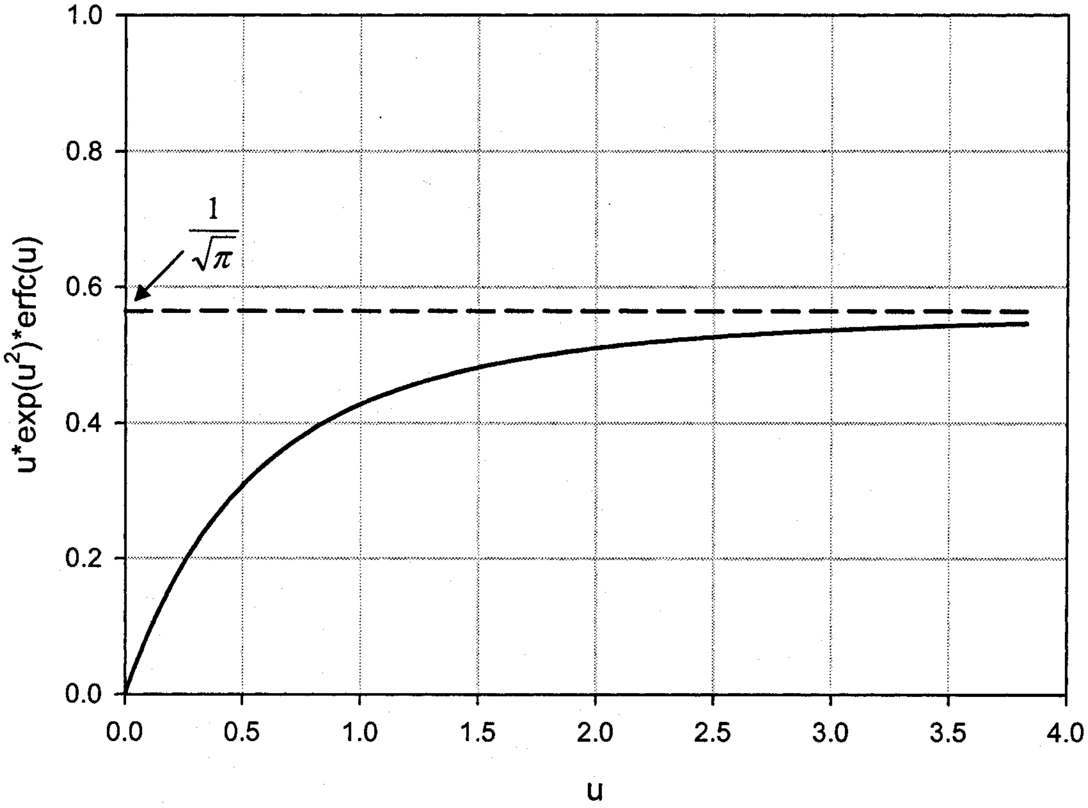

Fig. 6.1.3. Variation of $u \cdot \exp(u^2) \cdot erfc(u)$ with u

$$q\big|_{x=0} = \frac{1}{\sqrt{\pi t}}(T_M - T_0)\left(\frac{1}{1/\varepsilon_s + 1/\varepsilon_m}\right) \tag{6.1.7}$$

and this is identical to equation (3.2.17). It shows that the heat is transferred under condition of perfect contact, once u reaches about 4.

If the thermal resistance (*1/h*) originates from an air gap with the thickness of $\delta\,(x)$ and thermal conductivity of k_g, the interfacial heat transfer coefficient h is

$$h(x) = \frac{k_g}{\delta(x)} \tag{6.1.8}$$

6.1.2. Time dependence of interfacial heat flux

If the interfacial heat transfer coefficient h is not a function of time as shown in equation (6.1.8), the interfacial heat flux q does not have a value of infinity at time zero except x=0 (singular point). Equation (6.1.5) shows that the maximum heat flux is obtained at time zero but its value is finite and equal to $h(T_M - T_0)$. However, it begins to decrease as time of contact increases. The variation of $\exp(u^2)\cdot erfc(u)$ with u is plotted in Fig. 6.1.4, where $u = h\left(\frac{1}{\varepsilon_s} + \frac{1}{\varepsilon_m}\right)\sqrt{t}$.

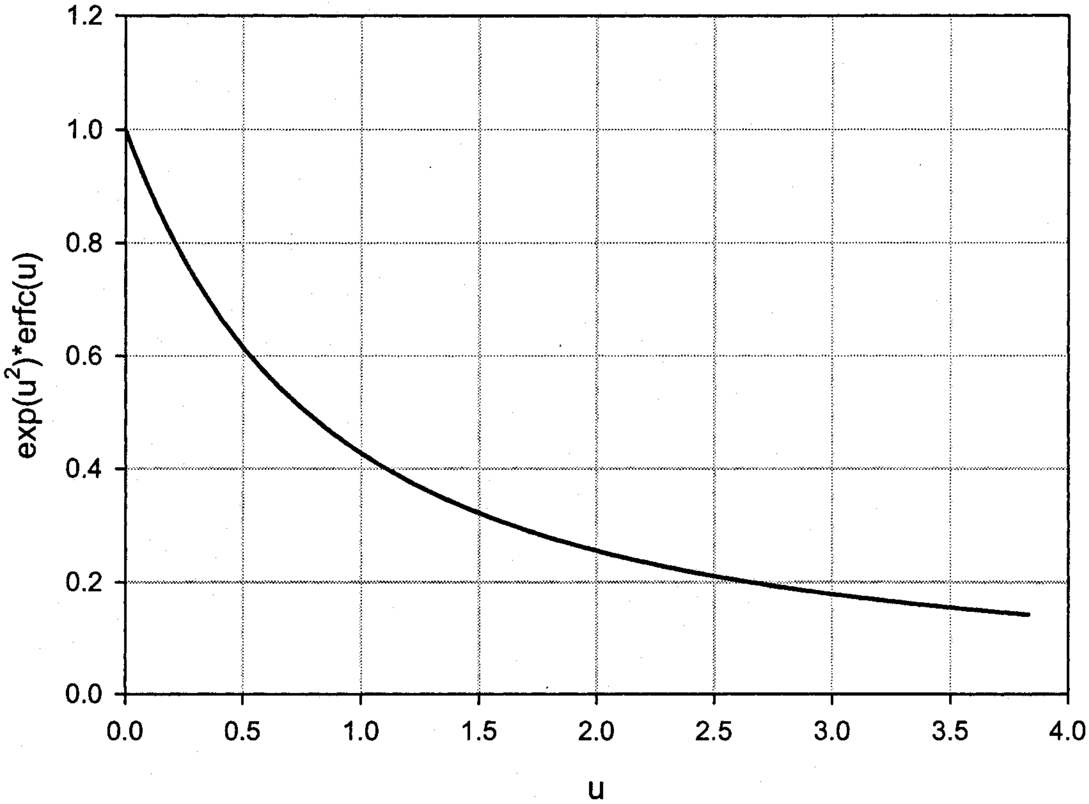

Fig. 6.1.4. Variation of $\exp(u^2)\cdot erfc(u)$ with u

6.1.3. Interface roughness and melt sag

As described previously, in real metal-mold interfaces, localized heat flows through real contact points between the metal and mold occur and result in a significant deviation from ideal perfect contact. This real non-flat interface is the most influential cause of thermal resistance at the interface. The scale of non-flat interface can be quantified by the roughness at the interface. The definition of the average roughness R_a is shown in Fig. 6.1.5. In addition, Fig. 6.1.6 shows the simplified saw-tooth shaped contact surface. In this diagram, the roughness (R_a) of the mold is $\lambda/4$.

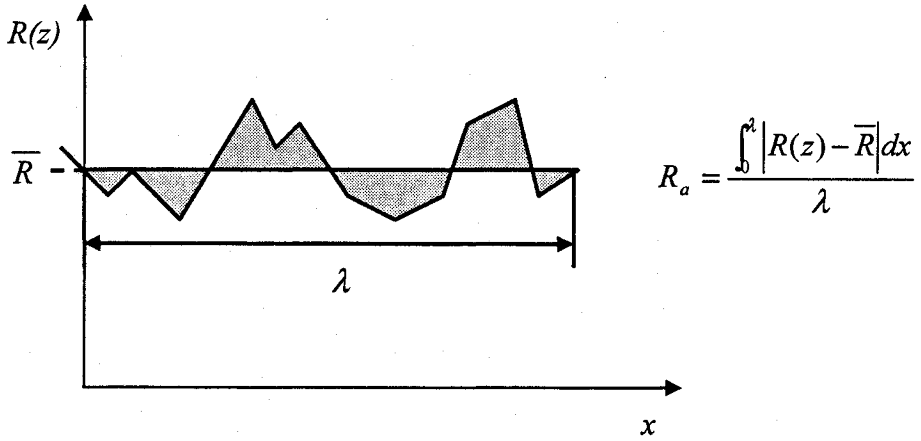

$$R_a = \frac{\int_0^\lambda \left|R(z)-\bar{R}\right| dx}{\lambda}$$

Fig. 6.1.5. Definition of average surface roughness R_a ($\bar{R}$ is an average line)

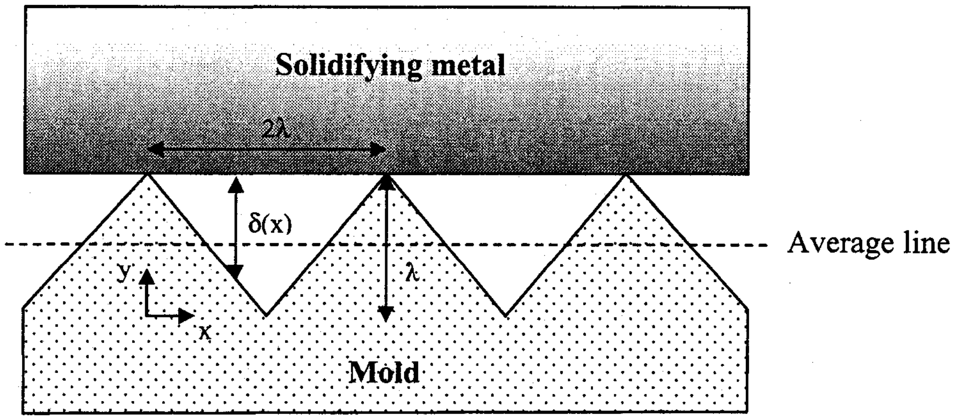

Fig. 6.1.6. Saw-tooth shaped metal-mold contact surface

From Fig. 6.1.6, when the melt hangs between two parallel-running peaks with distance 2λ apart, the melt sag (d_{sag}) depends on the melt surface tension (σ) and its metallostatic pressure (ΔP), in the case of a non-wetting substrate. The radius of melt curvature R is

$$R = \frac{\sigma}{\Delta P} = \frac{\sigma}{\rho g h} \tag{6.1.9}$$

where σ is the melt surface tension, ρ is the melt density, g is the gravity constant, and h is the melt height. As illustrated in Fig. 6.1.7, the melt sag can be calculated as

$$d_{sag} = R - \sqrt{R^2 - \lambda^2} \tag{6.1.10}$$

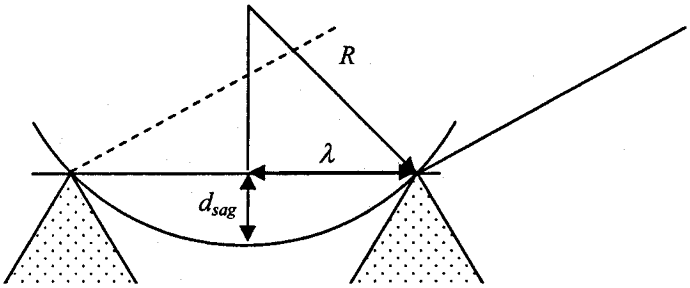

Fig. 6.1.7. Radius of curvature and melt sag

As an example, when an aluminum, magnesium, and carbon steel melt is poured on the rough mold surface with λ=100μm, the values of melt sag d_{sag} (μm) for various strip thicknesses, h, are summarized in Table 6.1.1. It shows that melt sag is almost negligible and that a flat surface of solidifying metal at the interface should be expected as shown in Fig. 6.1.6.

Table 6.1.1. Melt sag (μm) of aluminum and magnesium with various metal heads

Melt	*h=1mm*	h=5mm	h=10mm	h=50mm
Aluminum ($\sigma = 0.914 N/m$) [2]	0.13	0.63	1.3	6.3
Magnesium ($\sigma = 0.57 N/m$)	0.15	0.75	1.5	7.5
Carbon steel ($\sigma = 1.70 N/m$)	0.23	1.15	2.3	11.5

6.1.4. Interfacial heat flux in saw-tooth shaped contact surface

In the saw-tooth shaped interface of Fig. 6.1.6, the heat flux is a periodic function and its local value is governed by the thickness of the air gap $\delta(x)$. The variation of heat fluxes with different mold roughnesses is shown in Figs. 6.1.9 and 6.1.10. Table 6.1.2 shows the thermophysical properties of cast metals (pure aluminum and magnesium) and mold (copper and low carbon steel) used in this calculation. The thermal conductivity of the air was taken to be 0.05 W/mK.

Table 6.1.2. Thermophysical properties of metals (Al, Mg) and molds (Cu, steel)

Properties	Al	Mg	Cu	Steel
Initial temperature (C)	660	650	25	25
Specific heat (J/KgK)	1090	1017	380	430
Density (Kg/m^3)	2370	1740	8920	7860
Thermal conductivity (W/mK)	211	150	398	79.6
Latent heat (KJ/Kg)	398	362	203	277
Heat diffusivity (J/m^{2}Ks$^{1/2}$)	23346.87	16292.24	36729.56	16402.20

As discussed in chapter 3, the interfacial heat flux is affected by the harmonic mean of heat diffusivities in cast metal and cooling mold. Table 6.1.3 shows the harmonic mean of each metal and mold combination. $(HM)_{\varepsilon_s,\varepsilon_m} = \dfrac{2}{1/\varepsilon_s + 1/\varepsilon_m}$.

Table 6.1.3. Harmonic mean of metal (Al, Mg) and mold (Cu, steel) heat diffusivities

Metal-mold	Al-Cu	Al-Steel	Mg-Cu	Mg-Steel
$(HM)_{\varepsilon_s,\varepsilon_m}$	28547.64	19267.87	22572.10	16347.04

From Table 6.1.3, one can expect that the rate of metal-mold heat transfer in the Al-Cu system is the highest, while Mg-steel is the lowest as the heat flux is proportional to the harmonic mean of these heat diffusivities.

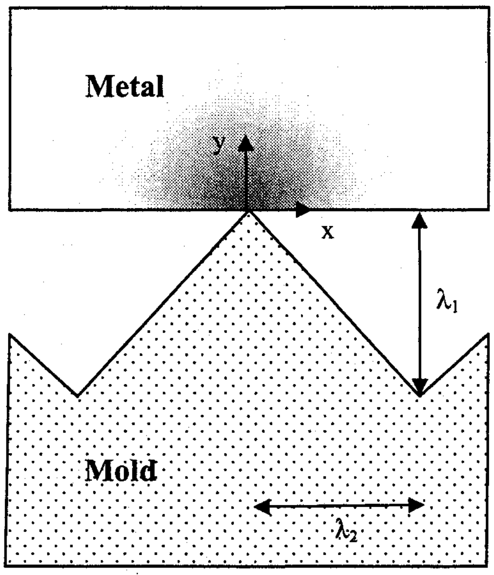

Fig. 6.1.8. Coordinate of saw-tooth shaped interface

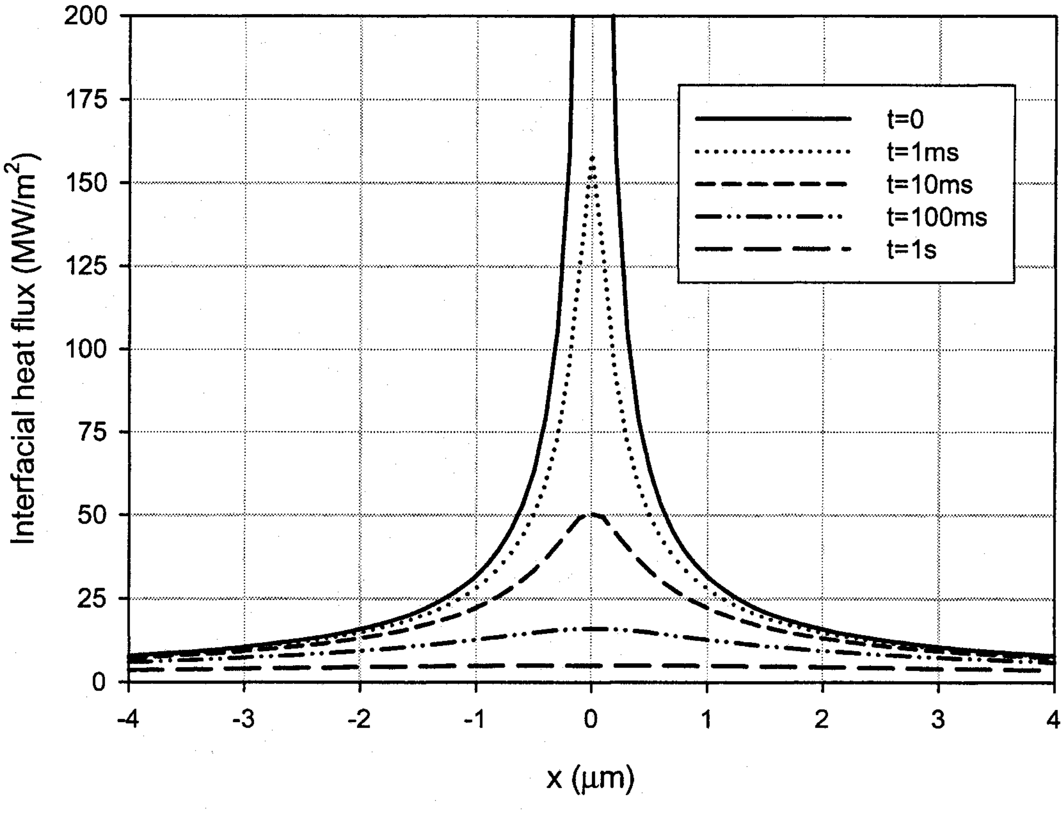

Fig. 6.1.9. Heat flux profile on saw-tooth shaped interface between Al melt and Cu mold (λ_1=λ_2=4μm, R_a=1μm)

Fig. 6.1.9 shows that, at the contact point (*x=0*), heat flux is the highest and decreases rapidly as the air gap increases up to the valley in mold surface. The deepest air gap thickness (4μm) exhibits the lowest value of heat flux. During the initial stage of heat transfer, because of the localized periodic heat flows, the heat transfer is two dimensional. Simultaneously, the heat is transferred in the downward and horizontal x directions from $x=0$ plane to $x=\pm\lambda$ planes. After about 1 second, the heat is nearly transferred unidirectionally downward.

Fig. 6.1.10 presents the calculation of heat flux with increased roughnesses R_a of 5μm. The increase in mold roughnesses results in a decrease in the rate of heat transfer because of the enlarged fraction of air pockets at the interface.

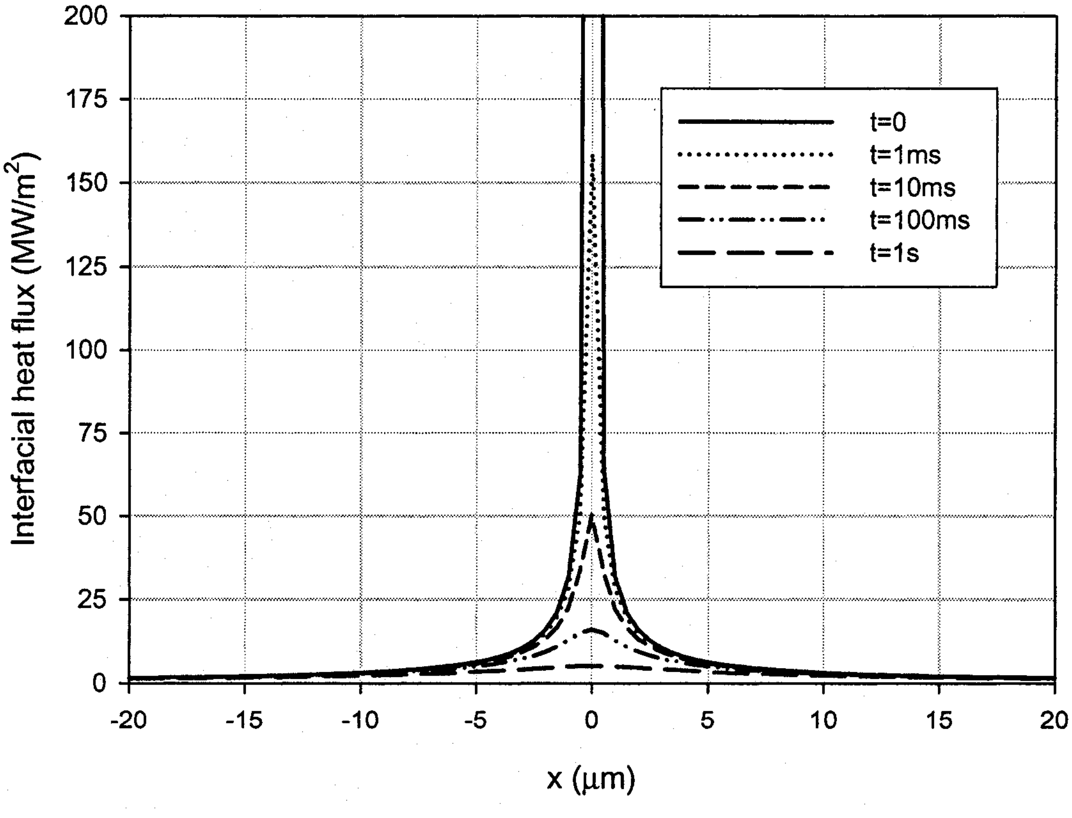

Fig. 6.1.10. Heat flux profile on saw-tooth shaped interface between Al melt and Cu mold ($\lambda_1=\lambda_2=20\mu m$, $R_a=5\mu m$)

In the laboratory, the interfacial heat flux measured is close to an average value of heat fluxes. Usually, the dimensions of the thermocouple (e.g. thermocouple diameter) embedded to measure the temperature history in mold is much bigger than the scale of mold roughness. Also, high heat fluxes at the peaks beneath the contact points are rapidly transferred to x-directions. i.e. laterally. Thus, it is meaningful to investigate and calculate the average interfacial heat flux, defined as

$$\bar{q} = \frac{\int_0^{\lambda_2} q(x)\,dx}{\lambda_2} \tag{6.1.11}$$

where λ_2 is the distance between the peak and the valley in the mold surface.

Substitution of equation (6.1.5) into (6.1.11) and change of variable reduces

$$\bar{q} = \frac{k_g(T_M - T_0)}{\lambda_2}\int_{u^*}^{\infty}\frac{1}{u}\exp(u^2)\,erfc(u)\,du \tag{6.1.12}$$

where $u^* = \frac{k_g}{\lambda_1}\left(\frac{1}{\varepsilon_s} + \frac{1}{\varepsilon_m}\right)\sqrt{t}$. Integration of the right hand side of (6.1.12) needs a numerical calculation. At time zero, because of the infinite value of heat flux at $x=0$, the average interfacial heat flux does not exist (improper integral) such as

$$\begin{aligned} \bar{q}\Big|_{t=0} &= \frac{\int_0^{\lambda_2} h(T_M - T_0)\,dx}{\lambda_2} = \frac{1}{\lambda_2}\int_0^{\lambda_2}\left(\frac{k_g}{(\lambda_1/\lambda_2)x}\right)(T_M - T_0)\,dx \\ &= \frac{k_g(T_M - T_0)}{\lambda_1}\int_0^{\lambda_2}\frac{dx}{x} = \frac{k_g(T_M - T_0)}{\lambda_1}\ln x\Big|_0^{\lambda_2} \to \infty \end{aligned} \tag{6.1.13}$$

The effect of mold roughness on the average interfacial heat flux $\bar{q}$ is plotted in Fig. 6.1.11. An increase in mold roughness is predicted to greatly reduce the average interfacial heat flux, especially in the initial stages of contact, and leads to a significant deviation from the condition of perfect contact.

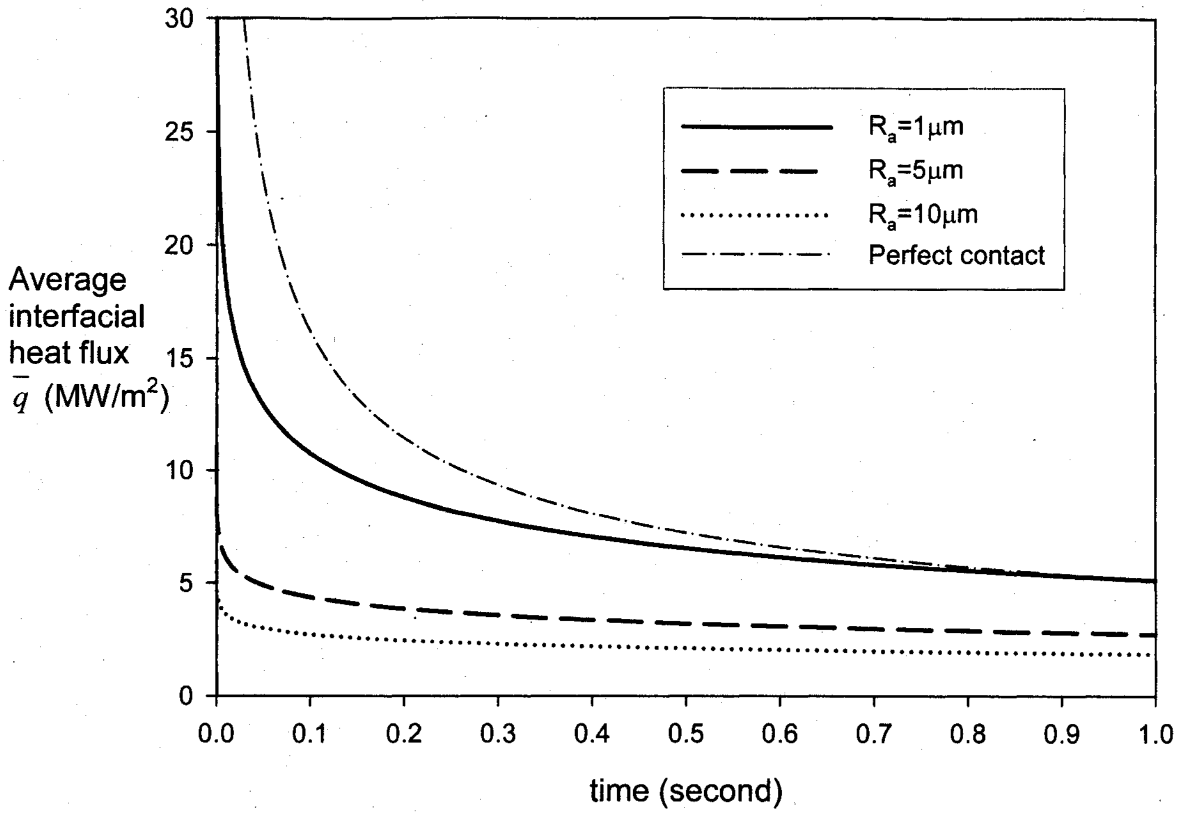

Fig. 6.1.11. Average interfacial heat flux vs time for different roughnesses between Al melt and Cu mold ($\lambda_1=\lambda_2$)

Even though the same roughness R_a can be assigned from the definition of Fig. 6.1.5 and Fig. 6.1.8, quite different morphology of surfaces can appear. Note that the surface roughness R_a is a function of λ_1 only from Fig. 6.1.8.

$$R_a = \frac{2\times(\frac{1}{2}\times\frac{\lambda_1}{2}\times\frac{\lambda_2}{2})}{\lambda_2} = \frac{\lambda_1}{4} \tag{6.1.14}$$

The following Fig. 6.1.12 reveals a very different surface morphology with the same roughness. These metal-mold interfaces result in different values of the average interfacial heat fluxes as shown in Fig. 6.1.13. The increase in the ratio of λ_1 / λ_2 produces the increased rate of interfacial heat flux. Therefore, the increase in peak density (Pc) of mold surface enhances the rate of heat transfer.

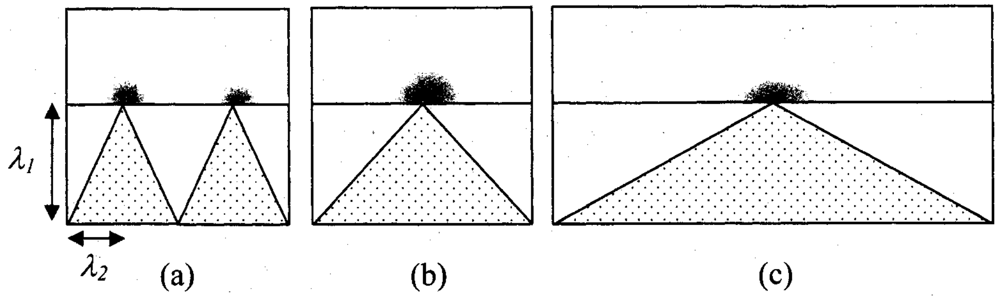

Fig. 6.1.12. Different surface morphology for the same roughness value (a) λ_1: λ_2= 2, (b) λ_1: λ_2= 1, (c) λ_1: λ_2= 1/2

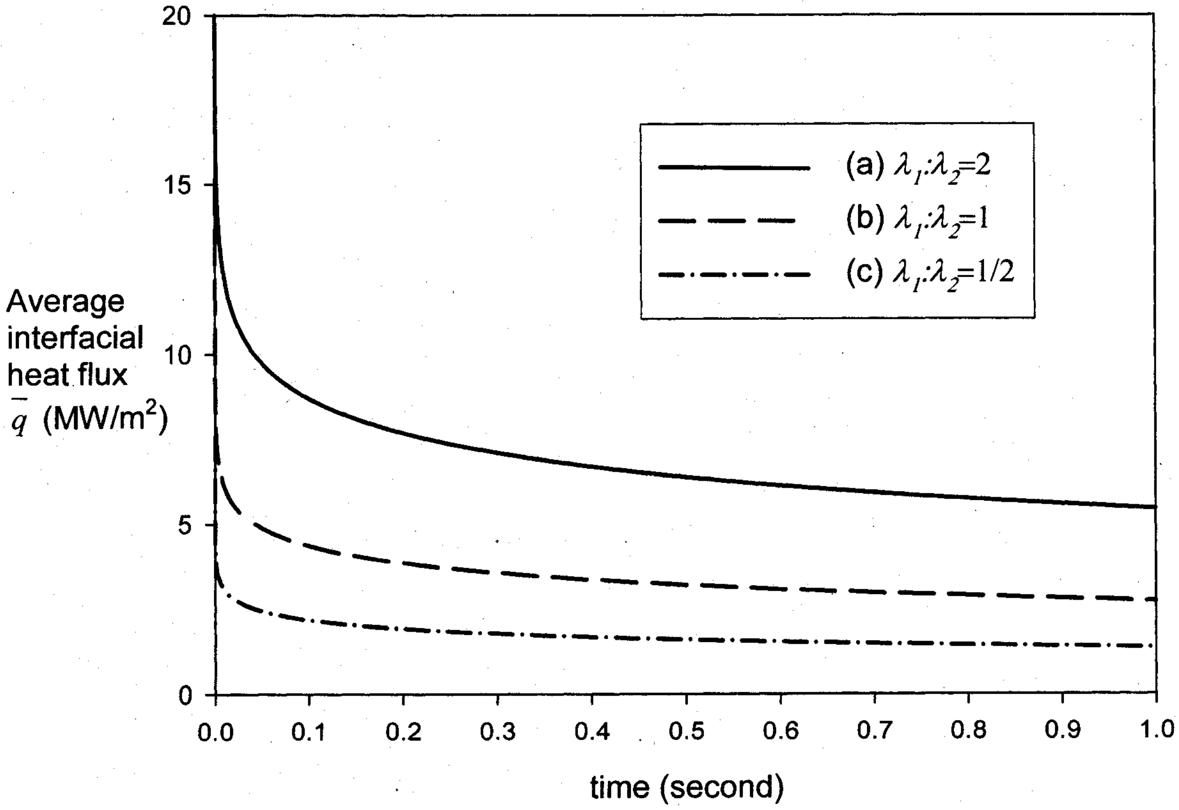

Fig. 6.1.13. Average interfacial heat flux vs time for Al-Cu system with different λ_1/λ_2 ratios (R_a=5μm)

Interfacial heat fluxes of different metal-mold systems are illustrated in Fig. 6.1.14 and Fig. 6.1.15. The mold surface roughness is fixed as 5μm and 10μm with the ration of $\lambda_1 / \lambda_2=1$. Because of the highest value of harmonic mean of heat diffusivities, the Al-Cu system exhibited the highest heat flux, while Mg-steel was the lowest.

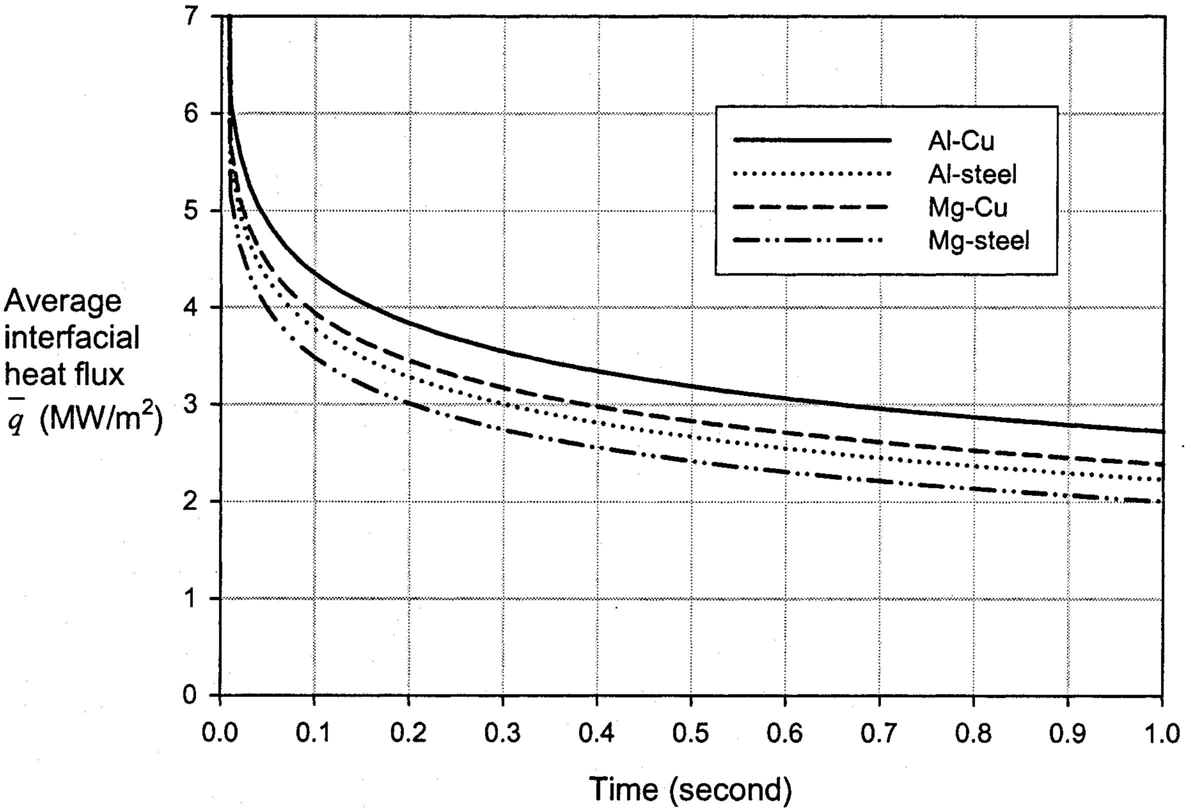

Fig. 6.1.14. Average interfacial heat flux vs time with different metal-mold systems ($\lambda_1=\lambda_2$, R_a=5μm)

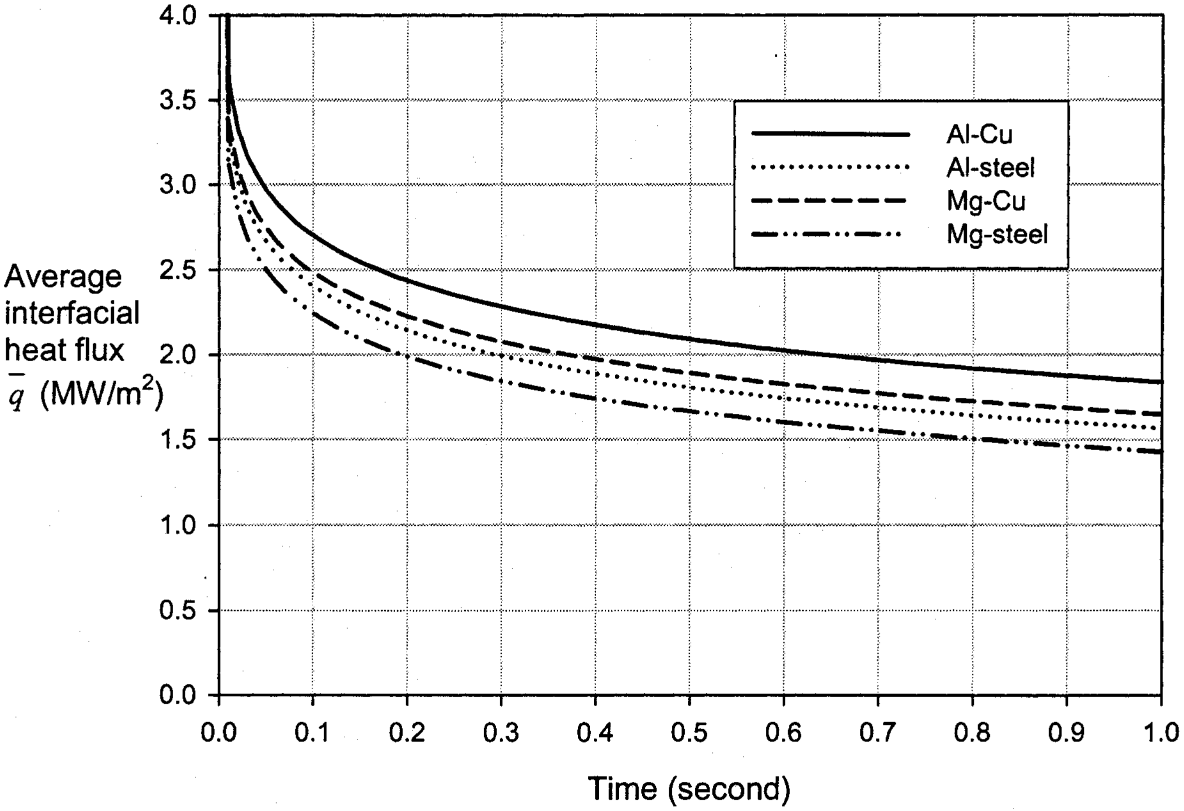

Fig. 6.1.15. Average interfacial heat flux vs time with different metal-mold systems (λ_1=λ_2, R_a=10μm)

6.1.5. Growth of solidified shell front

When the solidification of cast metals occurs, the release of latent heat is evolved at the solidification front. At y=*M* of solidifying shell front from Fig. 6.1.8, the heat flux at this front should be equivalent to the (average) interfacial heat flux $\bar{q}$ in equation (6.1.12).

$$\begin{aligned} q\big|_{y=M} &= \rho_s \Delta H_s \frac{dM}{dt} = q\big|_{y=0} = \bar{q} \\ &= \frac{k_g (T_M - T_0)}{\lambda_2} \int_{u^*}^{\infty} \frac{1}{u} \exp(u^2) erfc(u)\, du \end{aligned} \tag{6.1.15}$$

where ρ_s is the density of the solidifying metal, ΔH_s is a latent heat, *M* is the solidified shell thickness, and $u^* = \frac{k_g}{\lambda_1}\left(1/\varepsilon_s + 1/\varepsilon_m \right)\sqrt{t}$. From equation (6.1.15), it can be seen that the growth rate of solidified shell front, $\frac{dM}{dt}$, is directly proportional to the interfacial heat flux $\bar{q}$. Time integration of equation (6.1.15) is required to find the value of the solidified shell thickness *M* as

$$M = \frac{1}{\rho_s \Delta H_s} \int_0^t \bar{q}\ dt \tag{6.1.16}$$

Based on equation (6.1.16), the integration of Fig. 6.1.14 and 6.1.15 can be carried out. i.e. the area under the curve of heat flux versus time, divided by $\rho_s \Delta H_s$, gives the solidified shell thickness as a function of time. Calculated results for various metal-mold systems are shown in Fig. 6.1.16 and 6.1.17. Note that, although the values of interfacial heat flux of Al-Cu was the highest, the Mg-Cu system predicted the fastest growth rate of solidified shell thickness thanks to the lower density of magnesium (1740 kg/m^3) compared to that of aluminum (2370 kg/m^3).

To reach the solidified shell thickness of 3mm from Fig. 6.1.16, it was predicted to take 0.53 seconds in the Mg-Cu system. On the other hand, for the Al-steel system, it took

0.96 seconds when the mold roughness was fixed at 5 μm. The effect of increased mold roughness to 10 μm appears in Fig. 6.1.17. The increase in mold roughness predicted longer times for shell growth because of decreased values of the interfacial heat fluxes.

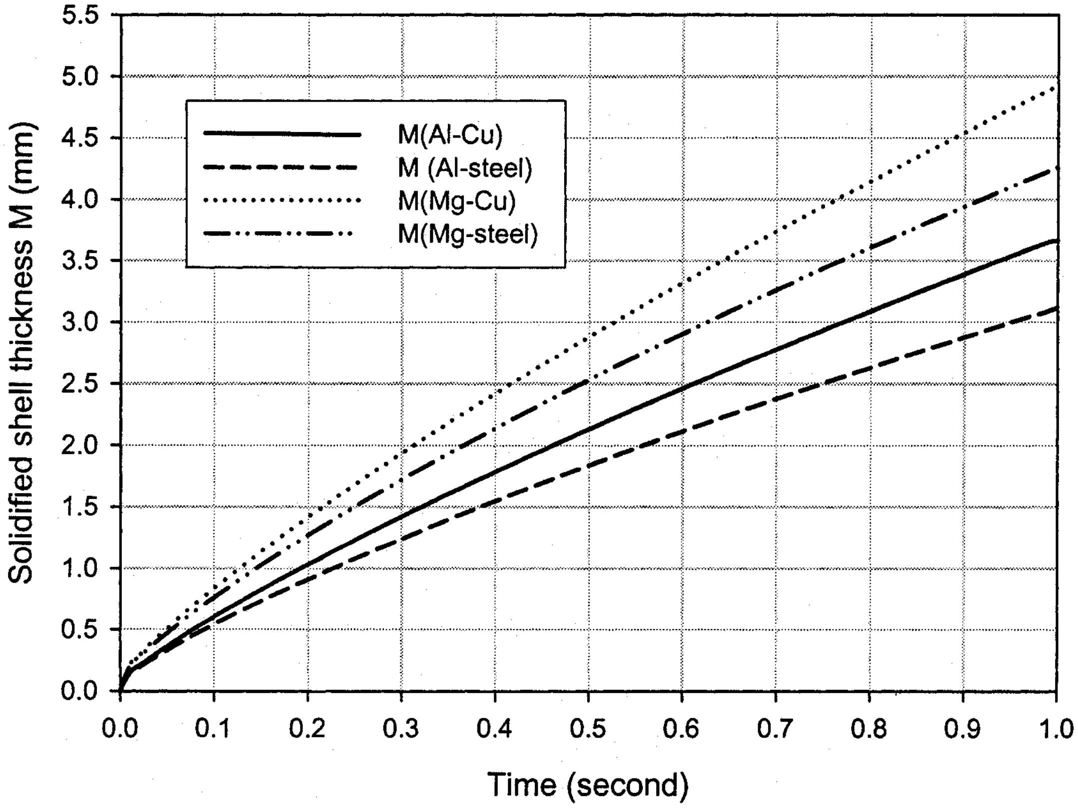

Fig. 6.1.16. Predicted solidified shell thickness vs time with different metal-mold systems ($\lambda_1=\lambda_2$, R_a=5μm)

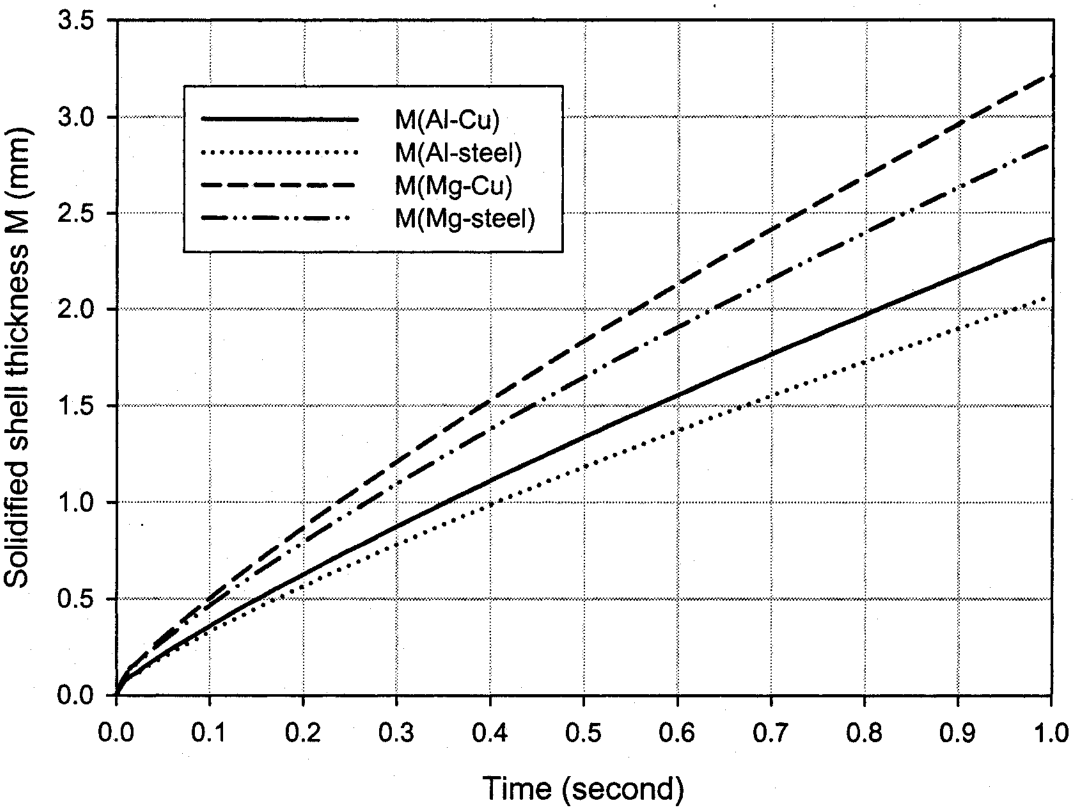

Fig. 6.1.17. Predicted solidified shell thickness vs time with different metal-mold systems ($\lambda_1=\lambda_2$, R_a=10μm)

6.2 MODELLING OF INTERFACIAL HEAT FLUXES

As seen from Fig. 5.4.4, the interfacial heat flux curve increases from a certain value of heat flux q_i to its maximum q_M and decays with time of contact. To simulate this behavior of an interfacial heat flux, the following assumptions are made:

i) From time zero to the time of attaining the maximum heat flux (t_P), the interfacial heat flux increases in a parabolic behavior.

ii) At $t = t_P$, the liquid metal comes into contact with the saw-tooth shaped rough mold surface.

iii) After time t_P, the heat transfer through points of direct contact between the metal and mold takes place. However, owing to shrinkage of the solidified skin at the contact points, the number density of the contact points decrease.

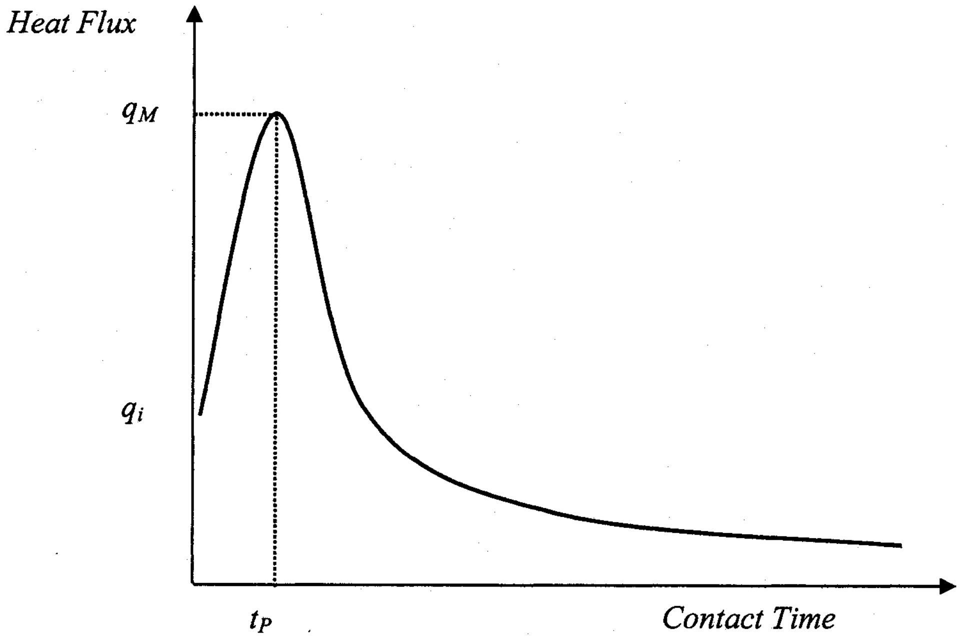

Fig. 5.4.4. Shape of an interfacial heat flux curve

The interfacial heat flux reaches its maximum at $t = t_P$ when the metal-mold contact is fully established. The time t_P depends on the wettability between the liquid metal and mold material so that it is determined empirically. The maximum heat flux at $t = t_P$ depends on the roughness of the mold and on the physicochemical properties of the cast metal and mold substrate. After $t > t_P$, the shrinkage takes place at the direct contact points and the number of these contacts points decrease as shown in Fig. 6.2.1.

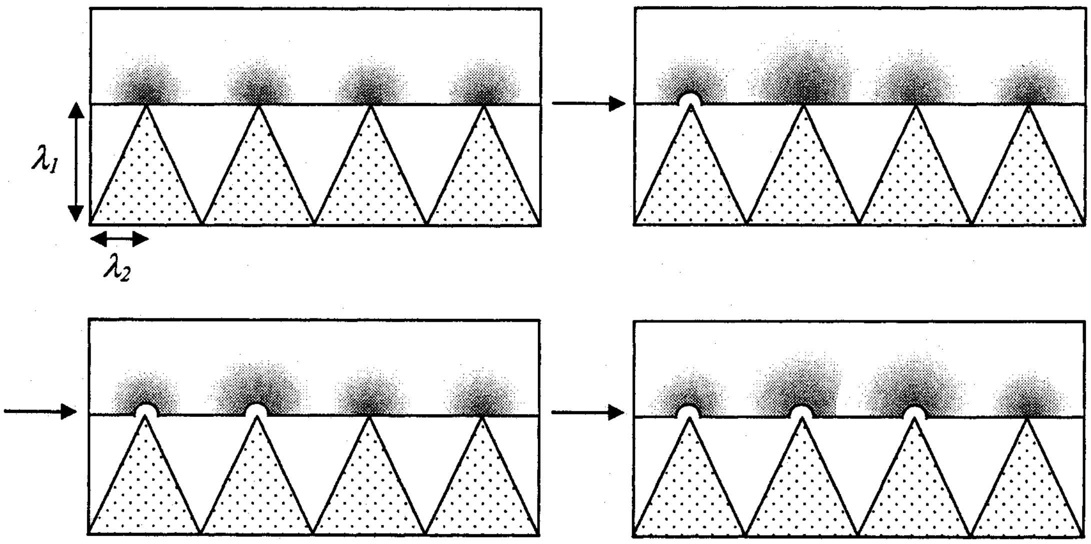

Fig. 6.2.1. Shrinkage at the point of direct contact

Because of the shrinkage of solidified skin and the take-off from the direct contact, in contact point, the direct metal-mold heat transfer does not occur any longer. As shown in Fig. 6.2.2, this implies the increase of λ_2. Note that the volume of air pockets is same between (a) and (b).

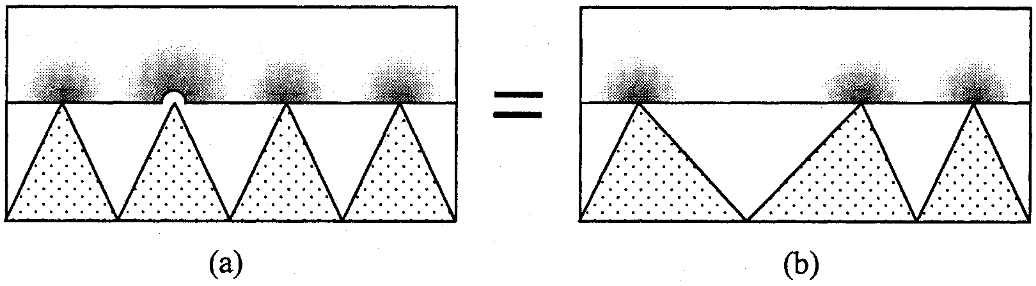
(a) (b)

Fig. 6.2.2. Equivalent surface morphology in shrinkage at the point of direct contact

As a worked example, AZ91 alloy with different superheats cast on a copper substrate was investigated in Fig. 6.2.3. The increase in superheat increased the value of interfacial heat flux. The increase in melt superheat may improve the fluidity of the melt which, in turn, would enhance wettability between the melt and the contacting mold. A copper substrate was used as the mold material and its roughness was about 4 μm (sand blasted). The maximum heat fluxes were observed about 130 mille-seconds following the moment of contact.

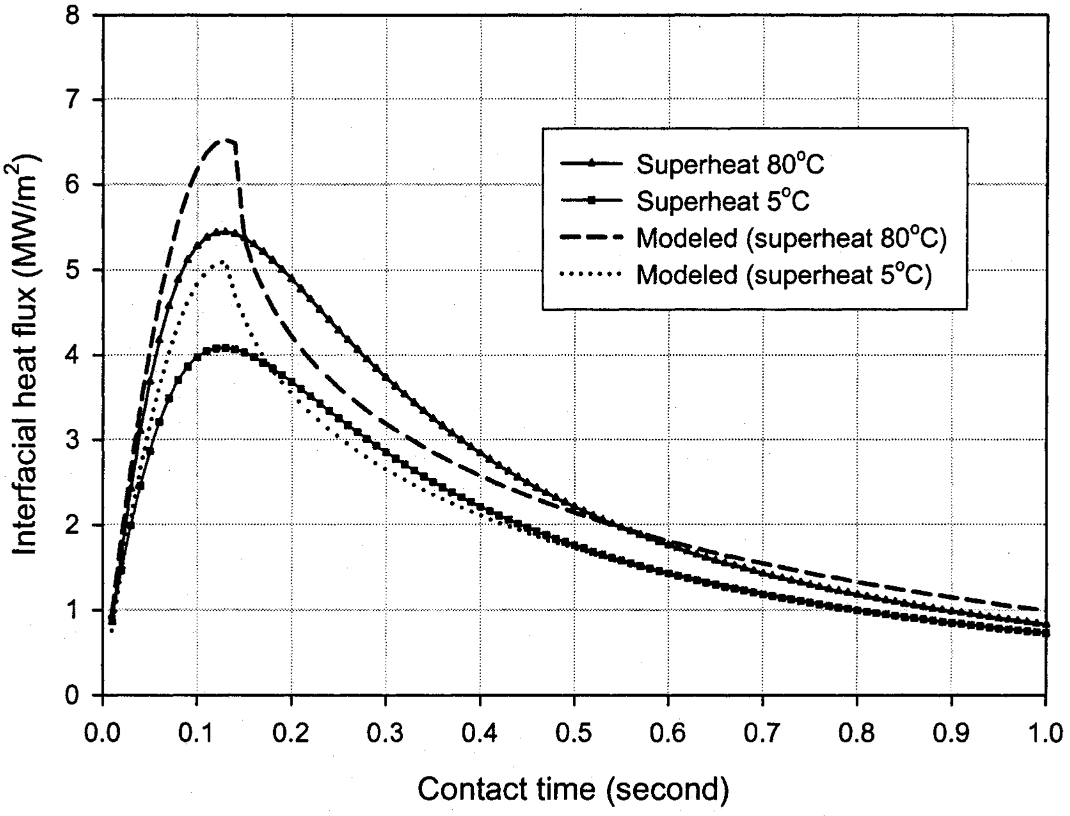

Fig. 6.2.3. Measured and modeled interfacial heat fluxes of AZ91 3mm strips cast on a copper substrate with different superheats (casting speed: 0.8m/s)

As seen, the model overestimated the maximum heat flux by 1 MW/m^2 more but the time average heat fluxes , $\widetilde{q}$, were very similar. The time average heat flux is defined below. It presents the average interfacial heat flux during the solidification of strips.

$$\tilde{q} = \frac{\int_0^{t_f} q\,dt}{t_f} \tag{6.2.1}$$

where t_f is the time taken to reach a complete solidification.

A 3mm AZ 91 magnesium strip with superheat 80°C, $\tilde{q}$ (measured) = 2.55 MW/m^2 and $\tilde{q}$ (modeled) = 2.53 MW/m^2. In the case of superheat 5°C, $\tilde{q}$ (measured) = 2.00 MW/m^2 and $\tilde{q}$ (modeled) = 2.03 MW/m^2.

6.3 EFFECT OF EXPERIMENTAL VARIABLES

6.3.1. Overall heat balance

When a liquid metal is fed onto the cooling mold, heat is lost simultaneously from the top surface to the atmosphere, and from the bottom surface by the mold substrate. The heat transfer from the upper surface is by radiation and natural convection, and that from the bottom surface is by transient state of conduction below the cast metal, together with convective and radiative transfer into the air pockets trapped. Then, the total heat loss necessary for complete solidification is a direct function of the superheat and the latent heat of the fusion.

$$\Delta Q_t = \rho \cdot d\{C_P(T_C - T_L) + \Delta H\} \tag{6.3.1}$$

where ρ is the density of liquid metal, d is the strip thickness, C_p is the specific heat, T_C is the casting temperature, T_L is the liquidus, and ΔH is the latent heat of fusion. Note that $\rho \cdot d\{C_P(T_C - T_L)$ is the sensible heat and $\rho \cdot d \cdot \Delta H$ is the latent heat component.

A heat balance relates the total heat loss necessary to complete solidification with the heat loss to the air by radiation ΔQ_r, and to the solid by conduction ΔQ_c. The heat loss due to radiation from the upper strip surface can be described by the equation:

$$\Delta Q_r = \int_0^{\tau} q_r dt \text{ where } q_r = \varepsilon\sigma(T_{Top}^4 - T_{air}^4) \quad (6.3.2)$$

where ε is the emissivity, σ is the Stefan Boltzmann constant (5.6703×10^{-8} W/m^{2}K^4), T_{Top} is a top surface temperature of the strip, and T_{air} is a temperature of atmosphere.

Heat loss by conduction is

$$\Delta Q_c = \int_0^{\tau} q_c dt \text{ where } q_c = -k\left.\frac{\partial T(x,t)}{\partial x}\right|_{x=0} \quad (6.3.3)$$

Therefore, substitution of the expressions for ΔQ_t, ΔQ_r, and ΔQ_c into the heat balance equation yields a formula from which the total time to complete solidification, τ, can be calculated.

$$\rho\cdot d\{C_P(T_C - T_M) + \Delta H\} = \varepsilon\sigma T_M^4 \cdot \tau - \int_0^{\tau} k\left.\frac{\partial T(x,t)}{\partial x}\right|_{x=0} dt \quad (6.3.4)$$

Here, heat loss by radiation is negligible by two orders of magnitude in the case of aluminum or magnesium castings (less than 1%).

6.3.2 Effect of superheat

As seen from chapter 6.3.1, the area under the curve of interfacial heat flux vs contact time represents the total energy absorbed at the interface. This area is balanced with the heat loss of superheat and latent heat release to give the final solidification time. The time integration of Fig.5.4.5 appears in Fig. 6.3.1.

From the heat balance equation (6.3.4) and Fig. 6.3.1, 2.56 MJ/m^2 of thermal energy should be dissipated in 3mm AZ91 strip with 80°C superheat. On the other hand, 1.98 MJ/m^2 is needed for 5°C superheat. This gives the final solidification time of 1.01 seconds and 0.97 seconds respectively. This implies that, even though the higher interfacial heat flux was observed at higher superheat, the final solidification time was almost same. Note that the integrated thermal energy contains the sensible heat term and that a larger superheat delays the start of solidification. With 80°C superheat, the solidification starts at 0.16 seconds, while it starts at 0.003 seconds for 5°C superheat.

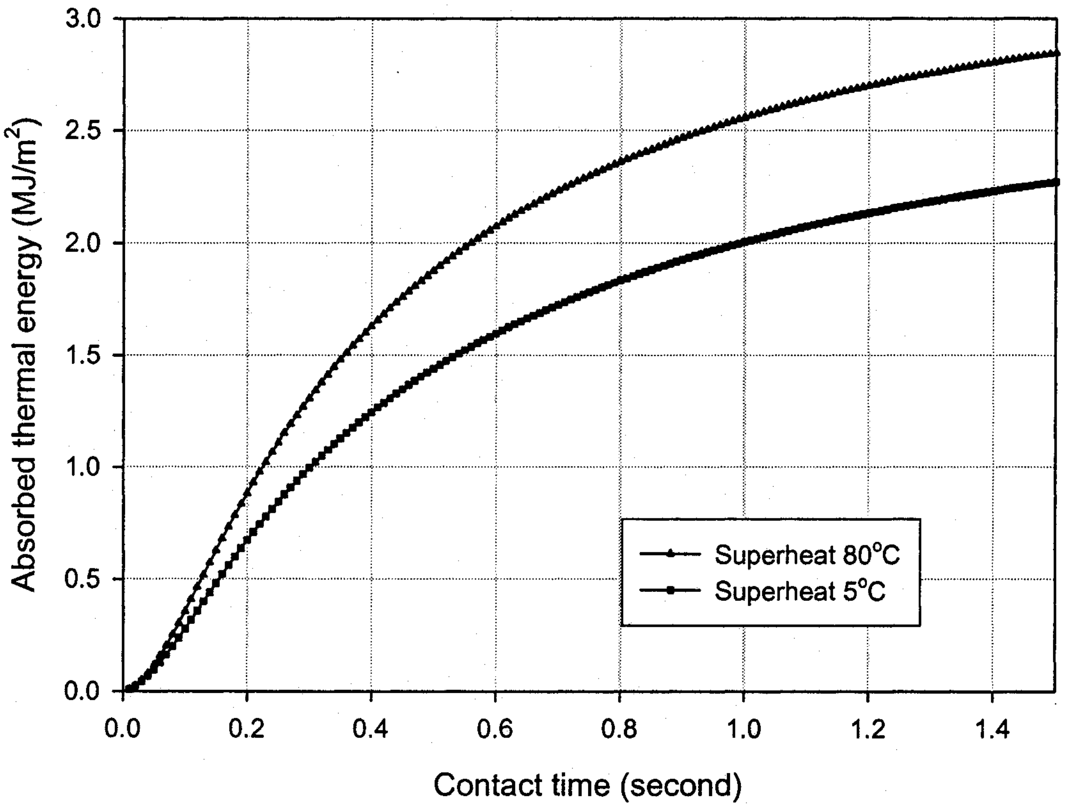

Fig. 6.3.1. Absorbed thermal energy of 3mm thick, AZ91 strips, cast on a copper substrate with different superheats

6.3.3 Effect of substrate material

Absorbed thermal energy with different mold materials in AZ91 casting is plotted in Fig. 6.3.2. Table 6.3.1 shows the time average interfacial heat flux and the solidification time obtained from Fig. 6.3.2 by heat balance.

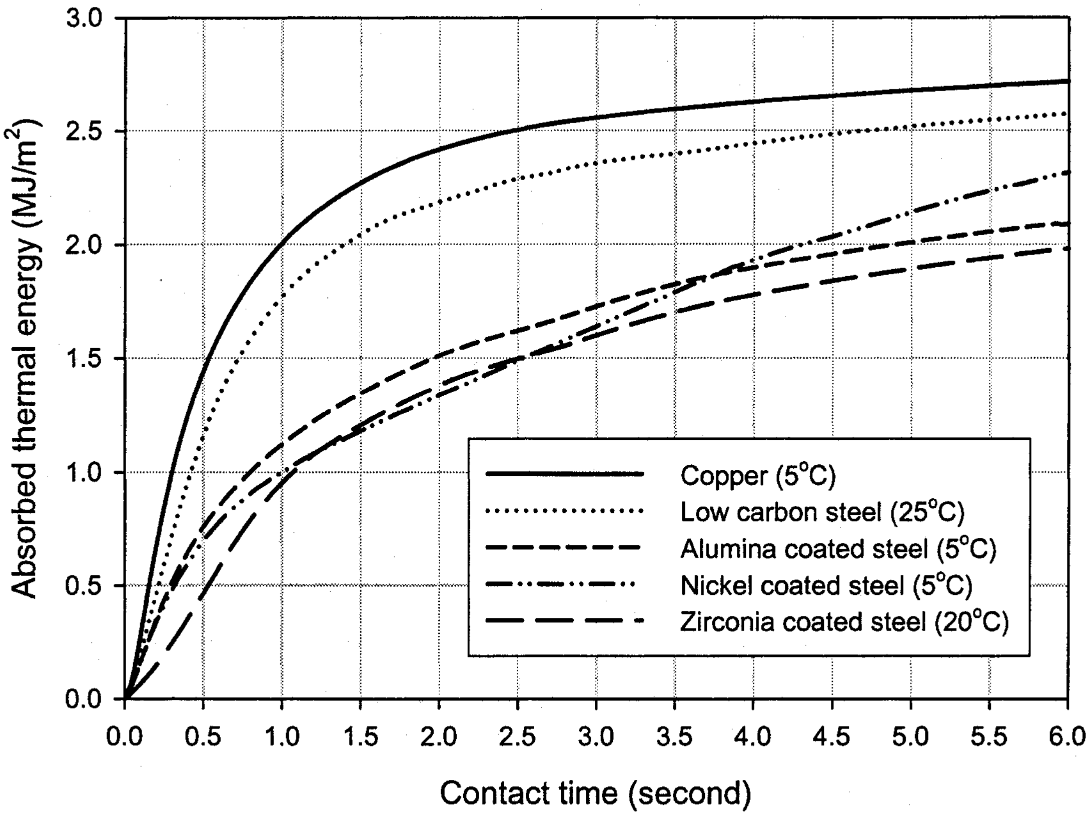

Fig. 6.3.2. Absorbed thermal energy of 3mm thick, AZ91 strips, cast on different mold substrates

Table 6.3.1. Time average interfacial heat fluxes and cooling rates for casting 3mm AZ91 strips

Substrate	t_f (second)	$\tilde{q}$ (MW/m^2)	Cooling rate (°C/s)
Copper	0.97	2.04	162.9
Low carbon steel	1.65	1.22	95.8
Alumina coated steel	4.73	0.42	33.4
Nickel coated steel	4.23	0.47	37.4
Zirconia coated steel	5.9	0.34	26.8

Similarly, for AM50 alloy, Fig. 6.3.3 shows the thermal energy absorbed into the substrate. Table 6.3.2 presents the time average interfacial heat fluxes as well as their cooling rates.

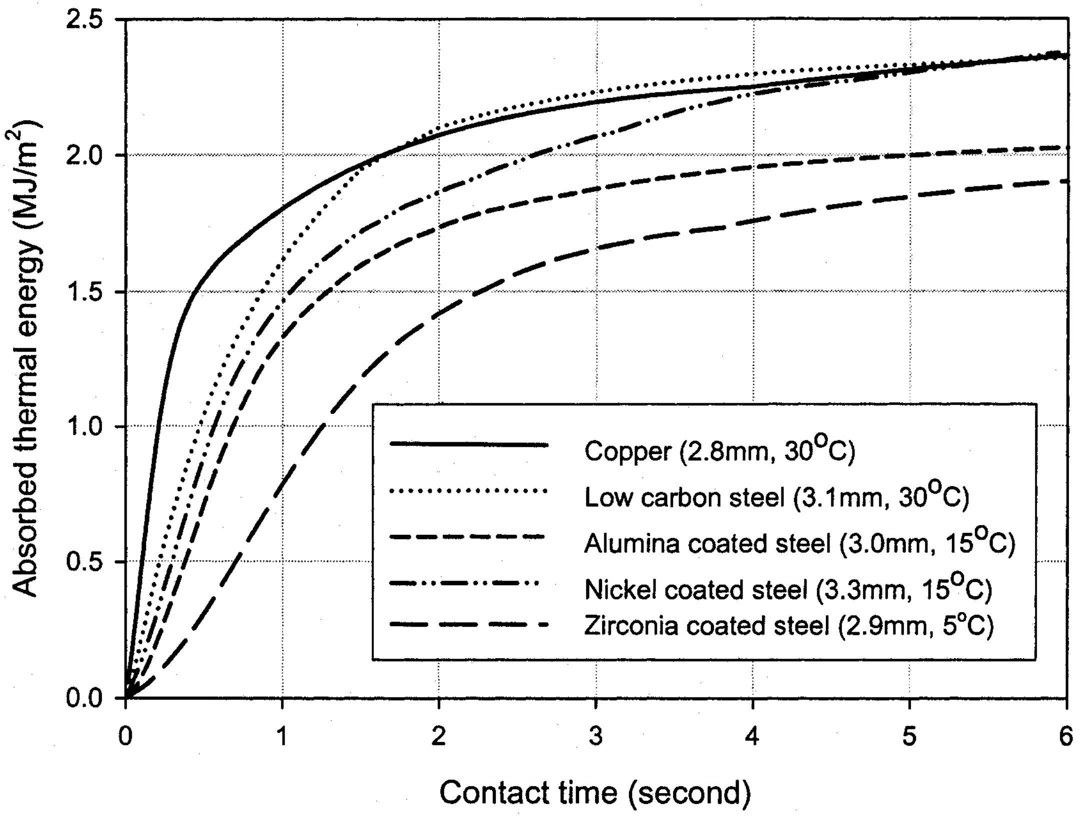

Fig. 6.3.3. Absorbed thermal energy of AM50 strips cast on different mold substrates

Table 6.3.2. Time average interfacial heat fluxes and cooling rates for casting AM50 strips

Substrate	t_f (second)	$\tilde{q}$ (MW/m^2)	Cooling rate (°C/s)
Copper	1.69	1.19	109.3
Low carbon steel	2.64	0.82	69.9
Alumina coated steel	6.16	0.33	30.1
Nickel coated steel	3.93	0.56	47.1
Zirconia coated steel	8.86	0.23	20.9

Compared to AZ91 alloy, lower values of the time average interfacial heat fluxes were the result of AM50's lower density and lower latent heat. Also, this average heat flux is sensitive to the thicknesses of strips. The increased strip thickness in nickel coated substrate resulted in the increase in the value of average heat flux. Note that even though the final solidification time, t_f, can be calculated from the heat balance, the temperature field in solidifying strip can be obtained by enthalpy method as shown in chapter 5.4.3.

Casting of magnesium alloys AZ91 and AM50 resulted in different levels of interdendritic porosity. According to Schaffer *et al.*[3], an increase in the freezing range, defined as the temperature difference between the liquidus and the solidus, increases the interdendritic porosity of magnesium alloys. The porosity of magnesium alloys obtained from density measurements of their cast product versus aluminum content is shown in Fig. 6.3.4. Previous to that work, Whittenberger and Rhines [4] had reported that porosity increased linearly with aluminum content up to the maximum freezing range for a 13 wt% aluminum alloy content. Zhang *et al.*[5] also reported a porosity level of 0.6% in a permanent mold casting using AZ91 and 1.7% in a die casting. In this experiment of AZ91 strip, the porosity level was about 1.1%.

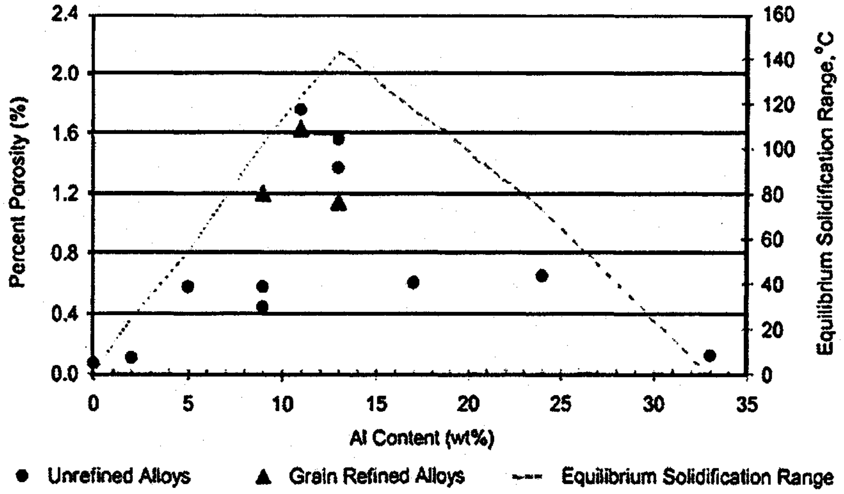

Fig. 6.3.4. Porosity vs. aluminum content (superheat: 70 °C) [3]

As prescribed, various mold substrates engender different cooling rates and subsequent microstructures. Based on the equation suggested by Feurer *et al.*[6] and the data of Grandfield *et al.*[7], there exists a relationship between the measured values of the SDAS and cooling rates experienced according to:

$$\lambda = 4.31(M \cdot t_f)^{1/3} \tag{6.3.5}$$

$$\text{where } M = -\frac{\Gamma \cdot D \cdot ln(C_L^m / C_0)}{m(1-k)(C_L^m - C_0)} \quad \text{and} \quad t_f = \frac{T_e}{\dot{T}} \tag{6.3.6}$$

In AZ91 magnesium alloy, λ is the SDAS (m), Γ is the Gibbs-Thompson coefficient (3.7×10^{-7} °C·m), D is the diffusivity of Al in Mg (2.7×10^{-9} m^2/s), C_0 is the starting composition (9%), C_L^m is the ending composition (25.7%), m is the slope of liquidus (-7.5°C/%Al), k is the distribution coefficient (0.35), t_f is the local solidification time, T_e is the temperature difference between the liquidus (595°C) and the eutectic temperature (437°C), and $\dot{T}$ is the cooling rate (°C/s). Substitution gives:

$$\lambda = 54.6 \cdot \dot{T}^{-1/3} \tag{6.3.7}$$

where λ is the measured SDAS (μm) and $\dot{T}$ is the theoretically "calculated" cooling rate (°C/s).

An alternative empirical relation between the cooling rate and the SDAS can be established from various articles in the literature [8-14]. These results derive from data associated with plaster molding, permanent molding, die casting, centrifugal atomization and laser remelting experiments. This relationship was found to apply over cooling rates through the mushy zone varying from 10^{-1} to 10^{6} °C/s.

$$\lambda = 39.8 \cdot \tau^{-0.32} \tag{6.3.8}$$

where λ is the measured SDAS (μm) and τ is the empirically "estimated" cooling rate (°C/s).

Fig. 6.3.5 shows the result of the SDAS versus the estimated cooling rates in the current work of AZ91 strip casting as well as the previous works by other researchers. Based on twin roll casting experiments, Allen *et al.*[15] measured corresponding SDAS values of AZ91 ranging from 7 to 9μm. This range coincides very well with values of the SDAS cast on low carbon steel and copper substrates in this work as shown in Fig. 6.3.5.

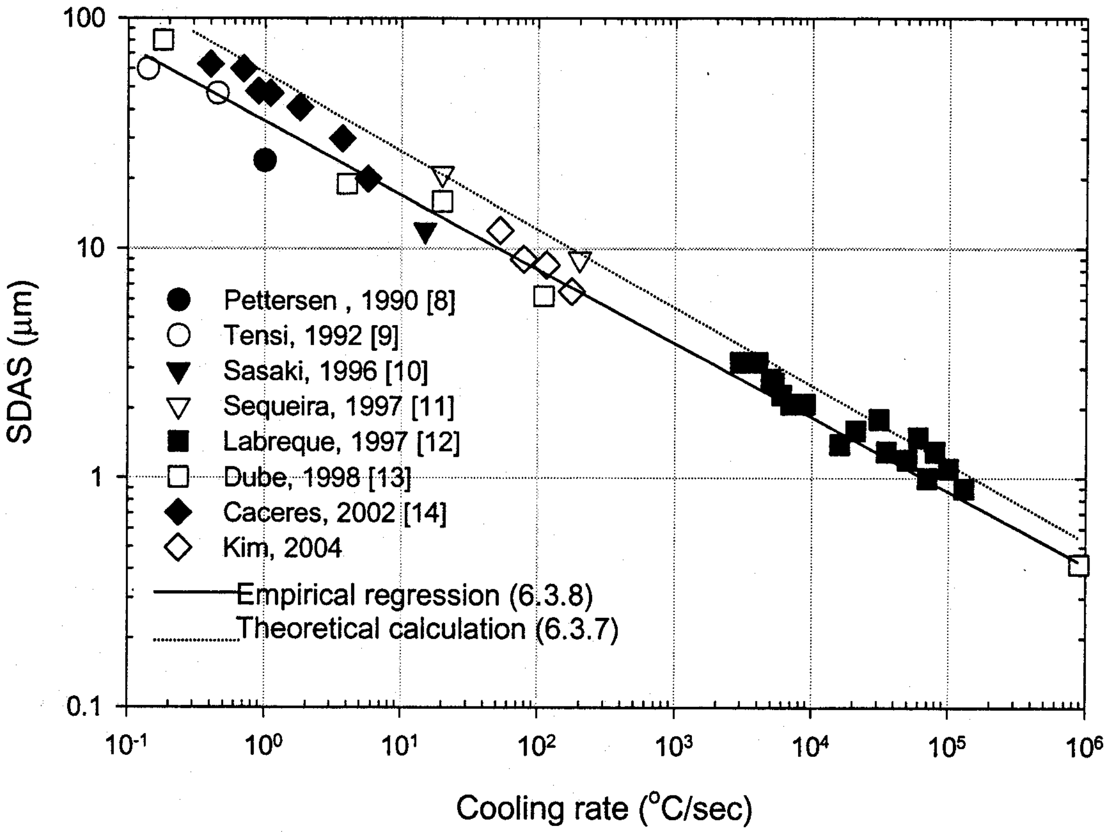

Fig. 6.3.5. Cooling rate vs. the SDAS from various literature

6.3.4 Effect of casting speed

In AA6111 aluminum alloy experiments, increase in casting speed produced thinner strips. In addition, thinner strips recorded higher time average heat fluxes and heat transfer coefficients. According to the data collected by Wang and Matthys [16], the time average interfacial heat transfer coefficient, $\tilde{h}$, is proportional to the speed of the moving mold:

$$\tilde{h} = 17.3 V_s^{\,0.65} \, (kW / m^2 K) \tag{6.3.9}$$

where V_s is the casting speed (m/s). In Fig. 6.3.6, these various heat transfer coefficients were plotted as a function of casting speed, together with the IMI Boucherville twin roll caster studied by Tavares *et al.*[17]

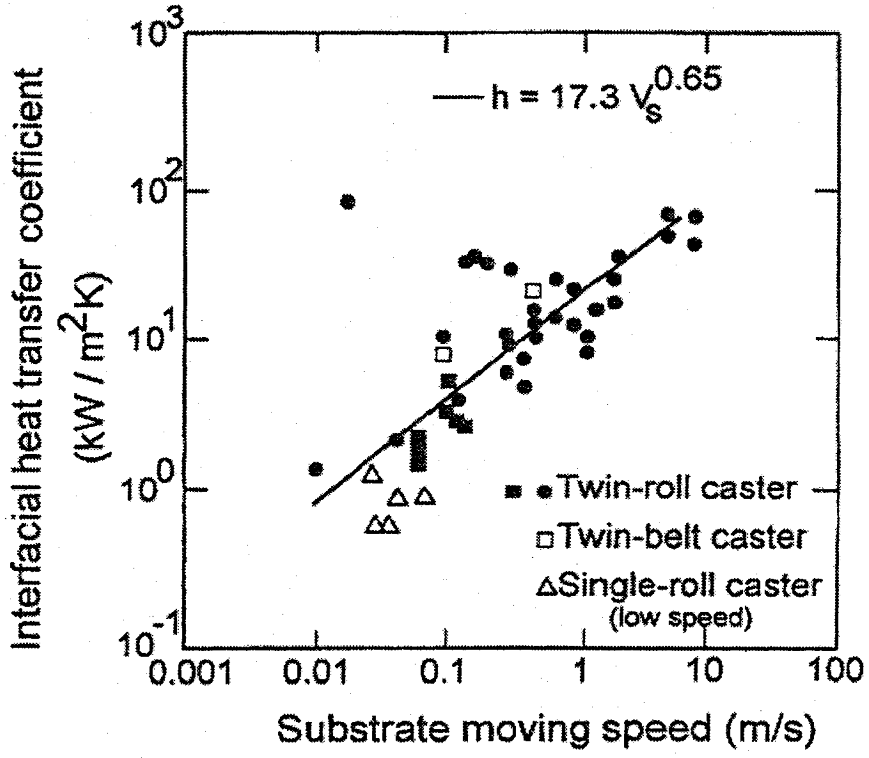

Fig. 6.3.6. Variation of average interfacial heat transfer coefficient with casting speed [16]

By integrating the value of the transient heat transfer coefficient over the time required for complete solidification, an average heat transfer coefficient can be defined:

$$\tilde{h} = \frac{\int_0^{t_f} h(t)\,dt}{t_f} \qquad (6.3.10)$$

From Eqn.(6.3.10), the average heat transfer coefficient for solidification could be calculated. Results are shown in Table 6.3.3. They reveal that the average heat transfer coefficient increased with increasing casting speed on a copper substrate but decreased slightly for a steel substrate.

Table 6.3.3. Average heat transfer coefficient for casting AA6111 strips

Substrate	Casting speed (m/s)	Strip thickness (mm)	$\tilde{h}$ (kW/m^{2}K)
Copper	1.2	1.1	9.3
Copper	0.6	3	6.2
Low carbon steel	1.1	1.2	3.3
Low carbon steel	0.8	3	5.0

6.3.5 Effect of grain refiner

The addition of grain refiner Al-5%Ti-1%B to AA6111 melt was successful in reducing the grain size. Even though the grain refiner is effective in the final product, the mechanism of grain refinement is still not clear. Many theories have been suggested such as the phase diagram theory, particle theory, peritectic bulk theory, and hetero-nucleation theory. More recently, duplex nucleation theory was suggested by adding synthetic TiB_2 crystals directly into liquid aluminum. It was observed that they do not nucleate α-Al, but pushed to grain boundaries to form a $TiAl_3$ layer on the TiB_2/melt interface, which subsequently nucleates the α-Al [18]. Homogenization of grain distribution and reduced grain size about 120μm could be achieved by grain refiner addition.

6.3.6 Effect of oil coating

Spraying oil (PAM) on the mold substrate dramatically improved the cast surface of AA6111. It was surmised that the presence of an oil film might replace any air gap formed during casting, or at least help fill the numerous micro-voids on the mold substrate, and thereby increase thermal contact between the liquid metal and the copper substrate. Given that the thermal conductivity of PAM™ oil is about 10 times higher compared to air, it can be predicted that the interfacial heat transfer increases once air pockets are filled with such an oil. Table 6.3.4 gives thermal conductivity of PAM™ oil and air.

Table 6.3.4. Thermal conductivity of PAM™ oil and air (W/mK)

Temperature (°C)	PAM™ / vegetable oil	Air
25	0.17	0.026
100	0.26	0.032
200	0.36	0.039

Loulou *et al.* [19] have reported that there was a general enhancement in the heat transfer between molten tin and a chill nickel mold substrate when the interfacial medium was filled with a better conductor than air. Their experiments involved tin droplets impinging on a nickel substrate, to which they had applied oil and/or grease coatings. When these lubricants were applied to the rougher substrate surfaces, smoother cast surfaces were achieved, as listed in Table 6.3.5. They also presented the increased heat flux when oil or grease coating was applied on the rough interface, as shown in Fig. 6.3.7.

As seen, in the case of the rougher chill nickel substrate (R_a = 15.58μm), the presence of oil or grease film greatly reduced the roughness of the cast surface of tin. However, for the smoother chill substrate (R_a = 0.66μm), the solidified surfaces were in all cases rougher than the substrate, but an oil film was most efficient in limiting the extent of this increased roughness. This type of behavior has also been observed by other researchers [20-21].

Table 6.3.5. Effect of an interfacial medium on the roughness of the bottom surface of a solidified droplet of tin

Film coating	Smooth Ni substrate $R_a = 0.66$ (μm)	Rough Ni substrate $R_a = 15.58$ (μm)
Oil	0.81	3.66
Grease	4.02	5.87
Air	1.42	12.27

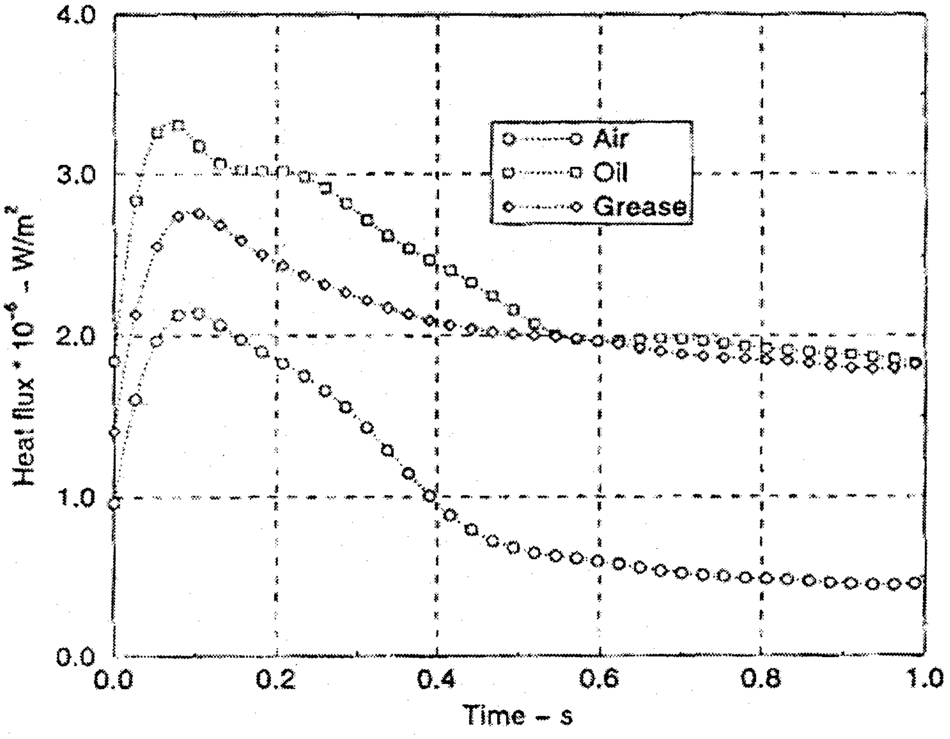

Fig. 6.3.7. Evolution of heat flux with different film coating [19]

REFERENCES

1. H. S. Carlsaw & J. C. Jaeger, *Conduction of Heat in Solids*, 2nd edition, Oxford, 1959

2. T. Iida & R. I. L. Guthrie, *The Physical Properties of Liquid Metals*, 2nd edition, Oxford, 1988

3. P. L. Schaffer, Y. C. Lee and A. K. Dahle, The Effect of Aluminum Conten and Grain Refinement on Porosity Formation in Mg-Al Alloys, *Magnesium Technology 2001*, TMS, New Orleans, USA, 2001, pp.87-94

4. E. J. Whittenberger and F. N. Rhines, Roigin of Porosity in Castings of Magnesium-Aluminum and Other Alloys, *J. Metals*, 1952, pp.409-420

5. Z. Zhang, A. Couture, R. Tremblay and D. Dubé, Microstructure and Mechanical Properties of Permanent Mold and Die Casting of AZ91 Magnesium Alloy, *Light Metals 1999*, CIM, Québec, Canada, 1999, pp.397-406

6. W. Kurz and D.J. Fisher: *Fundamentals of Solidification*, 3rd ed., Trans Tech Publications, 1989, pp.257-259

7. J. F. Grandfield, C. J. Davidson and J. A. Taylor, The Columnar to Equiaxed Transition in Horizontal Direct Chill Cast Magnesium Alloy AZ91, *Light Metals 2001*, TMS, New Orleans, USA, 2001, pp.911-916

8. K. Pettersen, O. Lohne and N. Ryum, Dendritic Solidification of Magnesium Alloy AZ91, *Metall. Mater. Trans. A.*, 1990, vol. 21, pp.221-230

9. H. M. Tensi and R. Rösch, Unidirectional Solidification of the Mg-Al Alloys AZ91HP and AM50HP with Quenching of the Solidification Front, *Magnesium Alloys and Their Applications*, DGM Verlag, Oberursel, Germany, 1992, pp.283-289

10. H. Sasaki, M. Adachi, T. Sakamoto and A. Takimoto, Effect of Solidified Structure of the Mechanical Properties of AZ91 Alloy, *Proc. 53rd Annual World Magnesium Conference*, Virginia, USA, 1996, pp.86-92

11. W. P. Sequeira, M. T. Murray, G. L. Dunlop, D. H. StJohn, Effect of Section Thickness and Gate Velocity on Evolved Microstructure and Mechanical Properties of High Pressure Die Cast Magnesium Alloy AZ91D, *Proc. TMS Symposium on Automotive Alloys*, Warrendale, USA, 1997, pp.169-183

12. C. Labrecque, R. Angers, R. Tremblay and D. Dubé, Inverted Disk Centrifugal Atomization of AZ91 Magnesium Alloy, *Can. Met. Quart.*, 1997, vol. 36, pp.169-175

13. D. Dubé, A. Couture, Y. Carbonneau, M. Fiset, R. Angers and R. Tremblay, Secondary Dendrite Arm Spacings in Magnesium Alloy AZ91D: From Plaster Moulding to Laser Remelting, *Int. J. Cast Metals Res.*, 1998, vol. 11, pp.139-144

14. C. H. Cáceres, C. J. Davidson, J. R. Griffiths, C. L. Newton, Effect of Solidification Rate and Ageing on the Microstructure and Mechanical Properties of AZ91 Alloy, *Mat. Sci. Eng. A*, 2002, vol. 325, pp.344-355

15. R. V. Allen, D. R. East, T. J. Johnson, W. E. Borbidge and D. Liang, Magnesium Alloy Sheet produced by Twin Roll Casting, *Magnesium Technology 2001*, TMS, New Orleans, USA, pp.75-79

16. G. X. Wang, Experimental & Numerical Study of Heat Transfer & Solidification for Molten Metal in Contact with a Cold Substrate, *Ph.D. Thesis*, University of California, Santa Barbara, 1995

17. R. P. Tavares, M. Isac, F.G. Hamel & R.I.L. Guthrie, Instantaneous Interfacial Heat Fluxes during the 4 to 8 m/min Casting of Carbon Steels in a Twin-Roll Caster, *Metall. Mater. Trans.*, Vol. 32B, 2001, pp.55-67

18. P. S. Mohanty & J. E. Gruzleski, Grain Refinement Mechanisms of Hypoeutectic Al-Si Alloys, *Acta Mater.*, Vol.44, No. 9, 1996, pp. 3749-3760

19. T. Loulou, E. A. Artyukhin & J. P. Bardon, Estimation of thermal contact resistance during the first stages of metal solidification process:II – experimental setup and results, *Int. J. Heat and Mass Transfer*, **42**, 1999, pp.2129-2142

20. M. Prates & H. Biloni, Variables affecting the nature of the chill zone, *Metall. Trans.* **3**, 1972, pp.1501-1510

21. C. A. Muojekwu, I. V. Samarasekera & J. K. Brimacombe, Heat transfer and microstructure during the early stage of metal solidification, *Metall. Mater. Trans.* **26B**, 1995, pp. 361-382

CHAPTER
7

CONCLUSIONS

7.1 MELT DELIVERY

Based on the experiments performed in this work, the slot type of nozzle proved to be the preferred design for melt delivery to the moving substrate. To achieve better surface quality and to diminish turbulence effects during the melt feeding process, a slot-type of refractory plate was placed underneath the mold's bottom to seal the sump prior to activation of the substrate, and metal feeding. The size of slot depended on the melt's properties such as viscosity and density, as well as casting speed, and controlled the flow rate of liquid metal.

7.2 HEAT TRANSFER ANALYSIS

The fundamentals of interfacial heat transfer and thermal history of solidifying strip were studied. The castability of magnesium alloys (AZ91 and AM50) and aluminum alloy of AA6111 were experimented and interfacial heat transfer was investigated for a variety of mold substrates. Important variables affecting the rate of interfacial heat transfer between the solidifying strip and the cold substrate were:

(i) Melt superheat
(ii) Thermophysical properties of the melt and the substrate
(iii) Wettability at the interface
(iv) Texture of the substrate
(v) Casting speed

The interfacial heat flux increases to reach its maximum and decreases with the time of contact. The maximum heat flux point appears when the metal-mold contact is fully established. To understand this behavior, a saw-tooth shape interface was modeled to calculate the interfacial heat flux. This model was particularly effective for explaining and simulating the decay of interfacial heat flux.

The maximum heat flux appeared about 0.1~0.2 seconds after the moment of thermal contact when the initial solidified skin was formed at the interface. The maximum heat flux increased up to 7 MW/m^2 on copper substrates and 3 MW/m^2 in steel substrates. Similarly, the maximum value of the interfacial heat transfer coefficient increased up to 15 kW/m^{2}K in copper substrate and 6 kW/m^{2}K in steel substrates. The rate of heat transfer in coated substrates was significantly delayed and reduced because of the high thermal resistance of the low conductivity coating layers at the interface.

The increase in superheat and the increase in casting speed resulted in an increase in heat flux. The addition of grain refiner slightly decreased the rate of heat transfer but was very effective in producing fine (vs columnar) grains. The oil spraying on the mold substrate increased the rate of interfacial heat transfer and improved surface quality remarkably.

The use of a highly conductive substrate enhanced the increase in cooling rate. Thinner strips exhibited faster cooling and higher cooling rates. The copper substrate recorded strip cooling rates of up to 200°C/s, while the low carbon steel substrate showed about 150°C/s.

7.3 MICROSTRUCTURAL ANALYSIS

Characterization of strip microstructures revealed that the finest grain size and minimum SDAS values were obtained when the copper substrate was used. Using various substrates, the SDAS varied from 7 to 15 microns in the AZ91 alloy and 11 to 25 microns in the AM50 alloy.

In the AA6111 alloy, the addition of grain refiner was very effective in reducing the grain size (140±20 microns) and the uniformity of microstructure. The coating of oil on the mold substrate dramatically improved the surface quality of cast strip.

7.4 FUTURE WORK

To clarify the initiation of solidification phenomena between the liquid metal and the mold, direct observation of triple point is required. It should reveal if there is any entrainment of an air film at the moving mold system, and help suggest the mechanisms for air gap evolution.

The optimal choice of interfacial medium (such as oil spray, graphite coating, or He atmosphere casting) should be found and its design to apply them on the belt casting process should be performed as well as the mechanical texture of belt surface.

7.5 STATEMENT OF ORIGINALITY

1. This is the first academic work reporting on the belt casting of magnesium alloys AZ91, AM50, and aluminum AA6111 alloys.

2. To simulate the behavior of an interfacial heat flux, a saw-tooth shaped metal-mold interface is suggested and modeled. This model can explain the shrinkage of solidified skin at the interface and the decrease in heat fluxes as a function of direct metal-mold contact points.

3. Using the small scale strip casting simulator, relationships between cast structure (microstructure, surface quality, porosity, etc.) and operational parameters (casting speed, mold substrate, melt superheat, etc.) were established.

APPENDIX I

A.1.1 RESPONSE TIME OF THERMOCOUPLE

When a step change in temperature is applied to a thermocouple, it takes time to respond for a given input and the temperature output can be expressed by [1,2]:

$$T(t) = A_O + A_1 \exp(-t/\tau_1) + A_2 \exp(-t/\tau_2) \qquad \text{(A1-1)}$$

where *E(t)* is thermocouple output, A_i are constants, and τ_i are modal time constants for mode *i*. These modal time constants τ_i are positive values which characterize the response time of the thermocouple used. To determine these modal time constants, the normalized temperature is defined firstly as:

$$E(t) = \frac{T(t) - T_i}{T_f - T_i} \qquad \text{(A1-2)}$$

where *T(t)* is thermocouple output, T_i is the initial temperature, and T_f is the final temperature which is the real input temperature. Here, T_i is equivalent to *T(0)* and T_f is $T(\infty)$. Thus, the normalized temperature E(t) can be expressed by:

$$E(t) = 1 - \frac{A_1}{A_1 + A_2}\exp(-t/\tau_1) - \frac{A_2}{A_1 + A_2}\exp(-t/\tau_2) \qquad \text{(A1-3)}$$

Note that $E(0) = 0$ and $E(\infty) = 1$. Once the normalized temperature is obtained from experiments, the modal time constants τ_i can be evaluated by curve fitting. Fig. A1-1 shows the typical response time curve of the thermocouple.

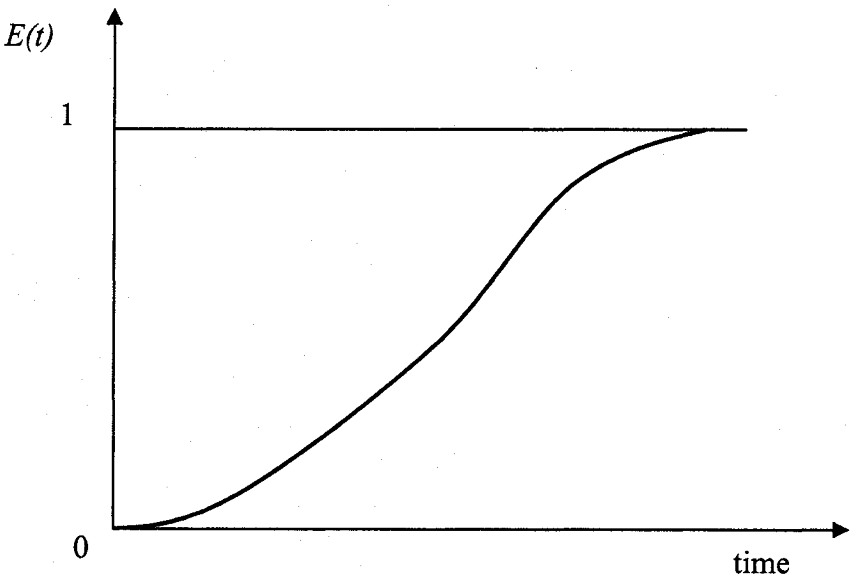

Fig. A1-1. Normalized temperature of responding thermocouple

A.1.2 TRANSFER FUNCTION

The expression (A1-3) is usually obtained by solving the second order differential equation (A1-4).

$$\alpha E''(t) + \beta E'(t) + E(t) = 1 \tag{A1-4}$$

where $\alpha = \tau_1 \tau_2$ and $\beta = \tau_1 + \tau_2$. Note that boundary conditions of this differential equation are:

$$\begin{aligned} &E(0) = 0 \\ &E'(0) = \frac{A_1}{A_1 + A_2}\left(\frac{1}{\tau_1}\right) + \frac{A_2}{A_1 + A_2}\left(\frac{1}{\tau_2}\right) = C \text{ (constant)} \end{aligned} \tag{A1-5}$$

Physically, the right hand side of (A1-4) is the real input applied to the system of interest and the solution *E(t)* is the response data of the signal output. Therefore, in general, the differential equation can be rewritten as:

$$\alpha E''(t) + \beta E'(t) + E(t) = R(t) \tag{A1-6}$$

where E(t) is the measured output and R(t) is the real input.

The second order differential equation (A1-6) can be solved by the Laplace transform. The Laplace transform is defined as:

$$L[f(t)] = F(s) = \int_0^\infty \exp(-st) \cdot f(t)dt \tag{A1-7}$$

Applying the Laplace transform to both sides of (A1-6) gives:

$$(\alpha s^2 + \beta s + 1)E(s) = R(s) \tag{A1-8}$$

Here, the transfer function *G(s)* is defined as *E(s)/R(s)* and can be expressed as:

$$G(s) = \frac{E(s)}{R(s)} = \frac{1}{(\alpha s^2 + \beta s + 1)} = \frac{1}{(\tau_1 s + 1)(\tau_2 s + 1)} \tag{A1-9}$$

The transfer function depends only on the properties of the system under consideration and is determined by the values τ_1 and τ_2. Therefore, the correction of the thermocouple signal to find out the real temperature input can be achieved by following steps:

(i) Evaluation of the Laplace transform of thermocouple output, *E(s)*

(ii) Evaluation of the Laplace transform of real input, *R(s) (=E(s)/G(s))*

(iii) Inverse Laplace transform of *R(s)* to determine *R(t)*

A.1.3 DISCRETIZATION OF MEASURED TEMPERATURE OUTPUT

To follow the steps above, the Laplace transform of the measured temperature output *E(s)* should first be found. However, the output signals of temperatures measured by thermocouples are neither analytical functions nor continuous functions. Instead, they are a set of discrete values governing a certain time interval and each interval is related to the frequency at which the temperature is measured. Therefore, the measured temperature output function *E(t)* should be expressed by an array of step functions.

Once the Heaviside function U_r is defined as:

$$U_r(t) = \begin{cases} 1 & t \geq r \\ 0 & t < r \end{cases} \tag{A1-10}$$

the graph of the Heaviside function can be drawn as Fig. A1-2.

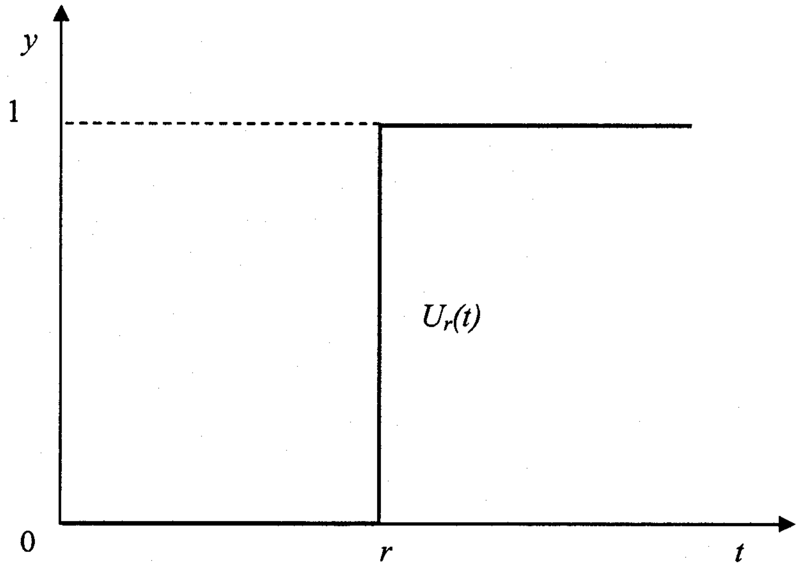

Fig. A1-2. Heaviside function

If any data set can be interpreted as a sum of Heaviside functions, as shown in Fig. A1-3, the measured temperature can be expressed as:

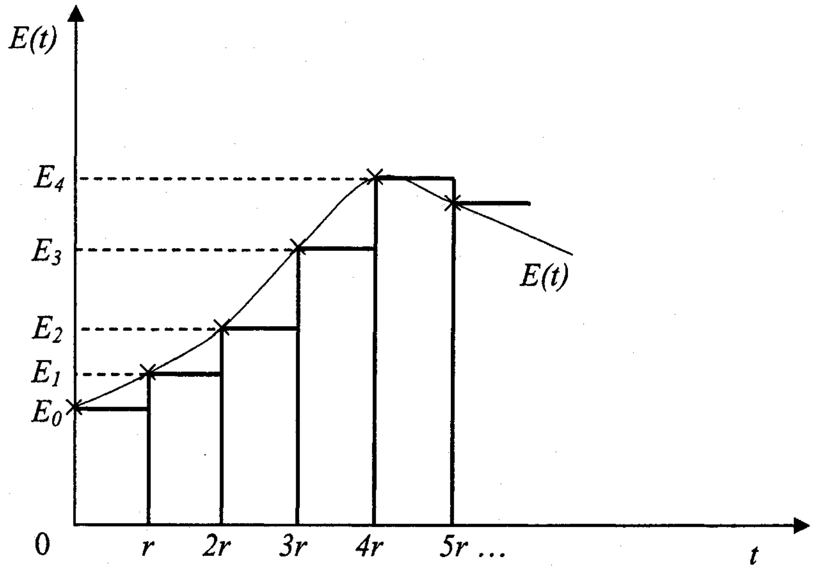

Fig. A1-3. Discretization of Thermocouple output signal, *E(t)*

$$\begin{aligned} E(t) &= E_o U_o + E_1 U_r + E_2 U_{2r} + E_3 U_{3r} + \cdots \\ &= \sum_{n=0} E_n U_{nr} \end{aligned} \qquad \text{(A1-11)}$$

Applying the Laplace transform to (A1-11) and its substitution to (A1-8) gives:

$$E(s) = \frac{1}{s} \sum_{n=0} E_n \exp(-nrs) \qquad \text{(A1-12)}$$

$$R(s) = \alpha s^2 \sum_{n=0} E_n \exp(-nrs) + \beta s \sum_{n=0} E_n \exp(-nrs) + \frac{1}{s} \sum_{n=0} E_n \exp(-nrs) \qquad \text{(A1-13)}$$

Finally, the inversion of (A1-13) to determine *R(t)* gives:

$$R(t) = \alpha \sum_{n=1} E_n \delta'(t-nr) + \beta \sum_{n=1} E_n \delta(t-nr) + \sum_{n=0} E_n U_{nr} \qquad \text{(A1-14)}$$

Here, $\delta(t)$ is a delta function which has the following characteristics.

$$\delta(t)=0 \quad \text{where} \quad t \neq 0$$

$$\int_{-\infty}^{\infty} \delta(t)dt = 1 \tag{A1-15}$$

In fact, many delta functions can be manipulated once they follow the properties above and one of those functions used further is:

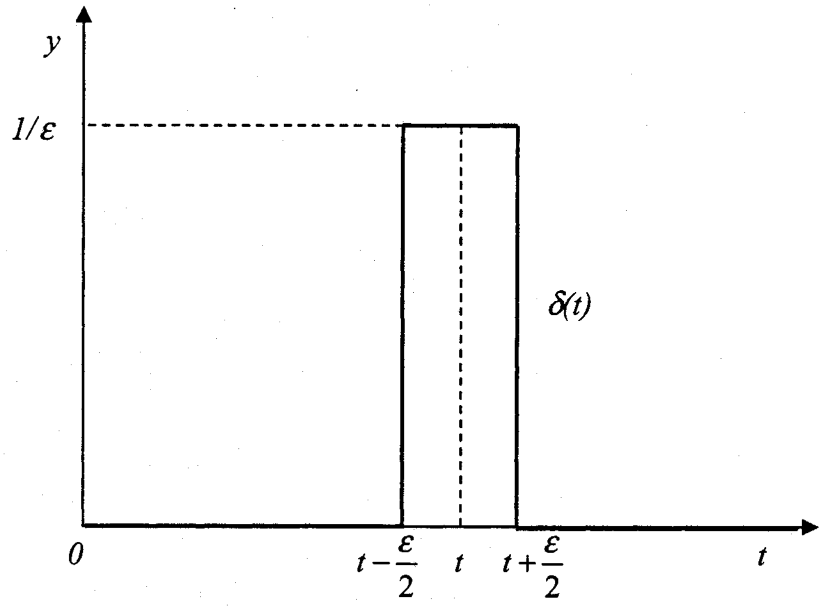

Fig. A1-4. Discretized delta function, *δ(t)*

Rewriting of (A1-14) using the discretized delta function gives the final solution (A1-16). Here, r is the measurement frequency.

$$\boxed{\begin{aligned} R(t) = & \left(E_0 + \frac{\beta(E_1 - E_0)}{2r} + \frac{\alpha(E_1 - E_0)}{r^2} \right) U_0 \\ & + \sum_{n=1} \left(E_n + \frac{\beta}{2r}(E_{n+1} - E_{n-1}) + \frac{\alpha}{r^2}(E_{n+1} - 2E_n + E_{n-1}) \right) U_{nr} \end{aligned}}$$

(A1-16)

A.1.4 WORKED EXAMPLE

As an example, assume that there is a thermocouple which follows the analytical response function (A1-17) and its plot is shown in Fig. A1-5. This analytical response function can be obtained by curve fitting empirically.

$$E(t) = 1 - \frac{5}{4}\exp(-\frac{t}{5}) + \frac{1}{4}\exp(-t) \qquad \text{(A1-17)}$$

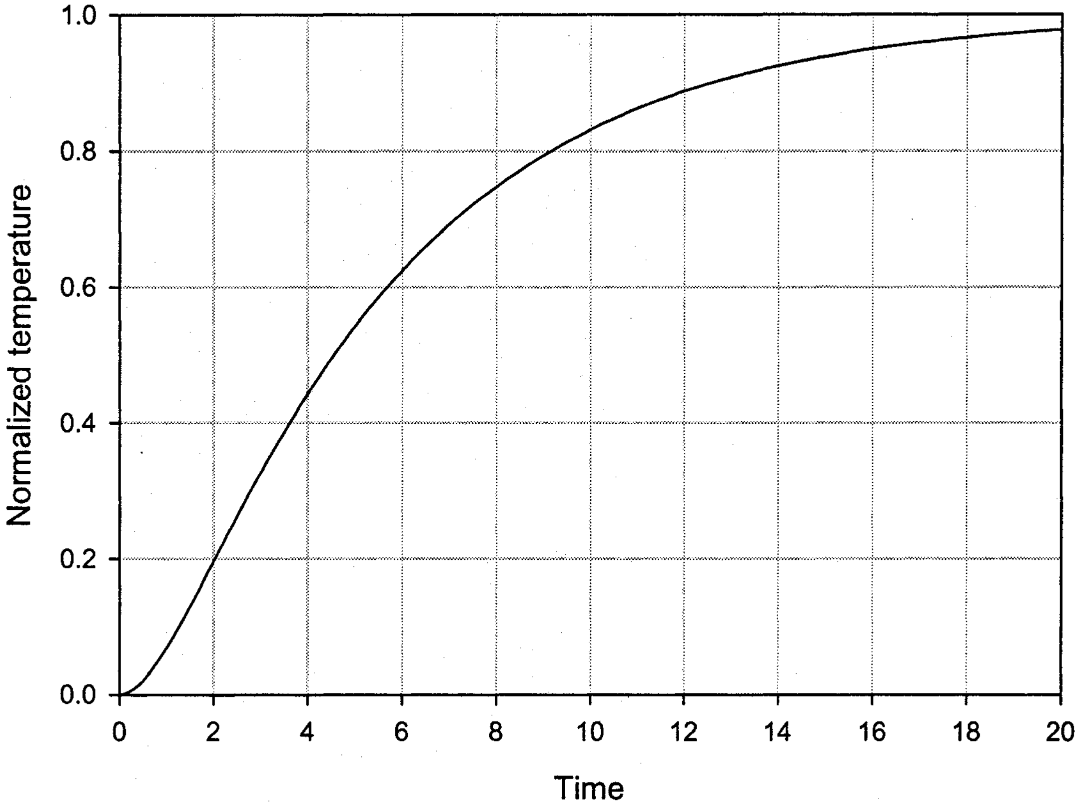

Fig. A1-5. Response time function of thermocouple (A1-17)

If this thermocouple is used in an experiment, the recorded temperature output E(t) and the real input R(t) can be calculated from the differential equation (A1-18).

$$5E''(t) + 6E'(t) + E(t) = R(t) \qquad \text{(A1-18)}$$

The solution of (A1-18) can be calculated using the transfer function and discretization of thermocouple output *E(t)*.

If the thermocouple output *E(t)* was known as an analytical function of (A1-19), direction differentiation and substitution to (A1-18) gives the solution of *R(t)*.

$$E(t) = 125 + 50\exp(-t) - \frac{100}{9}\exp(-2t) - \frac{2500}{18}\exp(-\frac{t}{5}) \tag{A1-19}$$

$$R(t) = 125 - 100\exp(-2t) \tag{A1-20}$$

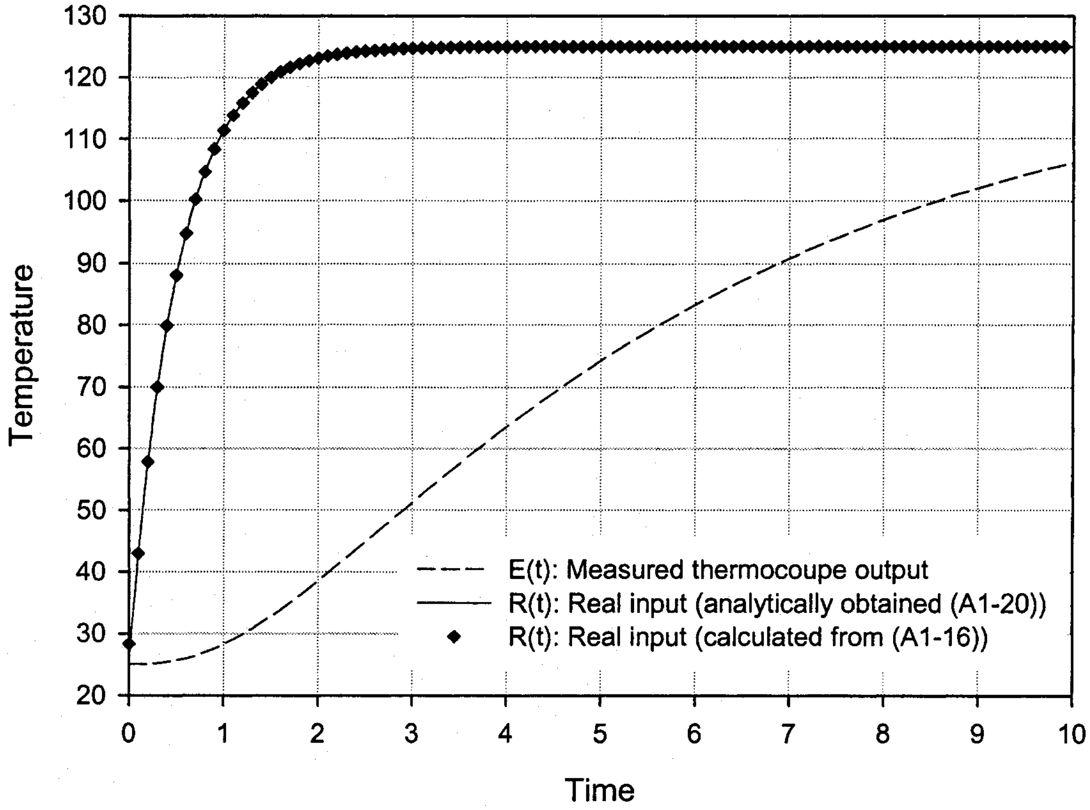

Fig. A1-6. Measured thermocouple output and real input (A1-18,A1-19)

However, in real experiments, analytical function of thermocouple output signal is not possible to obtain so that discretization of the output signal (A1-11) should be performed.

Assuming that the mathematical expression for the thermocouple output (A1-19) is not known, discretization of the output signal associated with solution formula (A1-16) gives a calculated real input. As shown in Fig. A1-6, they coincide very well. Table A1 presents the data sheet used to plot Fig. A1-6, while Fig. A1-7 presents the absolute error between them.

Table A1-1 Data sheet of Fig. A1-6

Time(t)	E(t)	R(t): analytical	R(t): calculated
0.0000	25.0000	25.0000	28.2637
0.1000	25.0062	43.1269	42.9948
0.2000	25.0456	57.9680	57.8387
0.3000	25.1424	70.1188	69.9940
0.4000	25.3129	80.0671	79.9478
0.5000	25.5671	88.2121	88.0990
0.6000	25.9106	94.8806	94.7743
0.7000	26.3451	100.3403	100.2410
0.8000	26.8698	104.8103	104.7180
0.9000	27.4821	108.4701	108.3846
1.0000	28.1776	111.4665	111.3876
1.1000	28.9515	113.9197	113.8472
1.2000	29.7979	115.9282	115.8618
1.3000	30.7108	117.5726	117.5120
1.4000	31.6842	118.9190	118.8638
1.5000	32.7119	120.0213	119.9711
1.6000	33.7879	120.9238	120.8783
1.7000	34.9064	121.6627	121.6216
1.8000	36.0619	122.2676	122.2306
1.9000	37.2491	122.7629	122.7296
2.0000	38.4633	123.1684	123.1385
2.1000	39.6997	123.5004	123.4736
2.2000	40.9542	123.7723	123.7483
2.3000	42.2230	123.9948	123.9735
2.4000	43.5023	124.1770	124.1581
2.5000	44.7890	124.3262	124.3094
2.6000	46.0801	124.4483	124.4335
2.7000	47.3728	124.5483	124.5353

2.8000	48.6648	124.6302	124.6188
2.9000	49.9539	124.6972	124.6873
3.0000	51.2380	124.7521	124.7436
3.1000	52.5154	124.7971	124.7897
3.2000	53.7846	124.8338	124.8276
3.3000	55.0441	124.8640	124.8587
3.4000	56.2928	124.8886	124.8842
3.5000	57.5296	124.9088	124.9052
3.6000	58.7534	124.9253	124.9224
3.7000	59.9636	124.9389	124.9366
3.8000	61.1593	124.9500	124.9483
3.9000	62.3400	124.9590	124.9578
4.0000	63.5053	124.9665	124.9657
4.1000	64.6545	124.9725	124.9722
4.2000	65.7875	124.9775	124.9776
4.3000	66.9039	124.9816	124.9820
4.4000	68.0035	124.9849	124.9856
4.5000	69.0861	124.9877	124.9886
4.6000	70.1516	124.9899	124.9910
4.7000	71.2000	124.9917	124.9931
4.8000	72.2312	124.9932	124.9947
4.9000	73.2452	124.9945	124.9961
5.0000	74.2420	124.9955	124.9972
5.1000	75.2218	124.9963	124.9982
5.2000	76.1846	124.9970	124.9990
5.3000	77.1304	124.9975	124.9996
5.4000	78.0596	124.9980	125.0001
5.5000	78.9721	124.9983	125.0005
5.6000	79.8681	124.9986	125.0009
5.7000	80.7479	124.9989	125.0012
5.8000	81.6115	124.9991	125.0014
5.9000	82.4593	124.9992	125.0016
6.0000	83.2913	124.9994	125.0017
6.1000	84.1079	124.9995	125.0019
6.2000	84.9092	124.9996	125.0019
6.3000	85.6954	124.9997	125.0020
6.4000	86.4668	124.9997	125.0021

6.5000	87.2235	124.9998	125.0021
6.6000	87.9659	124.9998	125.0021
6.7000	88.6941	124.9998	125.0022
6.8000	89.4083	124.9999	125.0022
6.9000	90.1089	124.9999	125.0022
7.0000	90.7960	124.9999	125.0022
7.1000	91.4699	124.9999	125.0022
7.2000	92.1307	124.9999	125.0021
7.3000	92.7787	125.0000	125.0021
7.4000	93.4142	125.0000	125.0021
7.5000	94.0374	125.0000	125.0021
7.6000	94.6484	125.0000	125.0021
7.7000	95.2475	125.0000	125.0020
7.8000	95.8349	125.0000	125.0020
7.9000	96.4109	125.0000	125.0020
8.0000	96.9756	125.0000	125.0019
8.1000	97.5292	125.0000	125.0019
8.2000	98.0721	125.0000	125.0019
8.3000	98.6042	125.0000	125.0019
8.4000	99.1260	125.0000	125.0018
8.5000	99.6375	125.0000	125.0018
8.6000	100.1389	125.0000	125.0018
8.7000	100.6305	125.0000	125.0017
8.8000	101.1124	125.0000	125.0017
8.9000	101.5849	125.0000	125.0017
9.0000	102.0480	125.0000	125.0016
9.1000	102.5020	125.0000	125.0016
9.2000	102.9471	125.0000	125.0016
9.3000	103.3834	125.0000	125.0016
9.4000	103.8111	125.0000	125.0015
9.5000	104.2303	125.0000	125.0015
9.6000	104.6413	125.0000	125.0015
9.7000	105.0442	125.0000	125.0014
9.8000	105.4391	125.0000	125.0014
9.9000	105.8262	125.0000	125.0014

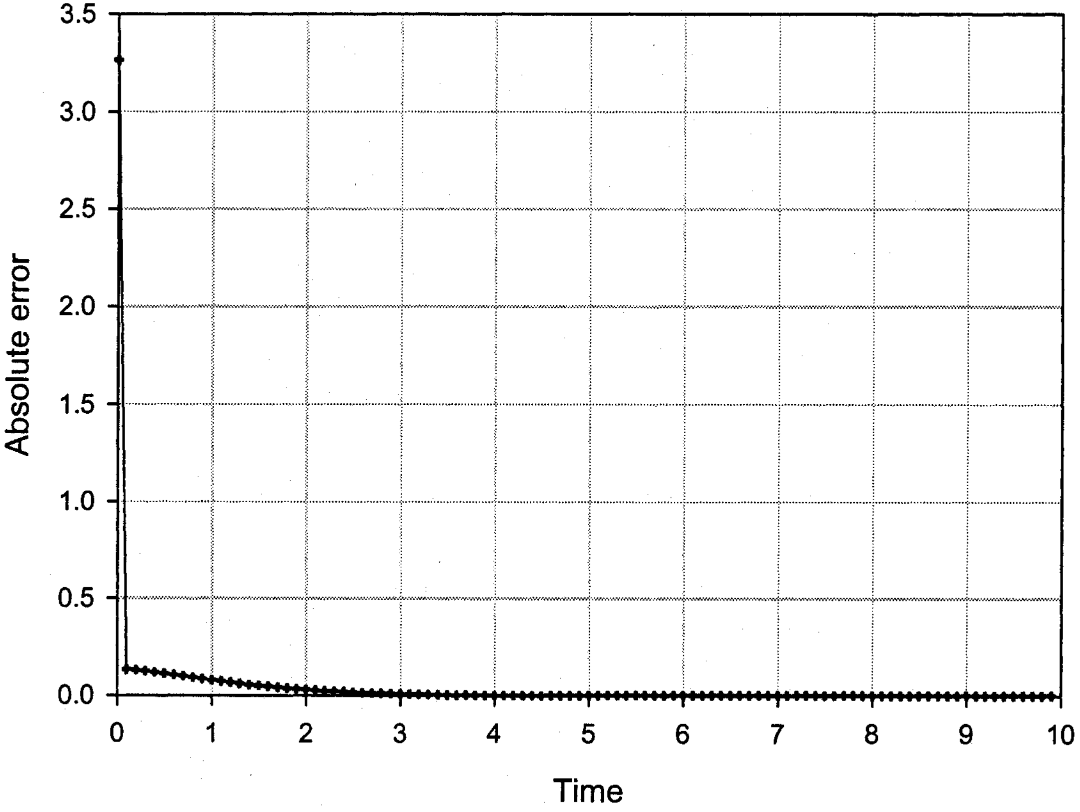

Fig. A1-7. Absolute error between the analytical *R(t)* and the calculated *R(t)*

REFERENCES

1. T. W. Kerlin, L. F. Miller & H. M. Hashemian, In-situ Response Time Testing of Platinum Resistance Thermometers, *ISA Transactions*, **17**, No. 4, pp. 71-88

2. H. M. Hashemian, K. M. Petersen, D. W. Mitchell, M. Hashemian, D. D. Beverly, In-Situ Response Time Testing of Thermocouples, *ISA Transaction*, **29**, No. 4, pp. 97-104

APPENDIX II

A.2.1 THE IHCP FORTRAN CODE

```
CHARACTER ARQ*30,XIMP*30
      DOUBLE PRECISION A(2001),B(2001),C(2001),D(2001),T(2001),
     *TUSE0(2001),
     *Q1R(2001),QR(2001),TUSE1(2001),TUSE2(2001),TUSE3(2001),
     *TRT1(2001),qcomp(2001),
     *TRT2(2001),TIME(2001),POS(2001),K,Q2(2001),Q1(2001),C1,C2,
     *C3,CR,CC,DC
      REAL TIMEX(2001)
      WRITE(*,1047)
 1047 FORMAT(5X,'ENTER THE NAMES OF THE FILES FOR :',/,8X,'- TEMPERATURE
     * READING ',//,8X,'- RESULTS : HEAT FLUX')
      READ(*,1048)ARQ
 1048 FORMAT(A30)
      READ(*,1048)XIMP
      write(*,1048)ximp
      OPEN(8,FILE='PROP.DAT',STATUS='unknown')
      WRITE(*,629)
 629  FORMAT(10X,'WHICH KIND OF COORDINATES DO YOU WANT TO USE ?',/,
     *15X,'[0]RECTANGULAR',/,15X,'[1]CYLINDRICAL',/,15X,'[2]ESPHERICAL'
     *)
      READ(*,*)S
      READ(8,*)RE,RI,CP,K,RO
      ENDFILE 8
      CLOSE(8,STATUS='KEEP')
      WRITE(*,1)RE,RI,CP,K,RO
 1    FORMAT(10X,'PROPERTIES AND CHARACTERISTICS OF THE SYSTEM',//,10X,
     *'EXTERNAL RADIUS(M) = ',F7.5,/,10X,'INTERNAL RADIUS (M) = ',F7.5,
     */,10X,'SPECIFIC HEAT (J/KG.K) = ',F8.2,/,10X,'HEAT CONDUCTIVITY (
     *W/M.K.) = ',F8.2,/,10X,'DENSITY (KG/M3) = ',F8.2,//)
 15   CONTINUE
      WRITE(*,2)
 2    FORMAT(10X,'DO YOU WANT TO CHANGE ANY OF THESE DATA ? Y[1] N[2]')
      READ(*,*)ICH
      IF(ICH .EQ. 1)GOTO 3
      IF(ICH .EQ. 2)GOTO 4
      GOTO 15
 3    WRITE(*,5)
 5    FORMAT(10X,'ENTER THE PROPERTIES ABOVE IN THE SAME SEQUENCE AND SE
     *PARATED BY COMMA ')
      READ(*,*)RE,RI,CP,K,RO
      OPEN(8,FILE='PROP.DAT',STATUS='unknown')
      WRITE(8,*)RE,RI,CP,K,RO
      ENDFILE 8
      CLOSE(8,STATUS='KEEP')
 4    CONTINUE
```

```
      WRITE(*,12)
 12   FORMAT(/,10X,'ENTER THE NUMBER OF NODES N - UP TO 100')
      READ(*,*)N
      DO40I=1,N
      POS(I)=(FLOAT(I-1)*(RE-RI)/FLOAT(N-1)+RI)*1000.
 40   CONTINUE
      WRITE(*,29)
 29   FORMAT(10X,'SELECT THE POSITION OF THE SECOND THERMOCOUPLE',/,12X,
     *'ACCORDING TO THE FOLLOWING TABLE: ',/,10X,'NODE NUMBER-DISTANCE
     *TO THE CENTER')
      WRITE(*,41)(I,POS(I),I=1,N)
 41   FORMAT(5(3X,I3,2X,F8.4))
      READ(*,*)NTC2
      WRITE(*,13)
 13   FORMAT(/,10X,'ENTER THE NUMBER OF TEMPERATURE READINGS')
      READ(*,*)NREAD
      WRITE(*,6)
 6    FORMAT(/,10X,'ENTER THE NUMBER OF TIME STEPS BETWEEN TWO READINGS'
     *)
      READ(*,*)NDIVT
      OPEN(7,FILE=ARQ,STATUS='unknown')
      DO7 I=1,NREAD
*     READ(7,*)TIME(I),TRT1(I),TRT2(I),QR(I)
          READ(7,*)TIME(I),TRT2(I),TRT1(I)
          QR(I)=TRT2(I)
*         QR(I)=TRT2(I)
 7    CONTINUE
          ENDFILE 7
      CLOSE(7,STATUS='KEEP')
      DELTAR=(RE-RI)/FLOAT(N-1)
      ALFA=K/(RO*CP)
      DO600I=1,N
      T(I)=TRT1(1)+(TRT2(1)-TRT1(1))/(POS(NTC2)-POS(1))*(POS(I)-POS(1)
     *)
 600  CONTINUE
      TUSE1(1)=T(NTC2-1)
      TUSE0(1)=T(NTC2-2)
      TUSE2(1)=T(NTC2)
      DO9999J=2,NREAD
      DELTAT=(TIME(J)-TIME(J-1))/FLOAT(NDIVT)
      DO9999JX=1,NDIVT
      JCONT=(J-2)*NDIVT+JX
      TIMEX(JCONT+1)=TIME(J-1)+FLOAT(JX)*DELTAT
      Q1R(JCONT+1)=QR(J)
      FO=ALFA*DELTAT/(DELTAR*DELTAR)
      B(1)=(TRT1(J)*FLOAT(JX)+TRT1(J-1)*FLOAT(NDIVT-JX))/FLOAT(NDIVT)
      C(1)=0.
      D(1)=1.
      DO 16 I=2,NTC2
      D(I)=1.+2.*FO
      R=FLOAT(I-1)*DELTAR+RI
      A(I-1)=FO*(-1.+S*DELTAR/(2.*R))
      C(I)=-FO*(1.+S*DELTAR/(2.*R))
      B(I)=T(I)
 16   CONTINUE
      A(NTC2-1)=0.
```

```
     D(NTC2)=1.
     B(NTC2)=(TRT2(J)*FLOAT(JX)+TRT2(J-1)*FLOAT(NDIVT-JX))/FLOAT(NDIVT)
     CALL TRI(NTC2,A,D,C,B,T)
     TUSE2(JCONT+1)=T(NTC2)
     TUSE0(JCONT+1)=T(NTC2-2)
     TUSE1(JCONT+1)=T(NTC2-1)
9999 CONTINUE
     DO50IM=1,JCONT
     Q1(IM)=-K*(3.*TUSE2(IM)-4.*TUSE1(IM)+TUSE0(IM))/(2.*DELTAR)
50   CONTINUE
     DO2222I=NTC2,N-1
     JFIN=JCONT-(I-NTC2)-1
     DO1111JKK=2,JFIN
     JI=(JKK-2)/NDIVT+2
     JF=(JKK-1)/NDIVT+2
     DELTN=(TIME(JI)-TIME(JI-1))/FLOAT(NDIVT)
     DELTPO=(TIME(JF)-TIME(JF-1))/FLOAT(NDIVT)
     CC=DELTN/(DELTPO*(DELTN+DELTPO))
     DC=DELTPO/(DELTN*(DELTN+DELTPO))
     IF(S .NE. 0)GOTO 51
     CR=1.
     GOTO 52
51   CONTINUE
     CR=((RI+FLOAT(I-1)*DELTAR)/(RI+FLOAT(I)*DELTAR))**(S)
52   CONTINUE
     C1=DELTAR*CR/K
     C2=RO*CP*CR*DELTAR*DELTAR*CC/K
     C3=RO*CP*CR*DELTAR*DELTAR*DC/K
     Q2(JKK)=Q1(JKK)*CR-RO*CP*CR*DELTAR*(CC*(TUSE2(JKK+1)-TUSE2(JKK))-
    *DC*(TUSE2(JKK-1)-TUSE2(JKK)))
     TUSE3(JKK)=TUSE2(JKK)*(1.-C2+C3)-C1*Q1(JKK)+C2*TUSE2(JKK+1)-C3*TUS
    *E2(JKK-1)
1111 CONTINUE
     IF(I .EQ. N-1)GOTO 7777
     DO 555 JCA=2,JFIN
     TUSE2(JCA)=TUSE3(JCA)
     Q1(JCA)=Q2(JCA)
555  CONTINUE
2222 CONTINUE
7777 CONTINUE
     DO556JCA=2,JFIN
     Q2(JCA)=-Q2(JCA)
556  CONTINUE
     OPEN(15,FILE=XIMP,STATUS='unknown')
     DO 444 JCA=2,JCONT-(N-NTC2)
     WRITE(*,456)TIMEX(JCA),Q1R(JCA),Q2(JCA),TUSE3(JCA)
456  FORMAT(2X,F9.3,2X,2F14.2,2X,2F9.2)
     WRITE(15,456)TIMEX(JCA),Q1R(JCA),Q2(JCA),TUSE3(JCA)
444  CONTINUE
     ENDFILE 15
     CLOSE(15,STATUS='KEEP')
     END

     SUBROUTINE TRI(N,A,D,C,B,X)
     implicit DOUBLE PRECISION(a-h,o-z)
     dimension A(2001),D(2001),C(2001),B(2001),X(2001)
```

```
      DO2I=2,N
       XMULT=A(I-1)/D(I-1)
       D(I)=D(I)-XMULT*C(I-1)
       B(I)=B(I)-XMULT*B(I-1)
 2    CONTINUE
      X(N)=B(N)/D(N)
      DO3I=N-1,1,-1
       X(I)=(B(I)-C(I)*X(I+1))/D(I)
 3    CONTINUE
      RETURN
      END
```

A.2.2 THE ENTHALPY METHOD FORTRAN CODE

```
      IMPLICIT DOUBLE PRECISION (A-H,O-Z)
      LOGICAL LSOLVE, LPRINT, CONVGE, PCOEFF

*     COMMON BLOCK
*     ------------
          parameter (NDT=10000, NDT1=NDT+1)
          dimension t(0:NDT),hf(0:NDT),dt(0:NDT),htc(0:NDT),st(0:NDT)

          character*32 fnamei,fnameo,pname
      COMMON/DEPVAR/ F(100,500),FO(100,500)
      COMMON/COEFF/  AP(100,500), AE(100,500), AW(100,500), AN(100,500),
     +          AS(100,500), CON(100,500)
      COMMON/PROPS/  GAM(100,500), RHO(100,500)
      COMMON/SRCE/   SC(100,500), SP(100,500)
      COMMON/GRDVAR/ X(100), XU(100), XDIF(100), XCV(100),
     +          Y(500), YV(500), YDIF(500), YCV(500),
     +          XL, YL, L1, L2, M1, M2
      COMMON/CINDEX/ IFIRST, JFIRST, IREF, JREF
      COMMON/CITER/  RELAX, ITER, ITSRT, MAXIT, MXTDMA
      COMMON/CLOGI/  LSOLVE, LPRINT, CONVGE, PCOEFF
      COMMON/RESID/  RES
      COMMON/SAV/ FX(5500),FA(5500),TIME,DELT,TT,hfb,stp,DI(50),DDI(50)
      COMMON/SOLID/  DH(100,500), DHO(100,500),DHOO(100,500),TS,TL,DHS
      COMMON/CPOO/CPO(100,500),DKG(5500),CG(5500)
      COMMON/PROB/   DEN, COND, CP,FL,CPI(100,500),CONDI(100,500)

*     END OF COMMON BLOCK
*     ------------------

*     DOMAIN DISCRETIZATION AND RELATED CALCULATIONS
*     --------------------------------------------
          write(6,9000)
      read(5,'(a)') pname
9000  format(1h ,17hInput file name: ,$)
           fnamei=pname(1:index(pname,' ')-1)//'.flux'
      fnameo=pname(1:index(pname,' ')-1)//'.stpsc1'
      open(3,file=fnamei,status='old')
      id=1
  11  read(3,*,end=100) t(id),st(id),hf(id)
```

```
*    tmax=amax1(tmax,tc1(id))
*    tmin=amin1(tmin,tc1(id))
     id=id+1
     go to 11
 100 close(3)
          do 12 m=1,id-1
 12       dt(m)=t(m+1)-t(m)
    CALL GRID
    CALL SETUP
    CALL DEFVAL

*   ASSIGN CODE CONTROL PARAMETERS AND PROBLEM-RELATED PARAMETERS;
PROVIDE
*   GUESS VALUES AND ASSIGN GIVEN VALUES FOR THE DEPENDENT VARIABLES;
DESIGN
*   A SUITABLE RESTART FACILITY; SETUP INTERACTIVE INPUT FORMAT, IF DESIRED.
*   ----------------------------------------------------------------------

    CALL START

C=======================================================================
===
    TS=502.0D0
    TL=650.0D0
    DHS=321000D0
*        DHS=0.0D0

    DO 15 I = 1, L1
     DO 15 J = 1, M1
      DHO(I,J)=DHS
       DH(I,J)=DHS
        DHOO(I,J)=DHS
*         CPO(I,J)=1200.0D0
                     CPO(I,J)=1080.0D0
15   CONTINUE

C==== TIME ITERATION LOOP ======
         TT=0
*        delt=0.01
*        F(1,2)=873
    do 22 m=1,id-1
*        TT=m*delt
    TT=t(m)
         delt=dt(m)
*        hfb=1.0D+6
         hfb=hf(m)
         stp=st(m)
*        hfb=20722.43*(F(1,2)-25)/sqrt(TT)
    CONVGE = .FALSE.
    ITER=0
          conv=0

C== ITERATION LOOP WITHIN A TIME STEP ====

10   ITER  = ITER + 1
```

```
C=======================================
   CALL PHI
C======================================
   CONV = DABS(RES)
C======================================
c   WRITE(*,*) 'Time = ',TT
c   WRITE(*,*) ' THE NUMERICAL SOLUTION CONVERGED.'
C   WRITE(*,*) ' NUMBER OF ITERATIONS : ', ITER
   WRITE(*,*) 'ITER=',ITER
*   WRITE(*,*) 'T(1,1)=',F(1,1)
        WRITE(*,*) 'T(1,15)=',F(1,15)
C=======================================================================
   IF ((CONV.GE.1.0D-3).AND.(ITER.LT.MAXIT)) GO TO 10

   IF (CONV.LT.1.0D-3) GO TO 33

   WRITE(*,*) 'Time = ',TT
c   WRITE(*,*) ' THE NUMERICAL SOLUTION CONVERGED.'
c   WRITE(*,*) ' NUMBER OF ITERATIONS : ', ITER
C   WRITE(*,*) 'ITER = ', ITER , '       T(1,2) =', F(1,2)

33   DO 30 I=1,L1
   DO 30 J=1,M1
   FO(I,J)=F(I,J)
   DHO(I,J)=DH(I,J)
   CPO(I,J)=CPI(I,J)
30   CONTINUE
   htc(m)=hfb/(F(1,1)-stp)
C========================================================
c      FX(m+1)=F(2,2)
c      FA(m+1)=F(16,16)
c      CG(m+1)=CPI(2,2)
c      DKG(m+1)=CONDI(2,2)
C==================================================================

          open(3,file=fnameo,status='unknown')
   write(3,9020) t(m), F(1,1),F(1,15),F(1,30),htc(m),ITER
9020  format(1h ,f9.4, 3(1h,,f8.4), 1h,f10.4,1h,i6)
*         IF (F(1,2).le.400) go to 23


C==================================================================
22          continue
C======================================================
23    END

C************************************************************************


*    -----------------
   SUBROUTINE  SETUP
*    -----------------

*    THE PURPOSE OF THIS SUBROUTINE IS TO SET UP ALL GRID-RELATED QUANTITIES
*    USED IN THE FORMULATION OF THE FINITE VOLUME METHOD
*    ---------------------------------------------------------------------
```

```
      IMPLICIT DOUBLE PRECISION (A-H,O-Z)

*     COMMON BLOCK
*     ------------
      COMMON/GRDVAR/ X(100), XU(100), XDIF(100), XCV(100),
     +           Y(500), YV(500), YDIF(500), YCV(500),
     +           XL, YL, L1, L2, M1, M2

*     END OF COMMON BLOCK
*     -------------------


*     GRID-RELATED VARIABLES PERTAINING TO THE X DIRECTION
*     ----------------------------------------------------

      XU(1) = 0.0D+00
      X(1) = XU(2)
      XDIF(1) = 0.0D+00
      XCV(1) = 0.0D+00

      DO 10 I = 2, L2
        X(I) = (XU(I) + XU(I+1)) * 0.5D+00
        XDIF(I) = X(I) - X(I-1)
        XCV(I) = XU(I+1) - XU(I)
10    CONTINUE

      X(L1) = XU(L1)
      XDIF(L1) = X(L1) - X(L2)
      XCV(L1) = 0.0D+00

*     GRID-RELATED VARIABLES PERTAINING TO THE Y DIRECTION
*     ----------------------------------------------------

      YV(1) = 0.0D+00
      Y(1) = YV(2)
      YDIF(1) = 0.0D+00
      YCV(1) = 0.0D+00

      DO 20 J = 2, M2
        Y(J) = (YV(J) + YV(J+1)) * 0.5D+00
        YDIF(J) = Y(J) - Y(J-1)
        YCV(J) = YV(J+1) - YV(J)
20    CONTINUE

      Y(M1) = YV(M1)
      YDIF(M1) = Y(M1) - Y(M2)
      YCV(M1) = 0.0D+00

      RETURN
      END

C**************************************************************************

*     --------------
      SUBROUTINE PHI
```

```
*   --------------

*   THE PURPOSE OF THIS SUBROUTINE IS TO CALCULATE ALL DEPENDENT
*   VARIABLES OTHER THAN U, V, P-PRIME, AND P
*   -----------------------------------------------------------

      IMPLICIT DOUBLE PRECISION (A-H,O-Z)
      LOGICAL LSOLVE, LPRINT, CONVGE, PCOEFF

*   COMMON BLOCK
*   ------------
C      COMMON/DEPVAR/ F(100,500)
      COMMON/DEPVAR/ F(100,500),FO(100,500)
      COMMON/COEFF/  AP(100,500), AE(100,500), AW(100,500), AN(100,500),
     +          AS(100,500), CON(100,500)
      COMMON/PROPS/  GAM(100,500), RHO(100,500)
      COMMON/SRCE/   SC(100,500), SP(100,500)
      COMMON/GRDVAR/ X(100), XU(100), XDIF(100), XCV(100),
     +          Y(500), YV(500), YDIF(500), YCV(500),
     +          XL, YL, L1, L2, M1, M2
      COMMON/CINDEX/ IFIRST, JFIRST, IREF, JREF
      COMMON/CITER/  RELAX, ITER, ITSRT, MAXIT, MXTDMA
      COMMON/CLOGI/  LSOLVE, LPRINT, CONVGE, PCOEFF
      COMMON/RESID/  RES
      COMMON/SAV/FX(5500),FA(5500),TIME,DELT,TT,hfb,stp,DI(50),DDI(50)
      COMMON/SOLID/  DH(100,500), DHO(100,500),DHOO(100,500),TS,TL,DHS
      COMMON/CPOO/CPO(100,500),DKG(5500),CG(5500)
      COMMON/PROB/   DEN, COND, CP,FL,CPI(100,500),CONDI(100,500)

*   END OF COMMON BLOCK
*   ------------------

*   ASSIGN APPROPRIATE IFIRST, AND JFIRST VALUES
*   -------------------------------------------

      IFIRST = 2
      JFIRST = 2

*   ASSIGN REQUIRED THERMOPHYSICAL PROPERTIES AND SOURCE TERMS
*   -------------------------------------------------------

      CALL DENSE
      CALL LATENT
      CALL CPCOND
      CALL GAMSOR

*   DETERMINE THE EAST COEFFICIENTS
*   ------------------------------

      DO 310 J = 2, M2
        DO 310 I = 1, L2

*   THE DIFFUSION COEFFICIENT (GAMMA) AT EAST CONTROL VOLUME FACE.

          GAMMA = 2.0D+00 * GAM(I,J) * GAM(I+1,J) * XDIF(I+1) /
     +       (GAM(I+1,J) * XCV(I) + GAM(I,J) * XCV(I+1) + 1.0D-50)
```

```
     IF (I.EQ.1) GAMMA = GAM(1,J)
     IF (I.EQ.L2) GAMMA = GAM(L1,J)

*    THE DIFFUSION TERM

     DIFF = GAMMA * YCV(J) / XDIF(I+1)

     AW(I+1,J) = DIFF

     AE(I,J) = AW(I+1,J)

310  CONTINUE

*    IN A SIMILAR FASHION, DETERMINE THE NORTH AND SOUTH COEFFS.
*    ----------------------------------------------------------

    DO 320 I = 2, L2
     DO 320 J = 1, M2

       GAMMA = 2.0D+00 * GAM(I,J) * GAM(I,J+1) * YDIF(J+1) /
   +       (GAM(I,J+1) * YCV(J) + GAM(I,J) * YCV(J+1) + 1.0D-50)

     IF (J.EQ.1) GAMMA = GAM(I,1)
     IF (J.EQ.M2) GAMMA = GAM(I,M1)

     DIFF = GAMMA * XCV(I) / YDIF(J+1)

     AS(I,J+1) = DIFF

     AN(I,J) = AS(I,J+1)

320  CONTINUE

*    OBTAIN AP AND CON TERMS; ALSO DO IMPLICIT UNDER-RELAXATION
*    ----------------------------------------------------------
    TS=502.D0
    TL=650.D0
    REL = 1.0D+00 - RELAX
    DO 330 I=2,L2
    DO 330 J=2, M2
    VOLUME = XCV(I) * YCV(J)
    APO=ABS(CPI(I,J)*VOLUME/DELT)
    APOO=ABS(CPO(I,J)*VOLUME/DELT)
    AP(I,J) = (APO+AN(I,J) + AS(I,J) + AW(I,J) + AE(I,J) -
   +SP(I,J) * VOLUME) / RELAX

    RE=DHO(I,J)-DH(I,J)
*        RE=ABS(DHO(I,J)-DH(I,J))

     CON(I,J) = SC(I,J) * VOLUME + APOO* FO(I,J)
   ++VOLUME*RE/(DELT) + REL * AP(I,J) * F(I,J)

330  CONTINUE

    CALL BOUND
```

```
    RES = 0.0D0
    DO 335 I=2,L2
    DO 335 J=2,M2
    RESID = AP(I,J)*F(I,J)-AS(I,J)*F(I,J-1)-AN(I,J)*F(I,J+1)
   +-AE(I,J)*F(I+1,J)-AW(I,J)*F(I-1,J)-CON(I,J)
335  RES = RES + DABS(RESID)

C**********************************************************************

    CALL SOLVE
     RETURN
    END

C**************************************************************************

*    ----------------
    SUBROUTINE SOLVE
*    ----------------

*    THIS SUBROUTINE IMPLEMENTS A LINE BY LINE-BY-LINE TDMA
*    TO SOLVE THE NOMINALLY-LINEAR DISCRETIZATION EQUATIONS
*    -----------------------------------------------------

    IMPLICIT DOUBLE PRECISION (A-H,O-Z)
    LOGICAL LSOLVE, LPRINT, CONVGE, PCOEFF

*    COMMON BLOCK
*    ------------
C     COMMON/DEPVAR/ F(100,500)
    COMMON/DEPVAR/ F(100,500),FO(100,500)
           COMMON/COEFF/ AP(100,500), AE(100,500), AW(100,500),AN(100,500),
   +          AS(100,500), CON(100,500)
    COMMON/GRDVAR/ X(100), XU(100), XDIF(100), XCV(100),
   +          Y(500), YV(500), YDIF(500), YCV(500),
   +          XL, YL, L1, L2, M1, M2
    COMMON/CINDEX/ IFIRST, JFIRST, IREF, JREF
    COMMON/CITER/  RELAX, ITER, ITSRT, MAXIT, MXTDMA
    COMMON/CLOGI/  LSOLVE, LPRINT, CONVGE, PCOEFF

*    END OF COMMON BLOCK
*    -------------------

*    VARIABLES PARTICULAR TO THE SOLVE SUBROUTINE
*    -------------------------------------------

    DIMENSION PT(500), QT(500)

*    -----------------------------------------------------------------

*    EACH ITERATION PERFORMS FOUR SWEEPS, (+VE) X, Y AND (-VE) X, Y DIRECTIONS

*    INDEX EQUAL TO ONE PERFORMS POSITIVE SWEEPS AND INDEX EQUAL TO TWO
*    PERFORMS NEGATIVE SWEEPS.
*
*    MXTDMA(NF) DENOTES THE MAXIMUM NUMBER OF ITERATIONS DESIRED FOR THE
*    DEPENDENT VARIABLE OF INTEREST (NF)
```

```
      DO 30 ITERSOL = 1, MXTDMA
        DO 30 INDEX = 1, 2
          DO 50 II = IFIRST, L2
            I = II
            IF (INDEX.EQ.2) I = L2 + IFIRST - II
            B = CON(I,JFIRST) + AW(I,JFIRST) * F(I-1,JFIRST) +
     +          AE(I,JFIRST) * F(I+1,JFIRST) + AS(I,JFIRST) *
     +          F(I,JFIRST-1)
            PT(JFIRST) = AN(I,JFIRST) / AP(I,JFIRST)
            QT(JFIRST) = B / AP(I,JFIRST)

*     PT AND QT ARE THE RECCURENCE VARIABLES FOR A TDMA
*     THE STARTING VALUES FOR THE RECCURENCE VARIABLES HAVE BEEN EVALUATED

            DO 55 J = JFIRST+1, M2-1
              B = CON(I,J) + AW(I,J) * F(I-1,J)
     +                 + AE(I,J) * F(I+1,J)
              DENOM = AP(I,J) - AS(I,J) * PT(J-1)
              PT(J) = AN(I,J) / DENOM
              QT(J) = (B + AS(I,J) * QT(J-1)) / DENOM
55          CONTINUE

            B = CON(I,M2) + AW(I,M2) * F(I-1,M2) + AE(I,M2) *
     +                 F(I+1,M2) + AN(I,M2) * F(I,M1)
            PT(M2) = 0.0D+00
            DENOM = AP(I,M2) - AS(I,M2) * PT(M2-1)
            QT(M2) = (B + AS(I,M2) * QT(M2-1)) / DENOM

*     INITIATING THE BACK-SUBSTITUTION.

            F(I,M2) = QT(M2)
            DO 60 J = M2-1, JFIRST, -1
60            F(I,J) = PT(J) * F(I,J+1) + QT(J)
50        CONTINUE

*     THE SWEEP IN THE X OR ITH DIRECTION IS NOW COMPLETE.

          DO 70 JJ = JFIRST, M2
            J = JJ
            IF (INDEX.EQ.2) J = M2 + JFIRST - JJ
            B = CON(IFIRST,J) + AS(IFIRST,J) * F(IFIRST,J-1) +
     +          AN(IFIRST,J) * F(IFIRST,J+1) + AW(IFIRST,J) *
     +          F(IFIRST-1,J)
            PT(IFIRST) = AE(IFIRST,J) / AP(IFIRST,J)
            QT(IFIRST) = B / AP(IFIRST,J)

            DO 75 I = IFIRST+1, L2-1
              B = CON(I,J) + AS(I,J) * F(I,J-1) +
     +                 AN(I,J) * F(I,J+1)
              DENOM = AP(I,J) - AW(I,J) * PT(I-1)
              PT(I) = AE(I,J) / DENOM
              QT(I) = (B + AW(I,J) * QT(I-1)) / DENOM
75          CONTINUE

            B = CON(L2,J) + AS(L2,J)*F(L2,J-1) + AN(L2,J) *
```

```
    +                F(L2,J+1) + AE(L2,J)*F(L1,J)
           PT(L2) = 0.0D+00
           DENOM = AP(L2,J) - AW(L2,J) * PT(L2-1)
           QT(L2) = (B + AW(L2,J) * QT(L2-1)) / DENOM

*    BACK-SUBSTITUTING.

           F(L2,J) = QT(L2)
           DO 80 I = L2-1, IFIRST, -1
80            F(I,J) = PT(I)*F(I+1,J) + QT(I)
70        CONTINUE

*    THE SWEEP IN THE Y OR JTH-DIRECTION IS NOW COMPLETE.

30   CONTINUE
     RETURN
     END
C*******************************************************************************

*    -----------------
     SUBROUTINE DEFVAL
*    -----------------

*     THE PURPOSE OF THIS SUBROUTINE IS TO ASSIGN DEFAULT VALUES TO
*     ALL DEPENDENT VARIABLES, DU'S, DV'S, NDS, AND LOGICAL CONTROL INDICES


     IMPLICIT DOUBLE PRECISION (A-H,O-Z)
     LOGICAL LSOLVE, LPRINT, CONVGE, PCOEFF

*    COMMON BLOCK
*    ------------
C     COMMON/DEPVAR/ F(100,500)
     COMMON/DEPVAR/ F(100,500),FO(100,500)
     COMMON/COEFF/  AP(100,500), AE(100,500), AW(100,500), AN(100,500),
    +           AS(100,500), CON(100,500)
     COMMON/PROPS/  GAM(100,500), RHO(100,500)
     COMMON/SRCE/   SC(100,500), SP(100,500)
     COMMON/GRDVAR/ X(100), XU(100), XDIF(100), XCV(100),
    +           Y(500), YV(500), YDIF(500), YCV(500),
    +           XL, YL, L1, L2, M1, M2
     COMMON/CINDEX/ IFIRST, JFIRST, IREF, JREF
     COMMON/CITER/  RELAX, ITER, ITSRT, MAXIT, MXTDMA
     COMMON/CLOGI/  LSOLVE, LPRINT, CONVGE, PCOEFF
     COMMON/SAV/FX(5500),FA(5500),TIME,DELT,TT,hfb,stp,DI(50),DDI(50)
     COMMON/SOLID/  DH(100,500), DHO(100,500),DHOO(100,500),TS,TL,DHS
     COMMON/CPOO/CPO(100,500),DKG(5500),CG(5500)
     COMMON/PROB/   DEN, COND, CP,FL,CPI(100,500),CONDI(100,500)
*    END OF COMMON BLOCK
*    -------------------

*    SET ALL DEPENDENT VARIABLES TO ZERO

     DO 10 I = 1, L1
     DO 10 J = 1, M1
          F(I,J) =  710.0D0
```

```
10   CONTINUE
    DO 20 I = 1, L1
    DO 20 J = 1, M1
          FO(I,J) = 710.0D0
20   CONTINUE

*    SET ALL LOGICAL CONTROL VARIABLES TO .FALSE.

    LSOLVE = .FALSE.
    LPRINT = .FALSE.
30   CONTINUE

    CONVGE = .FALSE.
    PCOEFF = .FALSE.

    RETURN
    END

C***********************************************************************

*    ---------------
    SUBROUTINE GRID
*    ---------------

*    THIS SUBROUTINE ALLOWS THE USER TO INPUT DOMAIN DISCRETIZATION INFO:
*    L1, M1, L2, M2, XL, YL, AND THE LOCATIONS OF THE MAIN-GRID CV FACES
*    (XU(I), I = 2, L1) AND (YV(J), J = 2, M1) MUST BE SPECIFIED

    IMPLICIT DOUBLE PRECISION (A-H,O-Z)

*    COMMON BLOCK
*    ------------
    COMMON/GRDVAR/ X(100), XU(100), XDIF(100), XCV(100),
   +          Y(500), YV(500), YDIF(500), YCV(500),
   +          XL, YL, L1, L2, M1, M2
    COMMON/CINDEX/ IFIRST, JFIRST, IREF, JREF
*    END OF COMMON BLOCK
*    -------------------

* NOTATION :
*       L1 - LAST NODE IN THE X-DIR.
*       L2 - SECOND TO LAST NODE IN THE X-DIR.
*       M1 - LAST NODE IN THE Y-DIR.
*       M2 - SECOND TO LAST NODE IN THE Y-DIR.
*       XL - TOTAL LENGTH OF CALC. DOMAIN IN THE X-DIR.
*       YL -  "    "  "  "    "    "  " Y-DIR.
*       XPOW - USED TO PRODUCE AN UNEVEN NODAL DISTRIBUTION IN X-DIR.
*       YPOW -  "  "   "   "  "    "      "      " Y-DIR.


    L1 = 50
    L2 = L1 - 1

    M1 = 30
    M2 = M1 - 1
```

```
      XL = 0.02D+00

      YL = 0.0035D+00

*      NOTE: L1 AND M1 MUST BE EVEN IN THIS PROBLEM TO ENSURE THAT THERE IS A
*         LINE OF U-VELS AT THE VERTICAL CENTER LINE, AND A LINE OF V-VELS
*         AT THE HORIZONTAL CENTER LINE OF THE SQUARE CAVITY: THIS IS ALSO
*         REQUIRED TO MAKE THE FOLLOWING POWER-LAW-GRID ALGORITHM SUITABLE

      XPOW = 1.0D+00
      YPOW = 1.0D+00

      DO 10 I = 2, L1
10       XU(I) = (DBLE(I-2) / DBLE(L1 - 2))**XPOW * XL

      DO 20 J = 2, M1
20       YV(J) = (DBLE(J-2) / DBLE(M1 - 2))**YPOW * YL

      RETURN
      END

C***********************************************************************

*     ----------------
      SUBROUTINE START
*     ----------------

*     THE PURPOSE OF THIS SUBROUTINE IS TO INPUT SUITABLE GUESS VALUES TO ALL
*     DEPENDENT VARIABLES, AND SPECIFY ALL PARAMETERS ESSENTIAL TO THE PROPER
*     SOLUTION OF THE PROBLEM OF INTEREST
*

      IMPLICIT DOUBLE PRECISION (A-H,O-Z)
      LOGICAL LSOLVE, LPRINT, CONVGE, PCOEFF
*           parameter (NDT=10000, NDT1=NDT+1)
*           dimension time(0:NDT),hfb(0:NDT),delt(0:NDT)

*     COMMON BLOCK
*     ------------
C       COMMON/DEPVAR/ F(100,500)
      COMMON/DEPVAR/ F(100,500),FO(100,500)
      COMMON/COEFF/  AP(100,500), AE(100,500), AW(100,500), AN(100,500),
     +            AS(100,500), CON(100,500)
      COMMON/PROPS/  GAM(100,500), RHO(100,500)
      COMMON/SRCE/   SC(100,500), SP(100,500)
      COMMON/GRDVAR/ X(100), XU(100), XDIF(100), XCV(100),
     +            Y(500), YV(500), YDIF(500), YCV(500),
     +            XL, YL, L1, L2, M1, M2
      COMMON/CINDEX/ IFIRST, JFIRST, IREF, JREF
      COMMON/CITER/  RELAX, ITER, ITSRT, MAXIT, MXTDMA
      COMMON/CLOGI/  LSOLVE, LPRINT, CONVGE, PCOEFF
      COMMON/SAV/FX(5500),FA(5500),TIME,DELT,TT,hfb,stp,DI(50),DDI(50)
      COMMON/SOLID/  DH(100,500), DHO(100,500),DHOO(100,500),TS,TL,DHS
      COMMON/CPOO/CPO(100,500),DKG(5500),CG(5500)
      COMMON/PROB/   DEN, COND, CP,FL,CPI(100,500),CONDI(100,500)
*     END OF COMMON BLOCK
```

```
*    -------------------

*    LET NF = 1 REPRESENT TEMPERATURE
*    --------------------------------

     DIMENSION    T(100,500)
     EQUIVALENCE  (F(1,1), T(1,1))

*    --------------------------------------------------------------------

*    SET LOGICAL CONTROL VARIABLES TO .TRUE. FOR NF = 1, 2, 3, 4, 5

     LSOLVE = .TRUE.

*    DEFINING THE FLUID PROPERTIES AND PROBLEM PARAMETERS.

     DEN = 2710.0D0

*    SET ALL PARAMETERS RELATED TO OVERALL AND LINE-BY-LINE ITERATIONS

     ITSRT = 0
     ITER = ITSRT
     MAXIT = 2000

*    RESET IREF AND JREF, IF DESIRED

     IREF = 16
     JREF = 16

     MXTDMA = 4

     RELAX = 0.9D+00


*    NOTE: IF ISTART = 1, THEN THE PROBLEM IS RUN FROM SCRATCH (ITER = 0)

*        IF ISTART > 1, THEN THE PROBLEM IS STARTED FROM THE RESULTS OF
*        THE LAST RUN: THE PROGRAMS EXPECT THIS DATA TO BE AVAILABLE IN
*        THE FORMAT (SEE DO LOOPS BELOW) ON FILE = 'DATAIN.DAT'


     ISTART = 1
     IF (ISTART.GT.1) THEN
           OPEN (UNIT = 51, FILE = 'DATAIN.DAT', STATUS = 'OLD')
     REWIND 51

     READ(51,*) ITSRT

     DO 9030 I = 1, L1
     DO 9030 J = 1, M1
     READ(51,*) X(I), Y(J), T(I,J)

9030  CONTINUE

     ITER = ITSRT
```

```
     CLOSE (UNIT = 51)

     ENDIF


    RETURN
    END
C***************************************************************************

*   ----------------
    SUBROUTINE DENSE
*   ----------------

*   THE PURPOSE OF THIS SUBROUTINE IS TO INPUT THE DENSITY AT ALL NODES.

    IMPLICIT DOUBLE PRECISION (A-H,O-Z)

*   COMMON BLOCK
*   ------------
C    COMMON/DEPVAR/ F(100,500)
    COMMON/DEPVAR/ F(100,500),FO(100,500)
    COMMON/PROPS/  GAM(100,500), RHO(100,500)
    COMMON/GRDVAR/ X(100), XU(100), XDIF(100), XCV(100),
   +          Y(500), YV(500), YDIF(500), YCV(500),
   +          XL, YL, L1, L2, M1, M2
    COMMON/CINDEX/ IFIRST, JFIRST, IREF, JREF
    COMMON/SAV/FX(5500),FA(5500),TIME,DELT,TT,hfb,stp,DI(50),DDI(50)
    COMMON/SOLID/  DH(100,500), DHO(100,500),DHOO(100,500),TS,TL,DHS
    COMMON/CPOO/CPO(100,500),DKG(5500),CG(5500)
    COMMON/PROB/   DEN, COND, CP,FL,CPI(100,500),CONDI(100,500)
*   END OF COMMON BLOCK
*   ------------------

*   LET NF = 1 REPRESENT TEMPERATURE
*   -------------------------------

    DIMENSION    T(100,500)
    EQUIVALENCE  (F(1,1),T(1,1))
*   -------------------------------------------------------------------

    DO 10 I = 1, L1
      DO 10 J = 1, M1

        RHO(I,J) = DEN

10  CONTINUE

    RETURN
    END

C***************************************************************************

*   -----------------
    SUBROUTINE GAMSOR
*   -----------------
```

```
*    THE PURPOSE OF THIS SUBROUTINE IS TO ASSIGN ALL DIFFUSION COEFFICIENTS
*    AND SOURCE TERMS
*
*    THIS SUBROUTINE CAN ALSO BE USED TO STORE CONVERGENCE MONITORING DATA
*
*
     IMPLICIT DOUBLE PRECISION (A-H,O-Z)

*    COMMON BLOCK
*    ------------
C     COMMON/DEPVAR/ F(100,500)
     COMMON/DEPVAR/ F(100,500),FO(100,500)
     COMMON/COEFF/  AP(100,500), AE(100,500), AW(100,500), AN(100,500),
    +           AS(100,500), CON(100,500)
     COMMON/PROPS/  GAM(100,500), RHO(100,500)
     COMMON/SRCE/   SC(100,500), SP(100,500)
     COMMON/GRDVAR/ X(100), XU(100), XDIF(100), XCV(100),
    +           Y(500), YV(500), YDIF(500), YCV(500),
    +           XL, YL, L1, L2, M1, M2
     COMMON/CINDEX/ IFIRST, JFIRST, IREF, JREF
     COMMON/CITER/  RELAX, ITER, ITSRT, MAXIT, MXTDMA
     COMMON/SAV/FX(5500),FA(5500),TIME,DELT,TT,hfb,stp,DI(50),DDI(50)
     COMMON/SOLID/  DH(100,500), DHO(100,500),DHOO(100,500),TS,TL,DHS
     COMMON/CPOO/CPO(100,500),DKG(5500),CG(5500)
     COMMON/PROB/   DEN, COND, CP,FL,CPI(100,500),CONDI(100,500)
*    END OF COMMON BLOCK
*    ------------------

*    LET NF = 1 REPRESENT TEMPERATURE
*    -------------------------------

     DIMENSION   T(100,500)
     EQUIVALENCE  (F(1,1),T(1,1))

*    ----------------------------------------------------------------



     DO 60 J = 1, M1
       DO 60 I = 1, L1

          GAM(I,J) = CONDI(I,J)/(RHO(I,J))
         SC(I,J) = 0.0D+00
         SP(I,J) = 0.0D+00

60   CONTINUE


     END
C*************************************************************************

*    ---------------
     SUBROUTINE BOUND
*    ---------------
```

```
*     THE PURPOSE OF THIS SUBROUTINE IS TO IMPLEMENT BOUNDARY CONDITIONS

      IMPLICIT DOUBLE PRECISION (A-H,O-Z)
      LOGICAL LSOLVE, LPRINT, CONVGE, PCOEFF
      parameter (NDT=10000, NDT1=NDT+1)
*           dimension time(0:NDT),hfb(0:NDT)

*     COMMON BLOCK
*     ------------
C       COMMON/DEPVAR/ F(100,500)
      COMMON/DEPVAR/ F(100,500),FO(100,500)
      COMMON/COEFF/  AP(100,500), AE(100,500), AW(100,500), AN(100,500),
     +          AS(100,500), CON(100,500)
      COMMON/PROPS/  GAM(100,500), RHO(100,500)
      COMMON/SRCE/   SC(100,500), SP(100,500)
      COMMON/GRDVAR/ X(100), XU(100), XDIF(100), XCV(100),
     +          Y(500), YV(500), YDIF(500), YCV(500),
     +          XL, YL, L1, L2, M1, M2
      COMMON/CINDEX/ IFIRST, JFIRST, IREF, JREF
      COMMON/CITER/  RELAX, ITER, ITSRT, MAXIT, MXTDMA
      COMMON/CLOGI/  LSOLVE, LPRINT, CONVGE, PCOEFF
      COMMON/SAV/FX(5500),FA(5500),TIME,DELT,TT,hfb,stp,DI(50),DDI(50)
      COMMON/SOLID/  DH(100,500), DHO(100,500),DHOO(100,500),TS,TL,DHS
      COMMON/CPOO/CPO(100,500),DKG(5500),CG(5500)
      COMMON/PROB/   DEN, COND, CP,FL,CPI(100,500),CONDI(100,500)
*     END OF COMMON BLOCK
*     ------------------

*     LET NF = 1 REPRESENT TEMPERATURE
*     -------------------------------

      DIMENSION   T(100,500)
      EQUIVALENCE  (F(1,1),T(1,1))

*     -----------------------------------------------------------------

*     NOTES: (1) IF ALL DEPENDENT VARIABLES ARE SPECIFIED AT THE BOUNDARY NODES,
*     NO SPECIAL PROCEDURES ARE NEEDED IN THIS SUBROUTINE; (2) AT ADIABATIC OR
*     SYMMETRY BOUNDARIES, GAMMAS ARE SET TO ZERO IN GAMSOR, AND NOTHING
*     IS NEEDED IN THIS SUBROUTINE.


*      TAMB=25.D0
*      HCOF1 = 10000.D0


      DO  129 I=1,L1
129         F(I,1) = F(I,2) - HFB*YDIF(2)/CONDI(I,1)
* 129     F(I,1) =  stp
*       F(I,M1) = F(I,M2)
C--------- BOTTOM========
C==HAS TO BE REVISED====
      DO  123  J=1,M1
C      BCOF1 = CONDI(2,J)/ (HCOF1 * XDIF(2))
```

```
*123  F(1,J) = (BCOF1 * F(2,J) + TAMB) / (1. + BCOF1)
*     F(L1,J) = F(L2,J) - HFB*XDIF(L2)/CONDI(L1,J)
    F(L1,J)=F(L2,J)
123       F(1,J)=F(2,J)
C--------- TOP=====
    TAMB=25.D0
          HCONV=5.27
          EMISS=0.5
          STB=5.67D-8

    DO  126 I=1,L1
          HRAD=EMISS*STB*(TAMB**2+F(I,M1)**2)*(TAMB+F(I,M1))
          HCOF2=HCONV+HRAD
    BCOF2 = CONDI(I,M2)/ (HCOF2 * YDIF(M2))

126   F(I,M1) = (BCOF2 * F(I,M2) + TAMB) / (BCOF2 + 1)
c     F(L1,J) = F(L2,J)

CEEEEEEEEEEEEEEEEEEEEEEEEEEEEEEEEEEEEEEEEEEEEEEEEEEEEEEEEE

    END

C***************************************************************************
    SUBROUTINE CPCOND
*     ----------------


    IMPLICIT DOUBLE PRECISION (A-H,O-Z)

*     ------------
    COMMON/DEPVAR/ F(100,500),FO(100,500)
    COMMON/PROPS/  GAM(100,500), RHO(100,500)
    COMMON/GRDVAR/ X(100), XU(100), XDIF(100), XCV(100),
   +           Y(500), YV(500), YDIF(500), YCV(500),
   +           XL, YL, L1, L2, M1, M2
    COMMON/CINDEX/ IFIRST, JFIRST, IREF, JREF
    COMMON/PROB/   DEN, COND, CP,FL,CPI(100,500),CONDI(100,500)

    COMMON/SOLID/  DH(100,500), DHO(100,500),DHOO(100,500),TS,TL,DHS
    COMMON/CPOO/CPO(100,500),DKG(5500),CG(5500)
     TS=502.D0
     TL=650.D0
     TM=660
                    TSS=589
                    P=(TM-TL)/(TM-TSS)
*     DKS=240D0
*      DKL=130D0
*      CS=1000.0D0
*      CL=1200.0D0
      DKS=198.0
      DKL=89.0
      CS=917.0
      CL=1080.0
     DO 310 J = 1, M1
    DO 310 I = 1, L1
```

```
*          CS=23.33+11.92d-3*F(I,J)-1.5d4/(F(I,J)**2)
*          CS=CS*1000/24.305
*                 DKS=60+0.05*F(I,J)
*     FLL=(F(I,J)-TS)/(TL-TS) : Linear
*     FS=(1/(1-P))*(F(I,J)-TL)/(F(I,J)-TM)
*                  FLL=1-FS : Lever
                   FLL=((F(I,J)-TM)/(TL-TM))**(1/(P-1))

    IF (F(I,J).GE.TL) FLL=1
     IF (F(I,J).LE.TS) FLL=0
    CONDI(I,J)=ABS((1-FLL)*DKS+FLL*DKL)
     CPI(I,J)=ABS((1-FLL)*CS+FLL*CL)

310  CONTINUE
     RETURN
    END



C***********************************************************************

    SUBROUTINE LATENT
*    ----------------


    IMPLICIT DOUBLE PRECISION (A-H,O-Z)

*    ------------
C     COMMON/DEPVAR/ F(100,500)
    COMMON/DEPVAR/ F(100,500),FO(100,500)
    COMMON/PROPS/  GAM(100,500), RHO(100,500)
    COMMON/GRDVAR/ X(100), XU(100), XDIF(100), XCV(100),
   +           Y(500), YV(500), YDIF(500), YCV(500),
   +           XL, YL, L1, L2, M1, M2
    COMMON/CINDEX/ IFIRST, JFIRST, IREF, JREF
    COMMON/PROB/   DEN, COND, CP,FL,CPI(100,500),CONDI(100,500)
    COMMON/SAV/FX(5500),FA(5500),TIME,DELT,TT,hfb,stp,DI(50),DDI(50)
    COMMON/SOLID/  DH(100,500), DHO(100,500),DHOO(100,500),TS,TL,DHS
    COMMON/CPOO/CPO(100,500),DKG(5500),CG(5500)

     DHS=321000D0
*         DHS=217546D0
     TS=502.D0
     TL=652.D0
     TM=660
                TSS=589
*      TSS: Equilibrium solidus, P: distribution coeff.
                P=(TM-TL)/(TM-TSS)

     DO 330 J = 1, M1
    DO 330 I = 1, L1
*     FL=(F(I,J)-TS)/(TL-TS) : LINEAR
*      FS=(1/(1-P))*(F(I,J)-TL)/(F(I,J)-TM) : LEVER
          FL=((F(I,J)-TM)/(TL-TM))**(1/(P-1))
*               FL=1-FS
```

```
*      IF (F(I,J).GT.TL) FL=0
     IF (F(I,J).GT.TL) FL=1
     IF (F(I,J).LT.TS) FL=0
     DH(I,J)=ABS(FL*DHS)

330  CONTINUE
     RETURN
     END
```

APPENDIX III

A.3.1 ENTRAINMENT OF AIR FILM

When the liquid metal moves along the substrate surface, an air or gas film can be entrained at the meniscus region by viscous drag. Considering one-dimensional incompressible flow of gas under steady-state condition in the coordinate system shown in Fig. A3-1, the equation of continuity and the equation of motion reduces to:

Continuity $$\frac{\partial v_x}{\partial x} = 0 \qquad \text{(A3-1)}$$

Motion $$\rho v_x \overset{0}{\cancel{\frac{\partial v_x}{\partial x}}} = \frac{\partial P}{\partial x} - \frac{\partial \tau_{yx}}{\partial y} = 0 \qquad \text{(A3-2)}$$

Combined with the viscous shear stress τ, equation (A3-2) can be reduced to:

$$\frac{d^2 v_x}{dy^2} = -\frac{1}{\mu}\left[\frac{dP}{dx}\right] \qquad \text{(A3-3)}$$

Integrating equation (A3-3) incorporating the boundary conditions given in equation (A3-4).

$$v_x = V_S \ @\, y = 0 \ \ and \ \ v_x = V_0 \ @\, y = \delta \qquad \text{(A3-4)}$$

where $V_0 = C_D\sqrt{2gH}$, V_S is substrate speed, and δ is air or gas film thickness.

From equations (A3-3) and (A3-4),

$$v_x = -\frac{1}{2}\left[\frac{dP}{dx}\right]\left(\frac{y^2 - \delta y}{\mu}\right) + \frac{(V_0 - V_S)y}{\delta} + V_S \qquad \text{(A3-5)}$$

Here, the appropriate pressure [1] is the capillary pressure given by

$$\Delta P = \frac{\sigma}{R} = \frac{\sigma \delta''}{(1+\delta'^2)^{3/2}} \approx \sigma \delta'' \tag{A3-6}$$

where primes denote differentiation with respect to x. Therefore, $\frac{dP}{dx} = \sigma \frac{d^3\delta}{dx^3}$.

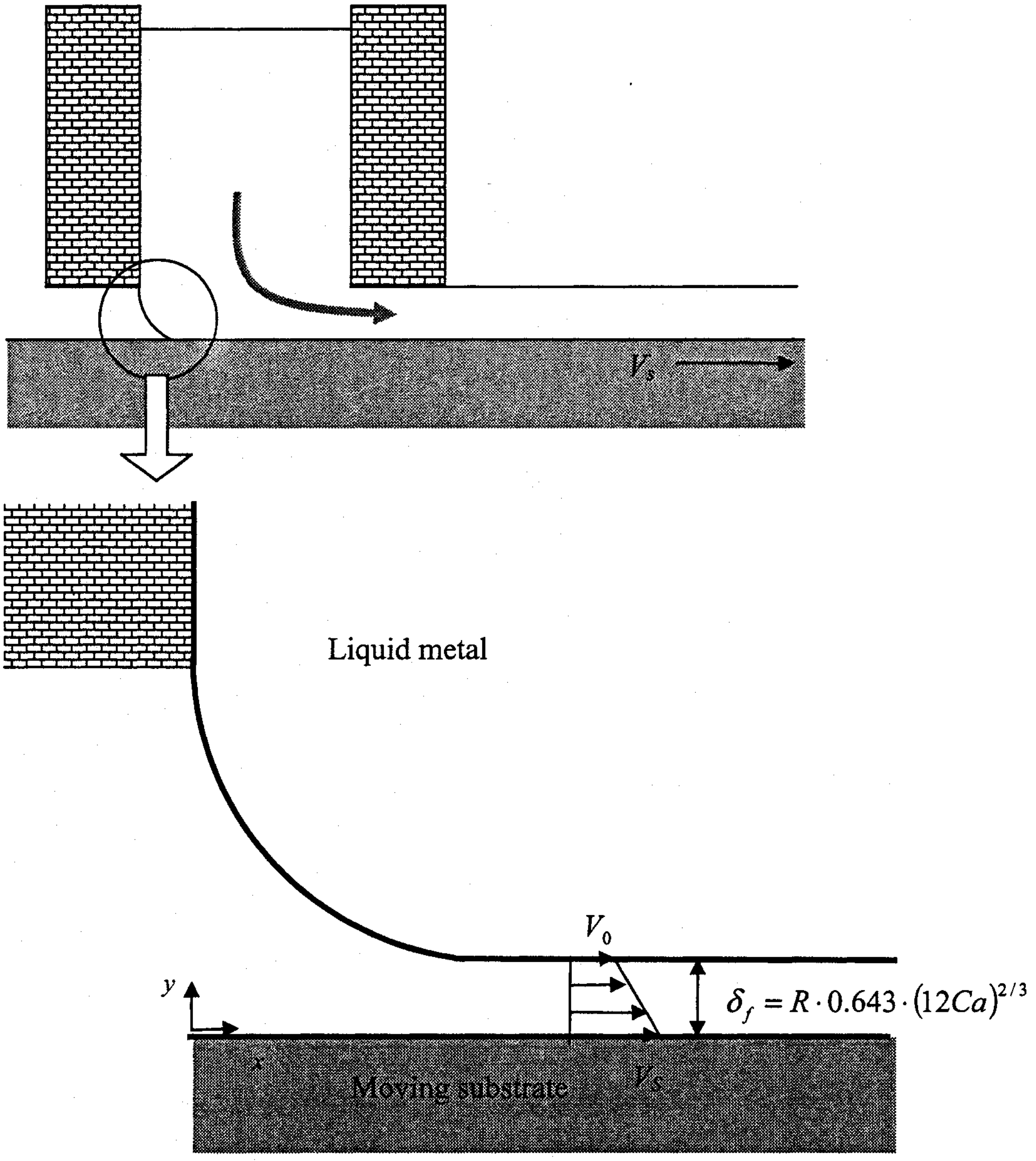

Fig. A3-1. Viscous planar flow of gas between a stagnant metal meniscus and a moving substrate

The parabolic velocity profile is

$$v_x = -\frac{\sigma}{2}\frac{d^3\delta}{dx^3}\left(\frac{y^2-\delta y}{\mu}\right)+\frac{(V_S-V_0)y}{\delta}+V_0 \tag{A3-7}$$

and the volumetric flow rate is given by

$$\dot{Q}=\int_0^{\delta(x)} v_x dy=\left(\frac{V_s+V_0}{2}\right)\delta+\frac{\sigma}{\mu}\frac{d^3\delta}{dx^3}\frac{\delta^3}{12} \tag{A3-8}$$

Far from the static meniscus region, the film thickness is constant as δ_f and the flow rate becomes

$$\dot{Q}=\overline{V}\cdot\delta_f \tag{A3-9}$$

where $\overline{V}=\frac{V_s+V_0}{2}$ is an average velocity.

From equation (A3-8) and (A3-9),

$$\delta^3\frac{d^3\delta}{dx^3}+\left(\frac{12\mu\overline{V}}{\sigma}\right)\delta=\left(\frac{12\mu\overline{V}}{\sigma}\right)\delta_f \tag{A3-10}$$

This third order differential equation (A3-10) is solved by Probstein [1], and the final film thickness is

$$\delta_f=R\cdot 0.643\cdot(12Ca)^{2/3} \tag{A3-11}$$

where R is the radius of curvature and Ca is the Capillary number (= $\frac{\mu\overline{V}}{\sigma}$).

Given the physical properties of air ($\mu=3.058\times10^{-5}\,Ns/m^2$) and $\overline{V}=1m/s$, the air film thickness is predicted as $\delta_f(Al)=11.7\mu m$ and $\delta_f(Mg)=14.8\mu m$. The maximum heat flux can be calculated from

$$q_M = h_M\left(T_{melt} - T_{substrate}\right) = \frac{k_g}{\delta_f}\left(T_{melt} - T_{substrate}\right) = \begin{cases} 2.713\, MW/m^2\, (Al) \\ 2.111\, MW/m^2\, (Mg) \end{cases} \qquad \text{(A3-12)}$$

REFERENCES

1. R. Probstein, Physicochemical Hydrodynamics, 2nd edition, John Wiley & Sons, 1994

APPENDIX IV

A.4.1 VALIDATION OF THE IHCP CODE

To validate the IHCP code programmed, analytical solution of interfacial heat flux and calculated values from the IHCP method are compared. Heat transfer through the mold with a constant interface temperature is chosen as a test analysis.

In this case, an analytical solution is available and obtained by

$$q = \frac{k_m (T_M - T_0)}{\sqrt{\pi \alpha_m t}} = \frac{(T_M - T_0)\sqrt{k_m C_{p,m} \rho_m}}{\sqrt{\pi}} \cdot \frac{1}{\sqrt{t}} \qquad \text{(A4-1)}$$

where T_M is a constant interface temperature, T_0 is an initial mold temperature, k_m is a thermal conductivity of mold, $C_{p,m}$ is a heat capacitiy, and ρ_m is a density of mold.

Temperature field inside mold has a form of an error function

$$T = T_0 + (T_M - T_0) \cdot erfc(-\frac{x}{2\sqrt{\alpha_m t}}) \qquad \text{(A4-2)}$$

where α_m is a thermal diffusivity of mold.

Using a given thermophysical property of copper mold as shown in Table A4-1, the time-dependent temperatures calculated at 1mm and 5mm from the interface are shown in Fig. A4-1.

Table A4-1. Thermophysical properties of copper mold

Properties	Cu
Initial temperature (°C)	25
Interface temperature (°C)	300
Specific heat (J/KgK)	380
Density (Kg/m^3)	8920
Thermal conductivity (W/mK)	398

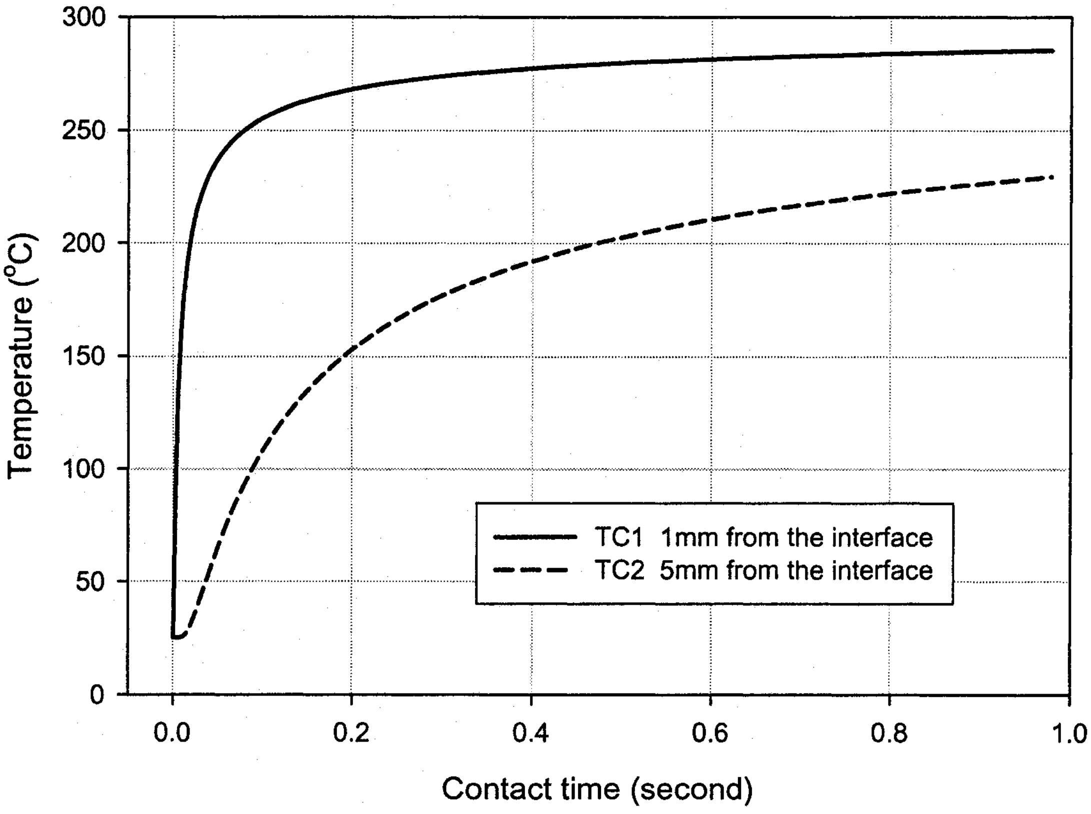

Fig. A4-1. Analytically calculated temperatures inside a copper mold

Then, the interfacial heat flux was calculated using the IHCP code based on the data from Fig.A4-1. The calculated values of heat flux as well as analytical solution are plotted together in Fig. A4-2. It reveals a good validation of the IHCP code used with the mean of relative error of about 0.7%.

In experiments, the standard deviation of thermocouple exists. If this deviation is ±1°C, the maximum error appears when the thermocouple TC1 (closer to the interface than TC2) overestimated the temperature and the TC2 underestimated the true temperature. Even in this case, the relative error was about 2%.

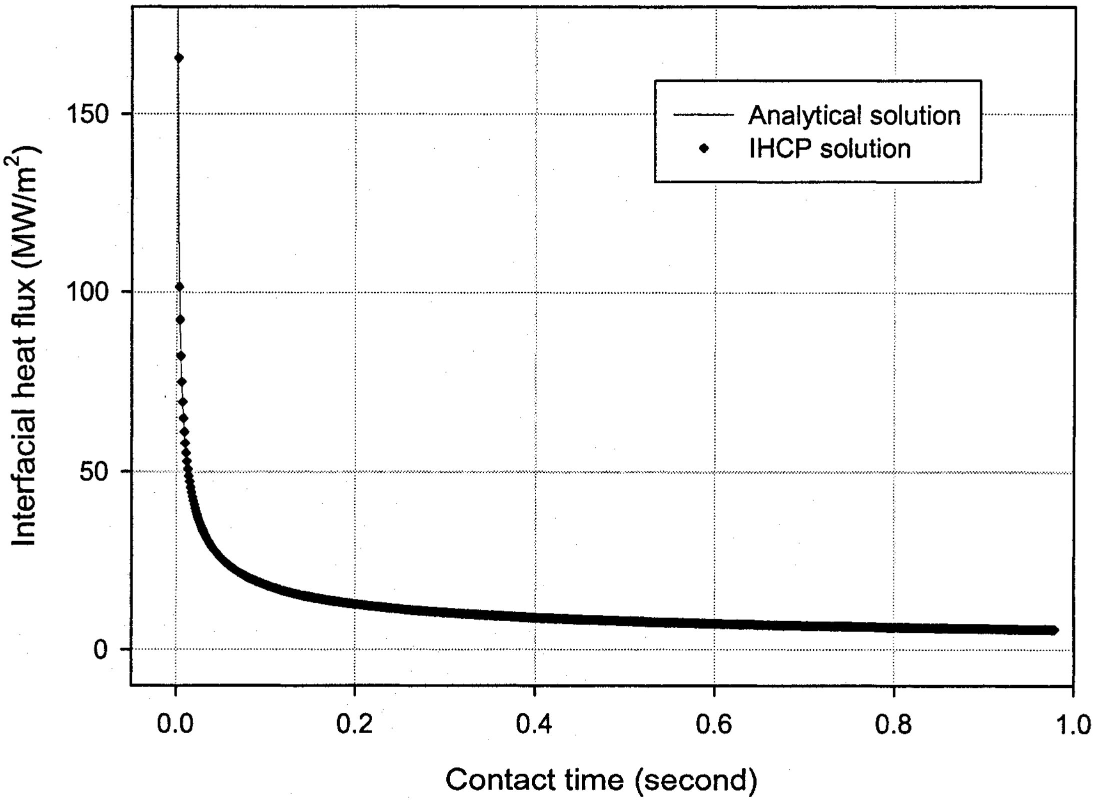

Fig. A4-2. Comparison of an analytical solution and the IHCP solution

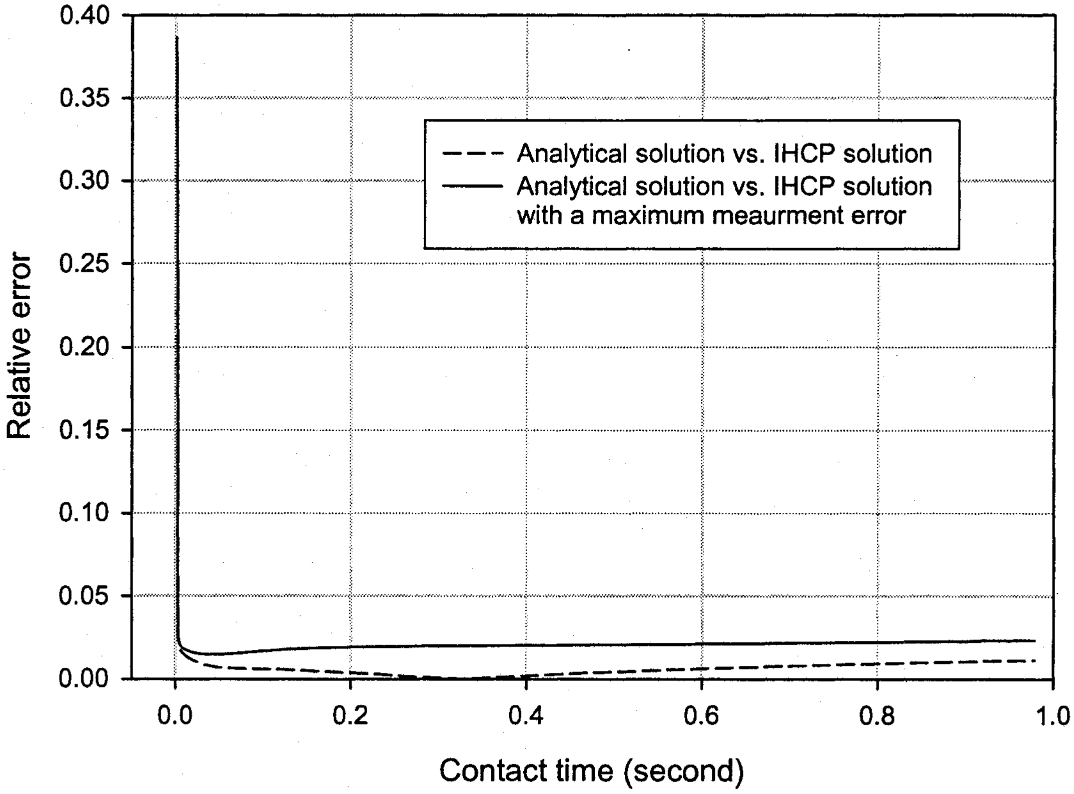

Fig. A4-3. Relative error between the analytical solution and the IHCP solution